First Observation of Accelerator Origin Neutrino Beam After Passing Through 250km of Earth

Takasumi Maruyama

30 November, 2000

abstract

We are performing the KEK-Kamioka long base-line neutrino experiment (K2K) to search for the neutrino oscillation suggested by the Kamiokande results. In order to carry out this experiment successfully, we prepared a pion monitor and a muon monitor as secondary beam monitors. The pion monitor measured kinematics of produced pions just after a production target to estimate neutrino beam properties and the muon monitor behind a beam-dump after a decay volume measured a muon profile to steer the neutrino beam.

The pion monitor successfully measured the pion kinematics. From this data, we can predict the energy spectrum of the neutrino beam at the near detector and Super-Kamiokande(SK). Regarding the ratio of neutrino event rate at the near detector and SK, we achieved the accuracy within $^{+9.1\%}_{-10.1\%}$ for the June run and $^{+5.4\%}_{-8.7\%}$ for the November run, in 1999.

The neutrino beam-line was successfully directed toward SK employing the Global Positioning System(GPS). We steered the neutrino beam direction to SK within 1 mrad with the muon monitor. The muon range detector as near detector measured the neutrino events. The neutrino beam direction to SK was confirmed by the muon range detector to be within 1 mrad. Measured properties of the neutrino beam: the profile of the neutrino beam and the energy spectrum and the angle of generated muons by charged current neutrino interactions, are consistent with the Monte Carlo(MC) expectation.

GPS system successfully synchronized the timing between KEK and SK. With utilizing this timing synchronization, $\sim 5.0\times10^{-6}$ reduction of background events is achieved, resulting 1.6×10^{-3} background events from atmospheric neutrinos.

In June and November, 1999, we injected a total of 7.5×10^{18} protons on the target of which 6.6×10^{18} is used for the analysis. Three fully contained neutrino events were observed in the fiducial volume of SK. Expected number of neutrino events at SK is calculated by use of the pion monitor and the near detector data to be $11.34^{+1.70}_{-1.83}$. The probability that we observed 3 events or less against this expectation is 0.80%. We definitely confirmed that the muon neutrino flux of the GeV energy region decreased after traveling 250 km. The standard model neutrino hypothesis is excluded with 98.4%C.L..

If we assume this deficit of the number of neutrino events is caused by the $\nu_\mu \to \nu_\tau$neutrino oscillation, the most probable combination of ($\sin^2 2\theta$, $\Delta\mathrm{m}^2$) in physical region is (1.0, 7.0×10^{-3}). At this point, the expected number of neutrino events at SK is 4.18, and probability of the case that we have 3 events is 18.2%.

Acknowledgements

I would like to express my great appreciation to my adviser, Professor A.Suzuki for introducing me to neutrino experiment. I acquired a great interest in the neutrino physics by his guidance. I would also thank him for supporting and guiding me throughout my graduate career.

I would like to show my appreciation to Professor K.Nishikawa as a spokes-person of K2K collaboration. His advise and encouragement were helpful for my thesis. He taught me a lot of things which are useful for my work. Without his help, I would never accomplish my thesis.

K2K benefits from the excellent leadership of its co-spokespersons Prof. Y.Totsuka, Prof. K.Nakamura and Prof. Y.Suzuki. They gave me advice and encouraged me in many cases.

The analysis presented in this thesis depends on the hard works of many people in the K2K collaboration: Prof. K.Kaneyuki, Prof. Y.Itow, Dr. M.Miura, Mr. S.Nakayama and Mr. S.Yamada from ICRR, Prof. M.Sakuda, Dr. Y.Oyama, Dr. T.Ishida, Dr. T.Kobayashi and Dr. Y.Hayato from KEK, Prof. T.Hara, Prof. S.Aoki, Dr. At.Suzuki, Dr. M.Kohama and Mr. T.Iwasita from Kobe University, Dr. T.Nakaya, Mr. H.Yokoyama, Mr. S.Mukai and Mr. A.Shima from Kyoto University, Mr. M.Yoshida from Osaka University, Mr. T.Kadowaki and Ms. H.Yokoyama from Science University of Tokyo and the members in USA, especially, Prof. C.K.Jung, Dr. J.Hill, Dr. W.Gajewski and Dr. S.Mine. I wish to express my special gratitude to them. I would like to thank especially for Dr. T.Ishii for his careful reading of manuscript.

I also thank to members of KEK beam channel group: Prof. M.Takasaki, Prof. K.H.Tanaka, Prof. M.Ieiri, Dr. H.Noumi, Mr. Y.Suzuki, Mr. Y.Yamanoi, Mr. Y.Katoh, Mr. M.Minakawa and Ms. E.Kusano. They gave me many suggestions for the construction of pion monitor and educations for beam properties. Without their helps, pion monitor would never be accomplished.

I am thankful to all people who maintains the 12 GeV Proton Synchrotron at KEK and Super-Kamiokande for the great effort to lead K2K experiment be successful. They gave us the pioneering long baseline neutrino experiment.

I should thank Mr. T.Inagaki for his work. I never forget hard but exciting days for the construction of K2K with him. He gave me many supports for my work.

Finally, I wish to express my deep gratitude to Dr. T.Hasegawa who is the leader of the K2K beam monitor group. His education, guidance and comments made this thesis completed.

Contents

List of Figures

List of Tables

Chapter 1

Introduction

The standard model[1, 2, 3] defines neutrino mass to be zero. Various experimental explorations have been performed to search for neutrino mass since the 1930's, when Pauli[4] predicted the existence of neutrino. The measurements are classified into three: (1)direct measurements, (2)$\beta\beta$ decay measurements, (3)neutrino oscillation measurements.

Direct measurements have been performed for three neutrino flavors, ν_e, ν_μ and ν_τ. For ν_e, the end point of the energy spectrum of the β decay electron is measured. In the process,

$$(Z, A) \longrightarrow (Z+1, A) + e^- + \bar{\nu_e},$$

the maximum electron energy must be E_{max}=m_i-m_f-m_e-m_ν, where m_i, m_f, m_e and m_ν show the masses of the initial nucleus, final nucleus, electron and neutrino, respectively. There have been many experiments using tritium β decay, which give upper limits of ν_e mass to be 2.5 eV[5]. But the fact that most of them give negative best fit values for the neutrino mass squared means there can be still unknown systematic errors in these measurements[6]. For ν_μ, the mass has been searched for using 2-body π decay at rest, $\pi \rightarrow \mu + \nu_\mu$. The given upper limit is 170 keV[7]. For ν_τ, the upper limit of the mass is given employing multi-body τ decay, $\tau \rightarrow 4(5)\pi + \nu_\tau$. This gives an upper limit of 18.2 MeV[8].

Neutrino-less $\beta\beta$ decay occurs only when the neutrino is its anti-neutrino. In other words, neutrino is a Majorana particle[9] . In this measurement, one measures the rate of neutrino-less $\beta\beta$ decay process,

$$(Z, A) \longrightarrow (Z+2, A) + 2e^-.$$

This decay rate is proportional to the weighted average of the heavy Majorana neutrino mass, $\langle m_\nu \rangle$. This phenomenon has never been observed, and the upper limit of the mass is obtained to be $\langle m_\nu \rangle$ $<$ 0.2 eV[10].

As a consequence of (1) and (2), only upper limits of neutrino mass have been given. These upper limits confirm that neutrino mass is very small and close to zero, even if it exists.

Neutrino oscillations were proposed by Z.Maki, M.Nakagawa and S.Sakata[11], and by B.Pontecorvo[12]. If the mass eigenstates of neutrinos are different from the weak eigenstates, the probability that the flavor α neutrino transforms to the flavor β after traveling distance L(km) is expressed by following formula:

$$P(\nu_\alpha \rightarrow \nu_\beta) \;=\; \sin^2 2\theta \; \sin^2\Big(1.27\Delta m^2 \frac{L}{E}\Big), \tag{1.1}$$

where, E shows the neutrino energy(GeV) and Δm^2(eV^2) shows the difference of the mass eigenvalues squared: $\Delta m^2 = m_2^2 - m_1^2$. Once the existence of neutrino oscillations is established, it means the neutrino mass is finite and lepton number is violated. This method is sensitive to very small Δm^2 if the proper distance L is chosen although this cannot measure the mass of the neutrino itself.

Regarding the neutrino oscillations, we have a strong indication from the atmospheric neutrino observation by the Kamiokande experiment. Atmospheric neutrinos are created in the atmosphere as follows. The interaction of primary cosmic rays from the universe with the atmosphere creates secondary pions and kaons. When the pions and kaons decay to muons, muon neutrinos are produced. Further, muon decay generates an electron neutrino and an (anti) muon neutrino. The ratio of muon neutrinos to electron neutrinos is reliably calculated by a Monte Carlo simulation (MC). An anomaly in the measured flavor ratio for atmospheric neutrinos was first recognized by the Kamiokande experiment[13]. IMB[14] and Soudan-II[15] experiments confirmed it. Table 1.1 shows the results of the atmospheric neutrino measurements. The observed lepton flavor ratio of numbers of events, (muon/electron), is compared to the ratio expected from MC predictions. These results clearly show that the muon neutrino flux decreases and/or the electron neutrino flux increases. Moreover Kamiokande showed an impressive zenith angle distribution of the double ratio in the multi-GeV energy region[13], as shown in Fig. 1.1. Fig. 1.2 shows the definition of the zenith angle. We can explain these phenomena by introducing neutrino oscillations with the parameters shown in Fig. 1.3[13]. This is a strong indication for neutrino mass and lepton mixing. Super-Kamiokande also measured the ν_μ/ν_e ratio to be smaller than predictions, as shown in table 1.1[16]. Their zenith angle distributions are shown in Fig. 1.4 along with MC expectations with and without neutrino oscillations[16]. Super-Kamiokande collaboration declared that they found an evidence for ν_μ oscillation based on these data.

	detector type	kt · year	$R(\nu_\mu/\nu_e)_{obs}/R(\nu_\mu/\nu_e)_{MC}$
Kamiokande (sub-GeV)	Water Cherenkov	8.2	$0.60^{+0.06}_{-0.05}$(stat.) ± 0.05(sys.) [13]
Kamiokande (multi-GeV)			$0.57^{+0.08}_{-0.07}$(stat.) ± 0.07(sys.)[13]
Super-Kamiokande (sub-GeV)	Water Cherenkov	33	0.63 ± 0.03(stat.) ± 0.05(sys.) [16]
Super-Kamiokande (multi-GeV)		33	0.65 ± 0.05(stat.) ± 0.08(sys.) [16]
IMB3	Water Cherenkov	7.7	0.54 ± 0.05 ± 0.012 [14]
Soudan-II	Iron calorimeter	3.9	$0.64 \pm 0.11\ ^{+0.06}_{-0.05}$[15]

Table 1.1: Summary of the measured R(μ/e) value of atmospheric neutrino experiments

This hint strongly urged us to study neutrino oscillations using an accelerator. The neutrino oscillation parameters ($\sin^2 2\theta$,Δm^2) suggested by the atmospheric neutrino measurements, (1.0, $10^{-3} \sim 10^{-2}$), are in reach if we set L/E of the experiment to be $10^2 \sim 10^3$ (from Eq. 1.1). In the accelerator experiments, the neutrino flux and their flavor is well known (almost pure muon neutrinos). Thus we can confirm the existence of neutrino oscillations very clearly.

In order to achieve this plan, we proposed[17] and are performing the KEK to Kamioka long baseline neutrino experiment (K2K). This is the first experiment in the world which has an earth scale baseline using an accelerator. In this experiment, L=250 km, $\langle E_\nu \rangle$=1.3 GeV and resulting L/E is roughly 200. Fig. 1.5 shows a schematic view of the K2K. Since the neutrino beam diverge after a long baseline, a far detector must be massive. Super-Kamiokande(SK) is quite proper for this purpose. We also have near detectors and secondary beam monitors inside KEK in order to measure the neutrino beam characteristics just after its generation.

In this experiment, the distance from the neutrino creation point to the detection point is fixed. Therefore we can see a clear oscillation pattern if we measure the neutrino energy precisely. Fig. 1.6 shows the expected oscillation patterns in two sets of typical neutrino oscillation parameters. The top figures show the probability of neutrino oscillations as a function of energy. The middle ones show the distortion of the neutrino flux at SK. The histogram shows the MC expected neutrino flux (units are "number of neutrinos/$\mathrm{cm}^2/10^{20}$POT(Proton On Target)"). The shaded one is the expected flux times probability. The bottom ones show the neutrino flux times the total cross section of neutrinos on water, which corresponds to the total expected number of events at SK. Distortion of the observed neutrino energy spectrum is definite evidence for the neutrino oscillation. In this thesis, we discuss the neutrino oscillation using K2K data taken during 1999. Because of small statistics, only the total

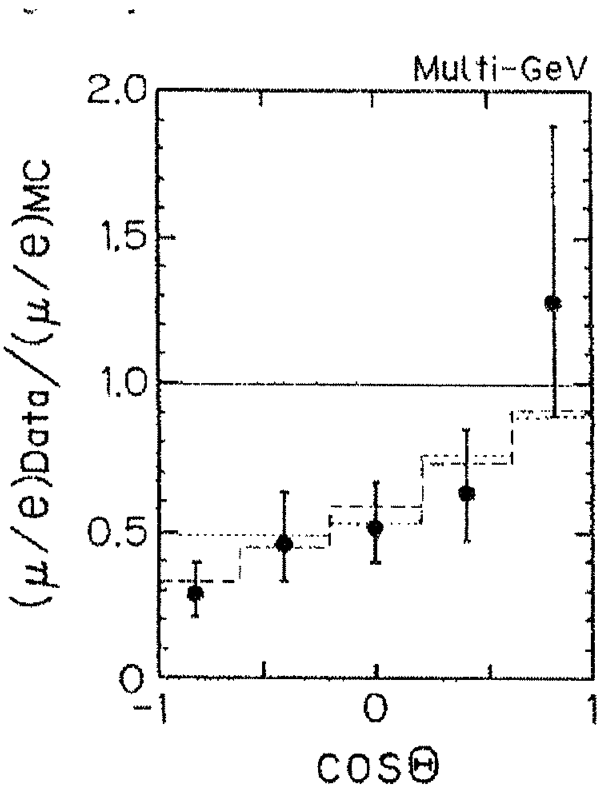

Figure 1.1: Zenith angle distribution of R(μ/e) in the multi-GeV energy range by Kamiokande [13]. The histogram shows the Monte Carlo prediction with neutrino oscillations with parameter sets ($\sin^2 2\theta$,Δm^2) corresponding to $\nu_\mu \leftrightarrow \nu_e$ ((1.0,1.8$\times$10^{-2}),dashes) and $\nu_\mu \leftrightarrow \nu_\tau$ ((1.0,1.6$\times$10^{-2}),dots) oscillations.

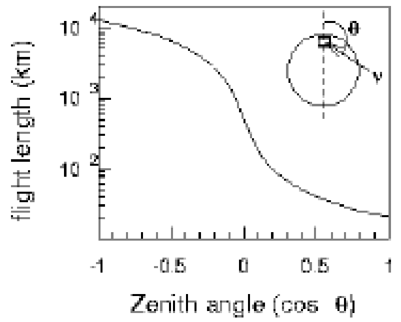

Figure 1.2: Neutrino flight length as a function of zenith angle, $\cos\theta$. The definition of zenith angle is also shown. $\cos\theta$ = -1 corresponds to upward-going and $\cos\theta$ = 1 corresponds to downward-going.

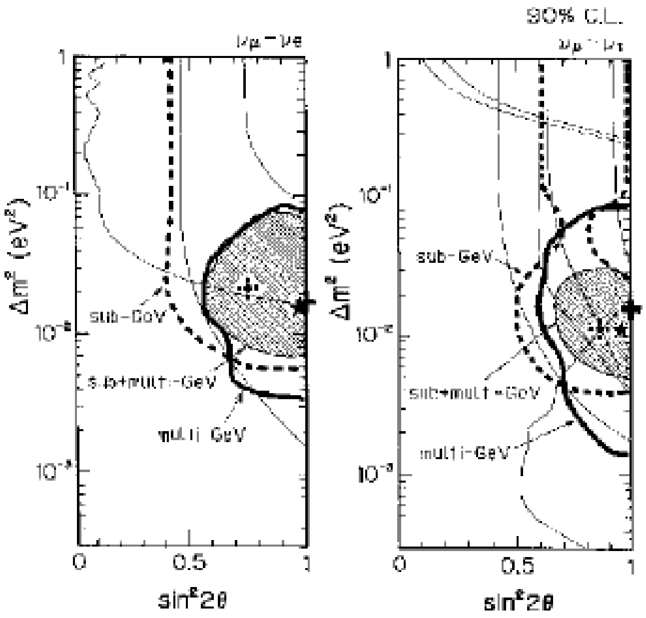

Figure 1.3: 90% C.L. allowed oscillation parameters ($\sin^2 2\theta$, Δm^2) for $\nu_\mu \leftrightarrow \nu_e$ (left) and $\nu_\mu \leftrightarrow \nu_\tau$ (right) oscillations[13]. Shaded regions show the allowed region by Kamiokande sub-GeV and multi-GeV data.

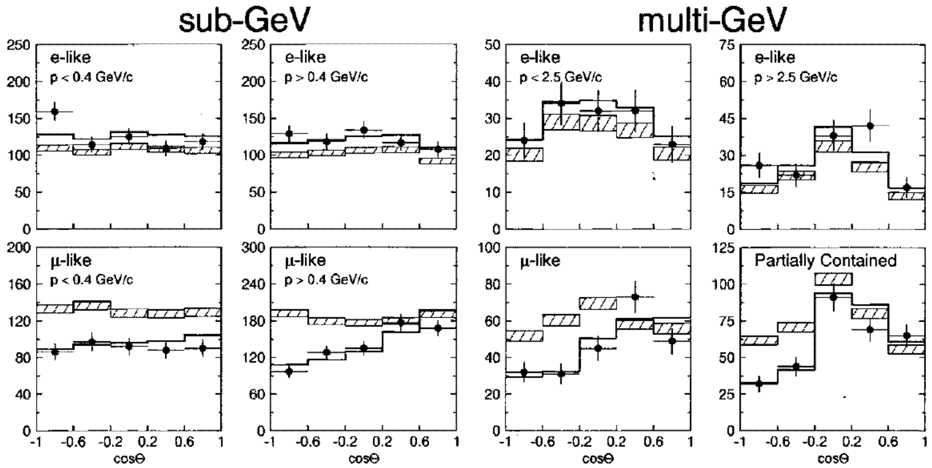

Figure 1.4: Zenith angle distribution of μ-like and e-like events for sub-GeV and multi-GeV data sets[16] by the Super-Kamiokande. Upward-going particles have cosΘ $\leq$ 0 and downward-going particles have cosΘ $\geq$ 0. Sub-GeV data are shown separately for p$\leq$400 MeV/c and p$\geq$ 400MeV/c. Multi-GeV e-like distributions are shown for p$\leq$2.5 GeV/c and p$\geq$2.5 GeV/c and the multi-GeV μ-like are shown separately for FC(Fully Contained in the fiducial volume of the Super-Kamiokande detector) and PC(Partially contained in the fiducial volume of the Super-Kamiokande detector) events. The hatched region shows the Monte Carlo expectation for no oscillations normalized to the data live time with statistical errors. The bold line is the best fit expectation for $\nu_\mu \longleftrightarrow \nu_\tau$ oscillations with the overall flux normalization fitted as a free parameter.

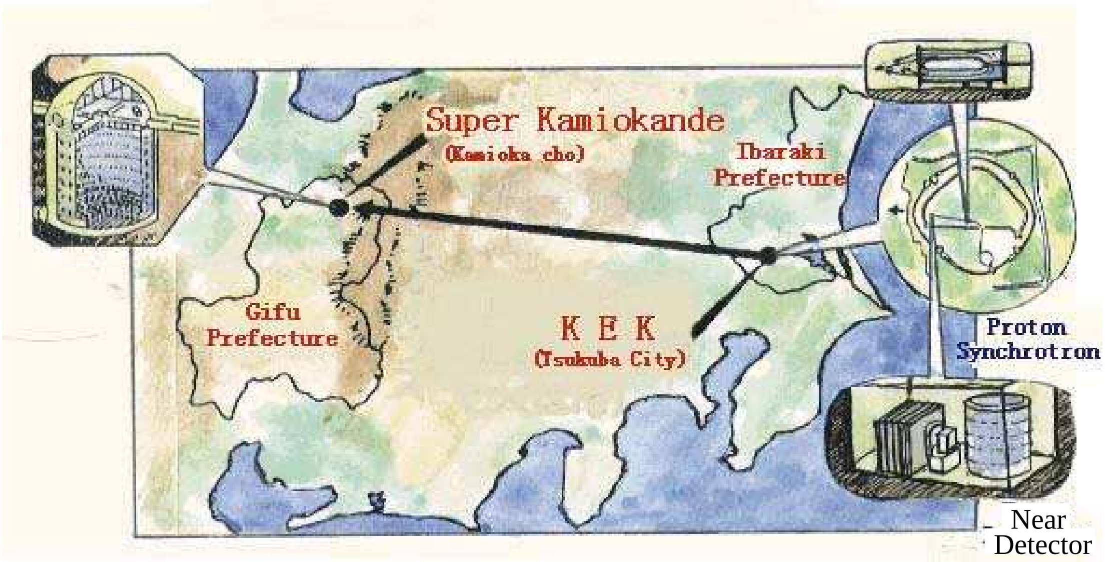

Figure 1.5: Schematic view of K2K

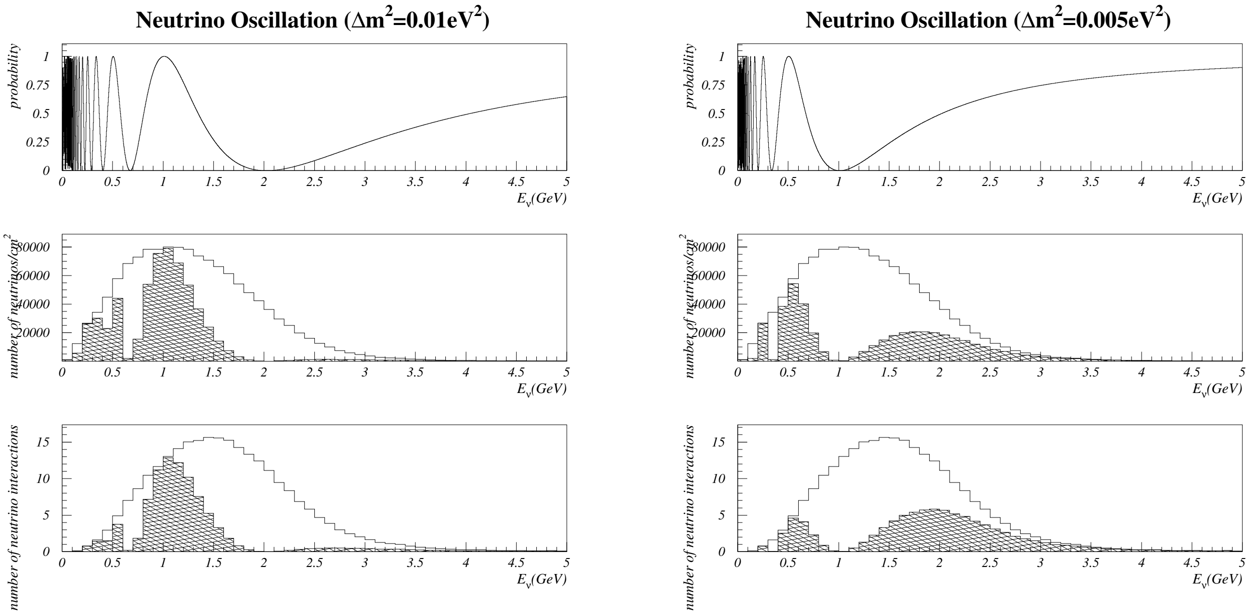

Figure 1.6: Neutrino energy spectrum distortion in the K2K in two Δm^2 cases. (Δm^2=0.01 (Left) and Δm^2=0.005 (Right), $\sin^2 2\theta$=1) In both the left and right figures, the top figure shows the probability of neutrino oscillations as a function of energy. The middle one shows the distortion of the neutrino flux at SK. The histogram shows the MC expected neutrino flux (units are "number of neutrinos/cm^2/10^{20}POT(Proton On Target)"). The shaded one is the expected flux times the probability. The bottom ones show the neutrino flux times the total cross section of neutrinos on water, which corresponds to the total expected number of events at SK.

number of neutrino events are used for the oscillation analysis instead of the energy spectrum.

In chapter 2, the key issues for the K2K are described. In chapter 3, we will describe the set-up of the K2K. In chapter 4, the hardware details of the muon monitor and the pion monitor are described. In chapter 5, Monte Carlo simulations which are used in this experiment are described. Further, we describe the measured properties of the neutrino beam, using the muon monitor (chapter 6), using the pion monitor (chapter 7) and using the near detector (chapter 8). Chapter 9 describes the way to get the expected number of neutrino events at SK. And chapter 10 describes the observation at SK. Finally we compare expected and observed number of neutrino events at SK. Its implication for the neutrino oscillation hypothesis is also discussed.

Chapter 2

Key Issues for KEK-Kamioka Long Baseline Neutrino Experiment (K2K)

As shown in Fig 1.5, K2K is the first experiment in the world which has an earth scale baseline using an accelerator. Therefore we have first trials to achieve this experiment, as follows;

1. Determination of the neutrino beam direction from KEK to SK with a few mrad precision.
2. Timing synchronization between KEK and Kamioka.
3. Prediction of the neutrino flux at SK based on the KEK measurement.

2.1 Precise Neutrino Aiming from KEK to Kamioka

2.1.1 Beam Direction Survey Employing Global Positioning System(GPS)

Beam-line at KEK has to be constructed with a correct direction in order to shoot SK with the neutrino beam. For this goal, in the construction of the beam-line, the ideal schedule would be that: (1) one defines the position of the production target, (2) measures positions of the target and SK to know the beam direction, (3) define the beam-line, (4) constructs the beam-line tunnel and places the beam-line elements along the beam-line, although it was parallelly processed in reality. Item (2) is the most difficult hurdle in these processes.

Strictly speaking, our job to achieve (2) is to know the latitude, longitude and height above the sea of the target at KEK and the SK detector. One may utilize the geodetic network, constructed so far by Geographical Survey Institute (GSI) with standard optical surveying and leveling, where one make local surveys independently at KEK and SK with referring to the nearest triangulation points. However it is known that the network has integrated distortion [18].

Thus we use GPS system to do this. This way is most reliable and indispensable at present [19].

GPS system consists of 27 operational satellites of US Naval Observatory (USNO). Each satellite contains an atomic clock system; satellites emit the timing signals from it. Moreover they also emits their own positions at the same time. The atomic clocks inside the satellites are monitored and calibrated using USNO Master Clock periodically. Orbits of the satellites are also calculated and renewed periodically. A GPS receiver installed on the ground receives the signals from 4$\sim$6 satellites simultaneously. It measures its own position (latitude and longitude and hight above the sea) and timing accurately.

We surveyed both the target position and SK using GPS receivers. A GPS receiver know its own position as explained above. However we use a relative measurement of GPS receivers since it can cancel out most of systematic errors* . We defined the origin at a triangulation point at KEK. And

---

* Relative measurement allow to measure both positions with a few mm precision, though a GPS receiver alone with precision of a 10 meter order. Cancelable errors are 1)the precision of the orbit of GPS satellite, 2)the condition of ionosphere and atmosphere, 3)the noise of the receiver and so on.

we transfered the survey point step by step, like KEK→Kamioka Town→Kamioka mine→SK. Except the final survey step, we surveyed each point using GPS. Final survey cannot use GPS system since SK is located 1000 meter underground in the Kamioka mine. SK survey was performed using normal optical survey and leveling from the entrance of the mine to the GPS surveyed points.

Reference[19] describes the details and the results of this measurement. Final positions of target at KEK and SK with global ellipsoidal coordinate system, WGS-84[20] are summarized in table 2.1.

	Latitude	Longitude	Height above the sea
Target at KEK	$36°09'14.9531''$(N)	$140°04'16.3303''$(E)	70.218m
SK	$36°25'32.5862''$(N)	$137°18'37.1214''$(E)	371.839m

Table 2.1: The positions of target at KEK and SK

As the results of this survey, direction of our beam-line was defined. For example, bending angle to the underground is $1°04'30''$.

We estimated the error of this direction, by GPS position reproducibility test after the construction of the beam line. According to this results, the error of the beam direction is less than 0.1 mrad. It is 10 times better than the physics requirement. We cleared the first barrier of the K2K requirement.

2.1.2 Experimental Proof of Neutrino Beam Aiming

Once beam-line was directed correctly, steering the beam and checking the direction of beam become essential.

We have two systems to check the neutrino beam direction. One system is the muon monitor to monitor muons which are the particles of decayed partner of neutrinos in the beam-line. The other is near neutrino detector, which detect the neutrino induced events directly.

The muon monitor has the advantage of being able to check the beam direction spill by spill since the muon intensity is high. This is the only way to check the stability of the beam direction in spill-by-spill basis, and to steer the beam during beam tuning. On the other hand, measuring the neutrino events takes long time to accumulate significant statistics. It is not useful for the beam tuning. However the validity of the beam direction tuned by muon distribution must be confirmed by neutrino distribution itself.

Location and set-up of these detectors will be described in chapter 3 and 4.

2.2 Timing Synchronization between KEK and Kamioka by GPS

Generally speaking, a ratio of signal to noise (S/N) of the neutrino experiment is small since cross section for neutrino is quite small. Therefore neutrino experiment uses the fast extracted beam from the accelerator, and get better S/N ratio employing the timing information. The timing information is indispensable for this experiment particularly because 250 km long baseline reduces the neutrino flux much.

We achieved the fast extraction of the beam successfully[21]. As a result, we have the potential of $\sim 10^6$ gain for S/N since our spill has 1.1 μs time length per 2.2 sec repetition. The remaining thing to do is to link the timing information from KEK to SK

We cannot connect KEK to SK using normal cables. Thus we employ the GPS system again to achieve this. As described in the section before, a GPS receiver can get absolute timing information on the earth in principle.

We installed GPS receivers both at KEK and SK for synchronization. These are non-military GPS receivers, nevertheless it can measure the time with 100 ns accuracy[†] . Beam firing time is recorded in the beam-monitors data at KEK. Furthermore we record the time information on each

---

[†] From 2000, we can get more accurate timing information thanks to the decision of the American government.

event at SK. Then we can identify the events associated with beam. Actually we measured the timing difference between GPS receivers at KEK and SK by moving atomic clock. As a result, difference $|T_{KEK}\text{-}T_{SK}|$ is 115 ± 273 ns[‡] . This shows GPS receivers give reasonable time information.

Reduction factor of background events is 10^{-6} level using this strategy as planned. Event rate induced by atmospheric neutrinos are about 8 events/day; This rate becomes negligibly small comparing to beam associated events after the timing cut.

2.3 Prediction of the Neutrino Properties at Kamioka by means of Measurement at KEK

2.3.1 Measurement by Near Detector

A near detector is located at 300 meter from the target. This detector measures the flux and the spectrum of the neutrino beam just after its creation. This information is used to predict the neutrino flux at SK.

2.3.2 Measurement by Pion Monitor

K2K would be much easier if neutrino source were a point like. Because, in this case energy spectrum at the near detector is same as SK, and intensity is reduced as a function of $1/r^2$ (r:distance from source to detector). However actual source is not point like. Strictly speaking, from SK the neutrino source is regarded as a point, but from the near detector it cannot because of too short distance between the source and the detector (100∼300 meter). Fig. 2.1 shows the schematic view of this situation. The near detector feels the length and the width of the decay pipe.

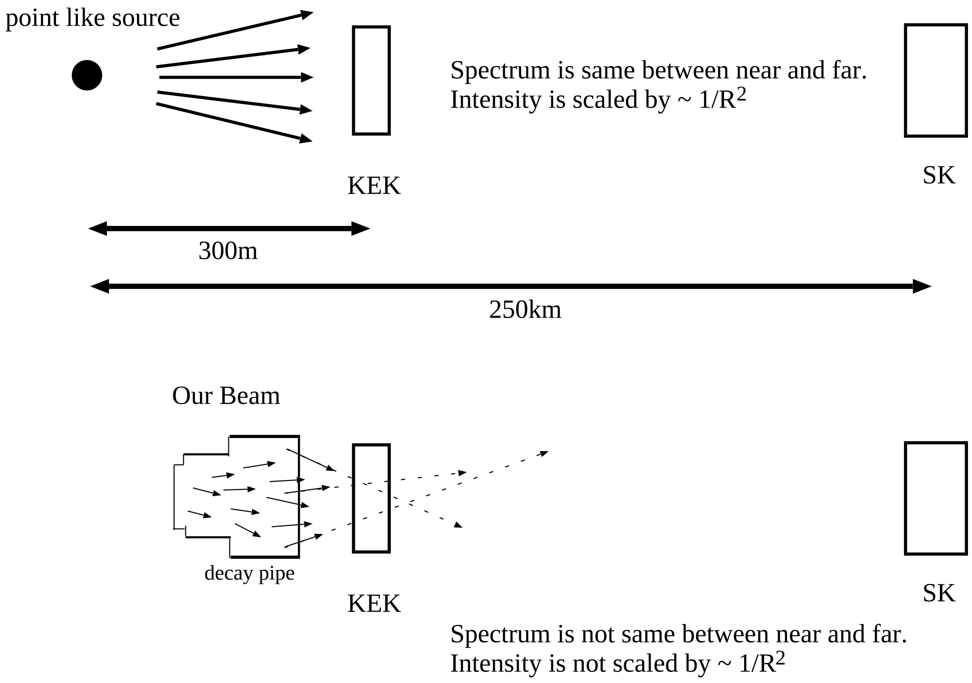

Figure 2.1: The schematic view of our beam

This means the energy spectrum at the near detector is different from SK and the intensity is not proportional to the $1/r^2$. In other words, the near detector information of the event number and energy spectrum is not enough to predict the neutrino flux at SK. Fig. 2.2 shows the neutrino

---

[‡] Error comes from our atomic clock

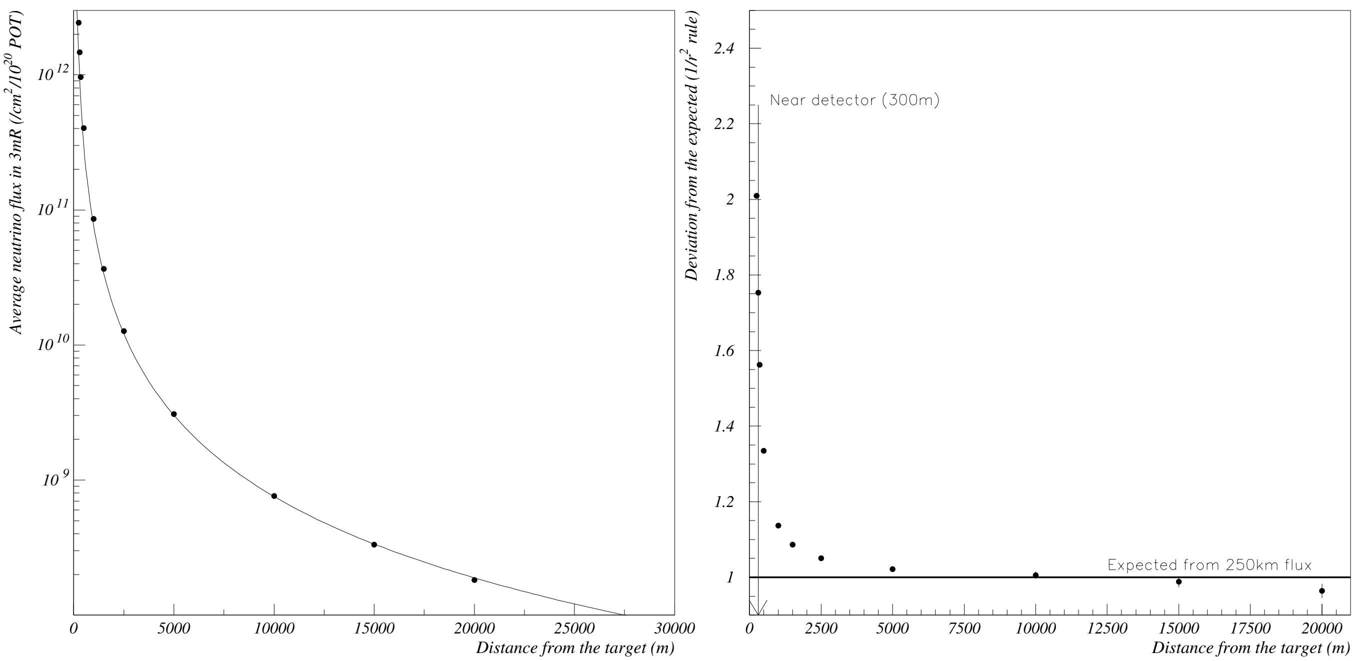

Figure 2.2: The average neutrino flux in 3m radius in various r positions and deviations from the expected 1/r^2 rule

intensity in 3 meter radius in various distances from the target and deviations from the expected 1/r^2 rule.

Needless to say, we have MC simulation to do it. But we have an large uncertainty of pion production model at the target in the simulation; Pion is the source of neutrino. This limits the simulation ability. We must reduce this uncertainty using other methods as much as possible.

To solve this problem, we designed a pion monitor. This detector measures the angle and the momentum of pions before the decay tunnel to know the property of neutrino sources. Because of the MC free analysis of the pion monitor, we do not have any problems even if real pion production is different from one used in the MC. Using this knowledge, we can predict the neutrino energy spectrum at an arbitrary distance.

Principles and designs of this detector will be described later.

2.4 Stability of neutrino beam

The stable quality: intensity, direction and spectrum, of the neutrino beam is indispensable for the K2K. They are proved by the secondary beam monitors and the near detector, as explained later.

Chapter 3

Experimental Set-up of K2K

The setup of the K2K consists of the KEK site and the Kamioka site, which are apart each other by 250 km. Schematic view of whole K2K is already shown in Fig. 1.5. Fig. 3.1 shows components of this experiment inside KEK in detail.

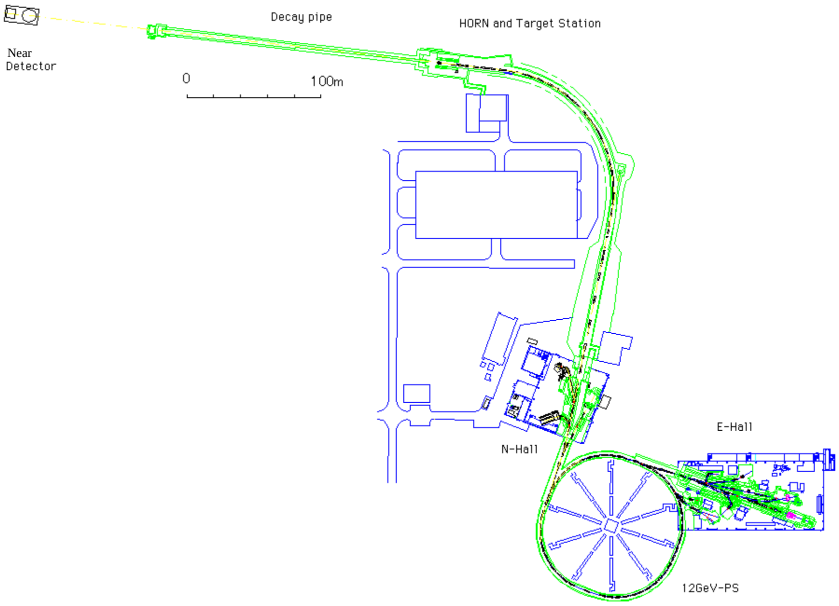

Figure 3.1: Setup in the KEK site consisting of the 12 GeV Proton Synchrotron, neutrino beam-line and near detector.

The neutrino beam-line to generate the neutrino beam and the near detector to measure the characteristics of neutrino beam are located inside KEK.

3.1 Horn Focused Wide Band Neutrino Beam Line at KEK

K2K has the following components as the beam-line as shown in Fig. 3.1.

1. KEK 12 GeV Proton Synchrotron(PS)
2. Proton extraction line
3. Horns (Magnet/Target)

4. Decay tunnel
5. Monitors

In this section, each component of this neutrino beam-line in Fig. 3.1 is described. ([22])

3.1.1 KEK 12 GeV Proton Synchrotron(PS)

Fig. 3.2 shows a schematic view of 12 GeV Proton Synchrotron. (Direction of this figure is different from Fig. 3.1.) The proton beam is extracted to the neutrino beam-line from the "EP1" beam channel.

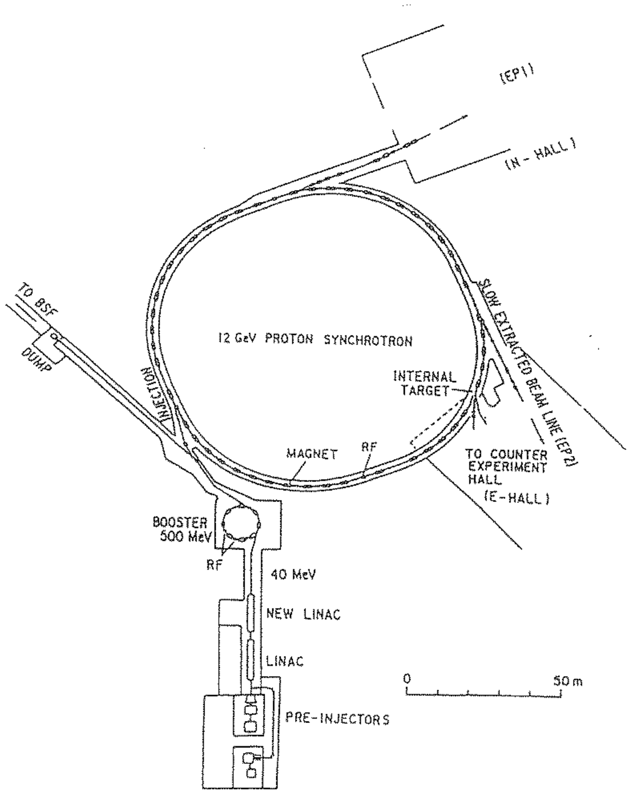

Figure 3.2: Schematic view of the 12 GeV Proton Synchrotron

Protons are accelerated by the following procedures:

- extraction of negative ions from an ion source,
- acceleration by a 750 keV Cockroft-Walton Accelerator,
- acceleration by a 40 MeV Alvarez-type LINAC,
- conversion of negative ions to positive ones with a carbon film,
- acceleration by a 500 MeV Rapid-Cycle Booster Synchrotron,
- acceleration by the 12 GeV Proton Synchrotron.

Accelerated protons are extracted from the 12 GeV PS in a fast extraction mode (Repetition: 2.2 sec, Spill :1.1 μsec). The micro-structure inside a single spill corresponds to the harmonic number of the main ring which is 9. As shown in Fig. 3.3, we can observe this micro-structure using Current Transformers(CTs: which we describe later) after extraction. For more details, see [23, 21].

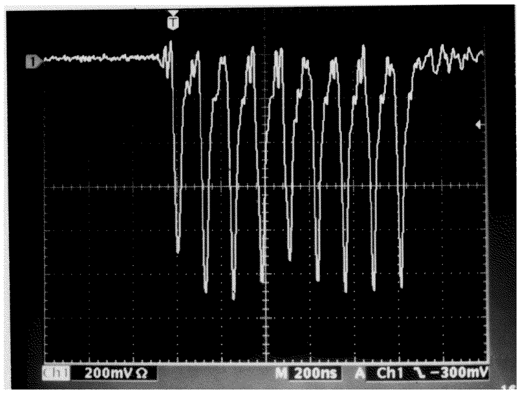

Figure 3.3: Oscilloscope photograph of the micro-structure in the beam

3.1.2 Primary Proton Beam Transport Line

We have a kicker magnet for the fast extraction at the extraction point of the accelerator. Kicker, septum, and bump magnets lead the proton beam to the neutrino beam-line [21]. Fig. 3.4 shows the neutrino beam-line after the extraction.

The proton beam direction is toward the north just after the extraction point and it must be bent towards Kamioka employing the results of survey (about 90° to the west). An arc section of the beam-line, which consists of 18 bending magnets and 18 quadrupoles, meets that request.

The target station was built after the arc section. The proton beam is finally focused on the neutrino production target at the target station. A steering magnet is placed just before the target to direct proton beam to SK, about 1° downward from the level of the production target (Fig. 5.1).

We use TRANSPORT[24] and DECAY-TURTLE[25] program to optimize the beam-line optics [19]. Thanks to this optimization, the actual transport efficiency of this beam-line is about 85%.

3.1.3 Horn Magnets and Target

There are two magnetic horns in the target station to efficiently focus the pions, the parent particles of neutrinos. Figs. 3.5 and 3.6 show the schematic view and the photograph of the two magnetic horns. The first horn has dimensions of 2.37 meter in length, and 0.70 meter in diameter. The second horn has dimensions of 2.76 meter in length and 1.65 meter in diameter, located 8 meter downstream of the first horn. It is needed to efficiently increase the neutrino flux in the forward direction since the momentum distribution of the secondary pions is wide (from 0 to 10 GeV/c).

Due to the low-energy feature of our experiment, our design is such that the target is inside the 1st horn in order to focus pions more efficiently. The horns and the target are made from Aluminum alloy. The target is 66 cm long and 20 mm in diameter in June, 30 mm in November. This length corresponds to 1.5 interaction lengths. MC simulation shows almost all protons interact* with the target thanks to the magnetic field inside the horn.

In contrast, other parts of the horn through which the secondary particles pass, are required to be as thin as possible in order to minimize the absorption losses of pions. Thus we designed and manufactured horns carefully so as to have mechanically enough strength to stand the electromagnetic force and thermal expansion.

We drive the horns every 2.2 sec with a 2 ms long 250 kA pulsed current like Fig. 3.7. We need to synchronize them with the fast extracted beam (1.1 μs bunch width) to generate the toroidal magnetic fields with respect to the beam axis [26]. We cannot use DC current because no power

---

* include elastic scattering

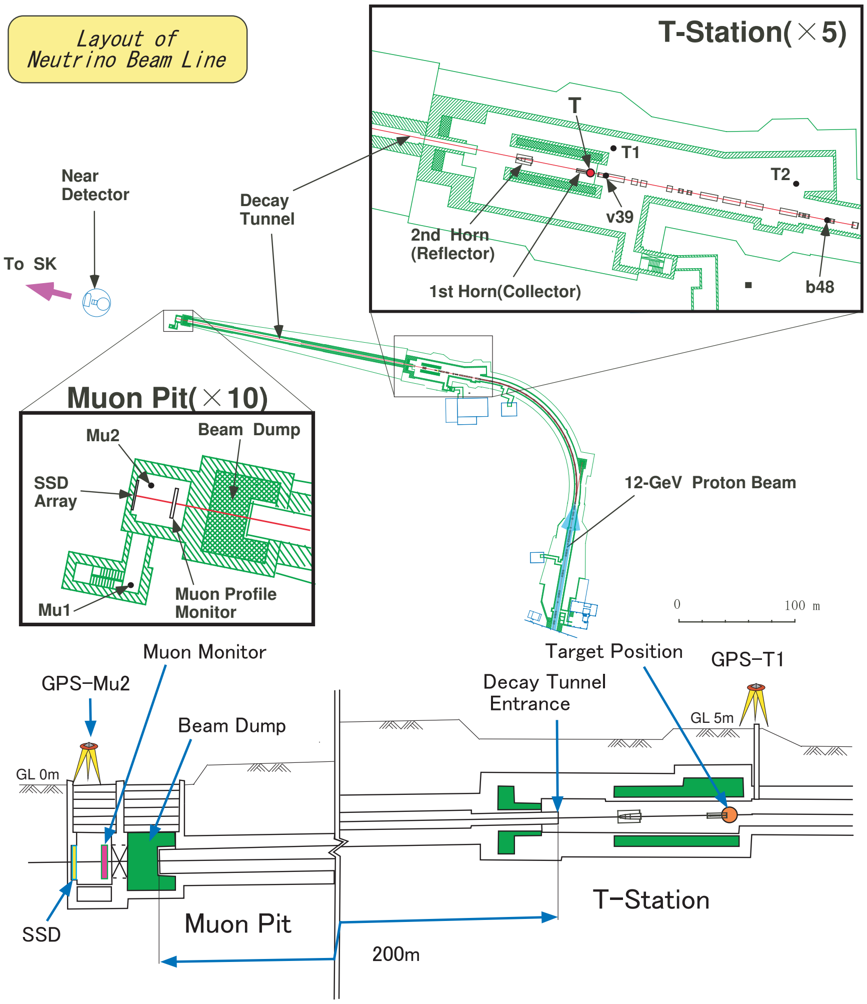

Figure 3.4: Schematic view of the neutrino beam-line and near detector, after 12 GeV-PS

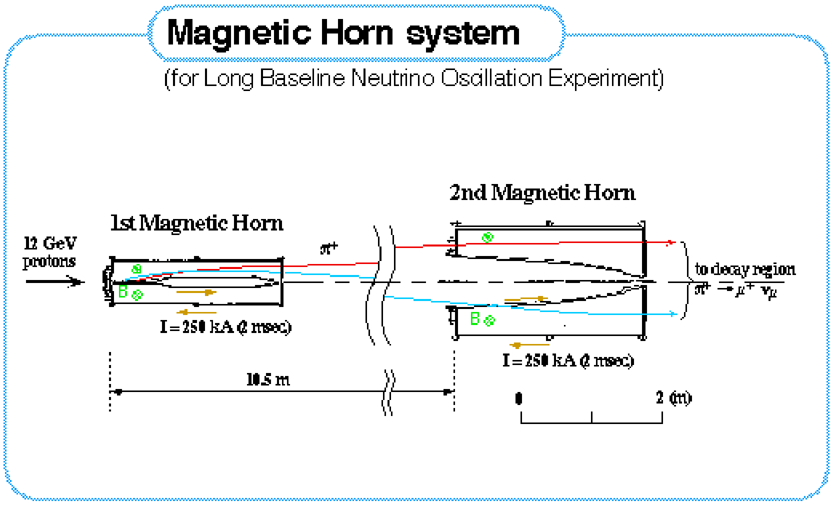

Figure 3.5: Schematic view of the horns.

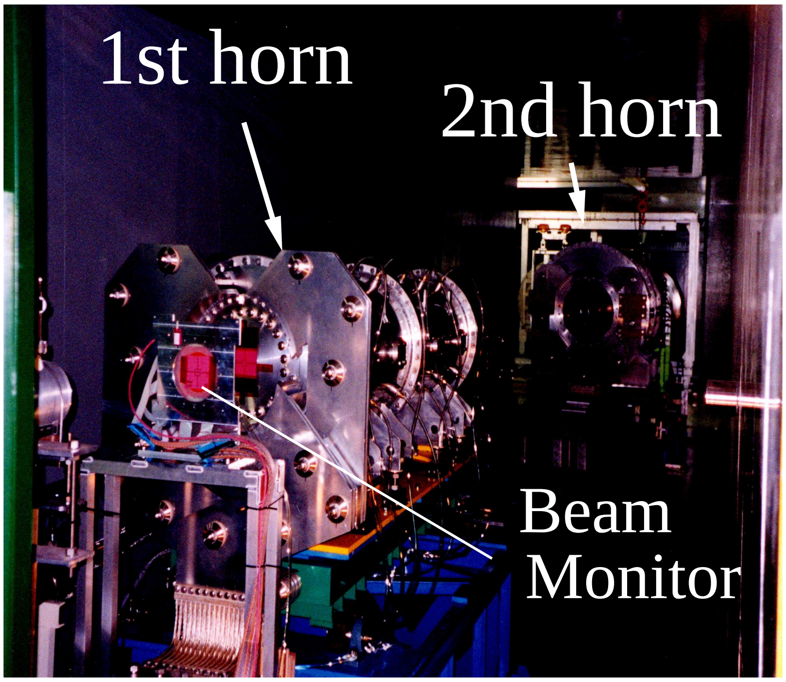

Figure 3.6: The photograph of the horns.

supply can provide 250 kA. Even if such a power supply exists, the horns could not dissipate the heat.

According to the calculation, the strength of the magnetic field B(kGauss) at R(cm) distance from beam center is given by;

$$B = \frac{I}{5.0 \cdot R}, \tag{3.1}$$

where I is the current supplied to the horn magnets in units of kilo-ampair. Hence we have 50 kGauss at R=1 cm. (This formula is correct in the air part of horn)

Fig. 3.8 shows the capability of our horn system. The Shaded region shows the MC simulated neutrino flux at SK with the horn current of 0 A, and the histogram shows that of 250 kA (target is 30 mmϕ). The simulated neutrino flux above 0.5 GeV using 250 kA current supplied to the horn magnets is about 22 times more than that of 0 kA.

Various measurements have been done to know the characteristics of this horn system. For example, magnetic field measurements using coil, performance test of the cooling system, and so on. These are summarized in [27, 28].

The measured radial dependence of magnetic field is consistent with the calculation [27]. However, we found some azimuthal direction dependence on magnetic field strength [28] like Fig 3.9. This causes some systematic error on the K2K analysis. It will be discussed later.

We must take the different beam conditions in June and November into account because our 1st horn was changed. We changed the diameter of the target part of the 1st horn in diameter from 20 mm ϕ to 30 mm ϕ in order to strengthen the weakest part against the electromagnetic force. Thus we can also change the current supplied to the horn magnets from 200 kA to 250 kA thanks to this building-up.

3.1.4 Decay Tunnel

The lifetime of pion: 2.6×10^{-8} sec ($c\tau = 7.8$ m) is prolonged by a Lorenz factor.

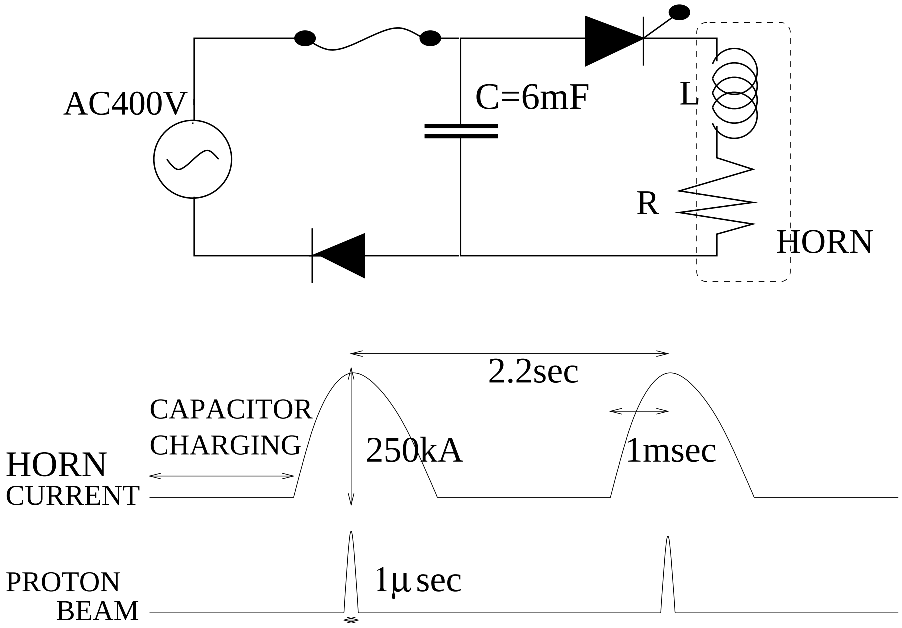

Figure 3.7: The pulsed current supplied to horn magnets[27]

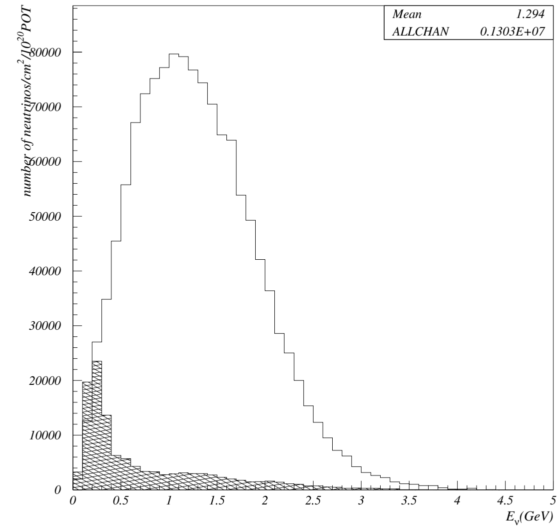

Figure 3.8: Capability of our horn system. The shaded histogram shows the MC simulated neutrino flux at SK with the current supplied to the horn magnets of 0 kA, and the histogram shows with that of 250 kA. (target is 30mm ϕ)

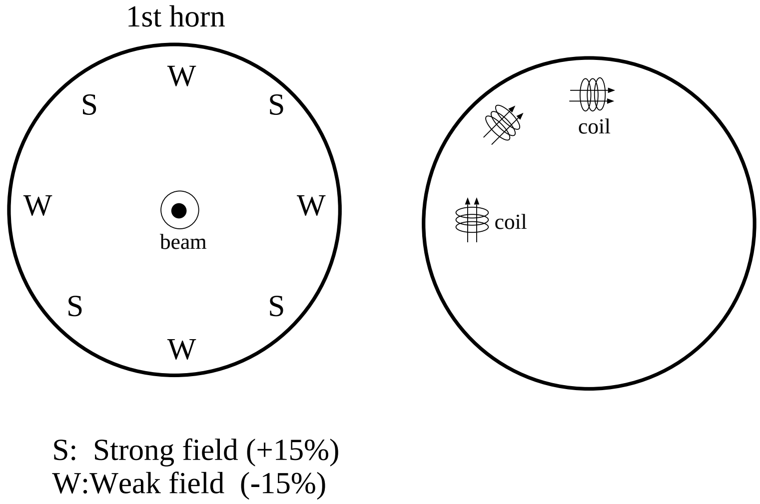

Figure 3.9: Measured horn magnetic field

In order to make pions decay to neutrinos efficiently, we designed a 200 meter long decay tunnel which has a radius of 0.75, 1.0 and 1.5 meter. Fig. 3.10 shows the schematic view of decay pipe of this experiment.

The muon monitor is installed after the beam dump to monitor the beam direction and intensity. It is described later (chapter 4).

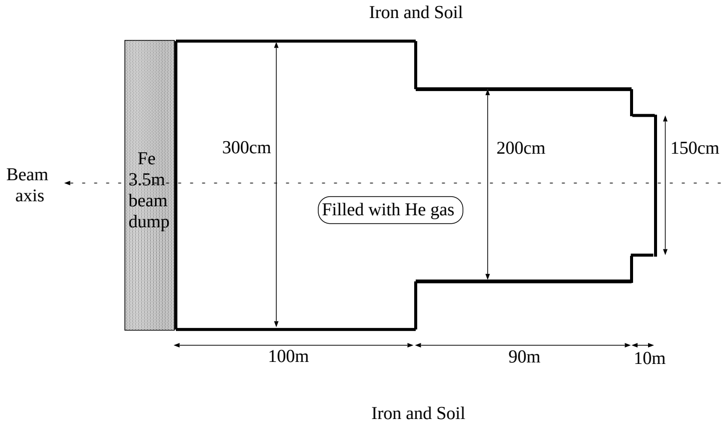

Figure 3.10: Schematic view of the decay pipe.

The decay pipe is filled up with helium gas because the interaction length of helium gas is about 5 times longer than air. (Interaction length of helium: 3.64 km(STP), that of Air: 0.731 km(STP)). It is also important to reduce the number of neutrinos produced in the gas which may cause uncertainty in this experiment.

3.1.5 Primary Beam Monitors

Current Transformer (CTs)

CT is a kind of coil sensitive to the beam current. The schematic view of CT is shown in Fig. 3.11.

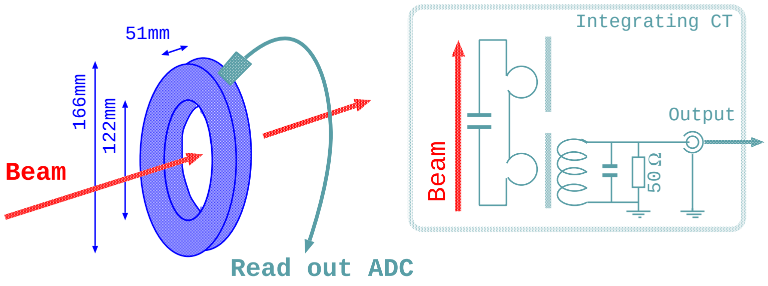

Figure 3.11: Schematic view of the CT

There are 13 CTs in the primary beam-line (Table 3.1). They are used as proton beam intensity monitors at various points. Comparison of these CT values gives information on the transport efficiency (= down stream intensity/ upstream intensity). The efficiency in the first run time is typically ~85% from the extraction point to the target.

Each CT is calibrated using pulse current and beam as well. The absolute proton number is known within 10%.

Segmented Plates Ionization Chambers (SPICs)

SPICs are used for the profile measurement of the primary protons. There are 28 SPICs in the beam-line from the extraction point to the entrance of the decay pipe (Table 3.1). The principle of ionization chambers is shown in Fig. 3.12

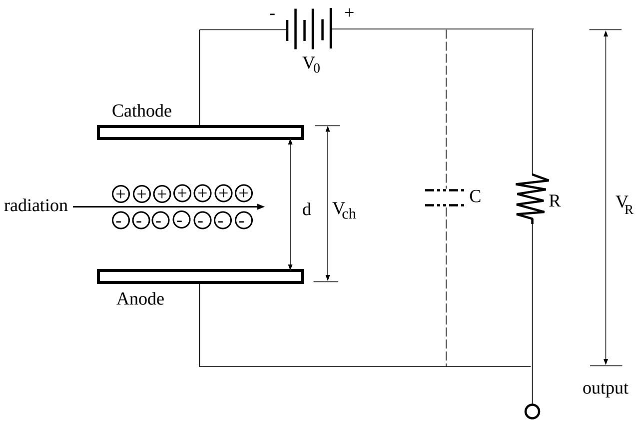

Figure 3.12: The principle of the ionization chamber

Filled gas in the detector is ionized by radiation. Created electrons (or positively charged ions) are gathered at the anode (or cathode) . Finally collected electrons (ions) can be taken as the electric signal. General properties of ionization chambers are described in [29].

The SPICs used in the K2K have segmented anode to measure the particle density in a place normal to the beam like Fig. 3.13.

It consists of three copper sheets with thickness of 28 μm. The central one is for the cathode plane (-HV), and the others are for horizontal and vertical readout cathode (GND) planes. The readout planes have 32 channels for x and y readout. The proton beam directly hits this chamber, thus this copper is as thin as possible. Most of(26 out of 28) the chambers have a 5 mm pitch stripe, except one chamber before the target which has a 1.27 mm pitch, and one chamber before the decay pipe which has a 2 cm pitch. These monitors are quite useful for the steering of the beam. The SPICs

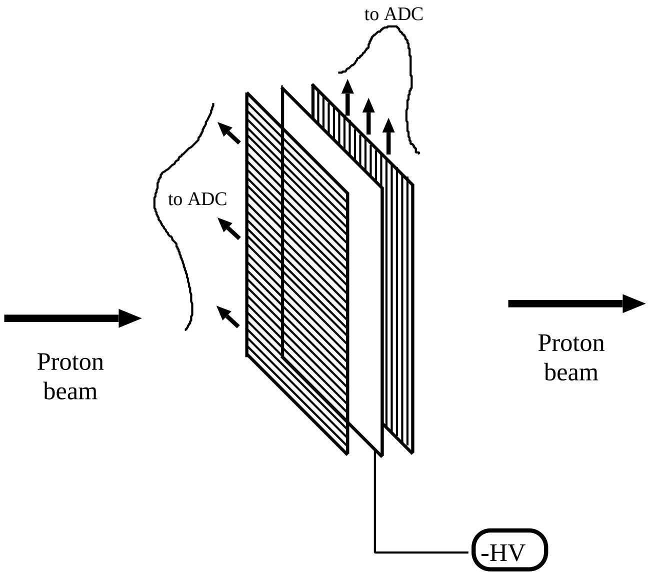

Figure 3.13: Schematic view of the SPIC used in the K2K.

used in KEK are described in [30].

Fig. 3.14 show the online display for beam-line monitors. English characters shows the monitor name; i.e. "V39 out" means the monitor located downstream of 39th vertical dipole magnet.

Table 3.1 summarizes name, type and the purpose of the beam-line monitor.

The apparatus of the muon monitor and the pion monitor are described in the next chapter.

Beam-line DAQ

As shown in Fig. 3.14, we prepare lots of monitors in the beam-line. We must change analog signals from these monitors to digital ones using electronics and computers.

Fig. 3.15 shows the beam-line DAQ system.

We need only charge information from these monitors, such as CTs or SPICs. Therefore we use normal charge-sensitive-type Analog-to-Digital Converters(ADCs) as front-end electronics. These ADCs are sensitive to the charge from 0.25 pC to 1000 pC typically.

The 12 GeV PS accelerator RF distributes the trigger signal for the DAQ. This timing is 1.1 ms earlier than the real beam. We use this signal after some adjustment. This timing is also used for horn firing. Further we make a dummy trigger pulse 1 sec after the real trigger to take the pedestal data. Gate widths for these ADCs are as follows:

1. about 1.2 μs for CT: this is as narrow as possible so as not to pick up the noise,
2. 2.0 μs for SPIC: This is for the drift time of electron.
3. 2.0 μs for muon monitor: Same reason as SPIC. Please see chapter 4 for more details.

We use 6 Personal Computers(PCs) as front-end DAQ machines. Each PC takes the digital data from electronics via PC-CCPbus interface system. Six PCs are to cover the total of about 400 meter of beam-line length. We divide the neutrino beam-line into the following 4 sections for convenience. 1)North Counter Hall, 2)near the Arc, 3)Target Station and 4)Muon pit. PCs are divided as shown in Fig. 3.15 to collect data efficiently. Finally one host PC gathers this information by means of 100 Mbyte/sec Ethernet.

In addition to the charge information, GPS data for beam firing time is taken by the VME module in the North Counter Hall. This is because the GPS receiver is installed there.

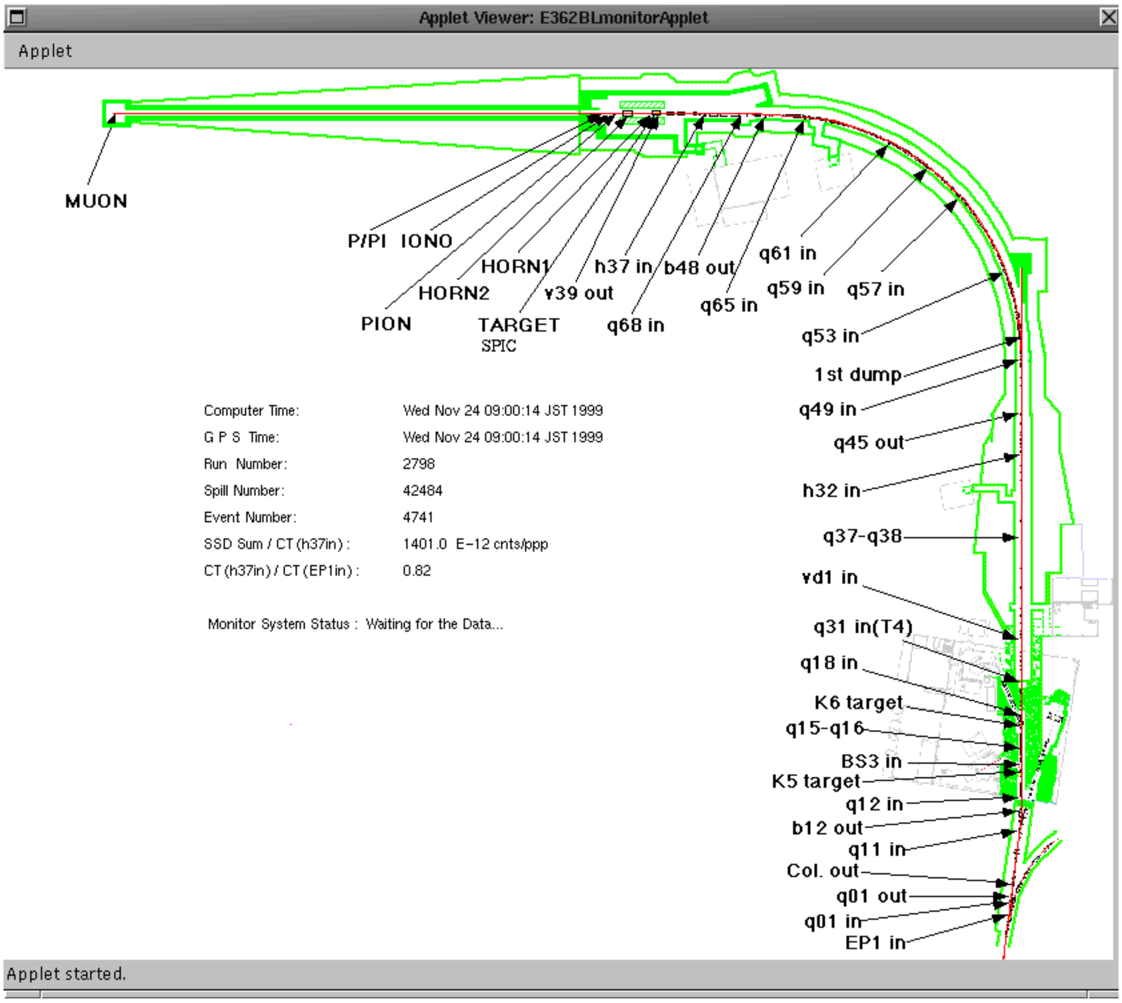

Computer Time: Wed Nov 24 09:00:14 JST 1999
G P S Time: Wed Nov 24 09:00:14 JST 1999
Run Number: 2798
Spill Number: 42484
Event Number: 4741
SSD Sum / CT (h37in) : 1401.0 E-12 cnts/ppp
CT (h37in) / CT (EP1in) : 0.82

Monitor System Status : Waiting for the Data...

Figure 3.14: Monitors in the neutrino beam-line

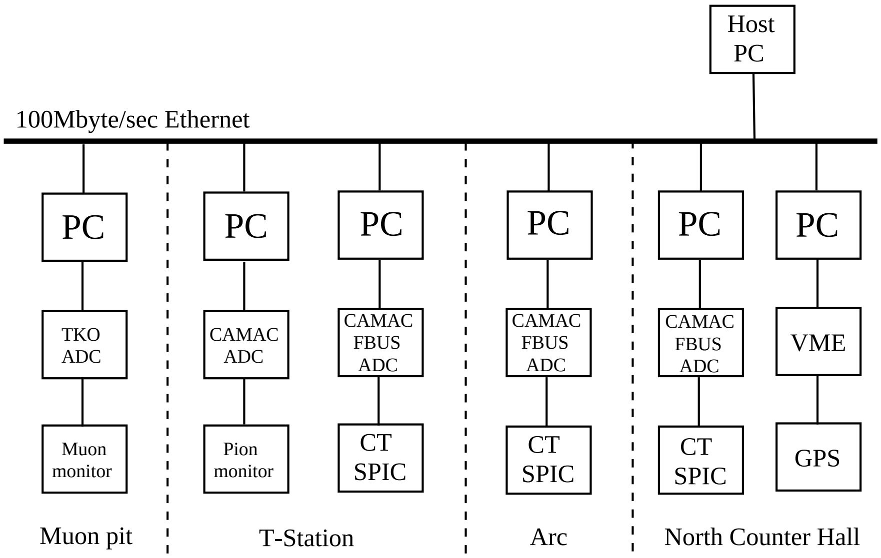

Figure 3.15: Beam-line DAQ system

Characters	monitor type	purpose	comment
EP1 in	CT,SPIC	intensity monitor and steering	5mm pitch
q01 in	SPIC	steering	5mm pitch
q01 out	SPIC	steering	5mm pitch
Col. out	SPIC	steering	5mm pitch
q11 in	CT,SPIC	intensity monitor and steering	5mm pitch
b12 out	SPIC	steering	5mm pitch
q12 in	CT,SPIC	intensity monitor and steering	5mm pitch
K5 target	CT,SPIC	intensity monitor and steering	5mm pitch
BS3in	SPIC	steering	5mm pitch
q15-q16	SPIC	steering	5mm pitch
K6 target	SPIC	steering	5mm pitch
q18 in	SPIC	steering	5mm pitch
q31 in	SPIC	steering	5mm pitch
vd1 in	CT,SPIC	intensity monitor and steering	5mm pitch
q37-q38	SPIC	steering	5mm pitch
h32 in	CT,SPIC	intensity monitor and steering	5mm pitch
q45 out	SPIC	steering	5mm pitch
q49 in	CT,SPIC	intensity monitor and steering	5mm pitch
q53 in	CT,SPIC	intensity monitor and steering	5mm pitch
q57 in	SPIC	steering	5mm pitch
q59 in	CT,SPIC	intensity monitor and steering	5mm pitch
q61 in	SPIC	steering	5mm pitch
q65 in	CT,SPIC	intensity monitor and steering	5mm pitch
q68 in	SPIC	steering	5mm pitch
h37 in	CT,SPIC	intensity monitor and steering	5mm pitch
v39 out	SPIC	steering	5mm pitch
target SPIC	CT,SPIC	intensity monitor and steering	1.27mm pitch
HORN1, HORN2	slow monitor	monitor horn current	
PION	Cherenkov counter	measure pions	described later
IONO	Ion Chamber	measure secondary particles	
P/PI	SPIC	measure secondary particle profile (projection)	2cm pitch
MUON	SI + IC	measure muon direction and intensity	described later

Table 3.1: Name, type and purposes of beam-line monitor. Please refer to Fig. 3.14.

3.2 Near Detector at KEK

As shown in Figs. 3.1 and 3.4, the near detector is located 300 meter from the target, the experimental hall is 24 meter in diameter and 16 meter in depth.

Fig 3.16 shows the schematic view of the near detector at KEK. From upstream to downstream are the 1 kilo ton water Cherenkov detector[31], the Scintillating Fiber Tracker[32], the Lead Glass Calorimeter[33] and the Muon range detector[34].

One kilo ton water Cherenkov detector is to check the analysis techniques of water Cherenkov detectors and to measure neutrino-water cross section. The Scintillating Fiber Tracker is to study neutrino interactions with its fine granularity. The lead glass calorimeter is to measure electromagnetic component in an event.

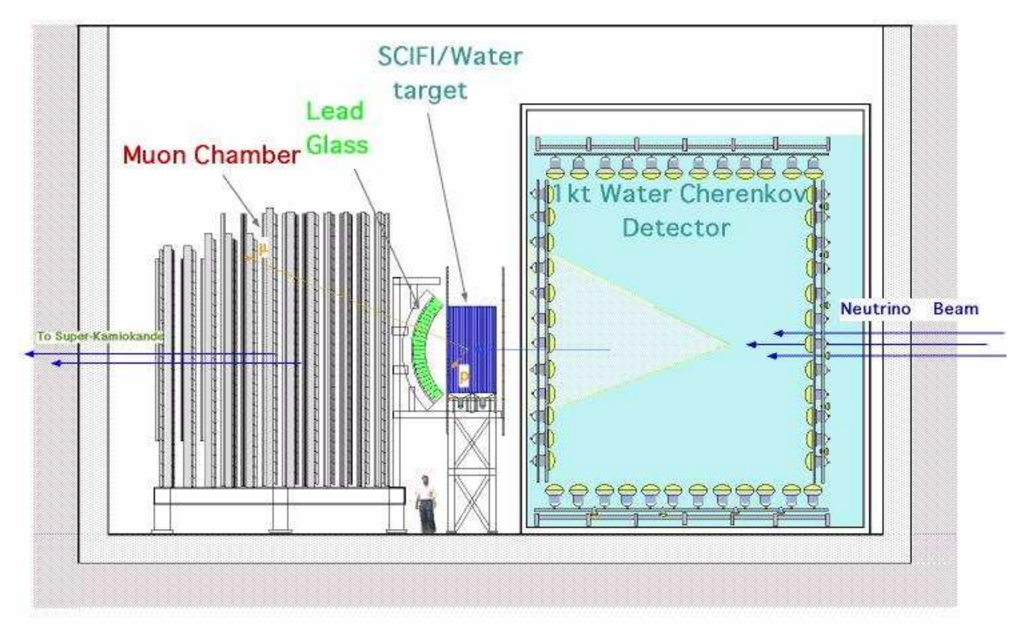

Figure 3.16: Schematic view of the near detector at KEK

The muon range detector is used to measure neutrino properties, for example intensity, profile and energy. The event rate measured by the muon range detector is used to calculate the expected number of neutrino events at the far detector. In this thesis, only the data of the muon range detector is used as the data of the near detector.

3.2.1 Muon Range Detector

This system consists of vertical and horizontal drift-tube layers interleaved with iron absorber. The energy of the muons is measured by the range method. The size of the layer is about 7.6 m × 7.6 m. We use 4 iron plates of 10cm thickness and 8 plates of 20 cm thickness. Total iron thickness of 2 meter covers up to 2.8 GeV muons.

Fig. 3.17 shows the detector. The left figure shows the top view and the right figure shows the side view. In both figures, the left side is upstream of the beam. (opposite direction against Fig. 3.16)

Table 3.2 summarizes the detail order of drift-tube and iron layers.

As shown in Fig. 3.18, 8 tubes make one module. We have modules of various length , from 245 cm to 760 cm. We use 760 cm modules for most drift-tube layers; however, we do not have enough to make all the layers. Therefore for some layers like the 4th horizontal drift-tube layer, we combine 2 short modules to make a layer.

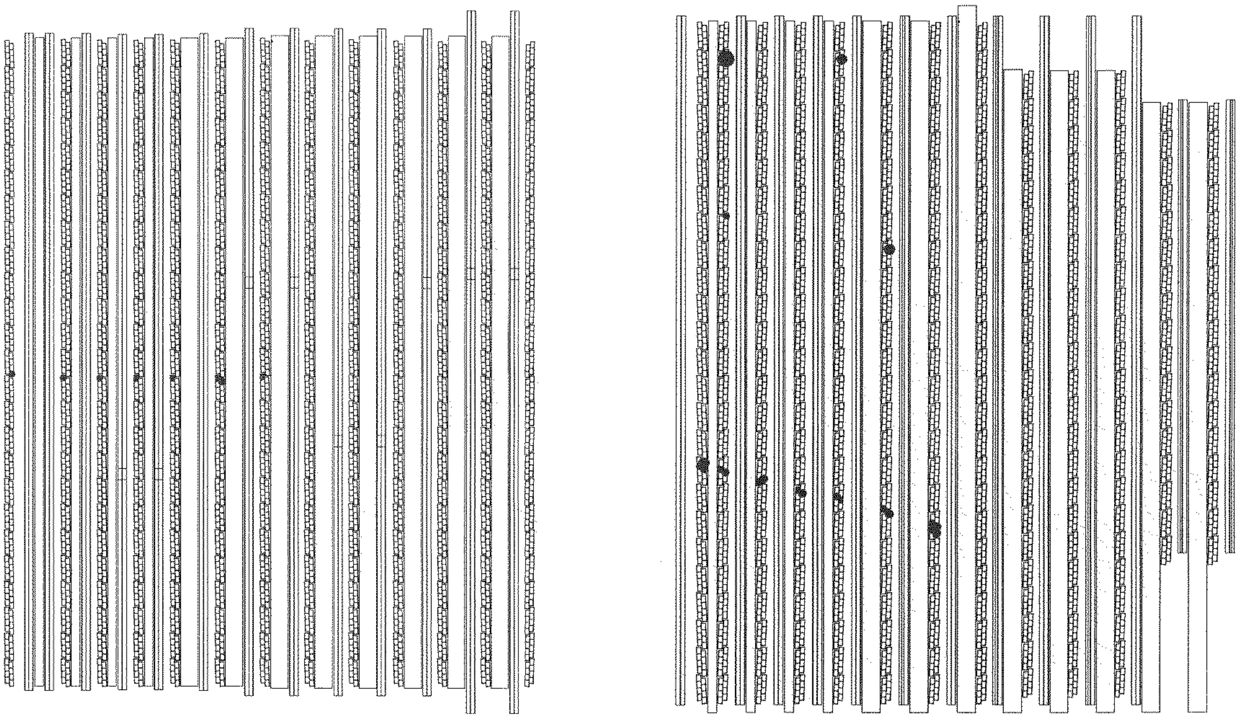

Figure 3.17: The schematic view of muon range detector. Left figure shows the top view and right shows the side view; In both figures, left side is upstream of the beam (opposite direction against Fig. 3.16).

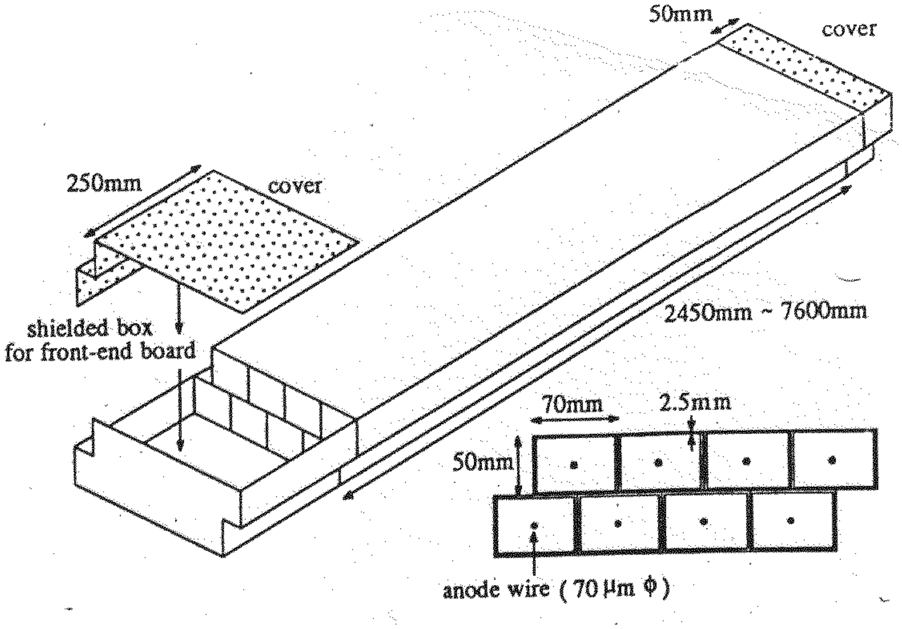

Figure 3.18: The schematic view of one muon drift-tube module [34]

Layer	H×V×t (cm^3)	cm × modules	cm × modules
chamber 1X (V)		760×25	
chamber 1Y (H)			760×25
Iron 1	750×763×10		
chamber 2Y (H)			760×25
chamber 2X (V)		760×25	
Iron 2	750×763×10		
chamber 3Y (H)			760×25
chamber 3X (V)		760×25	
Iron 3	750×763×10		
chamber 4Y (H)			(505+245)×25
chamber 4X (V)		760×25	
Iron 4	750×763×10		
chamber 5Y (H)			(505+245)×25
chamber 5X (V)		760×25	
Iron 5	750×763×20		
chamber 6Y (H)			760×25
chamber 6X (V)		760×25	
Iron 6	750×763×20		
chamber 7Y (H)			(290+474)×25
chamber 7X (V)		760×25	
Iron 7	755×780×20		
chamber 8Y (H)			(290+474)×25
chamber 8X (V)		760×25	
Iron 8	755×710×20		
chamber 9Y (H)			(474+290)×25
chamber 9X (V)		760×25	
Iron 9	755×709×20		
chamber 10Y (H)			(474+290)×25
chamber 10X (V)		760×25	
Iron 10	755×709cm×20		
chamber 11Y (H)			(300+474)×6+(290+474)×17
chamber 11X (V)		760×25	
Iron 11	755×674×20		
chamber 12Y (H)			760×1+(300+505)×16
chamber 12X (V)		505×25	
Iron 12	755×674×20		
chamber 13Y (H)			760×1+(300+505)×16
chamber 13X (V)		505×25	

Table 3.2: Arrangement of drift-tube and iron layers in muon range detector. H, V and t means horizontal size, vertical size and thickness, respectively. X and Y means direction of the measurement information; i.e. installation of drift tubes vertically allows us to measure x position of a charged particle.

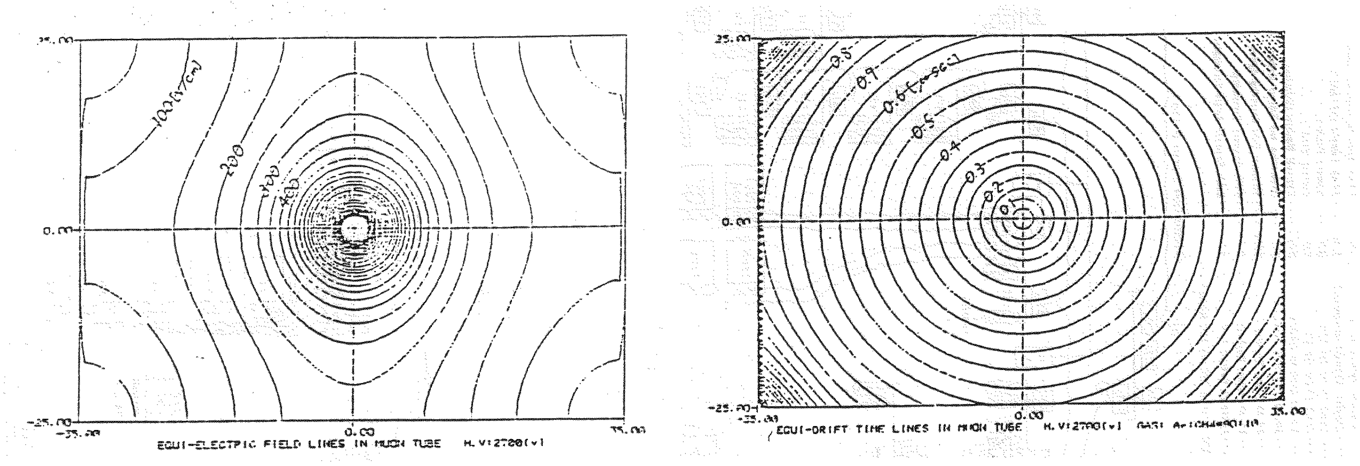

Figure 3.19: Typical electric field and drift time in the drift tube (calculation[34]) Left: electric field (V/cm) inside the drift tube. Right: drift time (μsec) inside tube.

We use P10(Ar 90% + CH_4 10%) gas for the drift tubes. The typical electric field and drift times of this drift tube are shown in Fig. 3.19. These values are from the calculations in ref.[34]. According to this figure, the maximum drift time of separated electron is about 1 μs.

The signal of the drift-tube is digitized in front-end electronics circuit. In the circuit, the signal is amplified by a factor of 100. A discriminator judges whether the amplified signal is over -30 mV or not and the timing information of the discriminated signal is digitized using 20 MHz clock if it exceeds 30 mV. The TDC dynamic range is 6bits (64 counts). Therefore this electronics covers 64×50 ns=3.2 μs time range. It is enough dynamic range to measure the neutrino induced signal because the spill itself is about 1 μs and the maximum drift time is also about 1 μs. TDC data with hit tube addresses are sent to a TKO[35] Memory module.

From timing information, we can reconstruct the track of a charged particle. The performance test was done using cosmic rays. It shows that we have a spatial resolution of about 2 mm. The performance of this detector is summarized in table 3.3.

Item	Performance
Hit efficiency	99%
Spatial resolution	2 mm
Energy threshold	250 MeV
Energy resolution	150 MeV
Angle resolution	8 degree
Vertex resolution	10 cm

Table 3.3: The detector performance of the muon range detector

3.3 Super-Kamiokande(SK) as a Far Detector

3.3.1 General Description of the Detector

Super-Kamiokande[36, 37] is a ring image type water Cherenkov detector. Super-Kamiokande detects the Cherenkov photons emitted by charged particles which have larger velocity than that of light inside material. Cherenkov photons are emitted along the particle direction with a half cone angle θ_C.

$$\cos\theta_C = \frac{1}{n\beta} \tag{3.2}$$

where, β is defined as $\beta = v/c$. (v is the particle velocity. c is velocity of light.) n is the refractive index of materials. The spectrum of Cherenkov light as a function of wavelength λ is

$$\frac{dN}{d\lambda} = \frac{2\pi\alpha x}{c}\sin^2\theta_c\frac{1}{\lambda^2} \tag{3.3}$$

where, α is the fine structure constant ($\sim 1/137$) and x is the length of the particle trajectory.

The Super-Kamiokande detector consists of about 50000 tons of pure water filled in a cylindrical water tank (diameter 39.3 meter and height 41.4 meter), a water and air purification system, photomultiplier tubes (PMT), electronics and online data acquisition system, and off-line computer facilities. Fig. 3.20 shows the schematic view of the detector. It is located 1000 meter underground (2700 meter water equivalent) in the Kamioka mine in Gifu Prefecture, Japan.

The reason that the detector is underground is to shield against cosmic ray muons. Compared to ground level, the intensity of muons is reduced by about 10^{-5} at the depth of Super-Kamiokande detector.

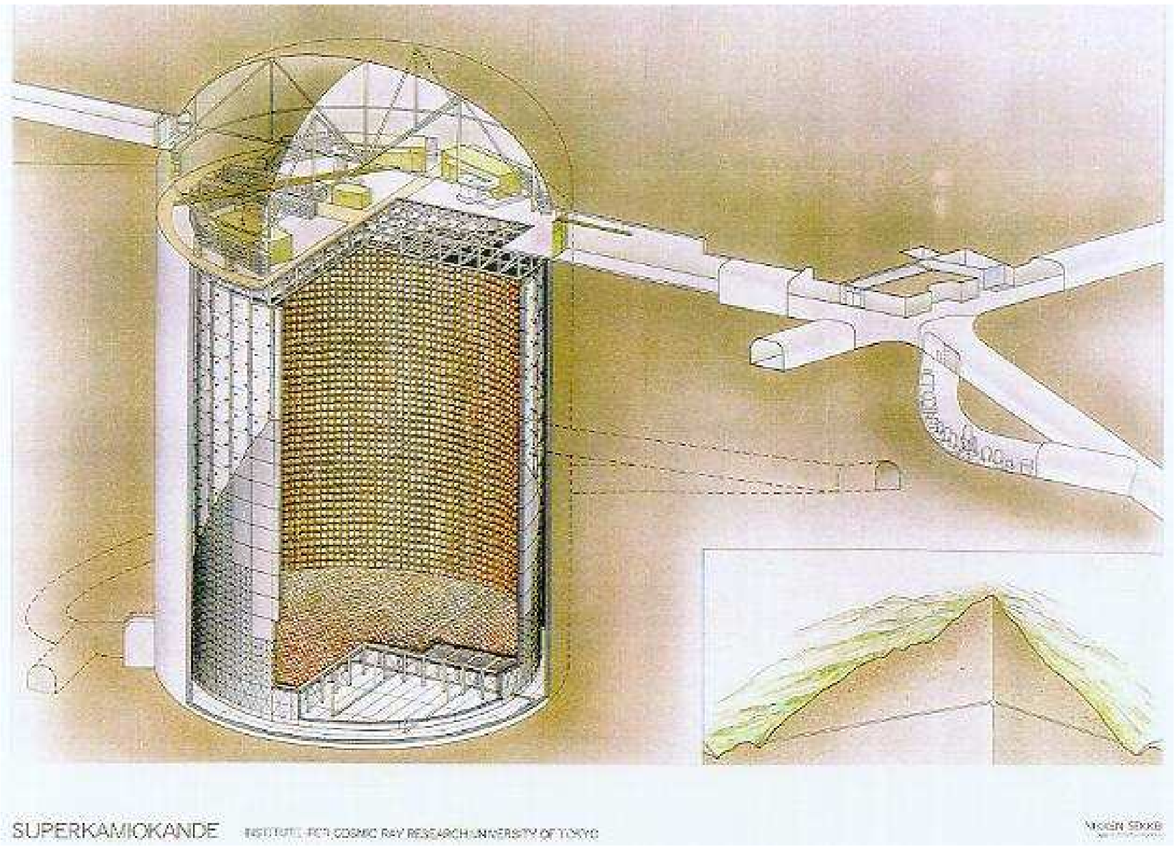

Figure 3.20: Schematic view of the far detector, Super-Kamiokande

There are two PMT layers inside the detector. One is inner detector(ID), and the other is outer detector(OD). The diameter, height and volume of inner detector are 33.8 m, 36.2 m and 32 kton respectively.

We have a total of 11460 20″ PMTs inside the ID. Seven thousand six hundred fifty of them are installed on the barrel wall, and the others are installed on the top and bottom wall. Each PMT was installed every 70 cm, and the area, which is insensitive to the photons, was covered by black-sheet to absorb the photons. The photo-cathode coverage is 40%.

The OD covers the ID completely. The thickness of the barrel part of the OD is 2.0 m, and that of the top and bottom part is 2.2 m. The OD has 1885 8″ PMTs. Each PMT was installed at the center of a 60 cm×60 cm wavelength shifter board. This causes efficient photon collection even using a small number of PMTs. Further we cover the board by Tyvek-sheet known as the reflective material to enhance the light collection. The OD plays important role to reduce the background. We can identify the cosmic ray muons which come from outside of SK using the OD. Two meter thickness layer of water prevents gamma rays and neutrons from entering the ID. Another important role of OD is to identify the going out muon events, which has vertex inside the ID but the end point of the track is outside of ID.

The ID and OD are optically separated from each other by black sheet and Tyvek sheet (Fig. 3.21).

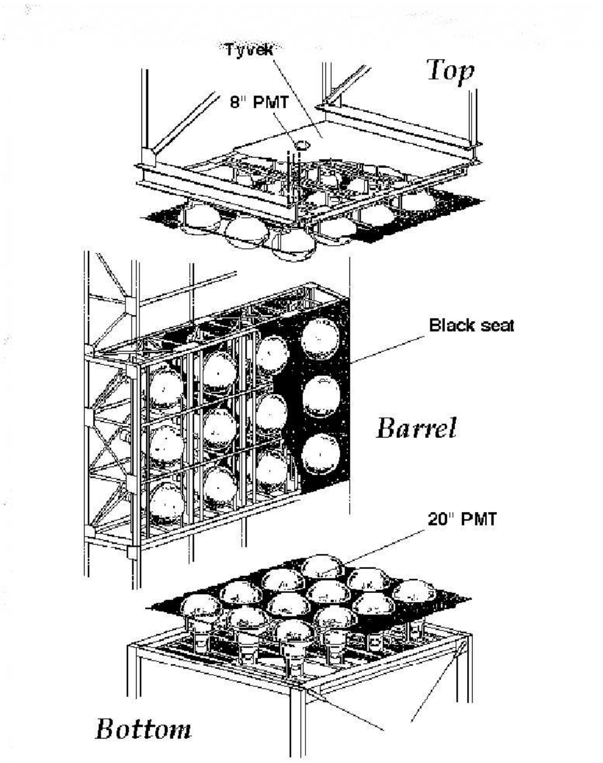

Figure 3.21: The schematic view of the frame which supports PMTs in SK

3.3.2 Photomultiplier Tube

Hamamatsu Photonics K.K developed 20″ PMT in cooperation with Kamiokande members originally[38]. The PMTs used in SK are improved from the original Kamiokande ones in some points. The size and shape of 20″ PMT is shown in Fig. 3.22.

The photo-cathode of this PMT is made of bi-alkali(Sb-K-Cs). This is suitable for the Cherenkov photon spectrum in the water. Fig. 3.23 shows the quantum efficiency of this PMT as a function of wavelength of photons. It has a peak around 410 nm, 21%.

This PMT has Venetian-blind type dynode. The bleeder-chain of this PMT is optimized to achieve good timing resolution and photon collection. The averaged collection efficiency is more than 70%. Due to this improvement, the one photo-electron peak is clearly seen and the Transit Time Spread (TTS) is 2.2 ns[39]. Since we know the response of this PMT is uniform in the magnetic

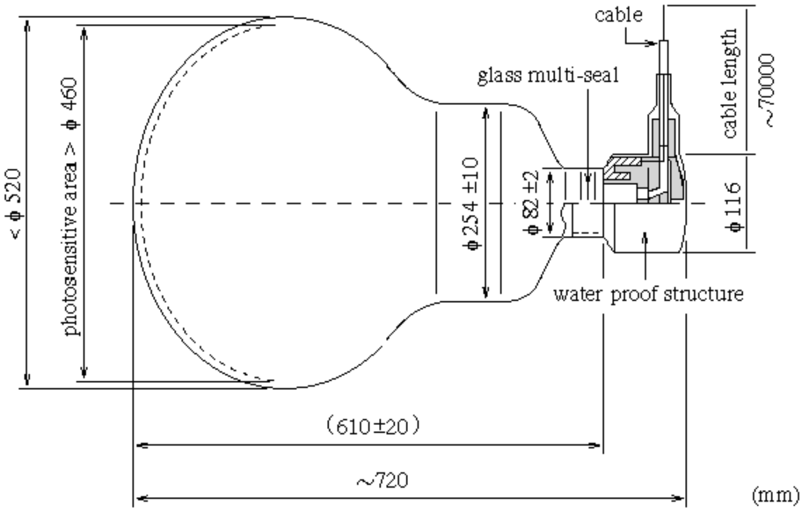

Figure 3.22: Schematic view of 20-inch PMTs used in the inner detector of SK

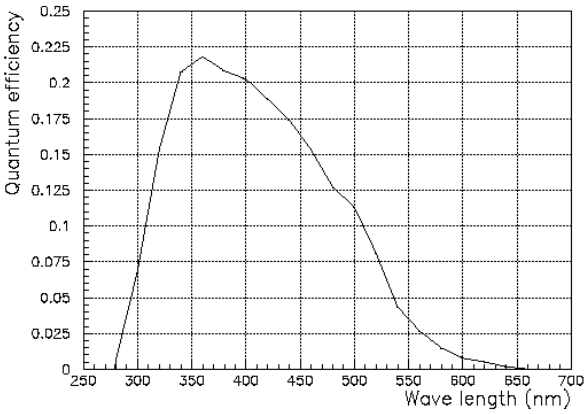

Figure 3.23: Quantum efficiency of 20-inch PMT as a function of wavelength of photons

field with less than 100 mGauss, we have 26 sets of Helmholtz coils surrounding SK. It achieves our requirement for magnetic field strength. The dark noise of each PMT is typically 3.1 kHz under the gain 10^7. We supply high voltage with -2000 V typically.

The PMTs used in the OD are 8″-R1408 type made by Hamamatsu Photonics. These were once used in the IMB experiment and have been recycled. The wavelength shifter boards surrounding the PMTs are 60 $\text{cm}^2 \times$ 1.3 cm(t). They absorb the ultra-violet photons and re-radiate blue light to which the PMTs are most sensitive. Due to these board, photon collection efficiency increases to $\sim$60%[40]. The timing resolution of a PMT itself is 11 ns and becomes 15 ns when the wavelength shifter is included. It is sufficient to tag the OD events although it is worse than the ID PMTs.

3.3.3 Water Purification System

Super-Kamiokande is filled with the 50000 tons pure water. It is made from natural water near the detector. The water purification system circulates 50 m^3 of pure water per hour to keep the quality. Quality monitor systems are installed at various places. The purpose of the water purification system is to remove radioactive materials and bacteria. This creates good water transparency. The radioactive materials, in particular ^{222}Rn, are background for the solar neutrino analysis.

Fig. 3.24 shows the water purification system. The solid line shows the main circulation of the water and the dotted line shows supplemental circulation line. The heat exchanger keeps the temperature of the water to be 13°C and prevents the growth of bacteria. The ion exchanger and cartridge polisher remove metal ions such as Ra and Th in the water. The ultra-violet sterilizer kills bacteria in the water. The gas in the water such as oxygen and radon, is removed by the vacuum degasifier and finally the ultra filter(UF) removes small dust with size an order of 10 nm.

After the water purification the concentration of radon which is 10^4 Bq/m^3 in the mine water is reduced to < 10 mBq/m^3 and the light attenuation length is kept to about 100 meter at the wavelength of 420 nm.

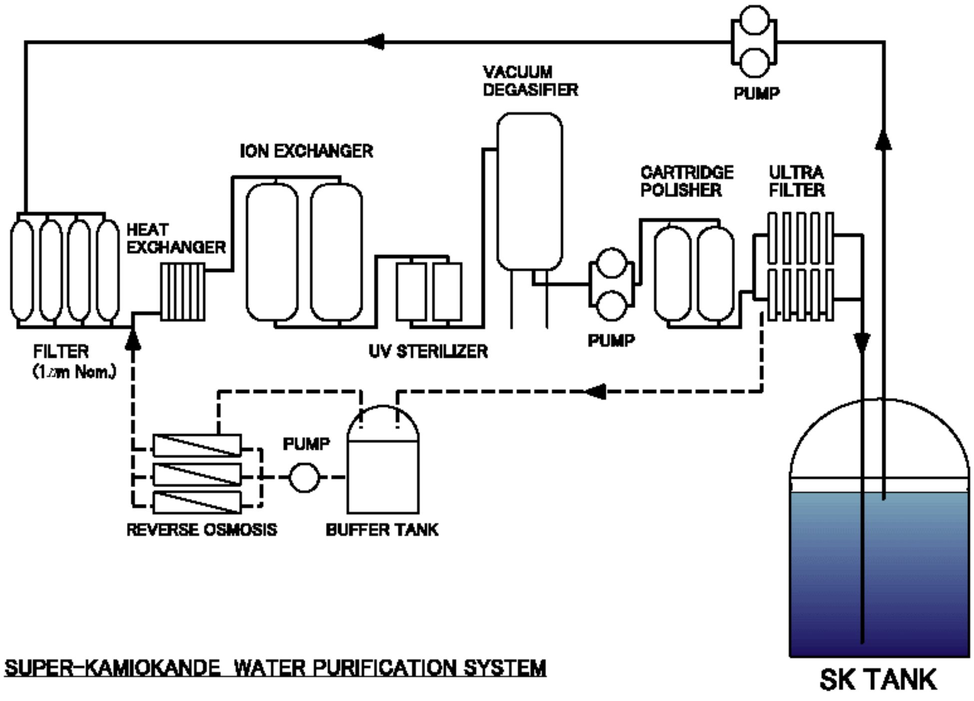

Figure 3.24: Water purification system of SK

3.3.4 Data Acquisition System

The top figure of Fig. 3.25 shows the electronics for the ID. This electronics system has two kinds of modules, one is the TKO[35] module and the other is the VME module.

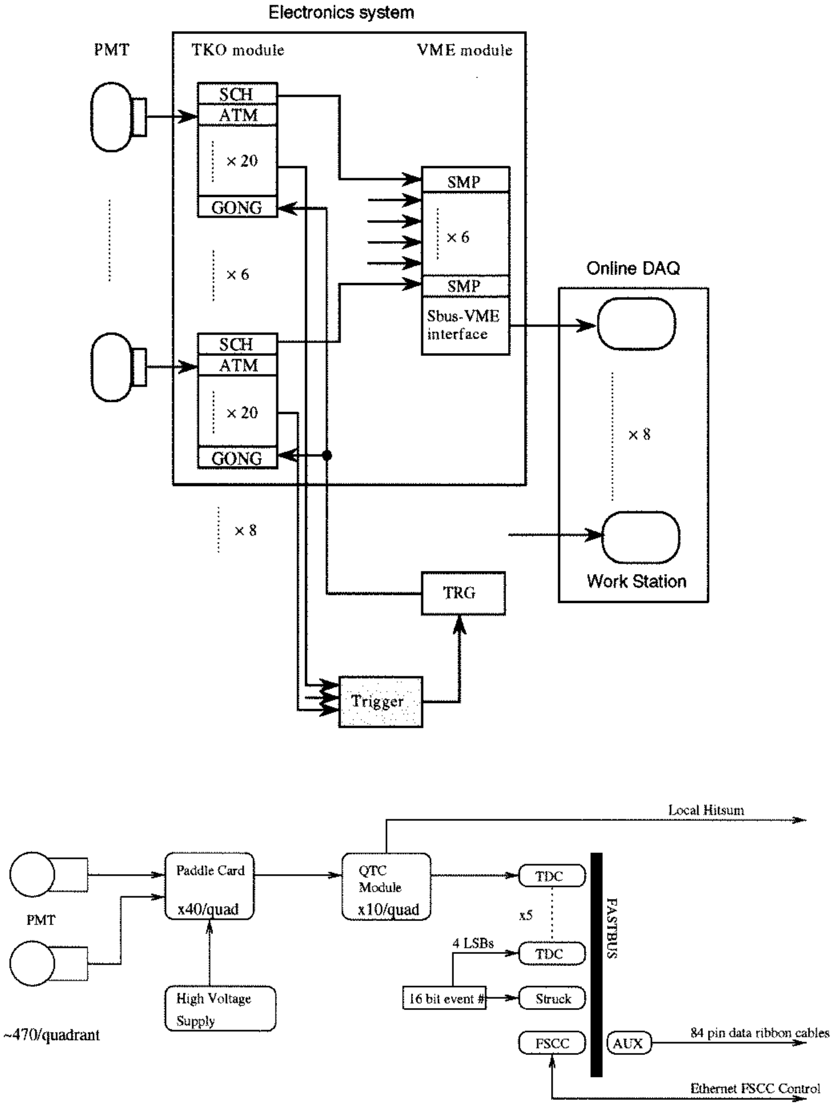

Figure 3.25: Data acquisition system of SK

We have total 48 TKO and 8 VME crates, and they are installed in separated 4 electronics huts. In the central hut, there is a VME module and a TRG module for the global trigger.

The PMT signal is handled by the TKO module at first. This system consists of up to 20 Analog Timing Modules (ATMs)[41], one Go/NoGo(GONG) trigger module and one Super-Controller Header bus interface (SCH) module.

A total of 934 ATMs are used for the ID. Each ATM handles the signals of 12 PMTs. The ATM gives the timing information with 0.3 ns resolution up to a 1.2 μs time range, and the charge information from 0.2 pC to 550 pC. Each channel has a pair of switching Time-to-Analog Converters(TACs) and Charge-to-Analog Converters(QACs). This pair of switching channels allow continuous measurements without dead-time. For example, we can measure muon decay events due to this.

Each channel of the ATM has an amplifier with a gain of 100 and a discriminator. The threshold of this discriminator is 100 mV, corresponding to 0.32 pC. A rectangular signal (width 200 ns and height 11 mV) is generated if the analog signal is over the discriminator threshold. These rectangular pulses from all the hit PMTs are added ("HITSUM" signal) and sent to the global trigger module in the central hut and simultaneously a gate window of 900 ns width is opened to start the time measurement in the TAC and the charge accumulation in the QAC. The QAC accumulates charge in a 400 ns time window and keeps it until the global trigger reaches. If the global trigger does not reach it within 1.3 μs, the stored data in the TAC and the QAC are cleared. However, when the global trigger reaches, charge and timing information are digitized by the ADC and sent via the SCH to the memory (SMP) in the VME module.

Pedestals of the ATMs are measured at an interval of 30 min. Only 1/8 of all the ATMs are measured at once.

The bottom figure of Fig. 3.25 shows the front-end part of this system. It consists of 40 paddle cards, 10 charge-to-digital converters(QTCs), 5 time-to-digital converters(TDCs) and one FASTBUS Smart Crate Controller(FSCC). A paddle card has 12 PMT channels. The signal and high voltage lines are AC coupled. The role of the puddle card is to pick off the PMT signals through a high voltage capacitor.

The QTC module converts the PMT analog signal to an ECL leveled logic pulse. The leading edge of the logic pulse corresponds to the transit time and the width of the pulse corresponds to the charge of the analog signal. Furthermore the QTC module provides the rectangular pulse with 200 ns width and 20 mV height and sends it to the trigger module in the central hut.

LeCroy 1877 Multi-hit Time-to-Digital Converter is used as the TDC module of the OD. One module has up to 96 ECL inputs. This TDC module has a resolution of 0.5 ns/channel. The TDC module serves as a pipeline buffer within 32 μs and digitizes 16 of the latest signals and stores them in memory. We reduce this width to 16 μs to reduce data size. The control and readout of the TDC modules are operated by the FSCC and the stored data is sent to the online machines.

3.3.5 Event Triggering System

We have 3 kinds of triggers for the ID. These are for high energy (HE), for low energy (LE) and super low energy (SLE) events. We have one trigger for the OD. Each of them is triggered by its own level of HITSUM signal independently.

HE is mainly used for the analysis of cosmic ray muon, atmospheric neutrino and proton decay events. This trigger requires more than 31 HITSUM signal coincidence within 200 ns. The trigger rate is 5~6 Hz. LE is mainly used for the solar neutrino analysis in the 5~6 MeV energy region. This requires 29 HITSUM signal coincidence. SLE trigger was made to bring down the threshold of the solar neutrino analysis to 4.6 MeV.

OD trigger is employed to cut the background from cosmic ray muons. This trigger requires 19 HITSUM coincidence from the QTC module for the OD. If the OD trigger was generated, it is sent to the TRG module.

A global trigger was generated if any trigger of the above 4 is generated. The data stored in the store module is read through the online workstation.

Chapter 4

Beam Monitors for Secondary Particles

4.1 Muon Monitor

4.1.1 Functionality of Muon Monitor

Location

Muon monitors (Fig. 4.1) are situated in a pit at the downstream of the beam dump. We have two kinds of muon monitors; one is an ionization chamber and the other is a silicon detector. The beam dump is located at the end of the decay pipe. It consists of 3.5 meter thick iron and 2 meter thick concrete. These materials correspond to about 5.5 GeV energy loss for a minimum ionizing particle.

The muon momentum distribution is shown in Fig. 4.2. Before the dump it has a peak at around 2.0 GeV/c. In the dump, muons lose energy of about 5.5 GeV, therefore only 2.1% of the muons are observed by the muon monitors. All the hadrons are absorbed by the dump except low energy neutrons.

In this case, muon monitors measure the properties of high energy pions and neutrinos, indirectly. Fig. 4.3 shows the momentum and angle of the pions, which produce the muons pass through the beam-dump. Distributions before the decay pipe are also overlaid. Muon monitors detect pions which have the angle within 10 mrad and the momentum above 5.5 GeV. Fig. 4.4 shows the momentum of the neutrinos coming from pions shown in Fig. 4.3. Open histogram shows the neutrinos coming from all pions, while shaded one shows those from pions shown in Fig. 4.3. Top; linear scale, bottom; log scale.

Goal of muon monitor

Of monitoring systems such muons, pions and neutrinos, we focus on the purpose of the muon monitor, as follows.

1. To monitor the direction of neutrinos (by means of monitoring the profile of muons) spill by spill.

   Fig. 4.5 shows the radial dependence of neutrino intensity and energy spectrum at Super-Kamiokande (MC).

   This figure shows the beam intensity changes less than 1% within 1 mrad (= 0.25 km distance) from the center thanks to the large decay angle of low energy pions. Energy spectrum is also stable within 1 mrad. Therefore the systematic error of the beam intensity coming from the angle of the beam is estimated to be less than 1% if the direction of the muons is known to better than 1 mrad. This error, further, can be reduced if we employ the near detector information.

2. To monitor the intensity stability of the beam spill-by-spill basis.

   There must be a correlation between the total amount of muons and that of neutrinos. We measure the intensity of muons to monitor the stability of the neutrino beam intensity.

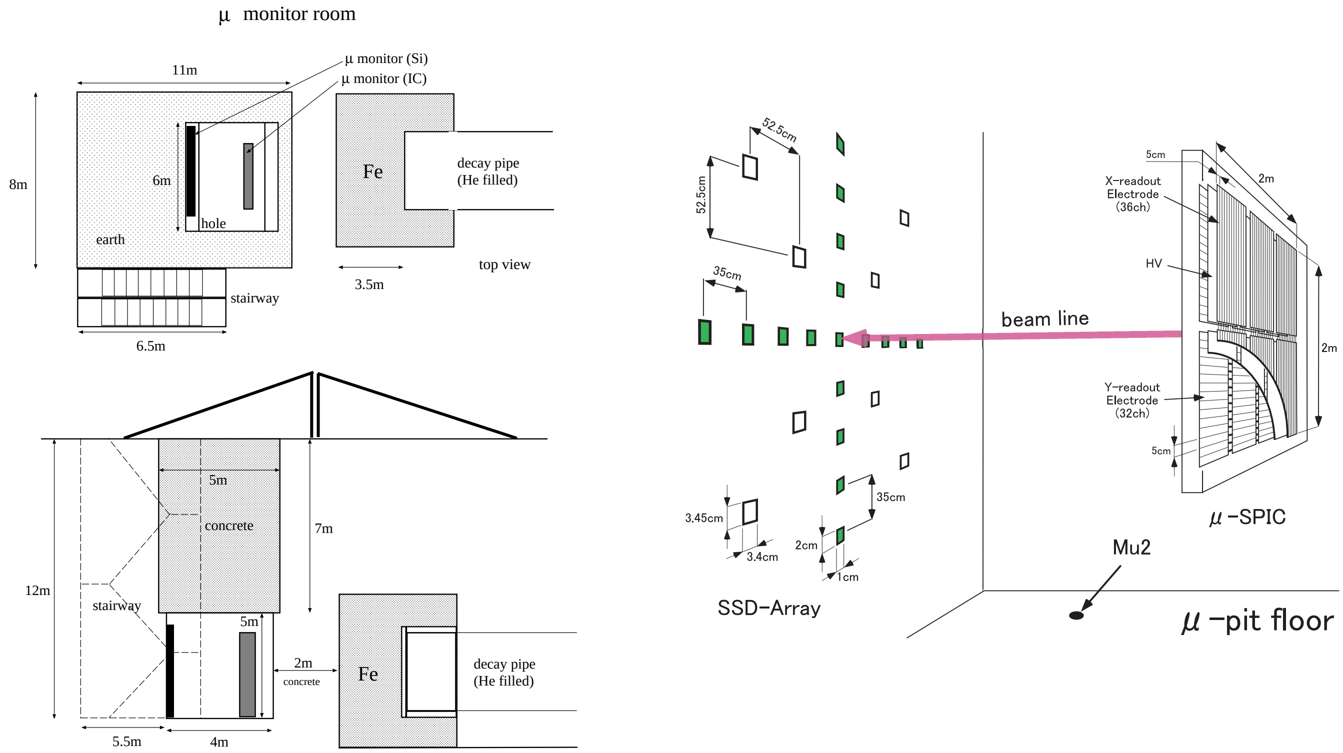

Figure 4.1: Left: the beam dump of the neutrino beam line and the muon monitor pit. Right: schematic view of muon monitors, silicon detectors array (Silicon Solid Detectors(SSD) array in the figure) and ionization chamber (μ-SPIC in the figure)

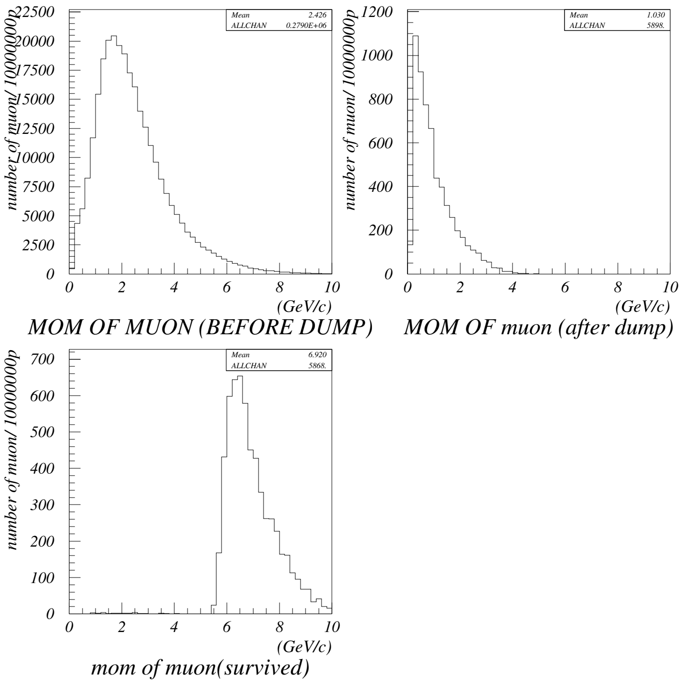

Figure 4.2: Muon momentum distributions. Top left figure shows the momentum of muons before the beam-dump, top right figure shows that of after the beam-dump, bottom left figure shows muon momentum before the beam-dump for only the surviving muons (MC)

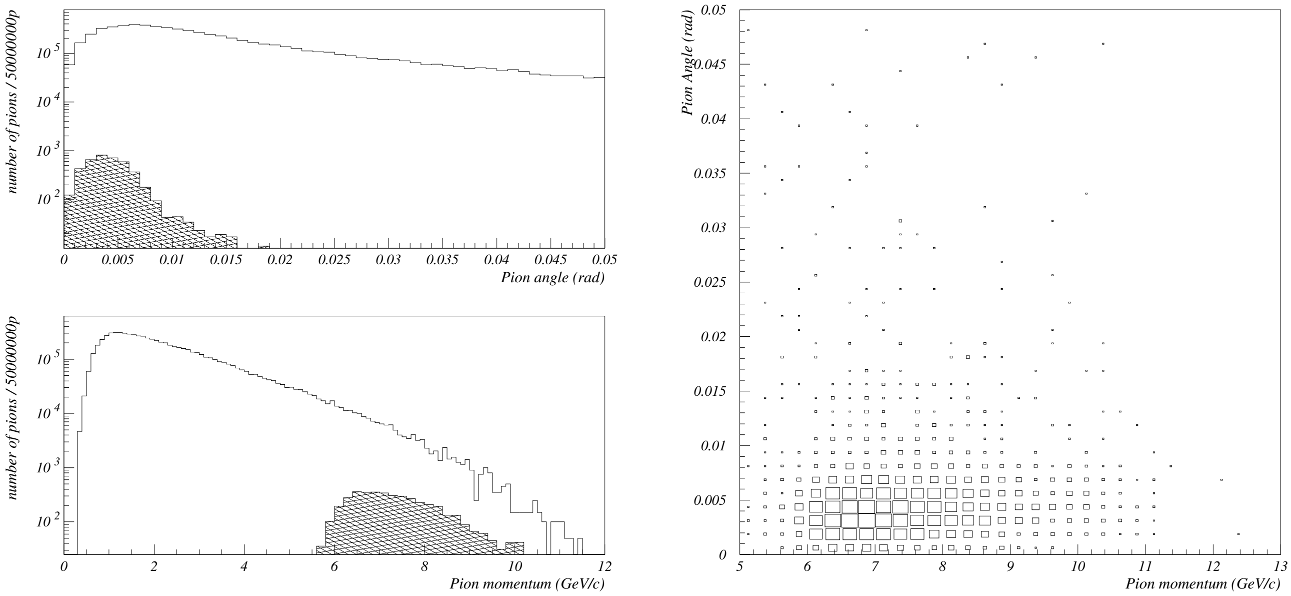

Figure 4.3: Momentum and angle of pions, which produce the muons pass through the beam-dump. Left-top: open histogram shows pion angle after 2nd horn, and shaded one shows pions which produce the muons pass through the beam-dump. Left-bottom: pion momentum. Right: scatter plot of pion angle and momentum for pions which produce the muons pass through the beam-dump.

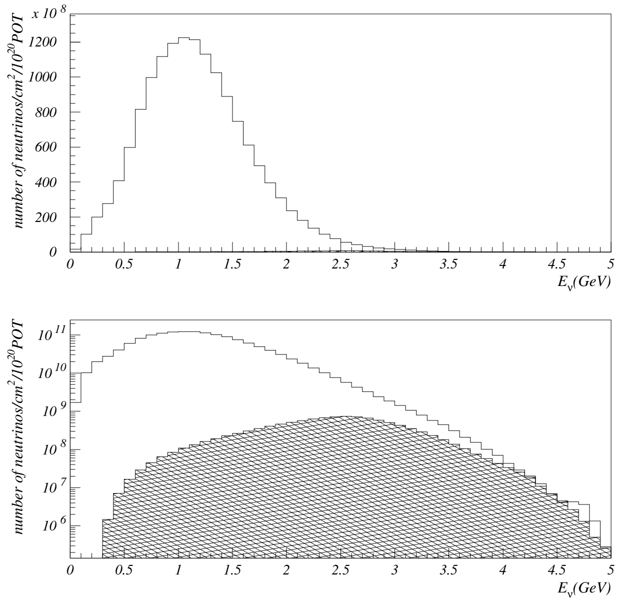

Figure 4.4: Momentum of the neutrinos coming from pions shown in Fig. 4.3. Open histogram shows the neutrinos coming from all pions, while shaded one shows those from pions shown in Fig. 4.3. Top; linear scale, bottom; log scale.

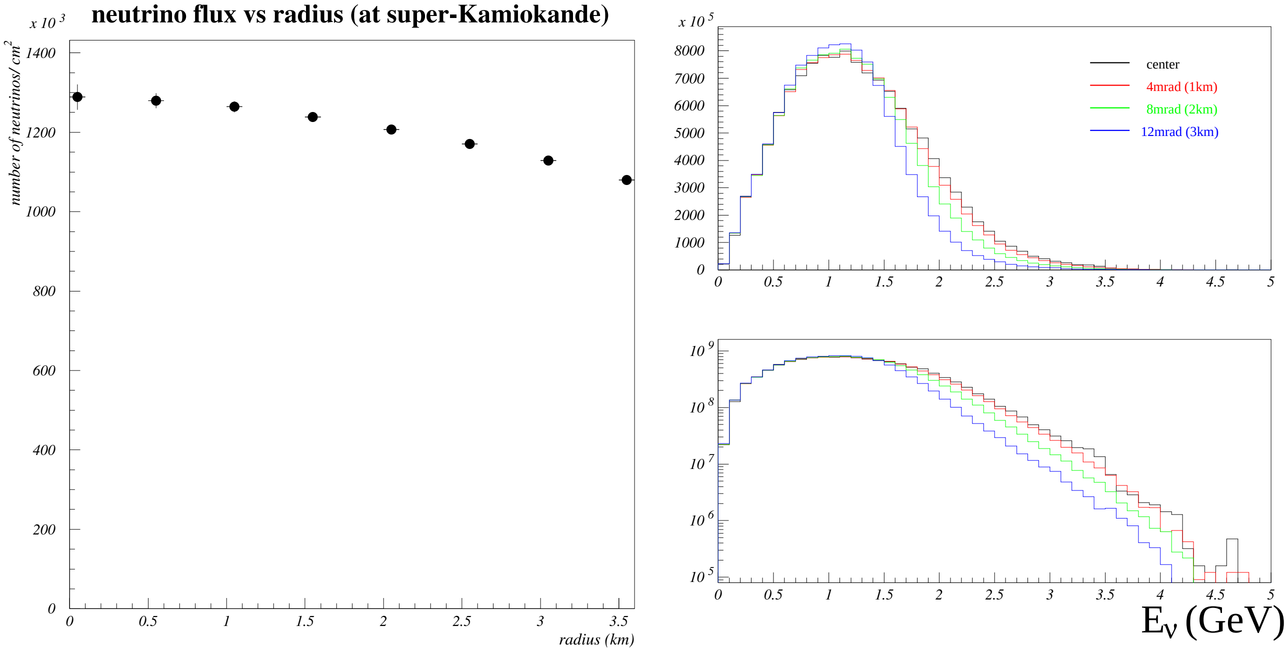

Figure 4.5: Neutrino profile at Super-Kamiokande (MC) and radial dependence of neutrino energy spectrum. Left: Neutrino profile, unit of the vertical axis are "number of neutrinos/cm^2/10^{20}POT". Right: radial dependence of neutrino energy spectrum.

4.1.2 Hardware Set up of Muon Monitor

Ionization Chamber

The ionization chamber is similar to those in the proton beam-line. Though primary proton beam intensity is about 6.0×10^{12}, the muon yield is only a few × 10^4/cm^2 level. Therefore, in order to create enough charge to be observable, the ionization chamber for the muon measurement has larger pads, (∼200 cm×5 cm). (Fig. 4.6)

There are three electric planes inside gas vessel. The gas vessel is filled with Ar gas. The structure of this chamber is similar to the SPIC inside the primary beam-line (Fig. 3.13). The readout plane has 36 channels in the horizontal axis and 32 channels in the vertical axis. Since it is difficult to make one large sheet, one plane is divided into 6 sheets with the size of 60 cm×90 cm. A readout stripe in each sheet is connected with an electric code. There are 1×25 cm and 2×15 cm insensitive gaps for horizontal and vertical axis, respectively.

Each gap between the two planes is 1cm whose accuracy is 100 μm guaranteed by the insulated spacer. One minimum ionizing particle generates about 100 ion pairs in this gap when it is filled up with Ar gas [29]. Thus each readout channel has a 100 pC level signal. We can use a normal charge sensitive ADC to read it.

Si detector

In addition to the ionization chamber, silicon detectors are installed for redundancy. A schematic view of the silicon detectors is shown in Fig. 4.7

Seventeen small-pad-type silicon detectors (size: 10 mm×20 mm, depletion layer is 300 μm) are installed horizontally and vertically. Nine large-pad-type ones (size: 34mm ×34.5 mm, depletion layer is 375 μm) are installed diagonally. One minimum ionizing particle generates about 2.3×10^4 ion pairs in the small Si pad and 2.9×10^4 ion pairs in the large Si pad.

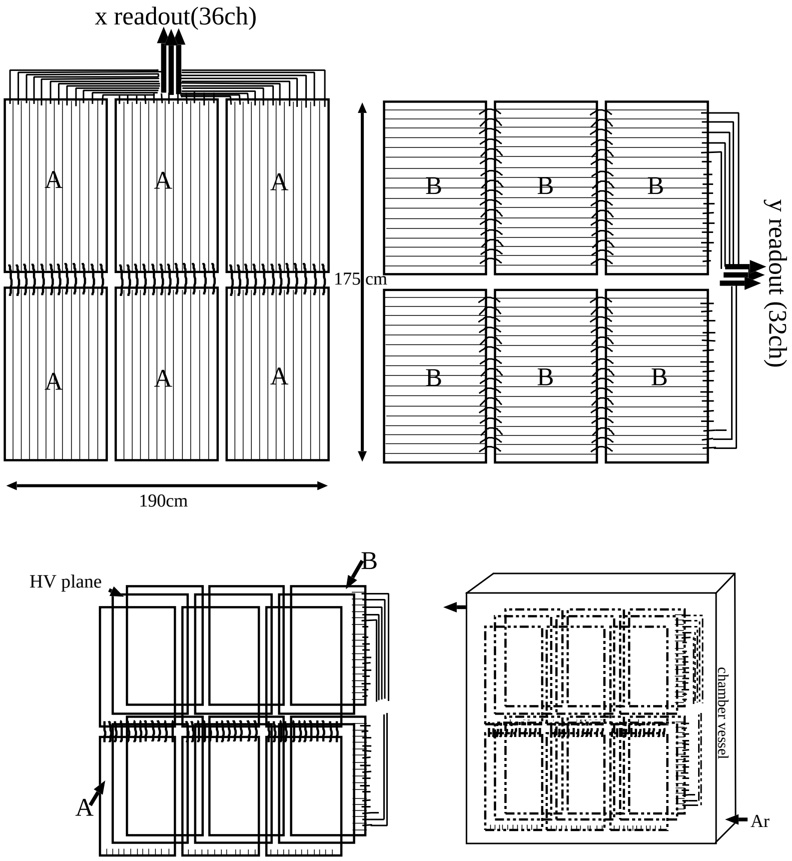

Figure 4.6: Ionization Chamber inside muon pit

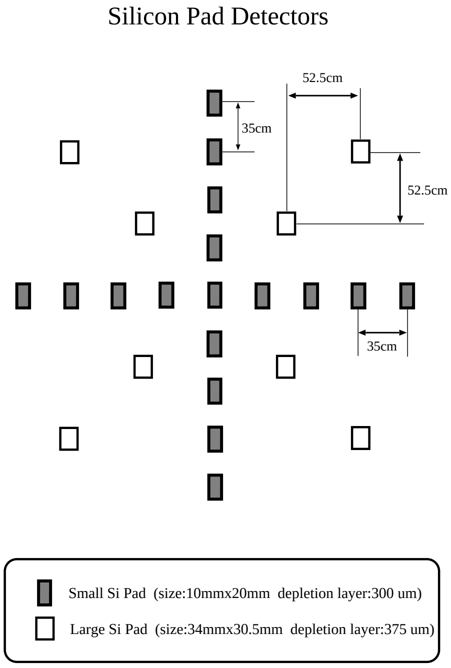

Figure 4.7: Si pad detectors inside muon pit

The small Si pad has about 100 pC level signal and the large Si pad has about 1 nC signal without any amplification.

4.1.3 Calibration of Muon Monitor

Ionization chamber

The calibration of the ionization chamber was performed employing muons in the muon pit (Fig. 4.8).

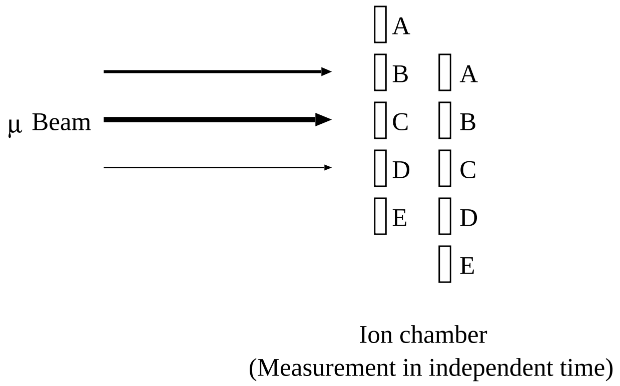

Figure 4.8: Calibration of the ionization chamber

Each strip of the ion chamber has 5 cm width. The same intensity beam enters the two different strips if it is moved to next strip position. For instance, the left side B strip has the same intensity source as the right side A strip in Fig. 4.8 if beam condition is stable.

The ionization chamber has a mechanical support system to move and an accurate position readout system for this calibration method. It is movable within ± 30 cm in both x and y direction. The accuracy of the readout system is 100 μm. The beam intensity is normalized by the CT.

However, this method has a large error propagation since only the ratios to the next strip can be taken in one movement. Thus the actual calibration method is arranged as follows (y direction is shown only as example):

1. The 32ch are divided into 4 groups (1 group has 8ch: Fig. 4.9 (a))
2. The relative gain ratios of the A to B and C to D are taken using 40 cm moving data. (Fig. 4.9 (b))
3. The relative gain ratio of B to C is taken using 55 cm moving data. (Fig. 4.9 (c))
4. The relative gain of each group is calculated.
5. The relative gain ratio of each channel in each group is taken using 5 cm moving data. (Fig. 4.9 (d), like Fig. 4.8)
6. Finally the relative gain of each channel is calculated.

Fig. 4.10 shows the relative gain obtained for horizontal and vertical directions.

Si detectors

The relative gain of the small Si detectors were measured using an LED light source. A schematic view of this calibration is shown in Fig. 4.11

They were measured one by one using this system. To check the reproducibility of the measurement and the stability of the LED, we periodically measure the same Si detector 9 times. It shows the

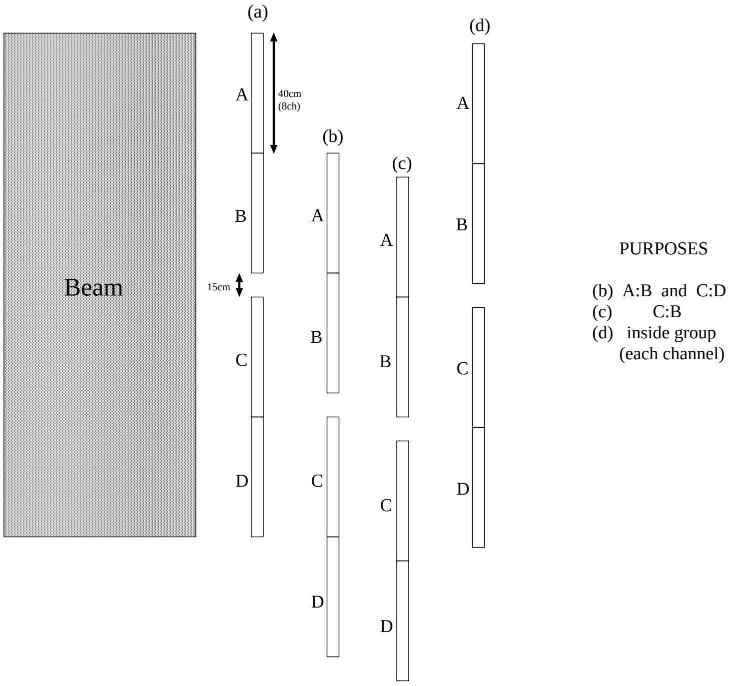

Figure 4.9: Calibration of the ionization chamber (actual method)

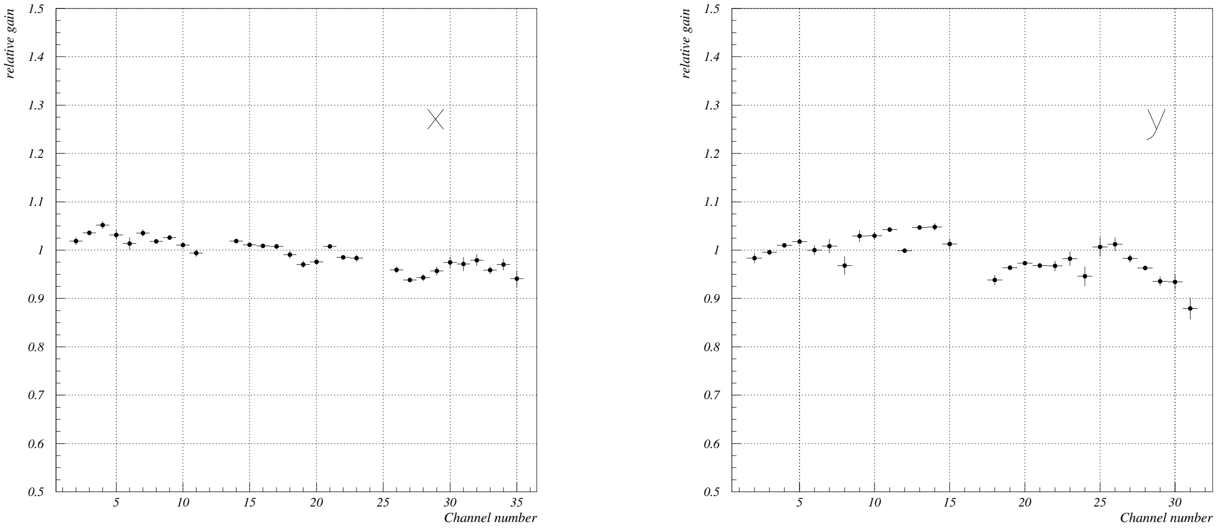

Figure 4.10: The relative gain of each ionization chamber channel, for horizontal (left) and vertical (right) directions .

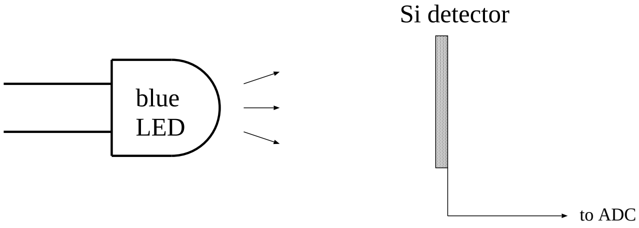

Figure 4.11: The gain measurement of the small Si pad detectors

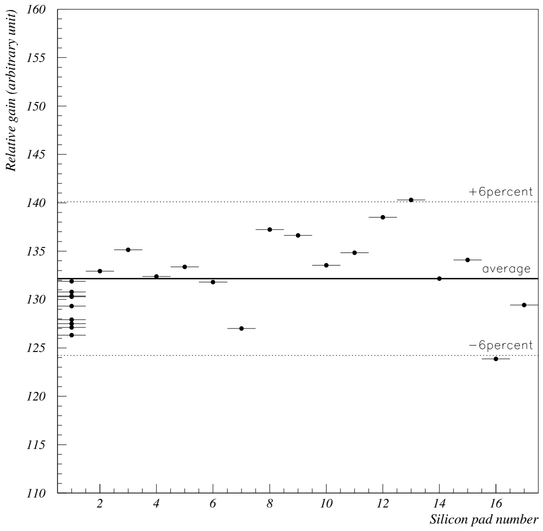

Figure 4.12: Results of the gain measurement of small Si pad detectors

reproducibility is about ± 2.3%. Fig. 4.12 shows this result. These measurements show the relative gain of the silicon detectors is consistent within about six percent.

We calibrated the gain of the large-type Si pad detector using the beam with setting Si pad perpendicular to the beam center (Fig. 4.13).

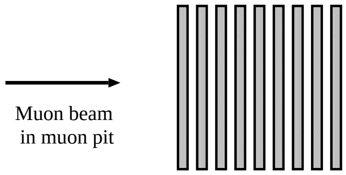

Figure 4.13: The relative gain calibration of large Si pad detectors

We had a 10% level difference of beam intensity along the beam line because of unstable beam during this calibration. This is because it was performed at a very preliminary stage of this experiment. Thus we quote the error of this relative gain as 10%. Results of this calibration are shown in Fig. 4.14

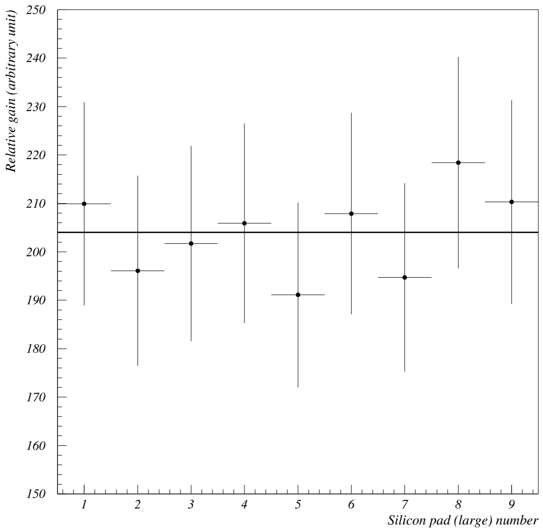

Figure 4.14: The relative gain of large Si pad detectors

4.2 Pion Monitor

4.2.1 Conceptual Design of Pion Monitor

As described in chapter 2, the aim of the pion monitor is to measure the momentum and the angle of pions after the 2nd horn. Charged pions decay only to a neutrino and a charged lepton after the pion monitor. The decay kinematics are completely known. Therefore we can calculate the neutrino spectrum at an arbitrary distance from pion angle and momentum information.

We use the pion monitor information to extrapolate the KEK neutrino flux to the SK neutrino flux. From the above discussion, the pion monitor can predict the neutrino spectrum at KEK, at SK, and their ratio with its own information. We can confirm our understanding of the beam by comparing the neutrino spectrum measured by the near detector with that of the pion monitor prediction.

Principles to measure angle and momentum of pions

1. Optics (Pie shaped spherical mirror and photon detectors)

   A spherical mirror is used to measure angle and momentum of pions. It has interesting properties; Cherenkov photons are focused on same ring at the focal plane if they are emitted by particles which have the same beta and angle. (Fig. 4.15) This focusing effect is independent of the particles' positions. This allows us to measure the angle and beta of the pions.

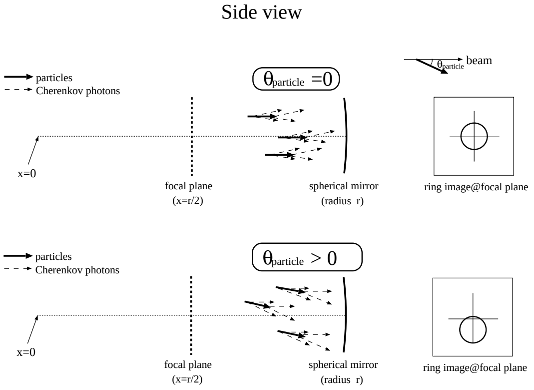

Figure 4.15: A principle of the spherical mirror

Furthermore we designed the spherical mirror to be pie-shaped like Fig. 4.16

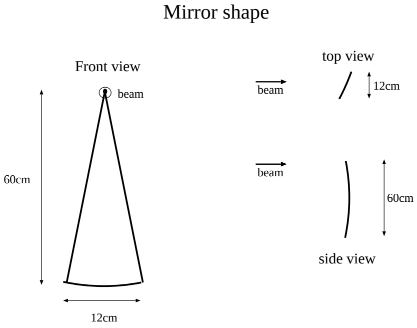

Figure 4.16: The spherical mirror of the pion monitor.

Initially, we planned to use a round mirror, however the reflected image is distorted if the round mirror has a kick angle. For example, Fig. 4.17 shows MC simulation results of this distortion in kick angle of 30 and 45 degree cases. These images are the Cherenkov photon distribution at the focal plane. The particles were assumed to have β=1 with the same angle around the mirror. The round mirror is 70 cm in diameter, and 4000 mm in radius of curvature. The Cherenkov radiator thickness and refractive index is assumed to be 30cm and n=1.0027, respectively. In this case, the radius of Cherenkov ring at the spherical mirror is ~2mm. The ring image from one particle is contained by the spherical mirror.

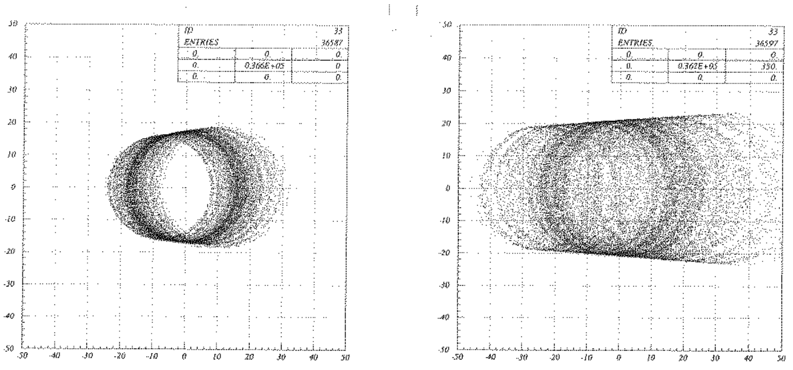

Figure 4.17: The ring image of the Cherenkov light on the focal plane using a round mirror. Left figure: round mirror with kick angle 30 degree. Right: 45 degree.

We define the "kick angle" as the angle between the beam direction and the normal of the spherical mirror around the beam center (Fig. 4.18). In the previous figure (Fig. 4.17), the angle of all particles is parallel to the beam direction.

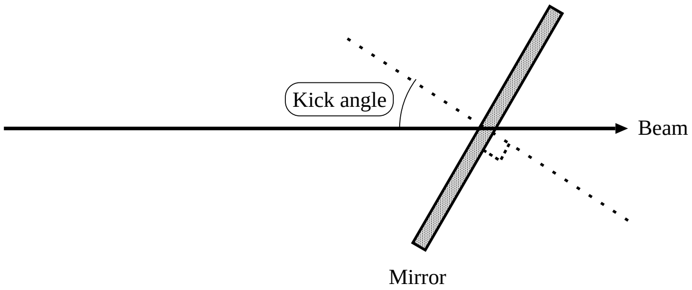

Figure 4.18: The definition of the kick angle of a spherical mirror

Our mirror must have a large kick angle because the photon detector at the focal plane has to avoid the primary beam. On the other hand, pie-shaped mirror does not create any distortion, as shown in Fig 4.19.

Moreover a pie-shape has an advantage of detecting only the radial divergence of the pions. Radial and azimuthal divergence to the beam are defined like Fig. 4.20. Pions have much larger radial divergence than azimuthal divergence. Thus a pie-shape is suitable for detecting the pion divergence. Since a round mirror is sensitive to all directions of the pion divergence, it is difficult to separate radial and azimuthal contribution.

We have to assume azimuthal symmetry of the π beam in using this shape since we are observing only 1/30 of the total beam. The systematic errors caused by this will be discussed later.

2. Photon detector

   A photon detector is installed on the focal plane like Fig. 4.21. One dimensional detector design has enough power to analyze the pions' kinematics. If we use a spherical mirror like Fig. 4.16,

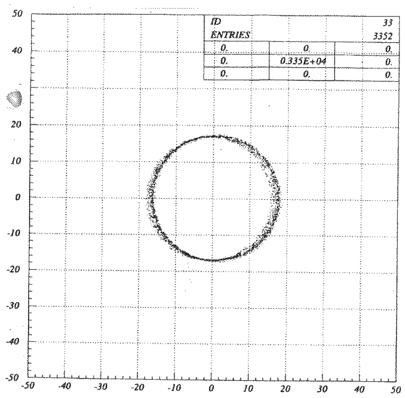

Figure 4.19: The ring image of the Cherenkov light on the focal plane using a pie-shaped mirror. The kick angle is 30 degrees. The condition of the particles is the same as Fig. 4.17

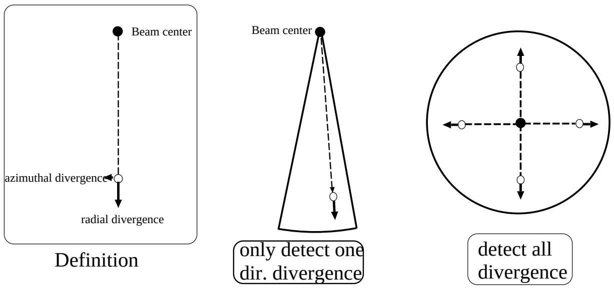

Figure 4.20: Radial and azimuthal divergence.

the Cherenkov ring image at the focal plane can move along vertical axis. MC simulation proves that the ring image moves predominantly along the vertical axis (Fig. 7.1).

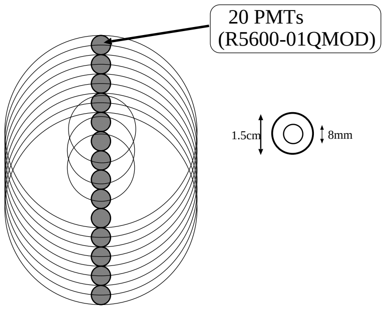

Figure 4.21: Position of the photon detectors with respect to the ring images

Principle to measure momentum of pions

1. Variable gas pressure

   It is essential to take data at various gas pressures for the measurement of the momentum of the pions. The Cherenkov threshold for a pion of given momentum varies with the gas pressure.

   Seven variable gas pressures are set for the pion momentum measurements. Those are summarized in Table 4.1

Pressure (atm)	Refractive index	Pion Cherenkov Threshold (GeV/c)
0.34	1.00047	4.6
0.42	1.00058	4.1
0.53	1.00074	3.6
0.68	1.000945	3.2
0.92	1.00128	2.8
1.24	1.00170	2.4
1.70	1.00236	2.0

Table 4.1: Gas Pressure set in the pion monitor run

Since we have to avoid severe primary proton beam background, the refractive index should be lower than n=1.00264 which corresponds to Cherenkov threshold of 12 GeV kinetic energy of proton. This limit the sensitivity for the pion momentum to be higher than ~2 GeV/c. Figs. 4.22 and 4.23 show the result of MC simulation for the momentum and beta distribution at the pion monitor location, respectively.

There are lots of electrons and positrons in the beam. The way to handle these backgrounds against pion signals will be discussed in chapter 7.

4.2.2 Hardware Set up of Pion Monitor

As shown in Fig. 4.24, the pion monitor is situated between the 2nd horn and the decay pipe. The right side of this figure is upstream of the beam. The pion monitor is designed to be retractable. It is moved to the beam-line only when we make a pion monitor run. Otherwise it is hidden at the escape position to protect it from radiation and not to disturb the beam.

The apparatus of pion monitor is designed based on the above principles. Technical points to be considered in designing it are as follows.

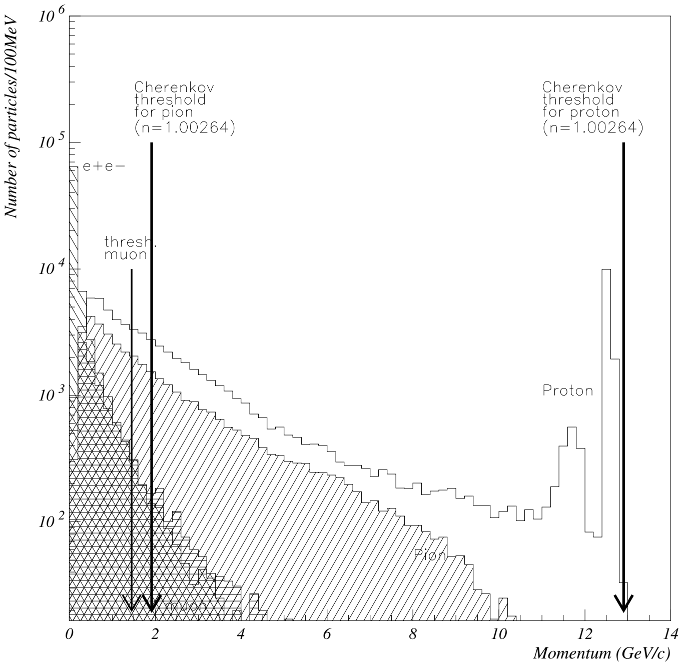

Figure 4.22: The momentum distribution of four kind of particles/10^5protons after the 2nd horn. (protons, pions, muons and electrons)

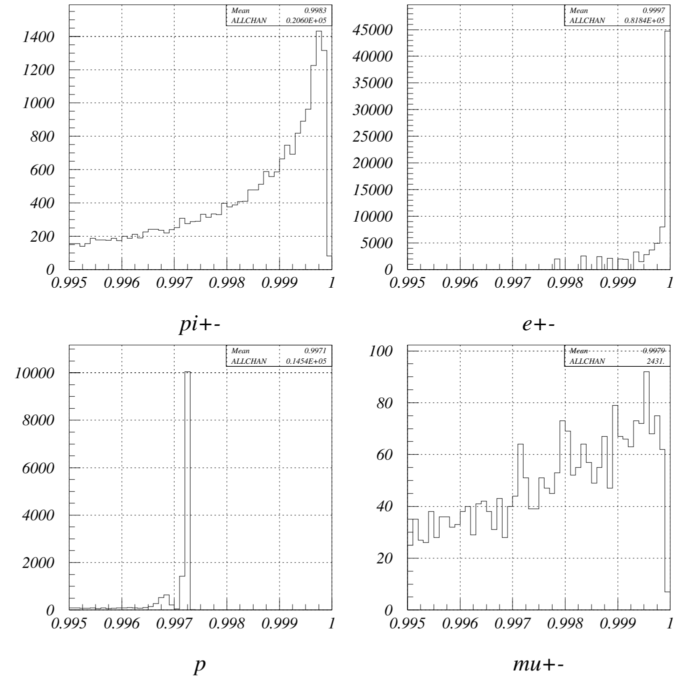

Figure 4.23: The beta(v/c) of various particles. Top left figure shows the beta of pions, top right is e^+e^-, bottom left is protons bottom right is muons.

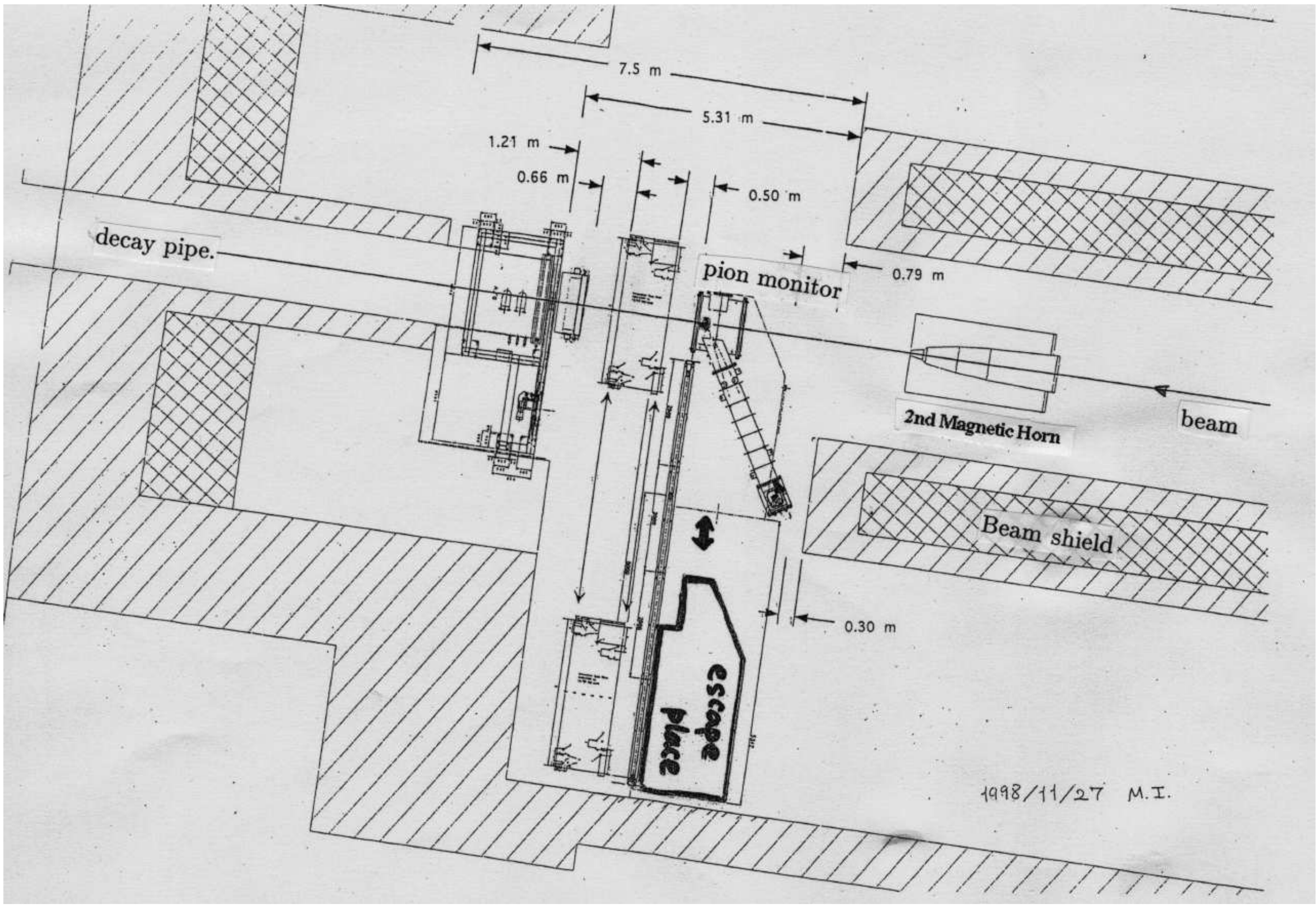

Figure 4.24: The 2nd horn, the pion monitor and the entrance of the decay pipe in the T-station

1. Radiation hardness. : The pion monitor is located in the primary beam-line. This causes severe radiation level.
2. Pulse response to intense photons.: The photon detector receives a lot of photons within 1μs. $1.0\times10^9/\mathrm{cm}^2$ level of photons comes to the photon detector.
3. Mechanical strength for gas pressure.: The gas vessel of the pion monitor has both inside and outside pressure because variable gas pressures are needed. We made a mechanical test for the window of the pion monitor using water, which is discussed later.
4. Large acceptance for the pion beam.: The pion beam is very broad after the 2nd horn (Fig. 4.25: radial distributions of pions).
5. Minimum material to the beam-line : This is not only for the small background creation (interaction between material and particles), but also for small heating up.
6. Remote control and monitoring system.: There is strong level of radiation around the pion monitor during and even after the beam-time. This requires a stable and remotely controllable system to handle various functions.

Designed pion monitor is shown in Fig. 4.26. The photograph of the gas vessel with the moving system of the pion monitor is shown in Fig. 4.27.

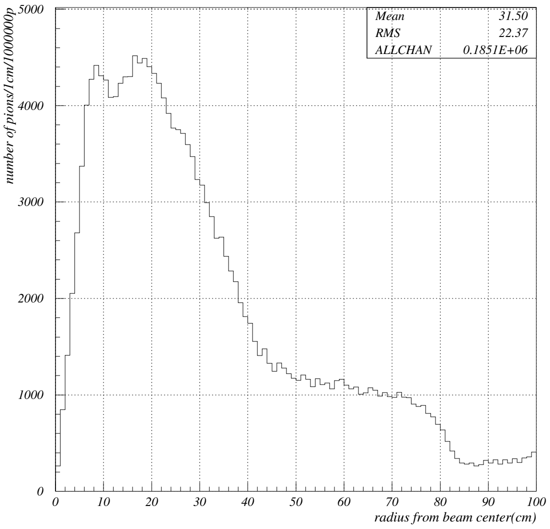

Figure 4.25: Radial distribution of pions after the 2nd horn (MC)

R&D was performed on the following items with serious care. We will explain these items in order.

1. Gas selection
2. Gas system
3. Spherical mirror
4. Photon detector
5. Gas vessel

6. Calibration system

7. Readout system

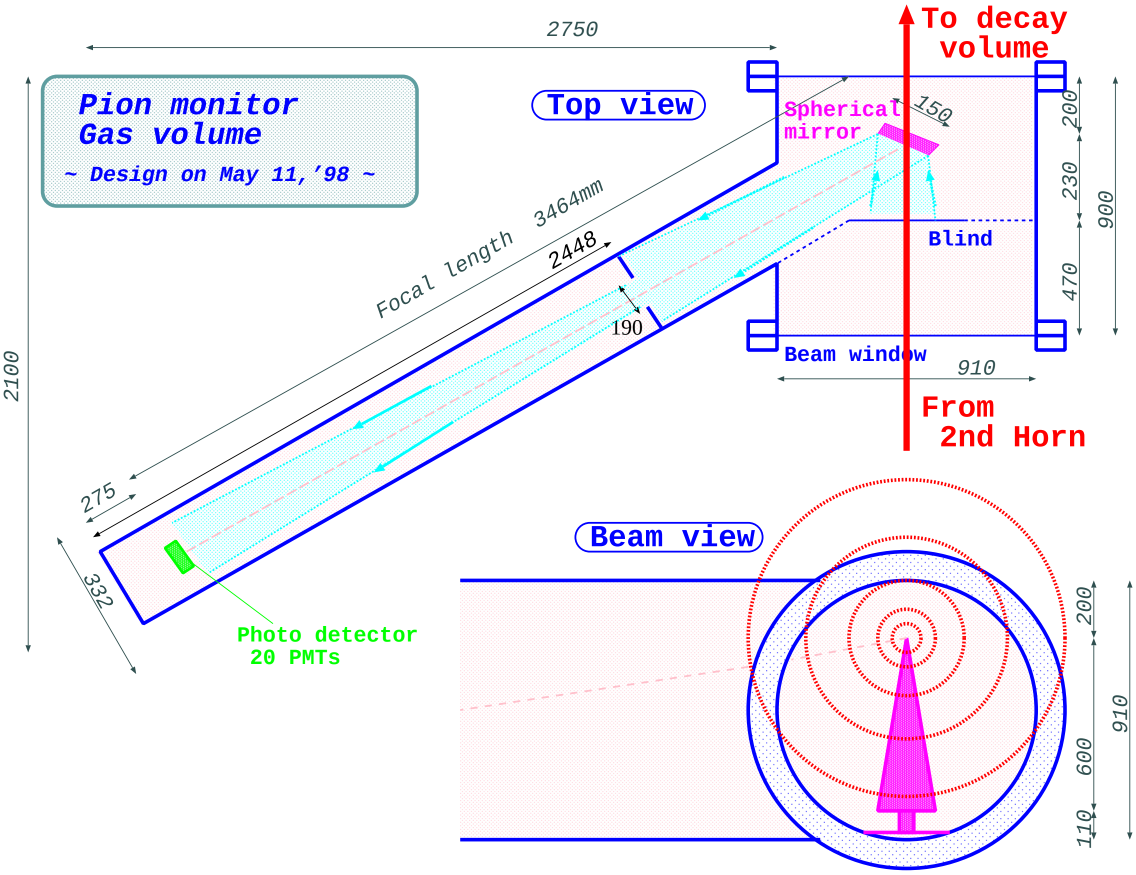

Figure 4.26: Pion monitor

Selection of gas

We want to measure the pion momentum as low as possible since it is important to know the low energy neutrino flux to investigate a lower Δm^2 region. This means that the refractive index should be as high as 1.00264, which corresponds to the Cherenkov threshold for 12 GeV kinetic energy protons.

Freon gas is the best solution to get such a high refractive index. It is good also from the safety point of view because it is not flammable or poisonous.

Refractive indices of various gases were studied. An interferometer was used to measure them as shown in Fig. 4.28.

The beam size of the He-Ne laser light is enlarged by the laser beam expander. It goes to the vacuum vessel which is separated into two regions inside. One part of it is kept at vacuum ($\sim$ 1 torr) and the other side is being filled with gas with a constant rate. In this system, interference stripes in the microscope move proportionally to the gas pressure. The number of stripes which pass through the one fixed point in the microscope area are counted as shown in Fig. 4.29. This number is related to the refractive index n by the following formula;

$$N = \frac{n-1}{\lambda_0/d}, \tag{4.1}$$

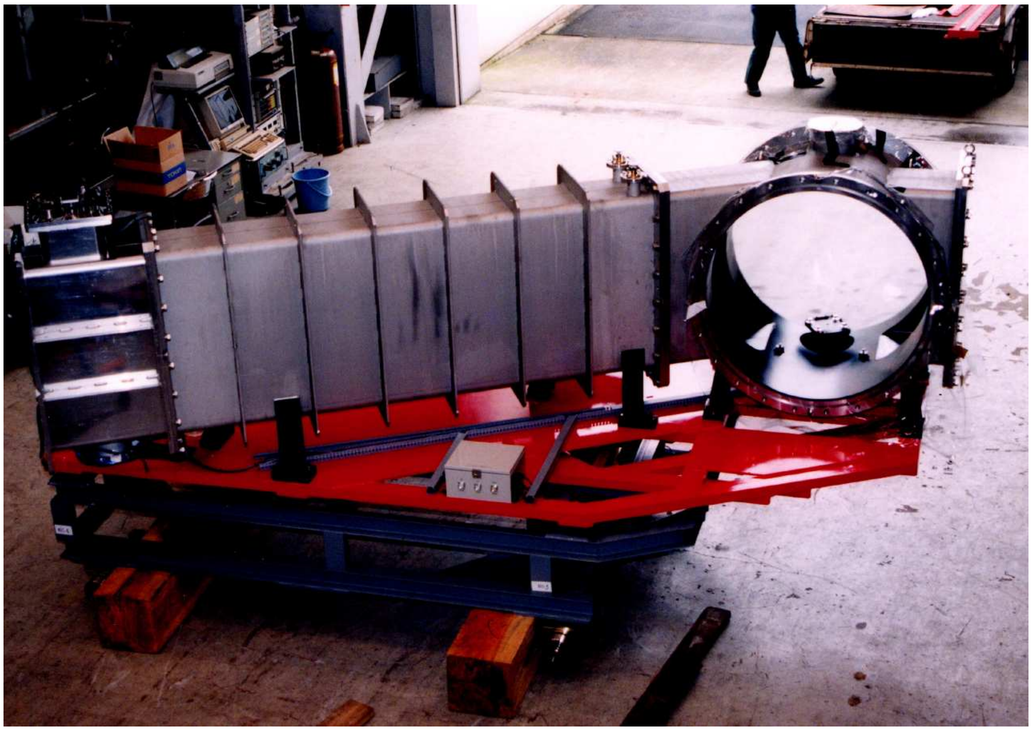

Figure 4.27: The photograph of the gas vessel with the moving system of the pion monitor

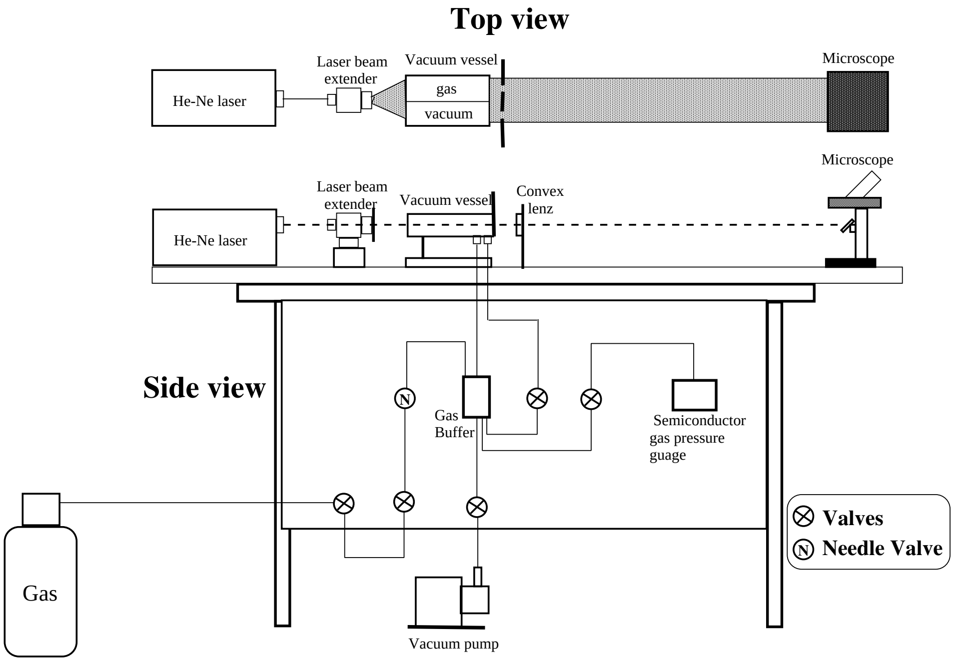

Figure 4.28: Interferometer

where, λ_0 is wavelength of laser (632.8 nm), d is length of the vacuum vessel (230.0 mm). In the example of Fig. 4.29, N=3 under $\Delta P=P_1-P_0$, thus the change in the refractive index is $(n-1)=8.254\times10^{-6}$.

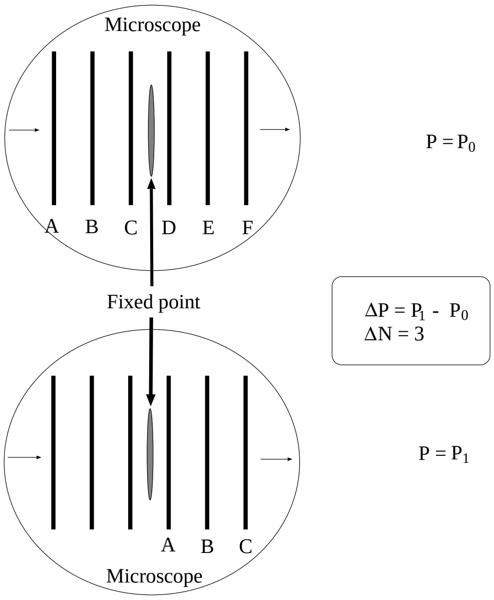

Figure 4.29: The interference stripes in the microscope.

It was concluded that R-C318 freon gas has the highest refractive index (n=1.00123, at 25°C, 1 atm. : Fig. 4.30)*

Gas system

A remotely controllable gas system is prepared to vary the freon gas pressure in the gas vessel.(Fig 4.31) It is a closed system, consisting of a gas supply system, a gas recirculation system and an interferometer calibration system.

The gas supply system consists of gas bottles, 100 meter long pipe with 1″ diameter to connect the highly irradiated target station to safe outside world, a lot of valves, gauges and so on. The 100 meter pipe has a heating system so as not to liquefy the gas.† To control the pressure below the 1 atm inside the gas vessel of the pion monitor, we have a rotary pump system nearby the pion monitor.

The gas recirculation system has a pump and a gas buffer. This system is designed to reuse the gas that is once filled in the gas vessel.

The interferometer calibration system is quite similar to the system in Fig. 4.28. It aims to measure the air contamination of the gas in this closed system. The contamination leads to lower indices of refraction than expected. Correction is needed for the refractive index if the contamination is found.

Air-tightness of the gas vessel of the pion monitor is tested employing the vacuum. The gas vessel kept the vacuum within 20 hours from 1.3×10^{-1} torr to 3.2×10^{-1} torr. This is stable enough, taking into account the refractive index of the freon gas.

Spherical mirror

The spherical mirror was made by Kokusai-Shouji K.K. The radius of curvature of the mirror is 6000 mm and the size is 600 mm×150 mm. It is made of Pyrex glass which is partially coated with Al and frosted by sand to make a pie-shape (Fig. 4.32). A hardness for the radiation and heating-up was

---

[*] The refractive index of this gas has a wavelength dependence. It is described in chapter 7. These values are for wavelength of 632.8 nm

[†] C_4F_8 has low vapor pressure. The vapor pressure is about 2.3 atm at a temperature of 20 degrees.

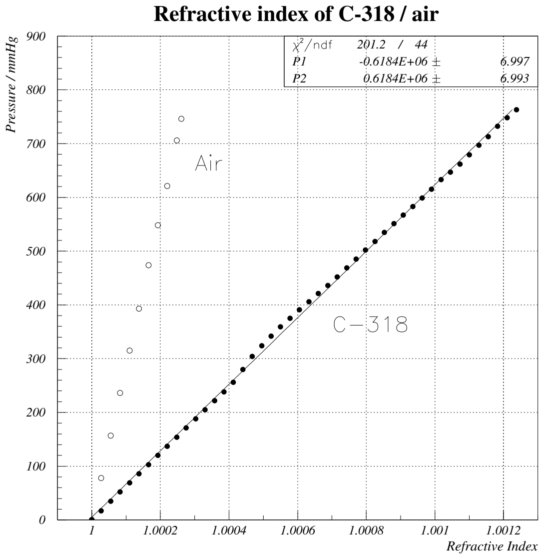

Figure 4.30: The result of the refractive index measurement

tested with intense proton beam before the K2K experiment. The quality of the optics was tested using an LED.

1. Test of radiation and heating-up hardness by a beam
   The test of heating up and radiation hardness to the beam was done at the KEK booster beam dump. The intensity of the KEK booster beam at this test was about 1.2×10^{12} ppp; the repetition rate was about 20 Hz; kinetic energy of the protons was 500 MeV; and the RMS width of the fitted one dimensional profile (using a Gaussian) is ~1 cm, while in the real K2K beam case, the intensity is 6.0×10^{12} ppp and the repetition rate is 1 pulse/2.2 sec. These parameters are summarized in table. 4.2

	K2K	Booster beam-dump
Beam intensity	6.0×10^{12}ppp	1.2×10^{12}ppp
Beam width	1μs	50ns
Repetition	1pulse/2.2sec	72pulse/4sec
Kinetic energy	12GeV	500MeV

Table 4.2: Comparison of proton beam parameters between the K2K experiment and the KEK Booster beam-dump

   This test beam is much more severe than the real one regarding heating up since the cooling time is 40 times shorter and dE/dX is as large as twice.

   The glass was exposed to a total of 6.3×10^{16} protons in this test. This corresponds to about 6 hours radiation of the real K2K beam. 4 cm × 4 cm × 6 mm(thickness) Pyrex glass stood under this severe situation. The Al coating part was not clouded by this radiation level, although this was checked only by eye, not quantitatively. It was concluded that the Al coated Pyrex glass mirror was strong enough to be used in the real experiment.

2. Test of optics quality using LED
   The optical quality of this spherical mirror was tested using an LED (Fig. 4.33).

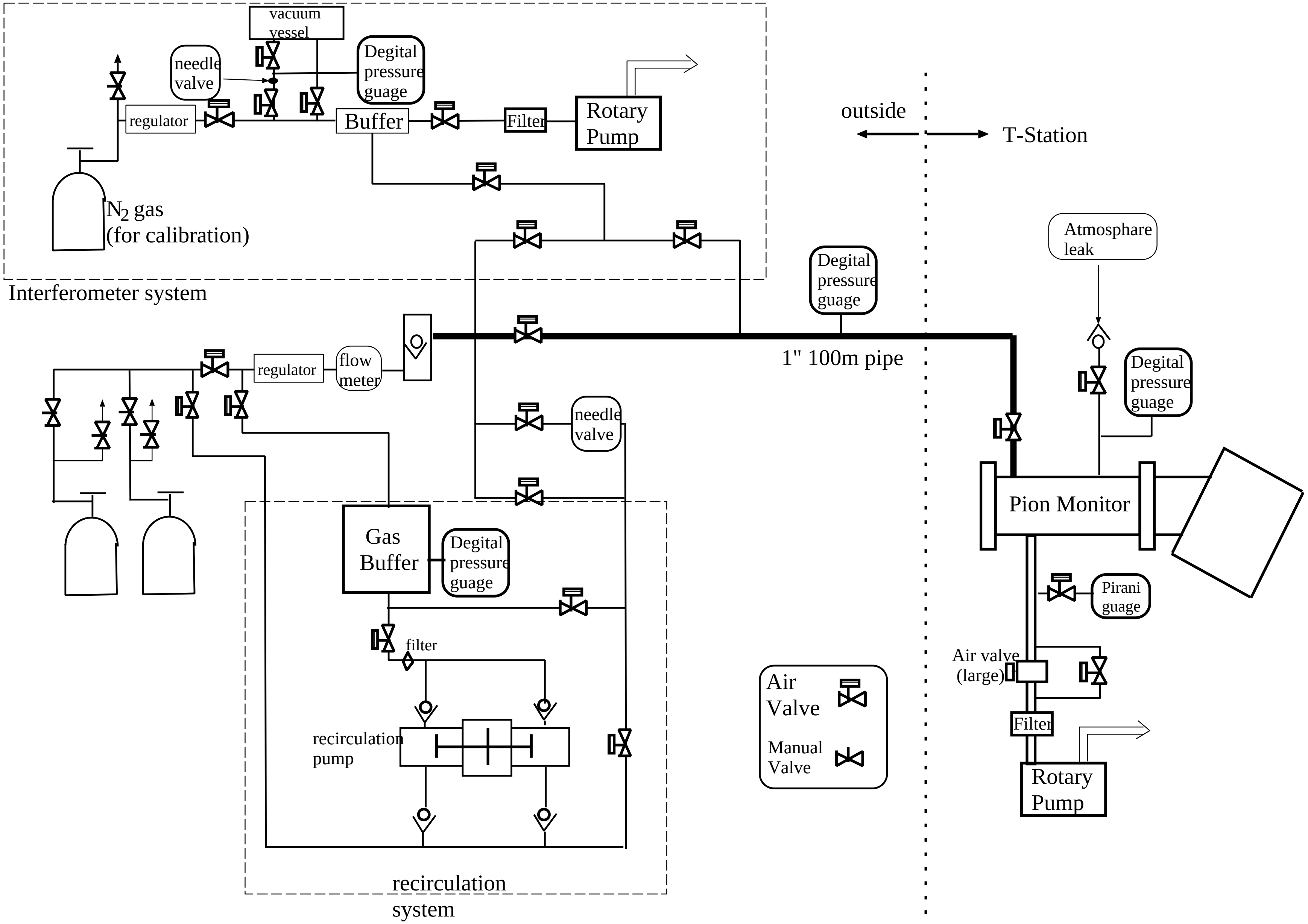

Figure 4.31: The gas system of the pion monitor

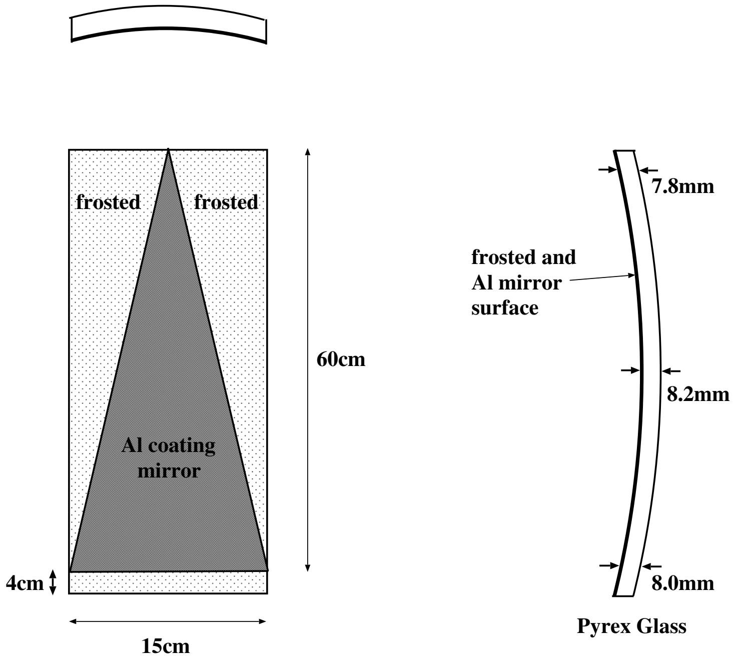

Figure 4.32: The pie-shaped spherical mirror

Figure 4.33: LED test of the spherical mirror

Spherical mirrors focus light emitted from a point source at the center of the sphere on the point source itself (Fig. 4.34). We can measure the radius of curvature and check the imperfection of the mirror by illuminating the mirror with a point source, an LED. By moving a camera to find the most focused image of the LED, we measured the radius of curvature to be 5827 mm. We also measured the level of aberration to be negligible.

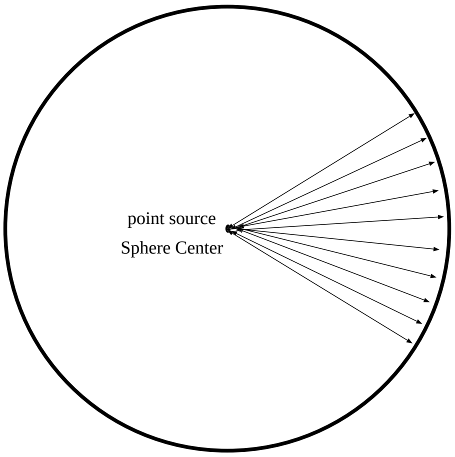

Figure 4.34: The characteristics of spherical mirrors. Spherical mirrors focus light emitted from a point source at the center of the sphere to the point source itself.

Photon detectors

Twenty modified R5600-01Q type PMTs (made by HAMAMATSU Photonics Corporation) are used for the photon detector.(Fig. 4.35)

These PMTs have 3 main different characteristics from standard ones(R5600-01).

1. Quartz window
2. Multi-Alkali(Sb-Na-K-Cs) photo-cathode material
3. Low gain

The reasons are following.

1. Quartz window

   This is for radiation hardness. It is well known that the standard window (BK7) gets dark under severe radiation while quartz is quite strong for radiation.

   In order to check it, radiation damage to a PMT window was tested at the K3 beam-line of KEK-PS. (Fig. 4.36)

   At first, we estimated total number of particles/cm^2 around PMT region for K3-line and K2K using a MC simulation. It is summarized in Table 4.3. [‡] This calculation shows K3 radiation has the same order of magnitude as the real experiment. This calculation has a large safety factor because the pion monitor is located far away from the beam-line except for pion monitor measurements.

   For a quantitative study of radiation damage, transparency ratios of BK7 and quartz were measured before and after this irradiation using a transmeter(Fig. 4.37).

[‡] The span of K2K here is assumed to be full span. (10^{20}POT).

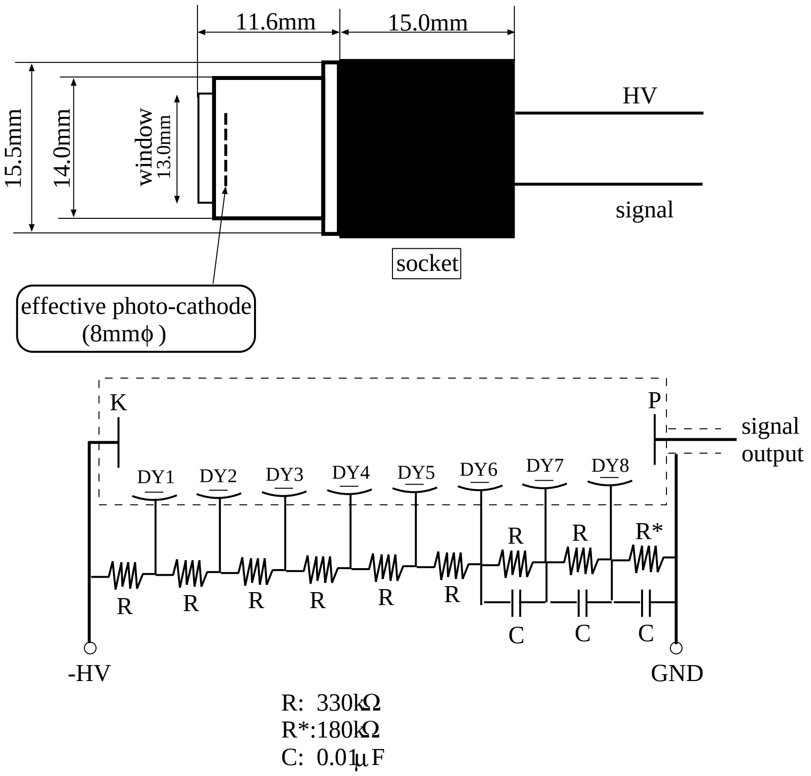

Figure 4.35: PMT used in the pion monitor (R5600-01Q modified)

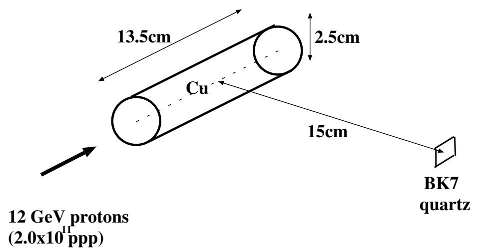

Figure 4.36: Radiation test at KEK-K3 line

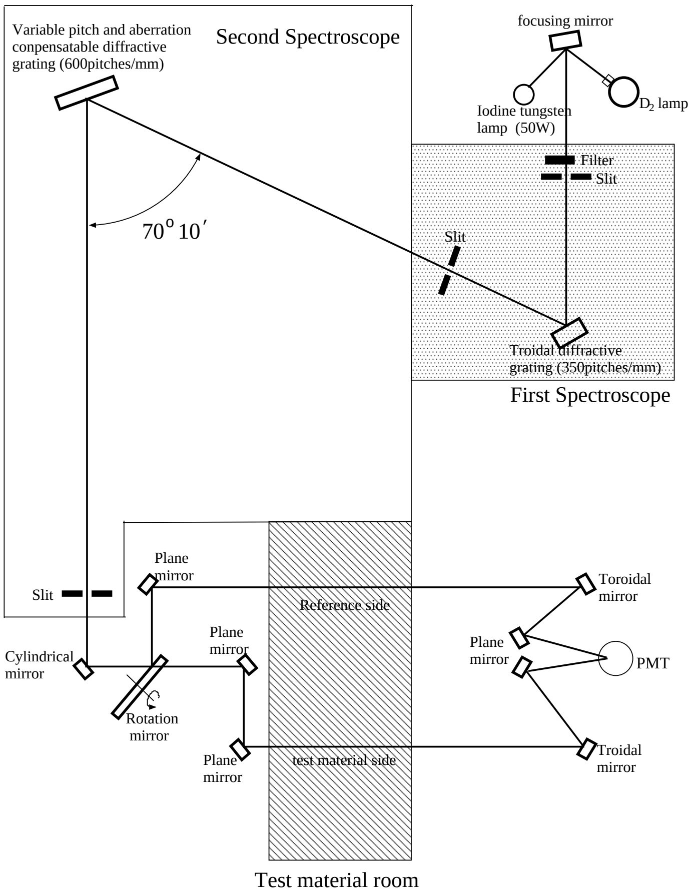

Figure 4.37: Principle of the transmeter

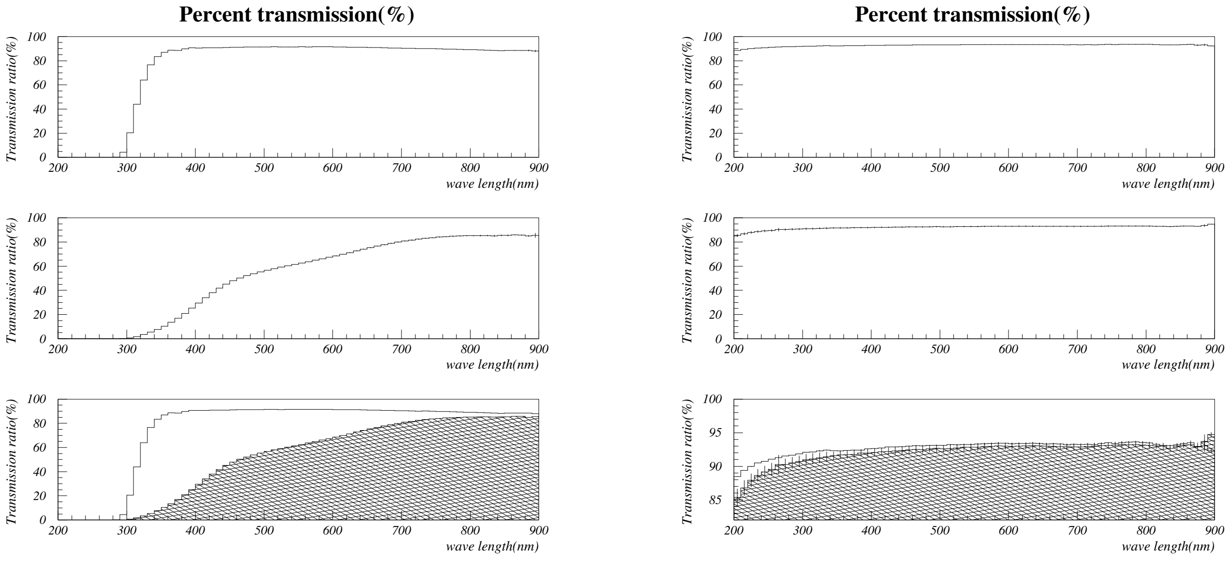

Figure 4.38: Deterioration of the PMT window: left figure: BK7 case, right figure: quartz case. In both figures, the top figure shows the transparency ratio BEFORE radiation, the middle shows AFTER radiation and the bottom shows comparison between BEFORE and AFTER radiation.

This transmeter is used to measure transparency ratio from 200 nm to 900 nm. Many slits and diffractive gratings were used to select the wavelength of light. Finally the light intensity which pass through the material is compared to the reference side (air). The transparency ratio is defined to be,

$$T(\%) = \frac{Material\ side\ light\ intensity}{Reference\ side\ light\ intensity} \tag{4.2}$$

Fig. 4.38 shows the results of the deterioration of the PMT window caused by radiation.

This measurement shows the deterioration of the PMT window made of quartz glass is very small under this level of radiation although the transparency ratio around 200 nm wavelength falls a few percent.

2. Multi-Alkali(Sb-Na-K-Cs) photo-cathode material:
This is for wide dynamic range of photo-cathode. With utilizing multi-alkali photo-cathode, there is no saturation of signal up to 10 micro ampere[42]. Standard bialkali cathode saturation at 0.1 micro ampere[42].

3. Low gain:
We need low gain PMT to avoid the signal saturation caused by the PMT base since the photon density is very high. With decreasing the multiplication in each dynode step, the gain of PMT (typically 10^6 for the standard PMT) is set to about 1000 with keeping stable operation.

- Relative gain calibration

We calibrated the relative gain of the 20PMTs using a Xe lamp. We provided isotropic light as much as possible using the Xe light with a diffuser. Fig. 4.39 shows the setup.

At first, we measured the position dependence of the Xe light intensity by moving one PMT like Fig. 4.39 (a). This position dependence is used for correction of the data.

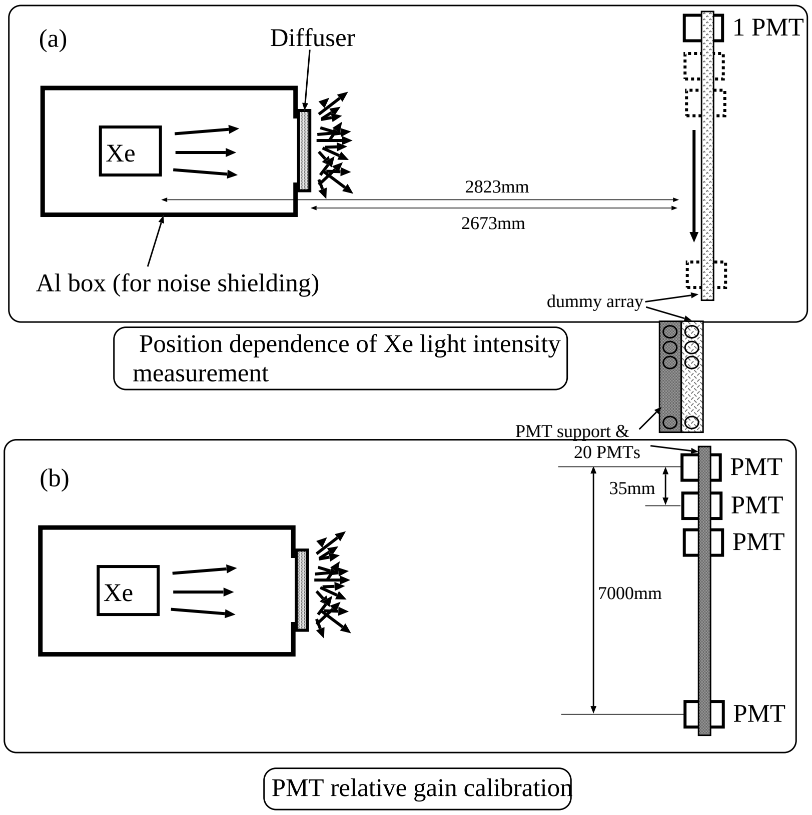

Figure 4.39: PMT relative gain calibration using Xe lamp

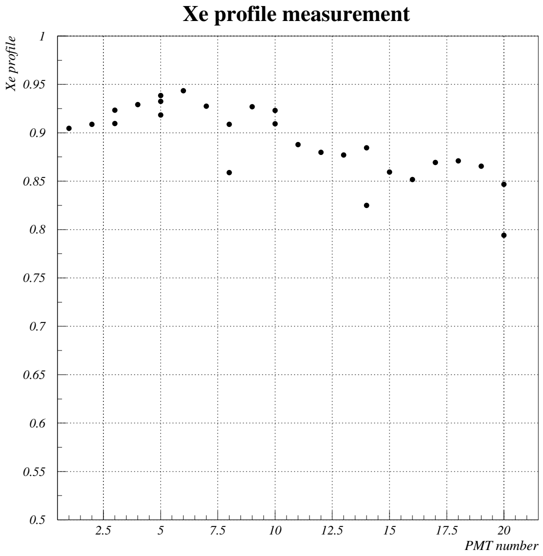

Figure 4.40: Position dependence of the Xe light intensity

The measured position dependence of Xe light intensity is shown in Fig. 4.40. The difference in the measurements at the same points shows that the reproducibility of this measurement is 7%. We monitor the stability of the Xe light intensity with summing up 20 PMTs signal.

Fig. 4.41 shows the relative gain factor of each PMT.

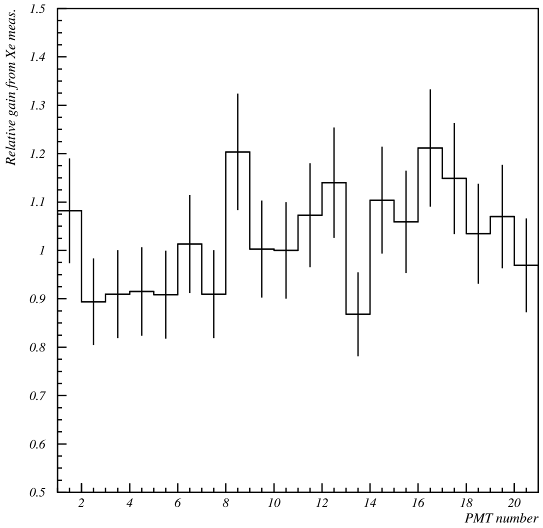

Figure 4.41: The relative gain constant measured by the Xe lamp

We quote 10% uncertainty for this factor since we must include the wavelength difference between Xe and Cherenkov light in addition to the measurement error.

- About the signal saturation of the PMT
  A MC simulation shows that the largest photon number of each PMT at the highest refractive index is $\sim 10^9$. According to Ref.[42], photo-cathode signal saturation starts at 6.0×10^8 photons, which is equivalent to 10 micro ampere of photo-cathode current. It is necessary to decrease light intensity using an optical filter or decreasing the beam intensity is needed.

Gas vessel

The gas vessel plays the following roles.

1. As the gas vessel: it should stand the various gas pressures. As described before, there are several designed gas pressure values including both negative and positive pressures.

   This detector is made from 5 mm thick stainless steel except for the beam window. This is thick enough to stand various gas pressures. However, the beam window must be as thin as possible because the beam goes through this part directly. We designed it like Fig. 4.42. The aluminum thickness was set to be 1 mm, and a pressure resistivity test was performed using water. The results are shown in Fig. 4.43. It shows the Al 1 mm window is strong enough for our use. The material thickness corresponds to 0.011 radiation lengths and 0.0025 interaction lengths. Therefore the multiple scattering effect for 2 GeV/c pions is less than 1 mrad, and the hadron interaction probability is negligibly small in this window.

2. As the precise optical alignment system.

   We need to fix the optics components tightly, hence we prepare a mirror support like Fig. 4.44 and a PMT support like Fig. 4.45.

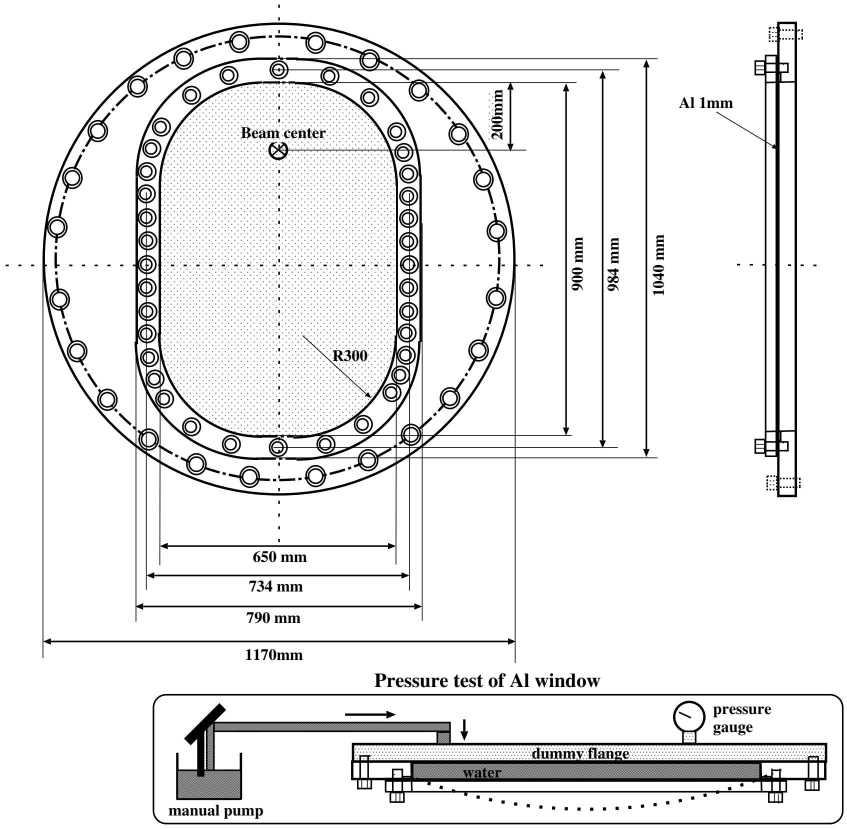

Figure 4.42: The beam window of the pion monitor and the pressure test.

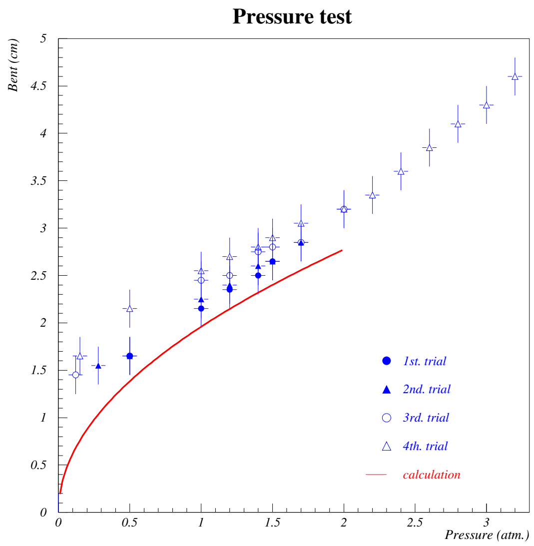

Figure 4.43: Results of the pressure test

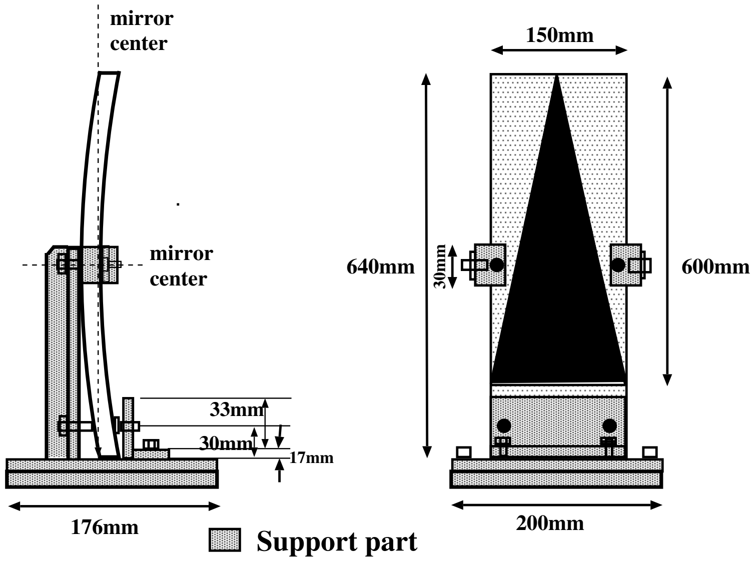

Figure 4.44: The mirror support system

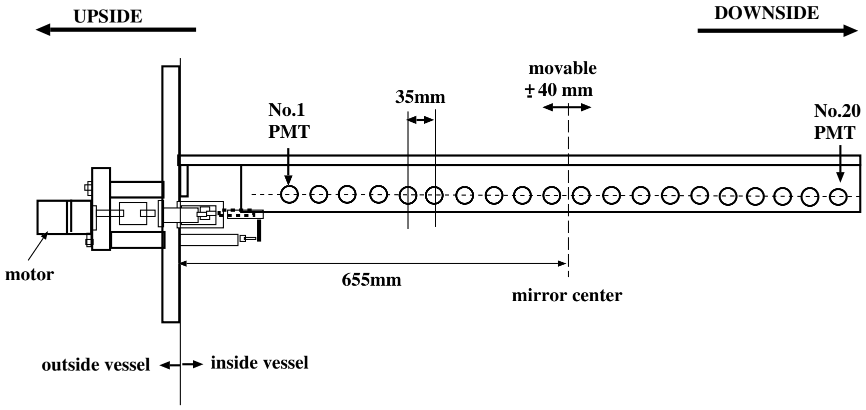

Figure 4.45: The PMT support system

An optical survey was done carefully to align these components. (Fig. 4.46.) The installation position of the spherical mirror was checked at first. Then, employing the laser beam, relative positions between the mirror and PMT was checked.

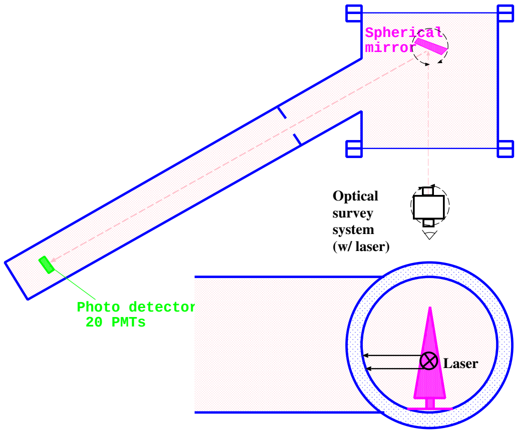

Figure 4.46: Alignment for the optics system

The accuracy of the measurement is 1/3600 degree. The MC simulation took these results into account. The radius of curvature and other properties of the spherical mirror are measured by this system. It is consistent with the LED test result described before.

The supports of the mirror and PMTs are movable in the gas vessel. The support of mirror rotates and that of the PMT array moves vertically. The accuracy of the setting of the mirror rotation angle is 0.01° and that of PMT height is 10 μm. Mirror rotation angle was changed to estimate the background coming from beam associated radiation as will be explained later (i.e. Fig. 7.15). The purpose of the moving of the PMT array will be explained.

3. Moving system: The pion monitor should be located far from the beam-line when it is not used, to avoid large radiation damage with remote control.

   The gas vessel is set on a movable support system like Fig. 4.47. We can move the detector from the measuring point to the escape position like Fig. 4.24. It is about 5 meter apart. We need about 11 minutes to move this distance.

   A highly reproducible mirror location is required. Reproducibility is within a few of 100 μm both in the horizontal and vertical directions, according to the results of the measurement using the optical survey system.

4. As a relative PMT gain calibration system: The PMT array is movable vertically with ±40 cm to the position of next PMT. We compare the PMT signal with same position (same light intensity) when pion monitor measurement take place.

   The result is compared with that of Xe relative calibration result. Fig. 7.38 shows the results of this check. Details is described later.

Laser calibration system

The pion monitor has a laser calibration system to check the mirror reflectivity. (Fig. 4.49)

A fixed 410 nm-wavelength dye laser emits light. The laser pulse is split with some of the light going to the gas vessel by way of 100 meter optical filter and some of the light going to a monitor PMT. Light reaching the entrance of the gas vessel is split again with some going to another monitor PMT to check the transparency of the optical fiber. The remaining light is directed towards the mirror and horizontally focused by the optical lens. Reflected photons at the mirror are detected by

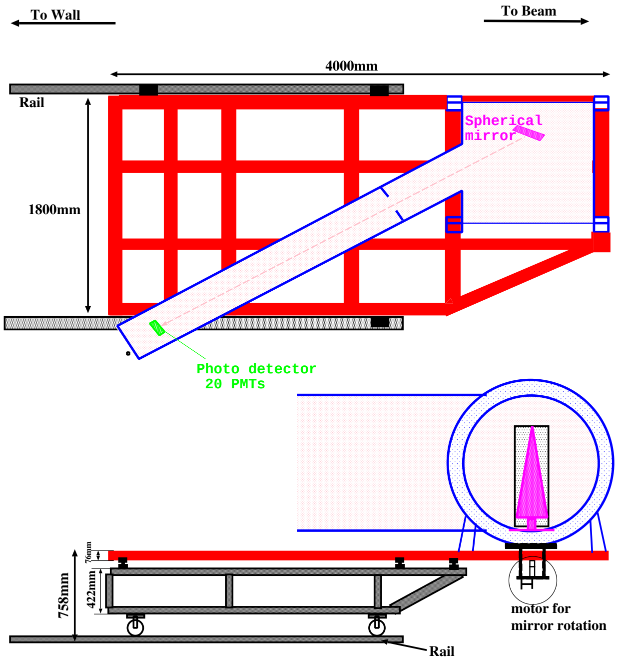

Figure 4.47: The movable support of the pion monitor

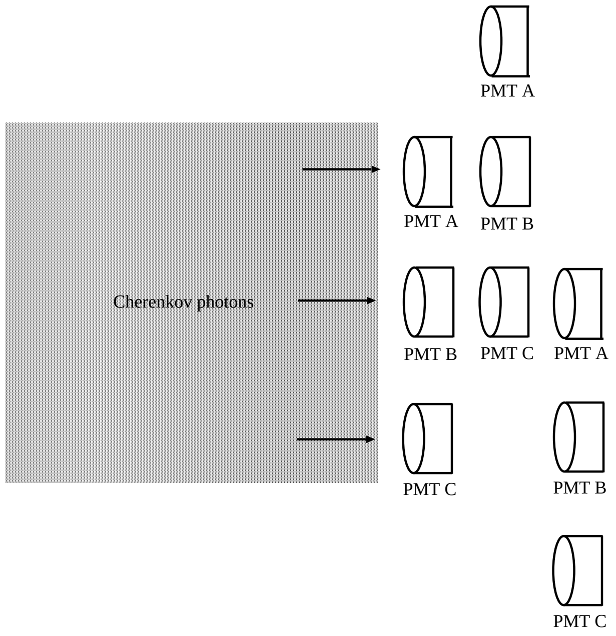

Figure 4.48: Relative PMT gain calibration using the beam

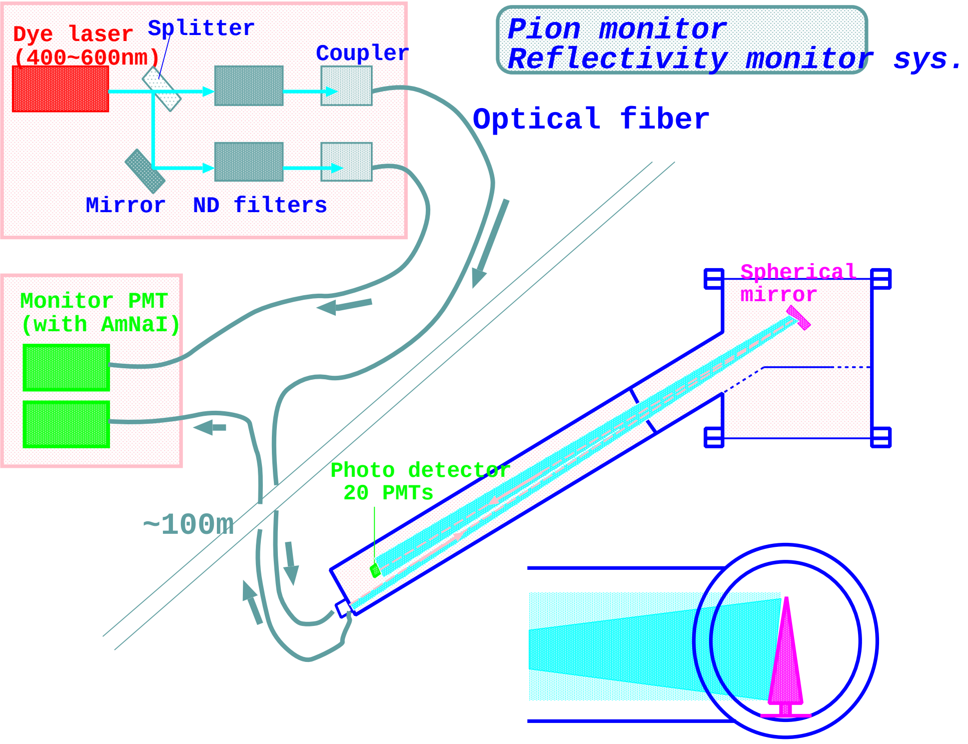

Figure 4.49: The mirror reflectivity monitor

the 20 PMTs. Since the beam size of the laser photons are expanded as if a point source is located at the entrance of the main body, there is one to one correspondence between the mirror reflected position and one PMT. The reflectivity of the mirror can be monitored from the pulse height of the PMTs.

A typical pulse height distribution of the 20 PMTs is shown in Fig. 4.50

About half the number of PMTs cannot detect the reflected photons because the mirror focuses the photons. The mirror shows a reduction of the reflectivity of less than 6% during the 1st-year run.

Readout system

A transformer should be put into the circuit since large noise came from the cable. CAMAC charge sensitive ADCs(20ch) are used for the front-end readout (Fig. 4.51).

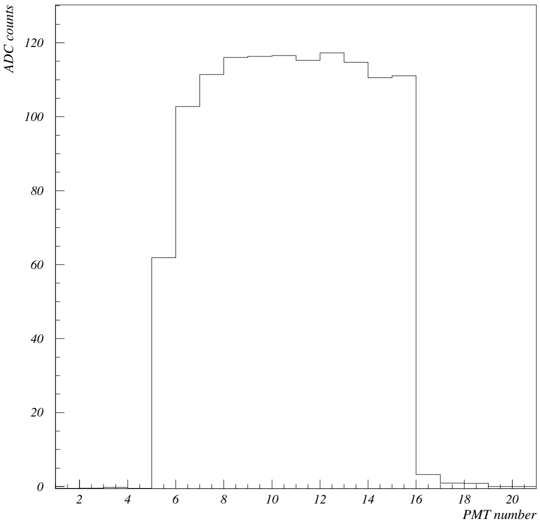

Figure 4.50: Results of the mirror reflectivity monitor

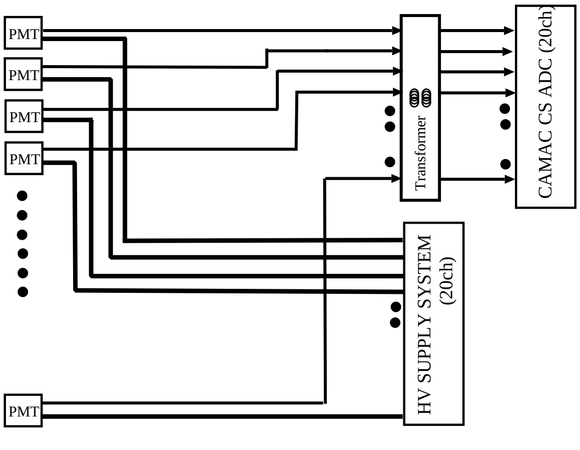

Figure 4.51: Read out system of the pion monitor

Chapter 5

Monte Carlo(MC) Simulation

5.1 MC Simulation for Neutrino Beam

This simulation cover the region from the target to SK. Their components are as follows:

1. Protons are injected to the target with the measured beam emittance.
2. Secondary pions and kaons are generated using a hadron production model in the target.
3. Generated particles are swum in the magnetic field of the horns.
4. Pions, kaons and muons are made to decay to a neutrino and/or an anti-neutrino. Since GEANT[43] does not simulate weak decays correctly* , kaon and muon decay is simulated with an original code.

We must take into account geometry difference between June and November 1999 in MC simulation since we changed the target part of the 1st horn, as described in chapter 3. Since the proton beam emittance was also changed, we also take it into account.

5.1.1 Proton Profile at Target

There are two SPICs between the last magnet and the target. A schematic view and a photograph of them are shown in Figs. 5.1 and 5.2, respectively. The SPIC just after the 39th Vertical dipole magnet, is called as "V39 out SPIC" and that of just before the target is called as "TARGET SPIC".

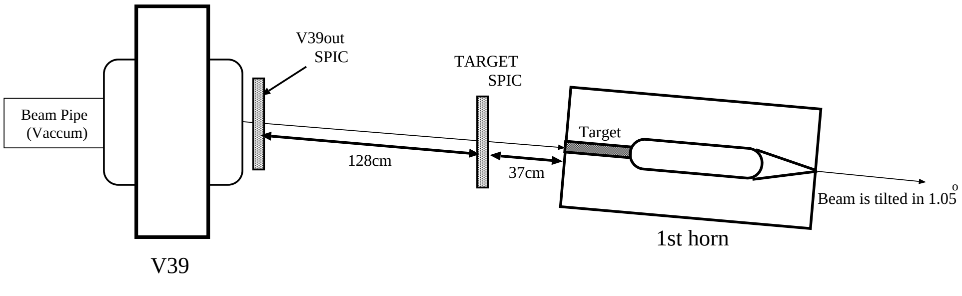

Figure 5.1: A schematic view of the SPICs, between the last magnet and the target

Fig. 5.3 shows the typical x and y projection image of protons in June. Each strip of "V39out SPIC" is 5 mm wide and that of "TARGET SPIC" is 1.27 mm, as summarized in Table 3.1. The emittance of protons can be calculated if it is assumed that protons do not cross over and image of protons are ellipse like.

---

* GEANT makes particles to decay only isotropically.

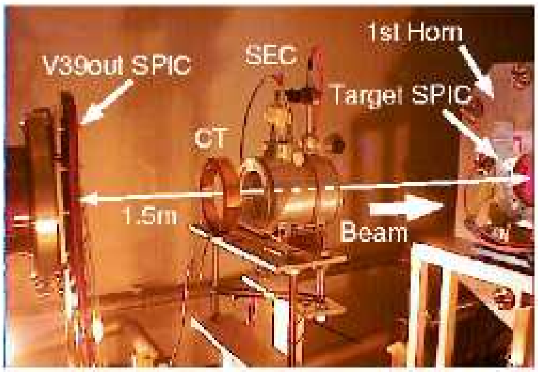

Figure 5.2: A photograph of the SPICs, between the last magnet and the target

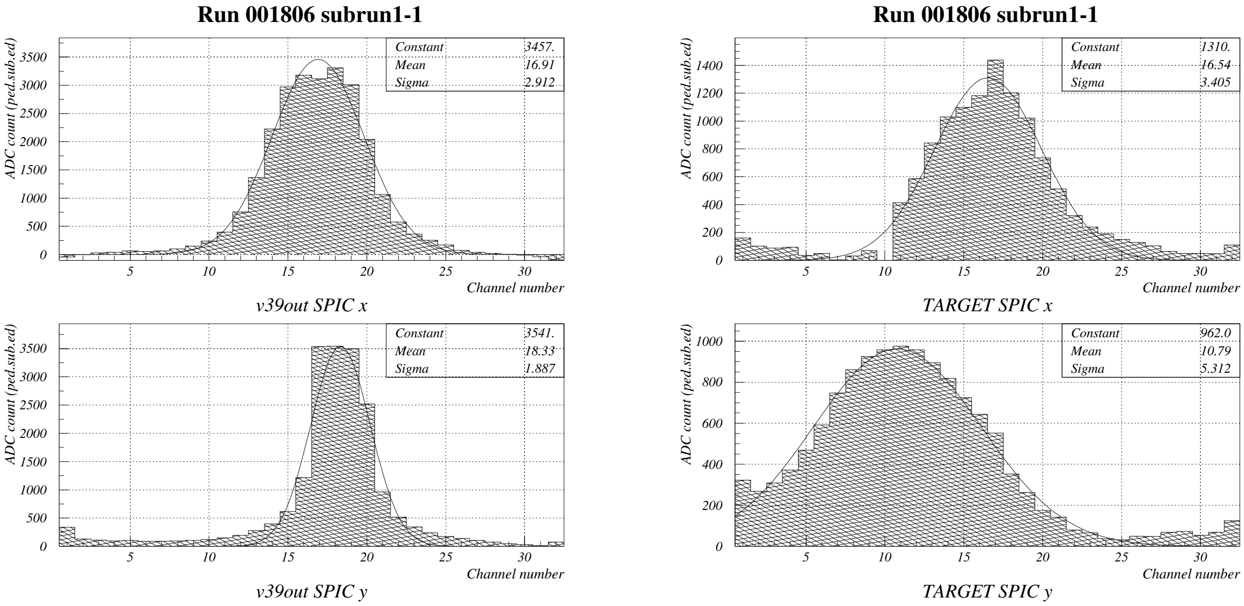

Figure 5.3: The Proton beam profiles measured by the two SPICs before the target. Strip width of "V39out" is 5 mm and that of "TARGET" is 1.27 mm

Fig. 5.4 shows the schematic view of this calculation and Fig. 5.5 shows the results of this calculation in June. x and y means position of the beam, dx and dy means beam divergence.

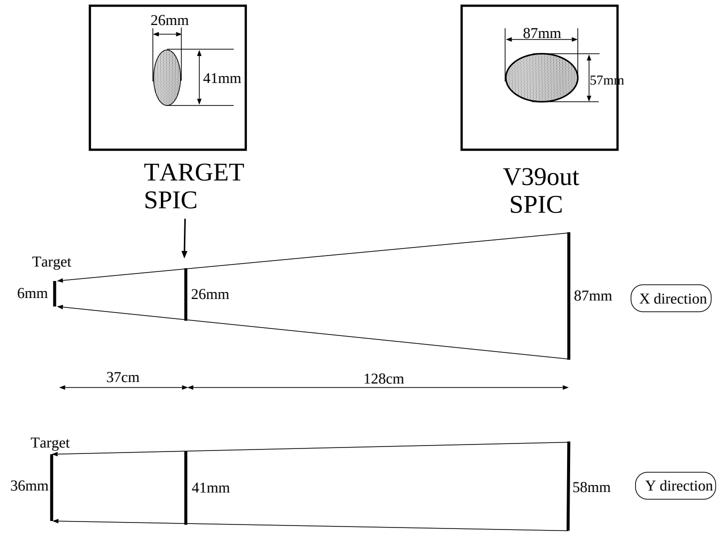

Figure 5.4: The schematic view of the proton emittance calculation. The values correspond to 3σ of a Gaussian fit of the profile data.

Fig 5.6 shows the same plots in November. The calculated proton beam profile at the target in November is wider than that in June for the horizontal direction.

5.1.2 Production of Secondary Pions and Kaons at Target

For the simulation of the secondary-pion production at the target there are some hadron production models. This is the largest ambiguity of this Monte Carlo simulation. There have been various pion production experiments in this energy region, however results of these experiments are different with each other.

Three kinds of pion production models are used.

1. FLUKA/GCALOR model [44] [45].
   This model has larger cross section for the p-Al interaction than other models. It tends to produce higher energy secondary pions.

2. Fit to measurements (I), Sanford-Wang[46].
   This model used results of the compilation of the measurements made by Lundy *et al.*(13.4 GeV)[47], Dekkers *et al.*(11.8, 18.8 and 23.1 GeV)[48], and Baker *et al.*(10.9, 20.9 and 30.9 GeV)[49]. The results of this compilation are described by Yamamoto and used by him for a comparison with his measurements [50]. Yamamoto's measurements agreed well with this compilation.

3. Fit to Measurements (II), Cho[51].
   This uses the result of the measurements performed by Cho's group few years later to resolve a question of low cross sections measured by Lundy *et al.*[47] with the same proton beam at Argonne and to have a better understanding of their neutrino beam. This experiment uses spectrometers to measure the accurate differential cross sections ($d^2\sigma/d\theta dp$). The results are fitted using Sanford-Wang formula with other experimental ([52],[53],[54],[55]) results.

Sanford-Wang formula is an empirical formula which gives quantitative description of the secondary particle production based on the characteristics of experimental data[46]. This formula has 8 parameters and is represented in Ref.[51] as follows;

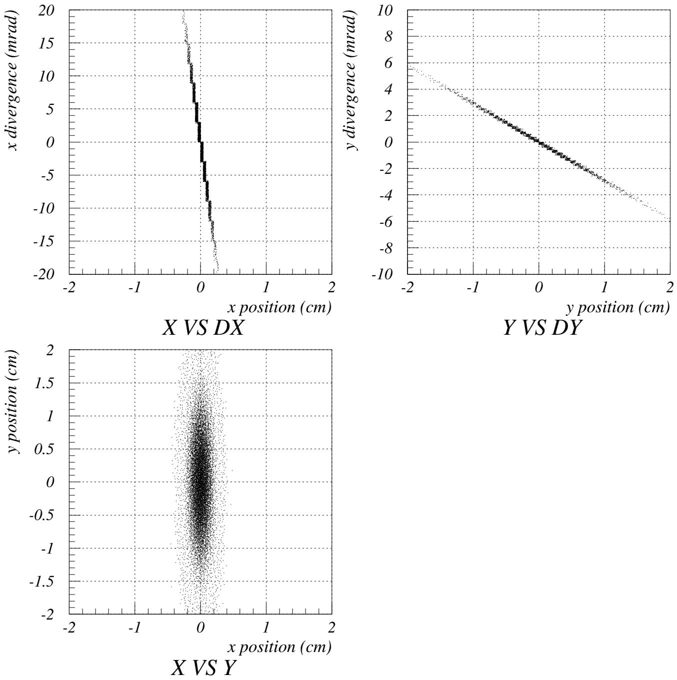

Figure 5.5: The results of the proton emittance calculation. Top-Left: x vs dx (x is the horizontal position, dx is the horizontal divergence of the beam), Top-Right: y vs dy, Bottom-Left: x vs y (proton profile at the target)

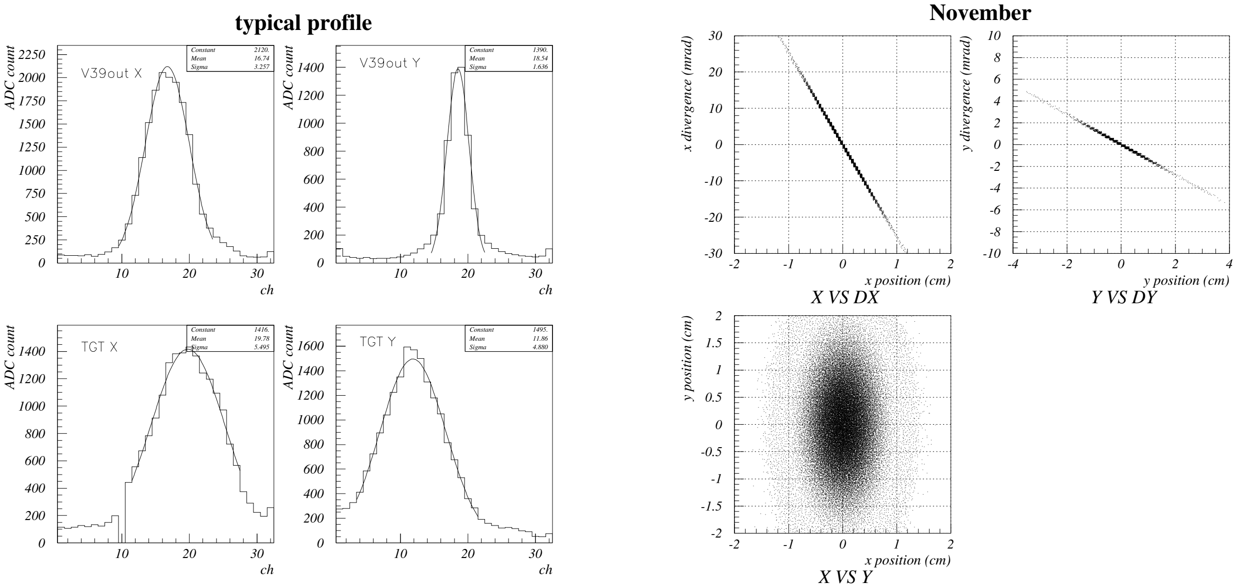

Figure 5.6: The Proton beam profiles measured by the two SPICs and the results of the proton emittance calculation.(November)

$$\frac{d^2n}{d\theta dp} = C_1 \cdot p^{C_2}\left(1-\frac{p}{p_B-1}\right)\cdot exp\left(-\frac{C_3 \cdot p^{C_4}}{p_B^{C_5}} - C_6 \cdot \theta(p - C_7 \cdot p_B cos^{C_8}\theta)\right), \tag{5.1}$$

where, $d^2n/d\theta dp$ is the differential particle yield per interacting proton, the C_i's are the constants to be found by fitting, p is the momentum of the secondary particle, θ is the angle between the secondary particle and the beam axis and p_B is the beam momentum. Cho *et al.* fitted the particle yield instead of the cross section. Fitted result about π^+ production in reference[51] is summarized in Table 5.1. Their measurements[51, 52, 53, 54] and fit results for π^+ and π^- in Ref.[51] are shown in Fig. 5.7.

	C_1	C_2	C_3	C_4	C_5	C_6	C_7	C_8
2. SW	227	0.65	4.05	1.63	1.66	5.03	0.172	82.7
3. Cho	196	1.08	2.15	2.31	1.98	5.73	0.137	24.1

Table 5.1: The fitted parameters of the Sanford-Wang formula by Sanford-Wang and Cho *et al.*[46, 51]. Only for π^+ production is shown here.

The GCALOR/FLUKA[†] model is interfaced to the GEANT package. Thus GEANT simulates everything using the GCALOR/FLUKA automatically.

In use of other hadron production models, only the interaction of protons more energetic than 10 GeV with the target aluminum is simulated according to (5.1). And the less energetic interaction is simulated according to GCALOR model. For the kaon production part, we also use the formula(5.1) with the kaon parameters in Ref. [46].

Dependence of the neutrino flux on the hadron production model is shown in Fig. 5.10.

5.1.3 Magnetic Field Generated by Horn Magnets

As already explained, horns work as toroidal magnets to focus positively charged particles. This magnetic field has to be considered in this simulation.

Calculated magnetic fields in the horns are used in the simulation. A measurement of the magnetic field at the air part of the 1st horn confirmed the reliability of the calculation [27].

The magnetic field inside the target is calculated with static approximation as a function of r. If one take into account the skin effect in the target, our magnetic field penetrates only ~ 5 mm [56].

5.1.4 Treatment of Particle Decay in Simulation

Pions

Pion is a spin-less particle. The decay is two body and isotropic. In this case, GEANT treatment is correct. Branching ratio is almost 100%, $\mu + \nu_\mu$ (Called $\pi^+\mu_2$). Hence only this mode is taken into account.

Kaons

Kaon is also a spin-less particle. Main contributions to the neutrino are as follows,

1. $K^+ \to \nu_\mu + \mu^+$ (63.51 %) (Called $K^+\mu_2$) [‡]
2. $K^+ \to \pi^0 + \mu^+ + \nu_\mu$ (3.18 %) (Called $K^+\mu_3$)
3. $K^+ \to \pi^0 + e^+ + \nu_e$ (4.82 %) (Called K^+e_3)

[†] FLUKA model was called if incident particle is above 10 GeV even when GCALOR model was called.

[‡] If particle charge is minus, please change the sign and neutrino to anti-neutrino in the formula.

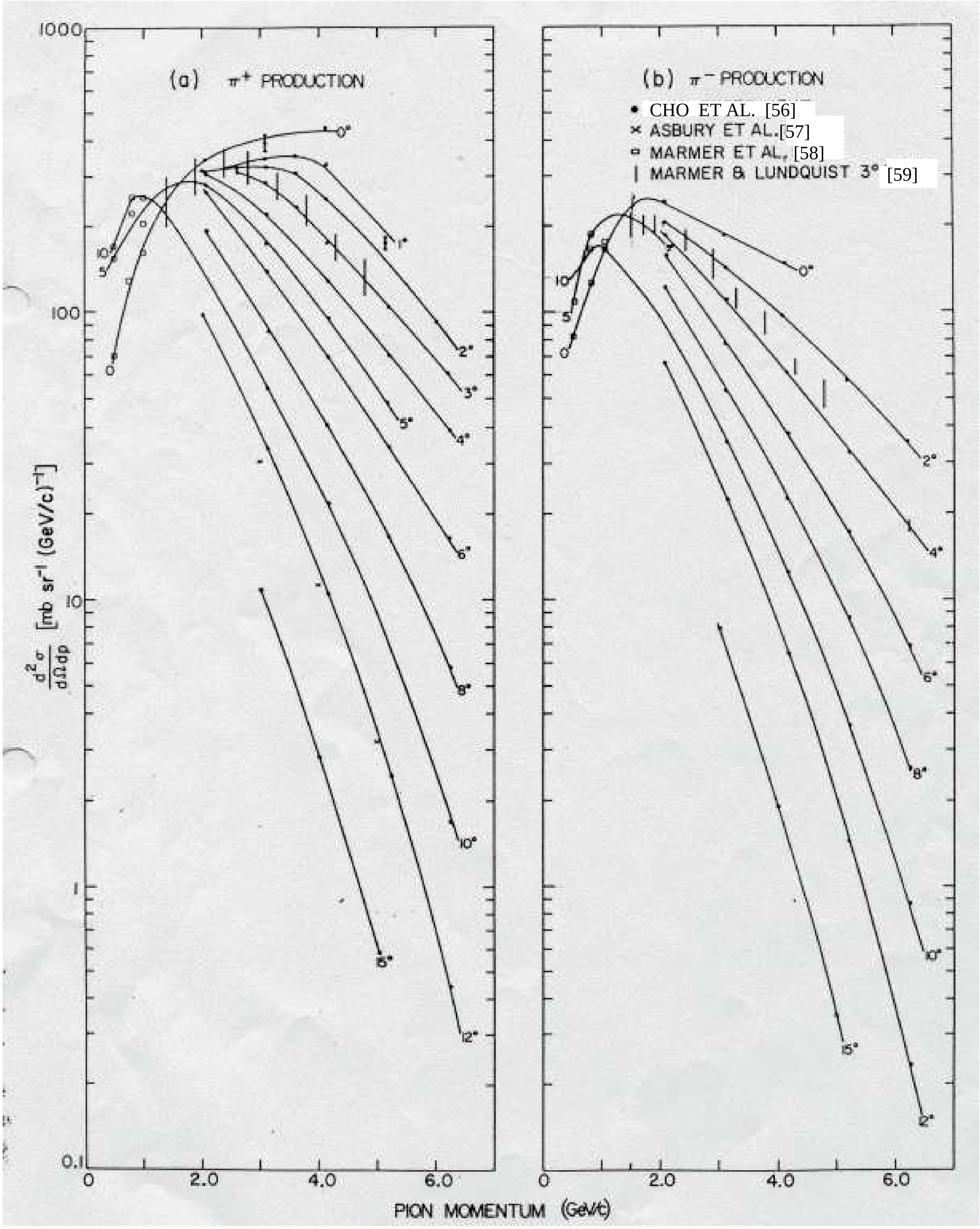

Figure 5.7: Results of the pion production measurements[51, 52, 53, 54] and fitted results by Sanford-Wang formula[46]. Left figure: π^+, right figure: π^-.

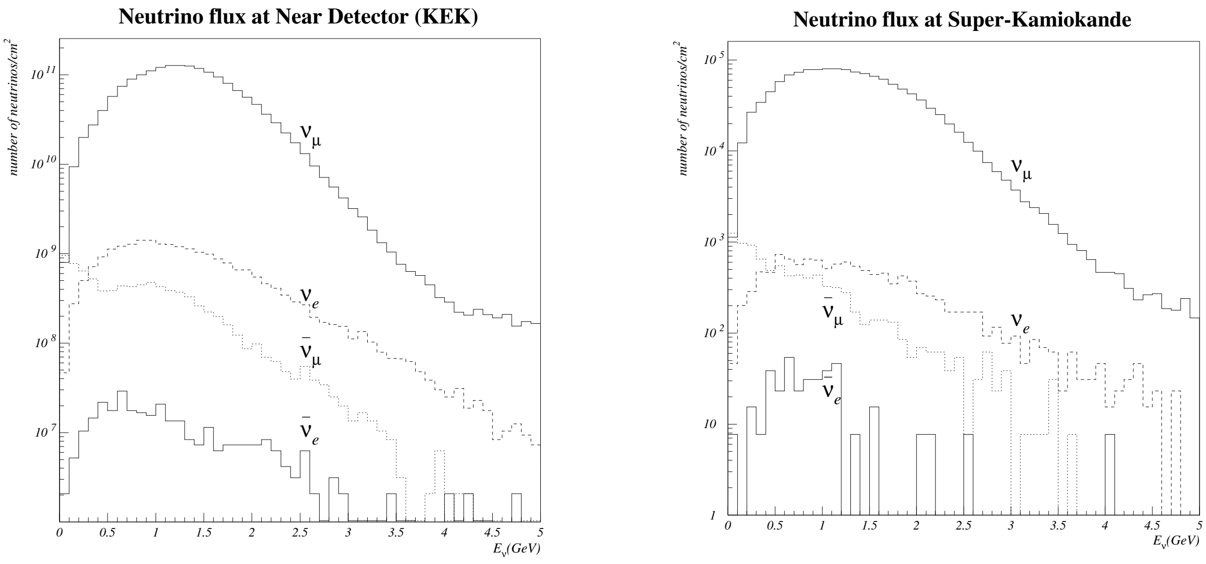

Figure 5.8: Flux calculation using Monte Carlo simulation. (Used hadron production model is Cho) Left figure: Neutrino flux at KEK, Right figure: Neutrino flux at SK

4. $K^0_L \rightarrow \pi^{\pm}+\mu^{\mp}+\nu_\mu$ (27.17 %) (Called $K^0\mu_3$)
5. $K^0_L \rightarrow \pi^{\pm}+e^{\mp}+\nu_e$ (38.78 %) (Called K^0e_3)

In fact, contributions of kaons are quite smaller than that of pions for ν_μ since K/π ratio in this energy region is less than 1/10 and the Lorenz boost of kaons is smaller than pions. For ν_e, muon decay is the dominant contribution.

ν_μ from $K^{\pm}_{\mu 3}$ and $K^0_{\mu 3}$ mode is neglected since ν_μ from these modes are especially small.

However other channels of kaon decay are taken into account correctly.

The treatment of the two body decay is same as the pion decay. Since the energy and angle distributions of the decay products in three body weak decay ($K^{\pm}_{e3}$,K^0_{e3}; [57] [58]) are not simulated correctly in GEANT, we use the following prescriptions;

1. GEANT finds decay point, and the 4-momentum of the kaon is given.
2. Make it randomly decay at rest according to the V-A theory with a self-made code.
3. Boost secondary particles

Muons

Muons decay, as "$\mu \rightarrow$ e + ν + $\bar{\nu}$" ($\pi^+\mu_2\mu^+$) , of which branching ratio is almost 100%. Since muon has a $\frac{1}{2}$ spin and polarization, it is taken into account when angle of decayed particles is calculated.[58]

5.1.5 MC prediction of Neutrino Properties at KEK and Kamioka

Considering the above effects, neutrino flux at KEK and at SK are calculated. Fig. 5.8 shows the results of calculation of November configuration. Used hadron production model is Cho. The averaged neutrino flux at KEK is 25 cm in radius and at SK 200 m in radius are shown.

According to this simulation, ν_e/ν_μ is 1.3%, $\bar{\nu_\mu}/\nu_\mu$ is 0.5%, $\bar{\nu_e}/\nu_\mu$ is $\sim 2\times 10^{-4}$.

Contributions from each decay mode (at KEK only) are shown in Fig. 5.9. As already explained, the dominant contribution to the ν_μ, $\bar{\nu_\mu}$, ν_e and $\bar{\nu_e}$ production is from the π^+, π^-, μ^+ and K, respectively.

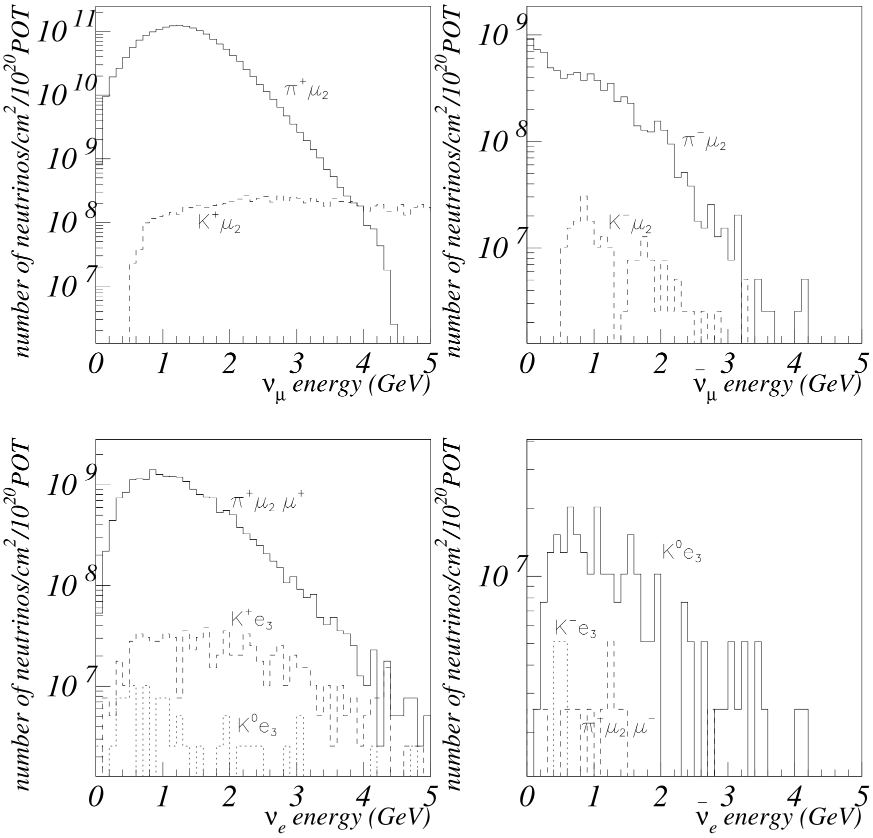

Figure 5.9: Contributions of each decay mode

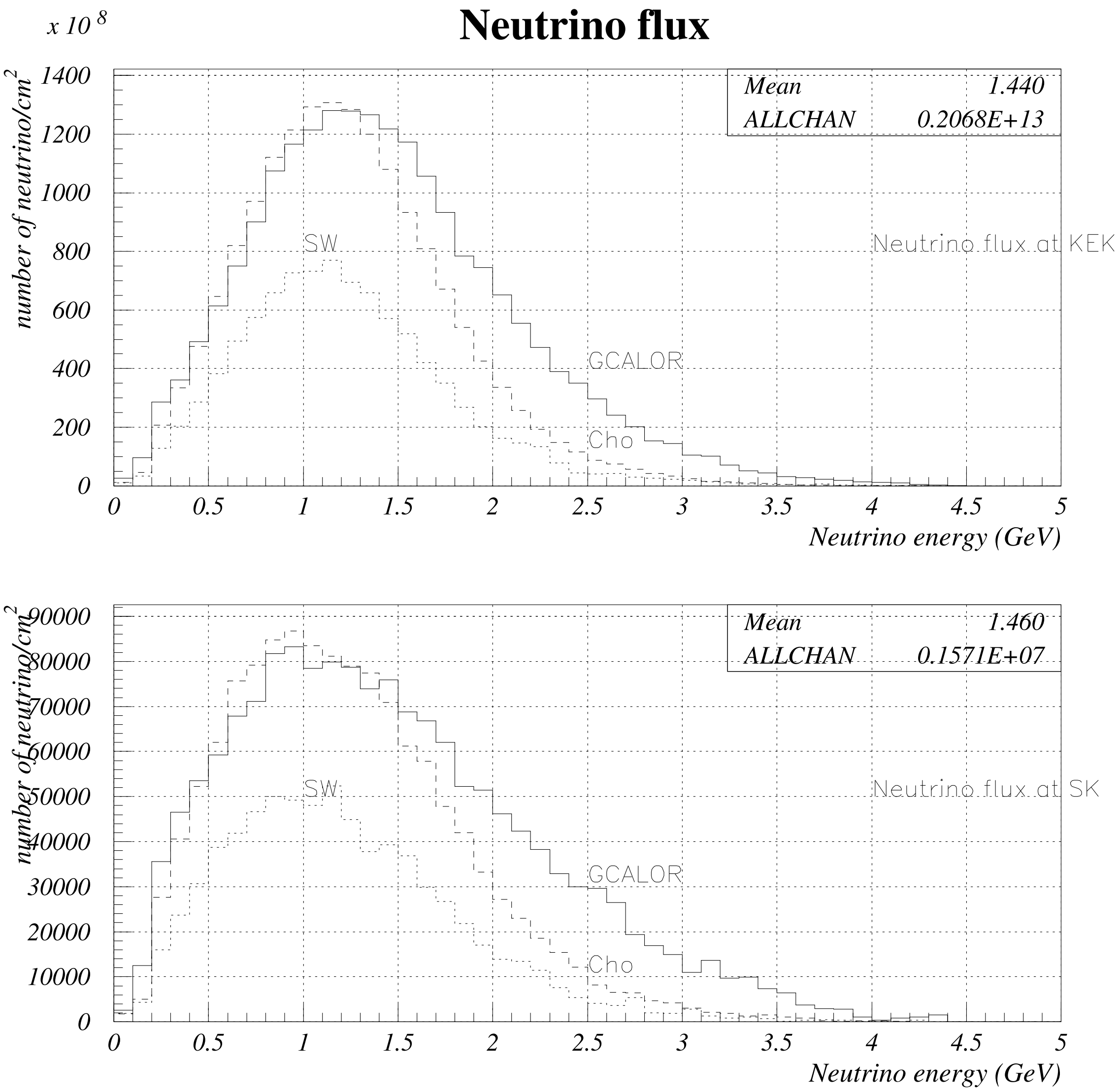

Figure 5.10: Dependence of neutrino flux on hadron production model.

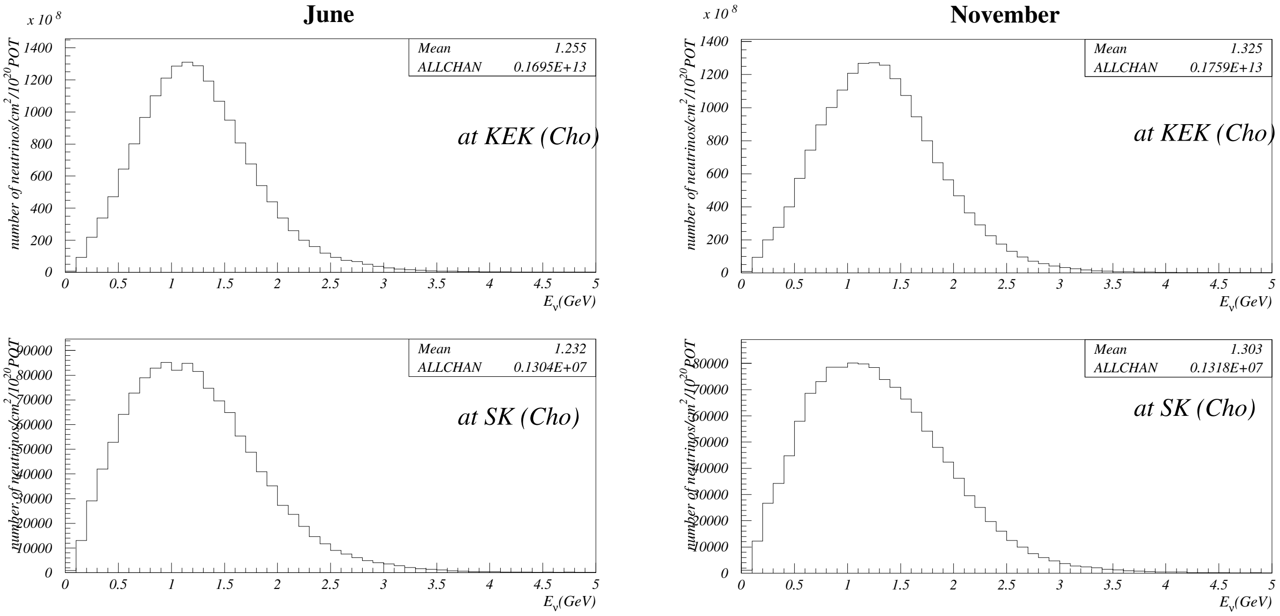

Figure 5.11: The ν_μ energy spectrum difference between June and November configurations. Top figures: neutrino flux at KEK, bottom figures: neutrino flux at SK. Left figures: in June, right figures: in November

The hadron production model dependence is shown in Fig. 5.10 for the ν_μ case.

The ν_μ energy spectrum difference between in June and November are shown in Fig. 5.11. The average energy of neutrino beam in November (1.30 GeV; SK) is higher than June (1.23 GeV; SK) because the current supplied to the horn magnets in November is higher than June. The both absolute fluxes are same within 1.1% because more pion absorption in the target existed in November configuration. MC simulation shows the difference of neutrino fluxes between using 200 kA and 250 kA as the current supplied to the horn magnets is ~15%. Therefore, pion absorption rate increases ~10% in November configuration than that of June.

5.2 MC Simulation for Neutrino Interactions

Average energy of neutrino flux used in the K2K experiment is ~1.3 GeV. These neutrinos interact with the target materials through charged current (CC) and neutral current (NC) of weak interaction. We have following sorts of neutrino interactions;

- CC quasi-elastic scattering $\nu N \to l N'$
- NC elastic scattering $\nu N \to \nu N$
- CC single pion production $\nu N \to l N' \pi$
- NC single pion production $\nu N \to \nu N' \pi$
- CC multi pion production $\nu N \to l N' m\pi$ (m Σ

The cross section of neutrino with an orbital electron is about 1/1000 of above interactions, thus we neglect it.

Ref.[59] summarized the basic idea of this simulation.

5.2.1 Quasi-Elastic Scattering Mode

This interaction occupy about 60% of total neutrino interactions at the energy region around 1 GeV. This scattering is 2-body reaction, hence out-going lepton momentum is definitely determined, once Q^2 (Q^2=-q^2= -$(p_\nu - p_\mu)^2$ΣΣ4-momentum transfer) is given.

We take account of form factors of nucleons since nucleons have internal structure. The hadron current part of neutrino-nucleon interaction has vector and axial vector form factors. This hadron current is expressed as follows[60];

$$< N'|J_{had}|N >= cos\theta_c \bar{u}(N')\Big[\gamma_\lambda F_V^1(Q^2) + \frac{i\sigma_{\lambda\nu}q^\nu \xi F_V^2(Q^2)}{2M} + \gamma_\lambda\gamma_5 F_A(Q^2)\Big]u(N), \tag{5.2}$$

where,F_V^1,F_V^2,F_A are the vector and axial vector form factors and represented as follows.

$$F_V^1(Q^2) = \Big(1 + \frac{Q^2}{4M^2}\Big)^{-1}\Big[G_E^V(Q^2) + \frac{Q^2}{4M^2}G_M^V(Q^2)\Big], \tag{5.3}$$

$$\xi F_V^2(Q^2) = \Big(1 + \frac{Q^2}{4M^2}\Big)^{-1}\Big[G_M^V(Q^2) - G_E^V(Q^2)\Big], \tag{5.4}$$

$$G_E^V(Q^2) = \frac{1}{\Big(1 + \frac{Q^2}{M_V^2}\Big)^2}, \quad G_M^V(Q^2) = 1 + \frac{\xi}{\Big(1 + \frac{Q^2}{M_V^2}\Big)^2}, \quad \xi \equiv \mu_p - \mu_n = 3.71 \tag{5.5}$$

$$F_A(Q^2) = \frac{-1.23}{\Big(1 + \frac{Q^2}{M_A^2}\Big)^2}, \quad M_V = 0.84(GeV^2/c^2), M_A = 1.01(GeV^2/c^2) \tag{5.6}$$

where, θ_c, M, M_V and M_A represent the Cabbibo angle, mass of nucleon, the vector mass to be determined by e-p scattering experiments and the axial vector mass to be determined by neutrino experiments, respectively. M_A value has 10% uncertainty.

Finally the Q^2 dependence of this reaction is expressed by following formula;

$$\frac{d\sigma^{\nu,\bar{\nu}}}{dQ^2} = \frac{M^2 G_F^2 cos^2\theta_c}{8\pi E_\nu^2}\Big[A(Q^2) \mp B(Q^2)\frac{(s-u)}{M^2} + C(Q^2)\frac{(s-u)^2}{M^4}\Big], \tag{5.7}$$

where, G_F is the Fermi constant, $(s-u) = 4ME_\nu - Q^2 - m^2$: m is mass of lepton.

$$\begin{aligned} A(Q^2) &= \frac{(m^2+Q^2)}{4M^2}\Big[\Big(4 + \frac{Q^2}{M^2}\Big)|F_A|^2 - \Big(4 - \frac{Q^2}{M^2}\Big)|F_V^1|^2 + \frac{Q^2}{M^2}|\xi F_V^2|^2\Big(1 - \frac{Q^2}{4M^2}\Big) + \\ &\quad \frac{4Q^2 F_V^1 \xi F_V^2}{M^2} - \frac{m^2}{M^2}\Big(|F_V^1 + \xi F_V^2|^2 + |F_A|^2\Big)\Big], \\ B(Q^2) &= \frac{Q^2}{M^2}F_A\Big(F_V^1 + \xi F_V^2\Big) \\ C(Q^2) &= \frac{1}{4}\Big(|F_A|^2 + |F_V^1|^2 + \frac{Q^2}{M^2}|\frac{\xi F_V^2}{2}|^2\Big) \end{aligned} \tag{5.8}$$

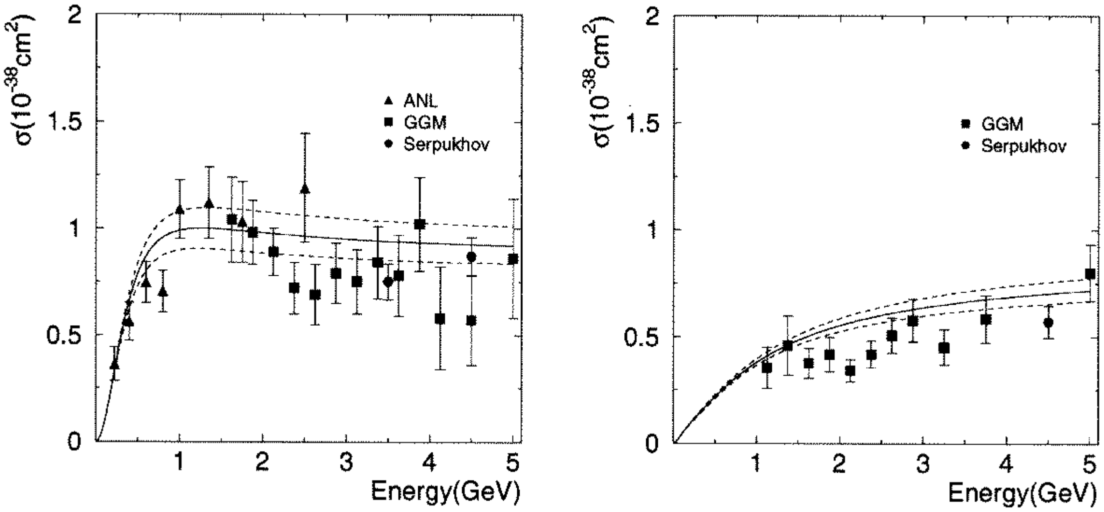

Figure 5.12: Calculated total cross sections of $\nu_\mu n \rightarrow \mu^- p$ (left) and $\bar{\nu_\mu} p \rightarrow \mu^+ n$(right) compared with the experimental data, ANL[61], GGM[62] and Serpukhov[63]. Upper and lower dashed lines show the cross section with M_A=1.11 and 0.91, respectively.

Fig. 5.12 shows the total cross section of $\nu_\mu n \rightarrow \mu^- p$ and $\bar{\nu_\mu} p \rightarrow \mu^+ n$ with M_A=1.01±0.10, compared with the experimental data. They are consistent within 10% uncertainty of M_A.

We take into account the Fermi motion and Pauli blocking effect of nuclei, such as ^{16}O. The Fermi momentum distribution is estimated from the e-^{12}C scattering in the ^{16}O case. The Fermi gas model is adopted to simulate the Pauli blocking and momentum of recoil nucleon is restricted to be larger than the Fermi surface momentum. (217 MeV/c in ^{16}O case) For the iron case, the treatment of Fermi momentum and Pauli blocking is same as the water case. Uncertainty due to this treatment is discussed later.

We also take account of the NC elastic scattering although most of this interaction is invisible with our detector. The total cross section is estimated by the following ratio of NC to CC cross section according to Ref.[64, 65] .

$$\begin{aligned}
\sigma(\nu p \rightarrow \nu p) &= 0.153 \times \sigma(\nu n \rightarrow e^- p) \\
\sigma(\nu n \rightarrow \nu n) &= 1.5 \times \sigma(\nu p \rightarrow \nu p) \\
\sigma(\bar{\nu} p \rightarrow \bar{\nu} p) &= 0.218 \times \sigma(\bar{\nu} p \rightarrow e^+ n) \\
\sigma(\bar{\nu} n \rightarrow \bar{\nu} n) &= 1.0 \times \sigma(\bar{\nu} p \rightarrow \bar{\nu} p)
\end{aligned}$$

5.2.2 Single Pion Production Mode

Single pion production is the next dominant interaction to the quasi-elastic scattering. This interaction produces one lepton and one pion through the following reactions.

- Charged current
  $\nu n \rightarrow l^- p \pi^0$ $\bar{\nu} n \rightarrow l^+ n \pi^-$
  $\nu n \rightarrow l^- n \pi^+$ $\bar{\nu} p \rightarrow l^+ n \pi^0$
  $\nu p \rightarrow l^- p \pi^+$ $\bar{\nu} p \rightarrow l^+ p \pi^-$
- Neutral current
  $\nu n \rightarrow \nu n \pi^0$ $\bar{\nu} p \rightarrow \bar{\nu} p \pi^0$

$\nu p \to \nu p \pi^0 \qquad \bar{\nu} p \to \bar{\nu} n \pi^+$
$\nu n \to \nu p \pi^- \qquad \bar{\nu} n \to \bar{\nu} n \pi^0$
$\nu p \to \nu n \pi^+ \qquad \bar{\nu} n \to \bar{\nu} p \pi^-$

This simulation is performed based on the Rein-Sehgal's model [66]. This model calculates the interaction through following two parts;

$$\begin{aligned} \nu + N &\to l + N^* \\ N^* &\to \pi + N' \end{aligned}$$

where, N^* is a baryon resonance state. In this model, $\Delta(1232)$ and other 17 resonance states with the mass below 2 GeV/c^2 are considered including their interference among them. The differential cross section, $d\sigma/dQ^2dE$, is expressed by the following formula if this interaction occurred through one resonance state.

$$\frac{d^2\sigma}{dQ^2dE_\nu} = \frac{1}{32\pi M_N E_\nu^2} \cdot \frac{1}{2} \cdot \sum_{spins} |T(\nu N \to l N^*)| \cdot \chi_{E_\nu} \cdot \delta(W^2 - M^2)$$

where,

E_ν	neutrino energy,
M_N	mass of nucleon,
W	invariant mass of πN system,
M	invariant mass of resonance,
$T(\nu N \to l N^*)$	amplitude of resonance,
χ_{E_ν}	decay probability of resonance.

The total cross section is obtained by integrating the above equation with Q^2 and E_ν. We restricted that the invariant mass W to be less than 2.0 GeV/c^2. Figs. 5.13 and 5.14 shows the total cross sections for charged current and neutral current interactions, compared with the experimental data.

The angular distribution of pion from $\Delta(1232)$ resonance is also calculated using this model. However, for other resonances, it is assumed to be isotropic in the rest frame of the πN system.

5.2.3 Multi Pion Production Mode

We assume that the multi pion production interaction occurs at W >1.4 GeV/c^2. The cross section and kinematics of this interaction is calculated based on the Bjorken scaling. The differential cross section using Bjorken scaling parameters is expressed;

$$\frac{d^2\sigma^{\nu,\bar{\nu}}}{dxdy} = \frac{G_F^2 M_N E_\nu}{\pi} \cdot \left[(1 - y + \frac{1}{2}y^2 + C_1)F_2(x) \pm y(1 - \frac{1}{2}y + C_2)[xF_3(x)]\right]$$

where,

$$\begin{aligned} C_1 &= \frac{m^2(y-2)}{4M_N E_\nu x} - \frac{M_N x y}{2E_\nu} - \frac{m^2}{E_\nu^2} \\ C_2 &= -\frac{m^2}{4M_N E_\nu x} \end{aligned} \tag{5.9}$$

where,

G_F	Fermi constant,

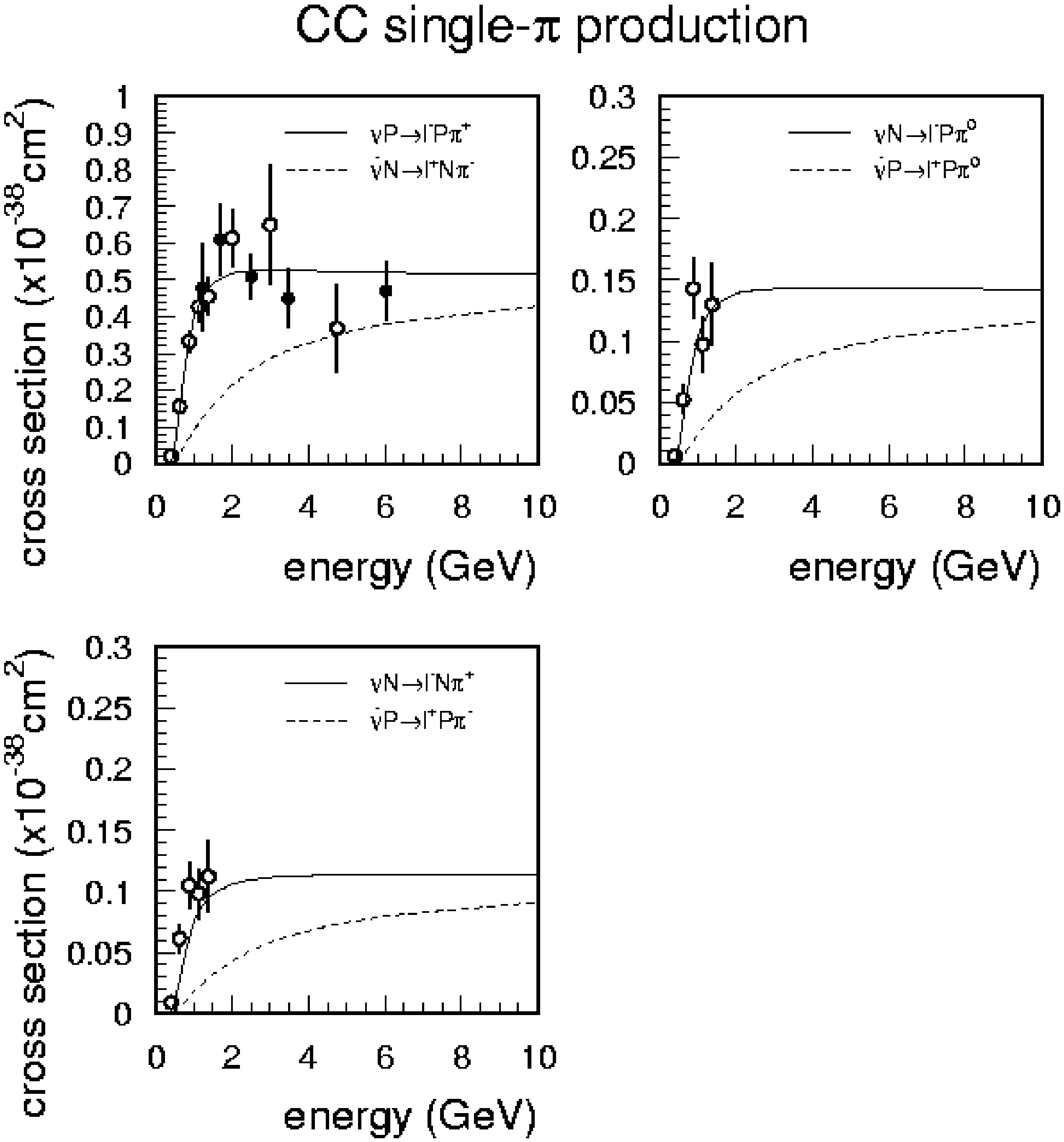

Figure 5.13: Calculated cross section of charged current single pion production. Open circles with error bars show the result of the ANL experiment[61], and closed circles show that of the GGM[62].

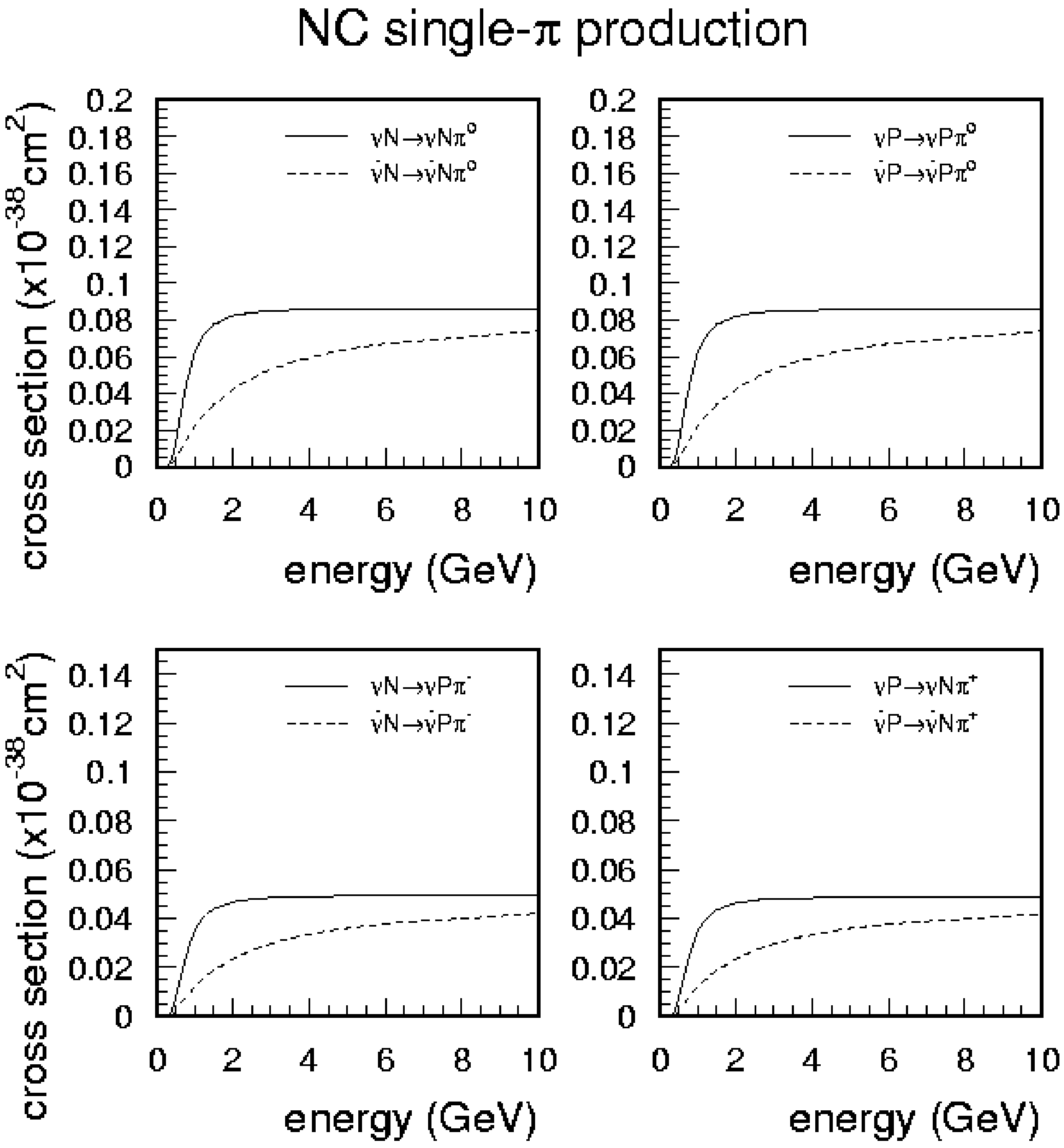

Figure 5.14: Calculated cross section of neutral current single pion production.

E_ν	neutrino energy,
M_N	mass of nucleon,
m	mass of lepton,
E_l	lepton energy,
x	Bjorken scaling parameter ($= Q^2/(2M(E_\nu - E_l)+M^2)$) and
y	Bjorken scaling parameter ($= (E_\nu - E_l)/E_\nu$).

Structure functions, $F_2(x)$ and $F_3(x)$, are calculated from GRV94[67]. The CC total cross section is obtained by integrating the above equation. Results of the integration are shown in Fig. 5.15.

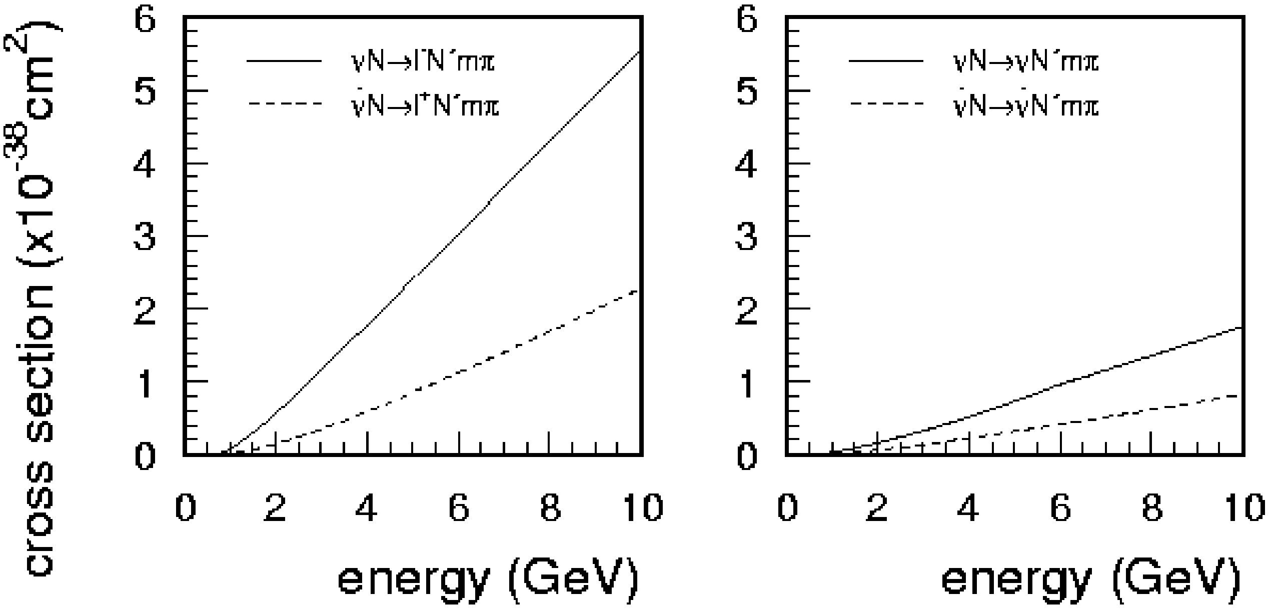

Figure 5.15: Calculated cross section of multi pion production interaction.

In the case 1.4 GeV/c^2 < W <2.0 GeV/c^2, final states of pions are taken into account employing following facts;

1. Multiplicity of charged pion $\langle n_c \rangle$ was measured by 15-foot bubble chamber at Fermi National Laboratory[68]. It is found to be $(0.06 \pm 0.06) + (1.22 \pm 0.03)\ lnW^2$. We estimated averaged pion multiplicity $\langle n_\pi \rangle$ including neutral pions, as follows;

$$\langle n_\pi \rangle \quad = \quad 0.09 + 1.83 lnW^2$$

   where, we assume $\langle n_{\pi^+} \rangle = \langle n_{\pi^-} \rangle = \langle n_{\pi^0} \rangle$ and $\langle n_{\pi^+} \rangle = 1/2 \langle n_c \rangle$.

2. We adopt Koba-Nielsen-Olesen(KNO) scaling, which reproduces the process, $\nu_\mu p \to \mu X^{++}$, in BEBC [69] data in order to determine the pion multiplicity in each event.
3. The charge of each hadron is randomly chosen under the charge conservation.
4. We consider Δ effect in the final state since bubble chamber experiment in Argonne clearly measured the Δ in multi hadron final states[70]. This Δ effect modifies the phase space.
5. We also consider forward-backward asymmetry measured by BEBC data. $\langle n_\pi^F \rangle$ ΣΣ$\langle n_\pi^B \rangle = (0.35+0.41\ lnW^2)/(0.50+0.09\ lnW^2)$

6. For neutral current, ratio of NC/CC is estimated in Ref.[71] with energy range (E_ν <3 GeV), and in Ref.[72] with energy range (E_ν >3 GeV).

$$\frac{\sigma(\nu N \to \nu X)}{\sigma(\nu N \to l^- X)} = \begin{cases} 0.26 & (\mathrm{E}_\nu < 3 \text{ GeV}) \\ 0.26 + 0.04(E_\nu/3 - 1) & (3 \text{ GeV} < \mathrm{E}_\nu < 6 \text{ GeV}) \\ 0.30 & (6 \text{ GeV} < \mathrm{E}_\nu) \end{cases}$$

$$\frac{\sigma(\bar{\nu} N \to \bar{\nu} X)}{\sigma(\bar{\nu} N \to l^+ X)} = \begin{cases} 0.39 & (\mathrm{E}_\nu < 3 \text{ GeV}) \\ 0.39 + 0.02(E_\nu/3 - 1) & (3 \text{ GeV} < \mathrm{E}_\nu < 6 \text{ GeV}) \\ 0.37 & (6 \text{ GeV} < \mathrm{E}_\nu) \end{cases}$$

In W >2.0 GeV/c^2, we use JETSET/PYTHIA[73] instead of above rules. Thanks to this, kaons etc. are also taken into account.

5.2.4 Coherent Pion Production Mode

Coherent pion production interaction means that neutrino interacts with the whole nucleus coherently. We consider following processes.

$$\begin{aligned} &\nu N \to l^- N \pi^+ \\ &\bar{\nu} N \to l^+ N \pi^- \\ &\nu N \to \nu N \pi^0, \quad \bar{\nu} N \to \bar{\nu} N \pi^0 \end{aligned}$$

where, $l^\pm$ is a charged lepton and N is a nucleus. The angular distribution of the pions produced by this process has a sharper peak at the forward direction than other processes and the nucleus is not broken. The energy transfer of this interaction is negligibly small.

The cross section and kinematics of this interaction is calculated employing the Rein-Sehgal model[74]. This model referred to Adler's partially conserved axial vector current theory[75].

$$\begin{aligned} \frac{d^3\sigma}{dx dy d|t|} &= \frac{G_F^2 M_N E_\nu}{\pi^2} \frac{1}{2} f_\pi^2 A^2 (1-y) \frac{1}{16\pi} \left[\sigma_{tot}^{\pi N}\right]^2 (1+r^2) \left(\frac{M_A^2}{M_A^2 + Q^2}\right)^2 e^{-b|t|} F_{abs} \\ r &= \frac{Ref_{\pi N}(0)}{Imf_{\pi N}(0)} \end{aligned}$$

where,

G_F	Fermi constant,
E_ν	neutrino energy,
M_N	mass of nucleon,
E_l	lepton energy,
x	Bjorken scaling parameter (= $\mathrm{Q}^2/(2\mathrm{M}(\mathrm{E}_\nu\text{-}\mathrm{E}_l)+\mathrm{M}^2)$),
y	Bjorken scaling parameter (= $(\mathrm{E}_\nu\text{-}\mathrm{E}_l)/\mathrm{E}_\nu$),
t	momentum transfer to nucleus ($=(\mathrm{p}_\pi\text{-}\mathrm{q})^2$) and
f_π	decay constant of pion.
b	80 GeV^{-2}
A	atomic number of the nucleus
F_{abs}	$F_{abs} = e^{-<x>/\lambda}$, $\lambda^{-1} = \sigma_{inel}^{\pi N}\rho$, ρ is nuclear density,
$< x >$	Mean free path of the pion in nucleus

Fig. 5.16 shows the total cross section of the coherent pion production on ^{16}O as the function of neutrino energy. As explained before, the coherent pion production mode is neglected for iron case.

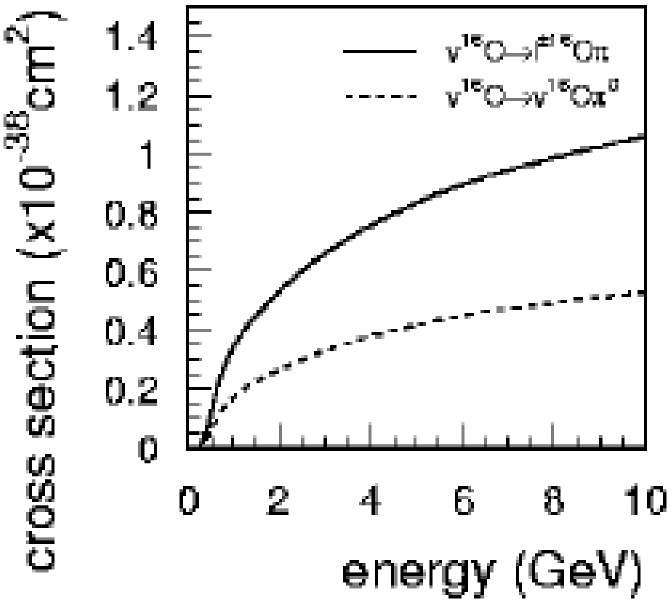

Figure 5.16: Calculated cross section of coherent pion production off ^{16}O nuclei.

Chapter 6

Characteristics of K2K Neutrino Beam I (Measurement by Muon Monitor)

In this chapter, we describe the beam characteristics measured by the muon monitor. Fig. 6.1 shows typical muon profiles in June and November beam configuration. The beam condition is different in June and November, as described in chapter 3. The numbering of the channels is such that from south to north for the x coordinate and from top to bottom for the y coordinate for both the Si detector and the Ionization Chamber.

The center of the Si system x, that of y, x direction of the ionization chamber and the y direction is 5ch, 5ch, 19.5ch and 18ch, respectively. Space between each channel is 5 cm and 35 cm for ionization chamber and silicon pad detector, respectively. The data point which have zero ADC count corresponds to insensitive region of the ionization chamber.

6.1 Muon Yield as a Function of Supplied Current to Horn Magnets

In order to prove that muons detected by the muon monitor really come from pion which is produced at the target, muon yield as a function of the current supplied to the horn magnets was measured during the engineering run. Fig. 6.2 shows the muon flux measured by the Si detector as a function of the current supplied to the horn magnets.

There are four measurement points (175 kA, 200 kA, 225 kA and 250 kA). Vertical axis shows relative muon flux. This is a sum of ADC counts for all the small Si detectors (Fig. 4.7) normalized with the proton beam intensity. Relative muon yield is well reproduced by the MC simulation. (The data and MC are normalized at 200 kA data point since uncertainty of absolute flux measurement is large. i.e.; thickness of Si depletion layer.)

From this result, we conclude that muon measured by the muon monitors reflect the information of the pion produced at the target. As a consequence, with utilizing the muon monitor information, we can monitor the neutrino beam which come from same pions with spill by spill basis.

6.2 Muon Yield with and without Horn/Target System

In order to estimate the neutrino yield produced by the pion which was created in the helium gas and/or the beam-dump, we compared the data with and without the horn/target system. Properties of pions produced at the target are well studied employing the pion monitor systematically, but that produced after the 2nd horn cannot be studied well. If there were a lot of such poorly-understood pions, our analysis strategy would have the large systematic uncertainty.

We estimated this yield using the muon monitor and the near detector. Employing the near detector has an advantage for directly measuring the neutrino yield. The muon monitor gives the information of the parent pions via measuring the decayed muons like Fig. 4.3. Here we describe the way using the muon monitor. That using the near detector is described in chapter 8.

Table 6.1 shows the data with and without the horn/target system.

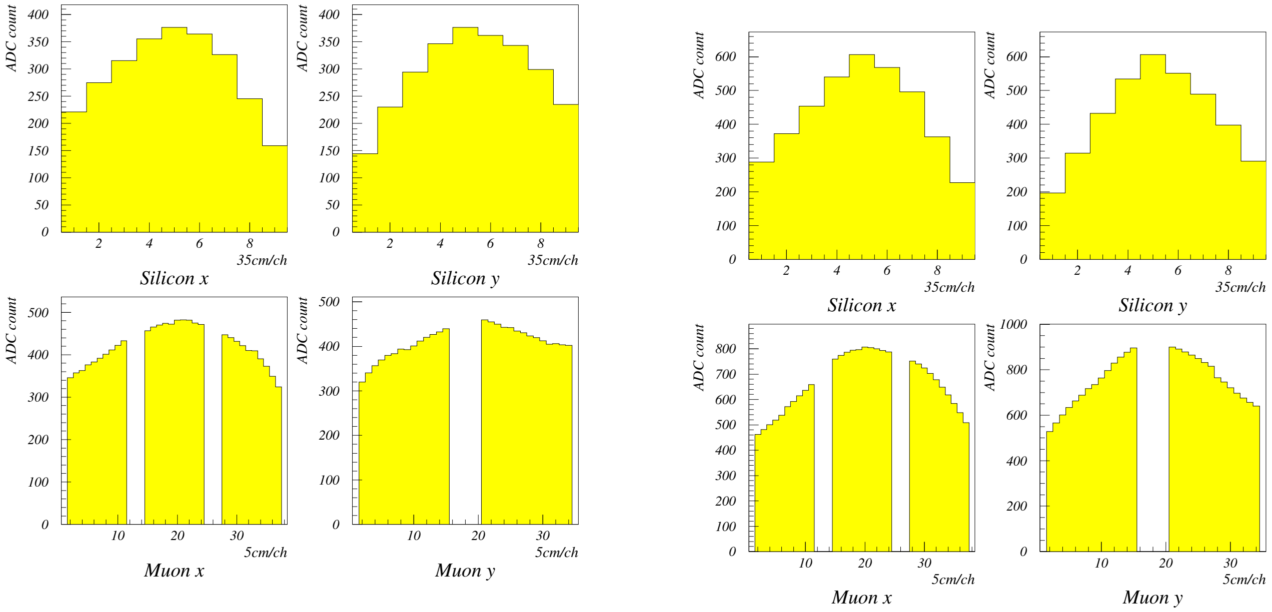

Figure 6.1: Typical muon profile detected by the muon monitors. Left: June (horn 200 kA, target 20 mmϕ), right: November (horn 250 kA, target 30 mmϕ). In each figure, top-left: small Si detector(horizontal direction), top-right: small Si detector (Vertical direction), bottom-left: Ionization Chamber (horizontal direction), bottom-right: Ionization Chamber (vertical direction)

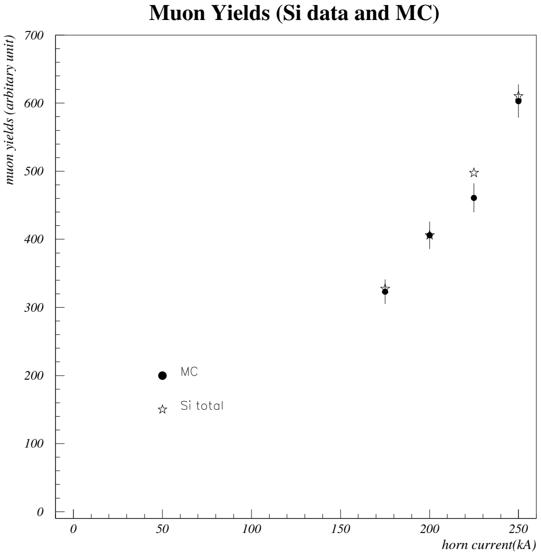

Figure 6.2: Muon yield as a function of the current supplied to the horn magnets. MC is normalized at 200 kA since uncertainty of absolute flux measurement is large.

	(Large 9) Si total ADC sum	CT ADC count
No horn, no target	1881	468.6 (~6.5×10^{11}protons)
With horn (250 kA)	85160	2883 (~4.0×10^{12}protons)

Table 6.1: Comparison of the muon monitor data with target/horn to data without target.

If proton shielding effect by the target is correctly taken into account (Fig. 6.3), the empty target ratio of the muon yield is calculated as follows:

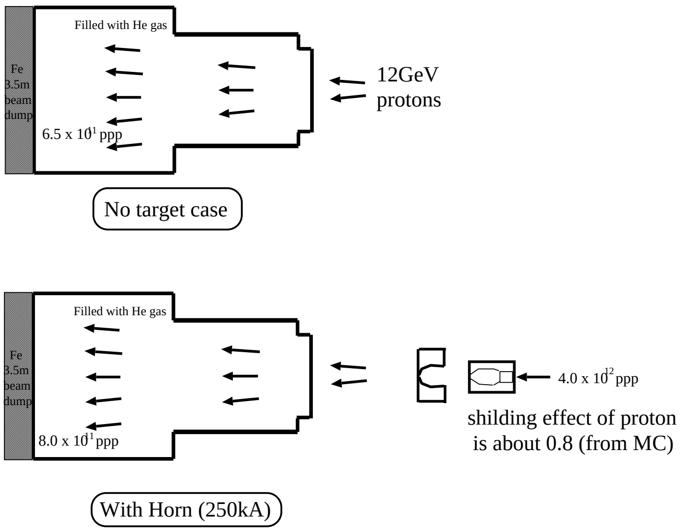

Figure 6.3: Schematic view of proton shielding effect by target

1. From empty target data, 6.5×10^{11} passed protons give 1881 ADC counts at the muon pit.
2. According to MC, 20% of 4.0×10^{12} protons pass the target without interaction. Thus 8.0×10^{11} protons come to the decay pipe even with horn.
3. Simply extrapolating the number of the empty target run, 8.0×10^{11} passed protons give 2315 ADC counts at the muon pit.
4. Therefore the ratio of muons created at the helium gas and/or dump is 2315/(85160-2315)=2.8%.

Dominant errors of this estimation are 1) relative CT value (±10%) and 2) shielding effect of protons $(80^{+20\%}_{-30\%})$. With error, contamination of helium gas and/or dump created muons is given to be $(2.8^{+4.5}_{-2.8})\%$. This value is consistent with the MC prediction, 3.8%, employing the same procedure.

This number proves that the pion yield produced after the 2nd horn is small in the high energy region, furthermore will be confirmed by the near detector data.

6.3 Stability of Muon Direction

6.3.1 Long Term Stability

To check the long term stability of the muon monitor center, we accumulate ADC count of each channel over 100 spills at first. (For example, Fig. 6.4 shows typical 100-spill accumulated data) After this accumulations, mean and RMS of each channel is calculated for on-spill data and off-spill data.* Off-spill data is used as the pedestal and subtracted from the on-spill data.

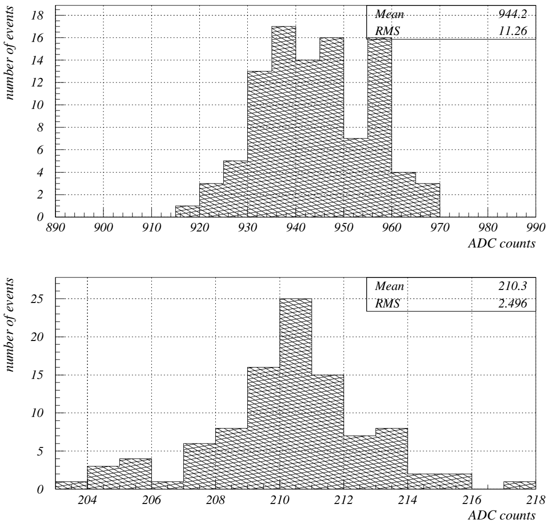

Figure 6.4: 100 spills accumulated data of the 20th Ionization Chamber channel. Top: accumulated data for on-spill, bottom: accumulated data for off-spill. The off-spill data is used as pedestal.

After applying the "100-spill accumulation", the muon profile is fitted with (asymmetric) Gaussian for Ion chamber (Si) to obtain the center (Fig. 6.5). Here we use only central 5 channels for the fit of the Si detector data.

Time variations of the center are shown in Figs. 6.6, 6.7, 6.8 and 6.9. These figures show the time variations for full June and November data taking period. In each figure, "GPS" line corresponds to the direction of Kamioka. Further, drawn line, "1mrad", corresponds to 20 cm (200 m×0.001) from the central position at the muon monitor position.

Time variation of the center is consistent in both detectors. We confirm the center is within 1 mrad. We conclude that the neutrino beam is aimed to SK with 1 mrad accuracy.

6.3.2 Short Term Stability

Next we check the short term stability. In this case, we use on-spill data spill-by-spill basis. However off-spill data is 100-spill averaged and subtracted as pedestal. This is because the off-spill value is stable enough. For example, in Fig. 6.4, RMS of off-spill data is 2.5 counts. This is less than 1% of signal.

Figs. 6.10 and 6.11 show results of this analysis during typical 1000 spills in November. To check the consistency, we overlaid the results of the 100-spill accumulation. The consistency between results of the long term stability analysis and the short term stability analysis is good. For more quantitative analysis, we took projection of Figs. 6.10 and 6.11. They are shown in Fig. 6.12. This

---

* off-spill data is taken after one second of each on-spill data

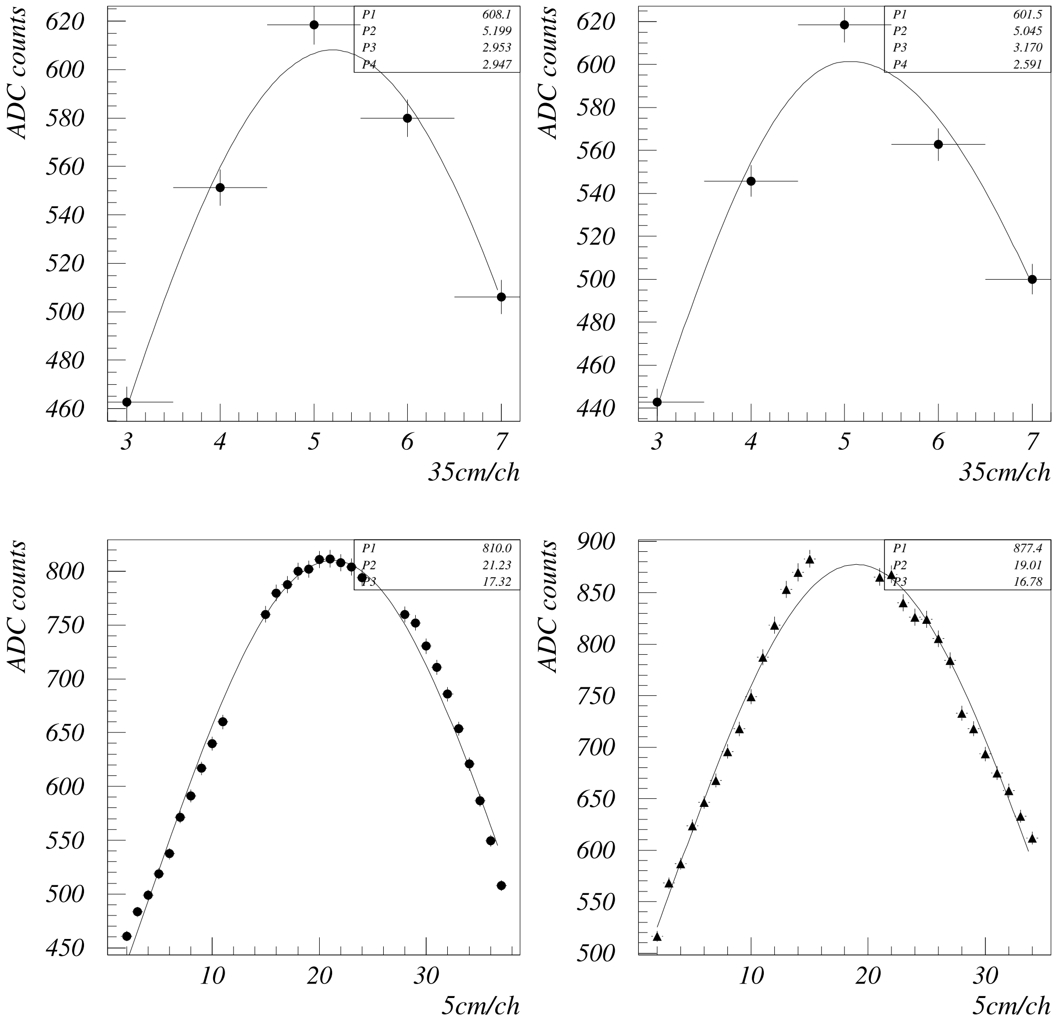

Figure 6.5: Fit to calculate the center of muon profile. Top-left: Si x data fitted with asymmetric Gaussian, top-right: Si y with asymmetric Gaussian, bottom-left: Ion Chamber x with Gaussian, bottom-right: Ion Chamber y with Gaussian.

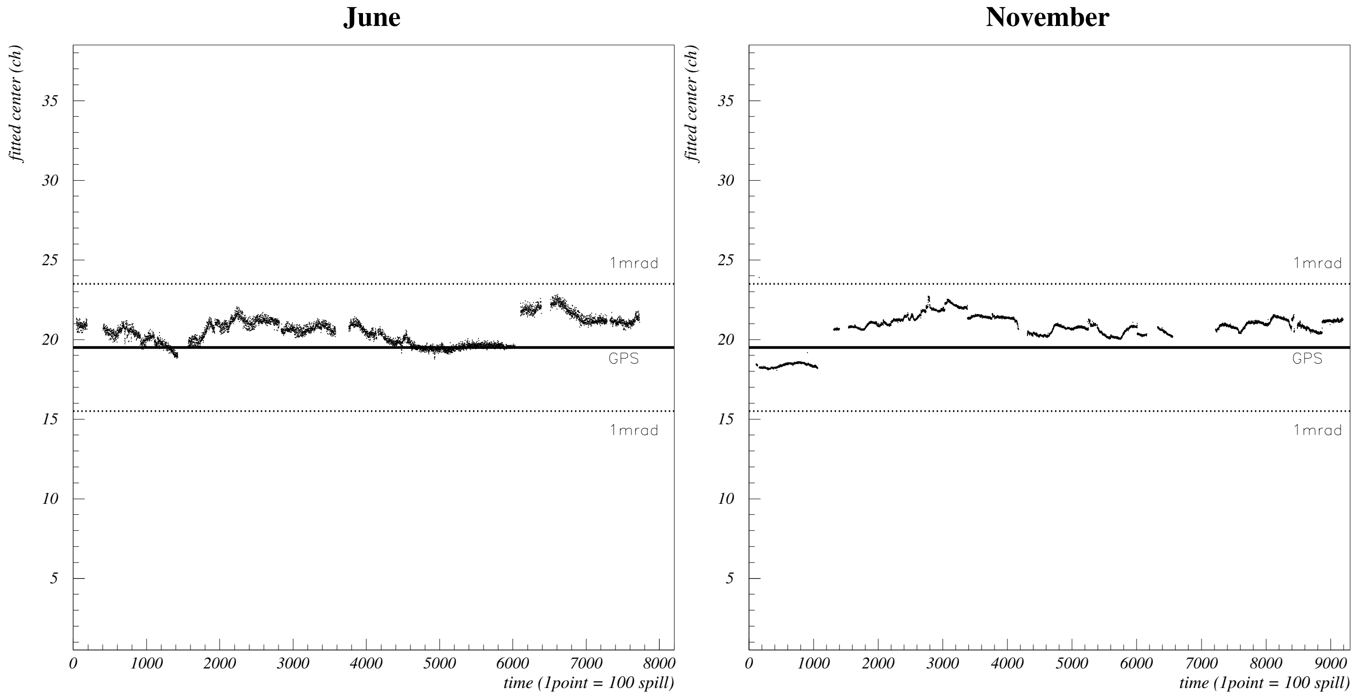

Figure 6.6: Time variation of the fitted center (IC x). Left: June data, Right: November data

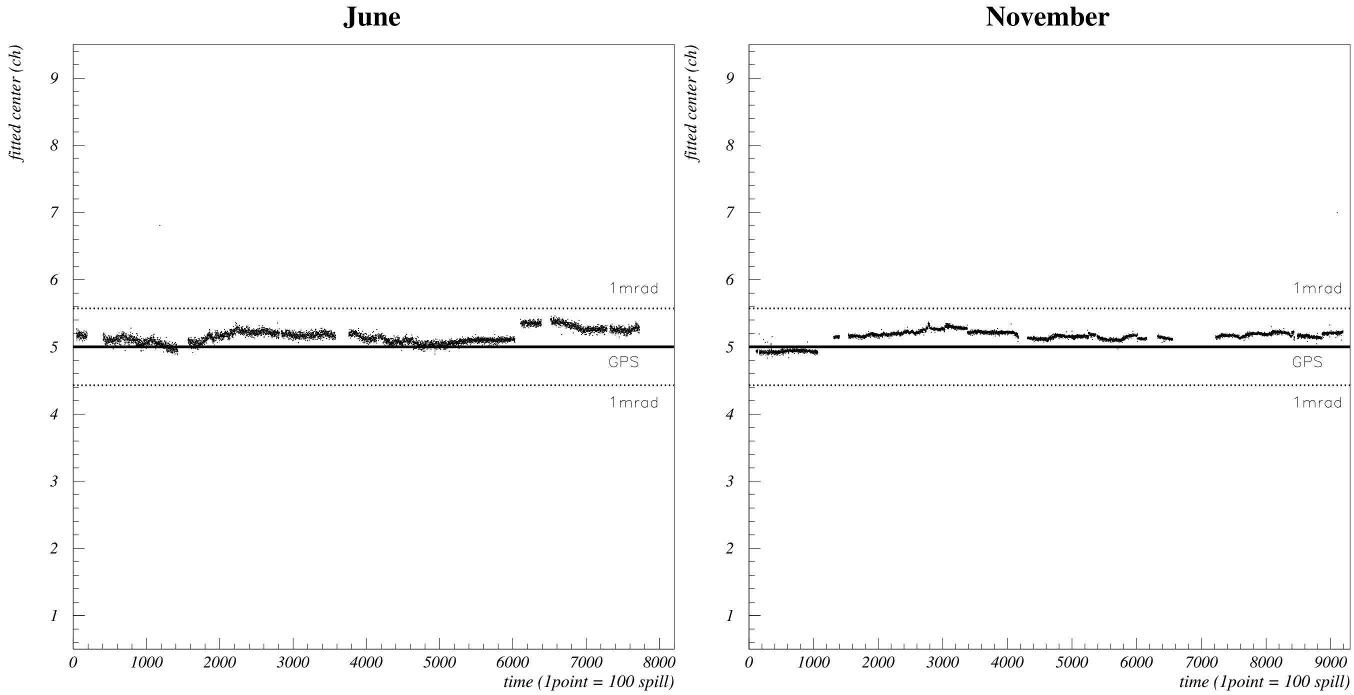

Figure 6.7: Time variation of the fitted center (Si x). Left: June data, Right: November data.

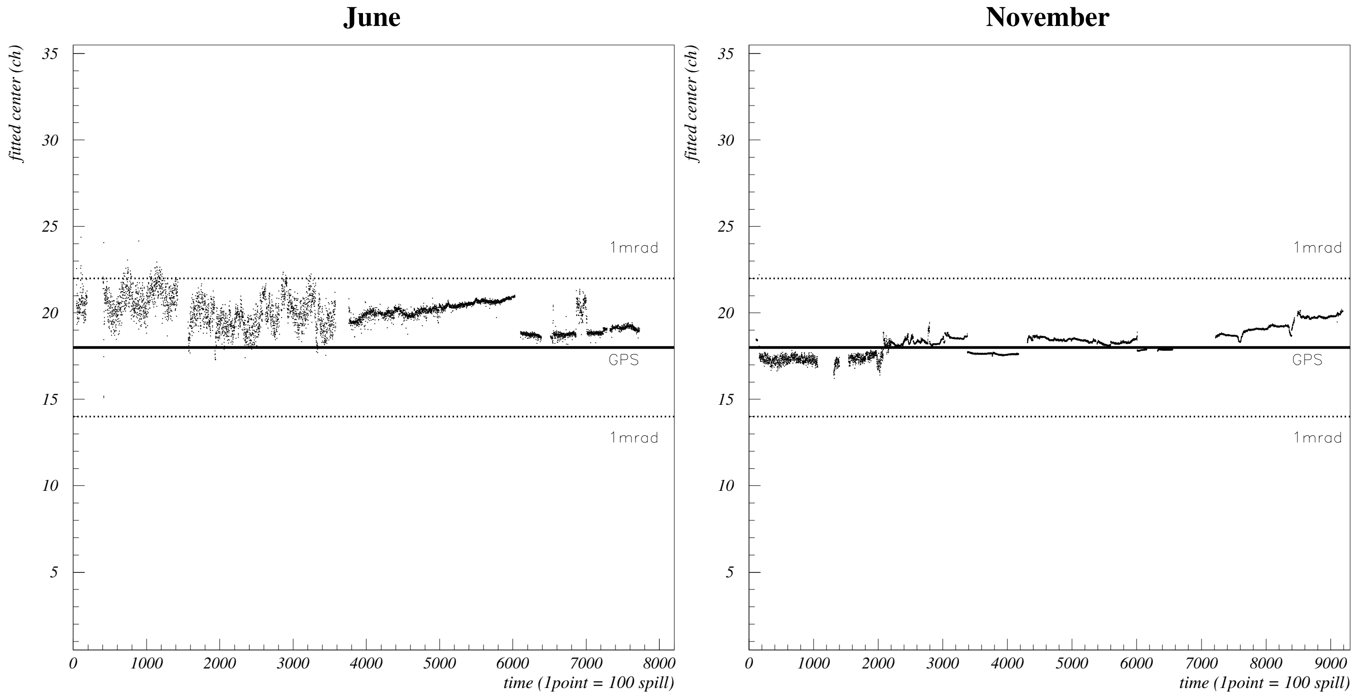

Figure 6.8: Time variation of the fitted center (IC y). Left: June data, Right: November data.

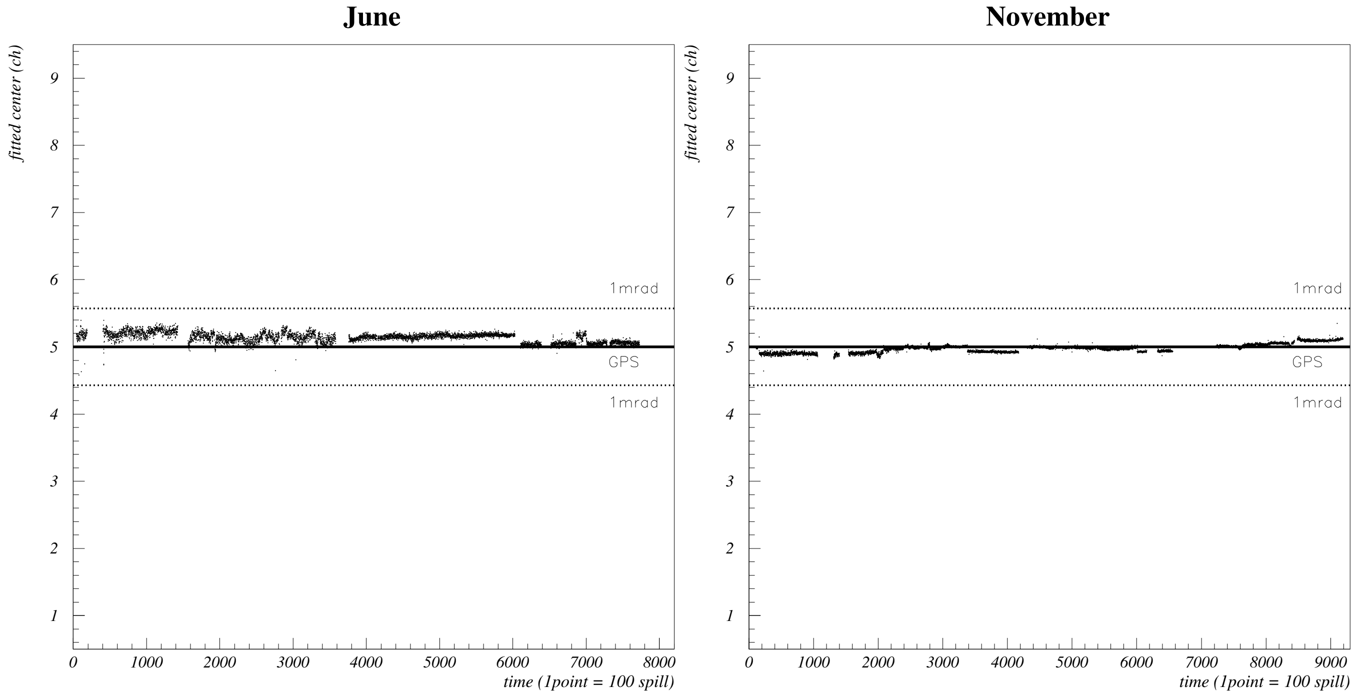

Figure 6.9: Time variation of the fitted center (Si y). Left: June data, Right: November data.

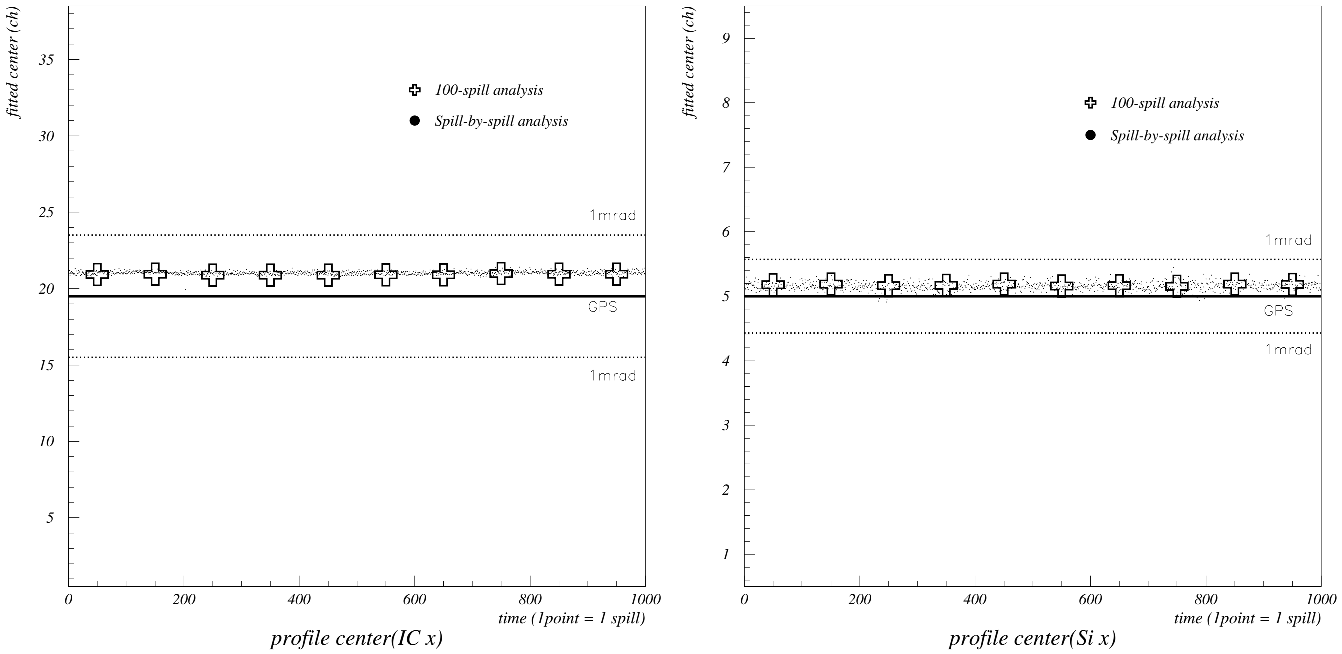

Figure 6.10: The fitted center of the spill-by-spill analysis during typical 1000 spills in November. Left: IC(x), right: Si(x). The results of 100-spill analysis are overlaid.

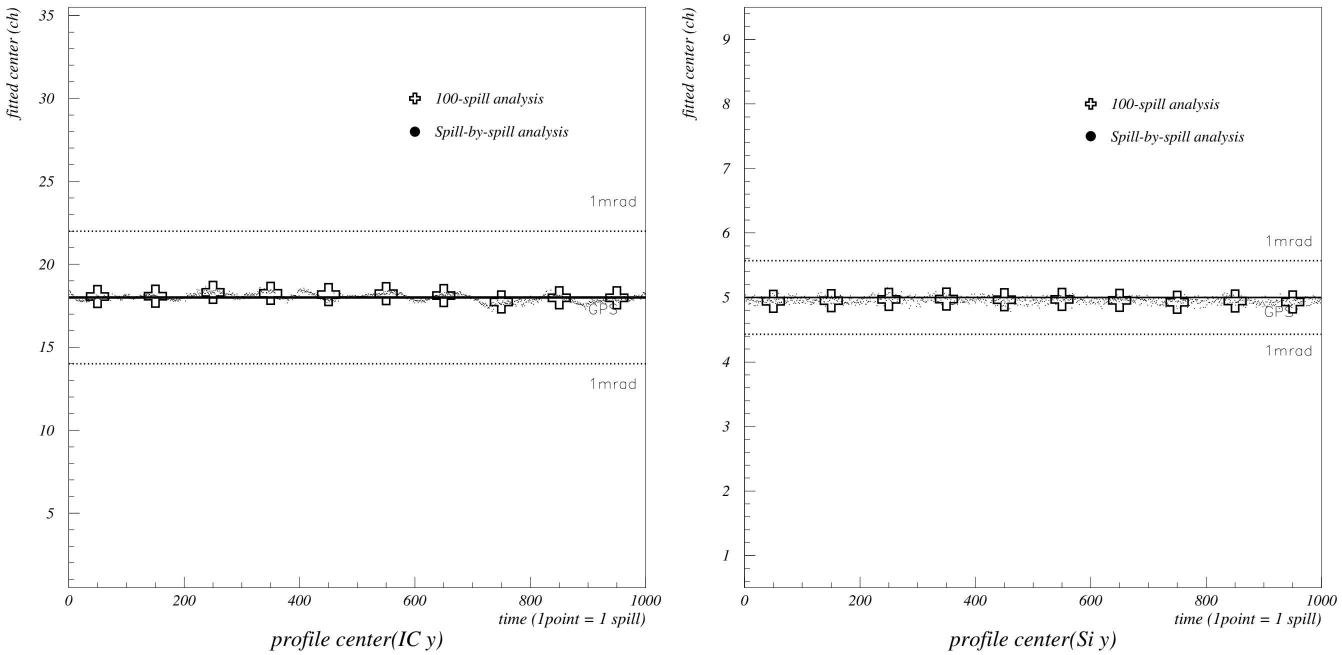

Figure 6.11: The fitted center of spill by spill during typical 1000 spills in November. Left: IC(y), right: Si(y). The results of 100-spill analysis are overlaid.

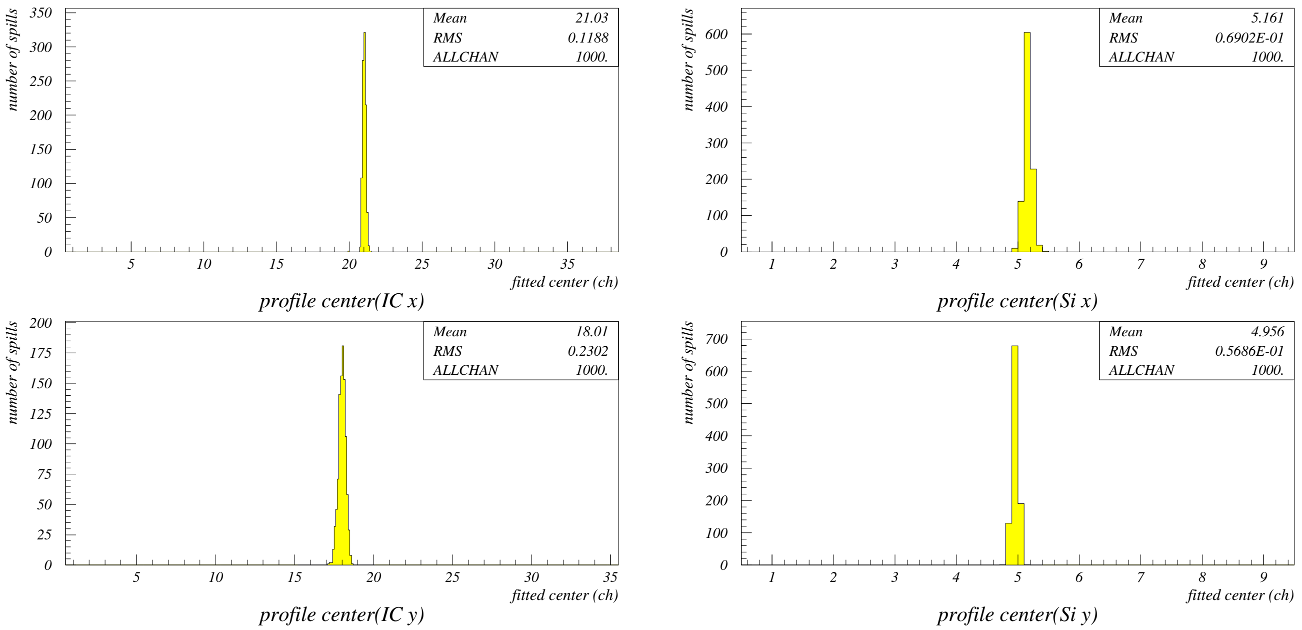

Figure 6.12: Projection of fitted center (spill by spill)

projection shows typical short term stability of the muon profile. Table 6.2 summarizes the results of the spill-by-spill analysis. All detectors show stability of fitted center of better than 2.4 cm. The angular stability is better than 0.12 mrad even if we take the worst RMS values.

	Fitted center value (dist. from GPS point)	RMS of projection
Si x	~5.6cm	2.4cm
Si y	~1.5cm	2.0cm
IC x	~7.7cm	0.6cm
IC y	<1.0cm	1.2cm

Table 6.2: Fitted center (spill by spill: 1000 spills)

6.4 Stability of Muon Yield

Fig. 6.13 shows the time variation of muon and proton intensity during the June run. Fig. 6.14 shows that of the November run. In this section, we define the "CT" as the ADC counts of CT, "Si sum" as the summing-up of ADC counts of 17 small Si pad detectors and "IC sum" as that of ionization chamber. CT indicates the primary proton intensity, on the other hand, Si sum and IC sum show the secondary muon intensity. (Si sum/CT) and (IC sum/CT) should be constant if the muon yield correlates linearly with the primary beam intensity.

We see (Si sum/CT) and (IC sum/CT) are stable within 6% in June and November configuration. The mean values of June and November themselves are different because of the different currents supplied to the horn magnets. (IC sum/Si sum) is also stable. It confirms these detectors are observing same muons.

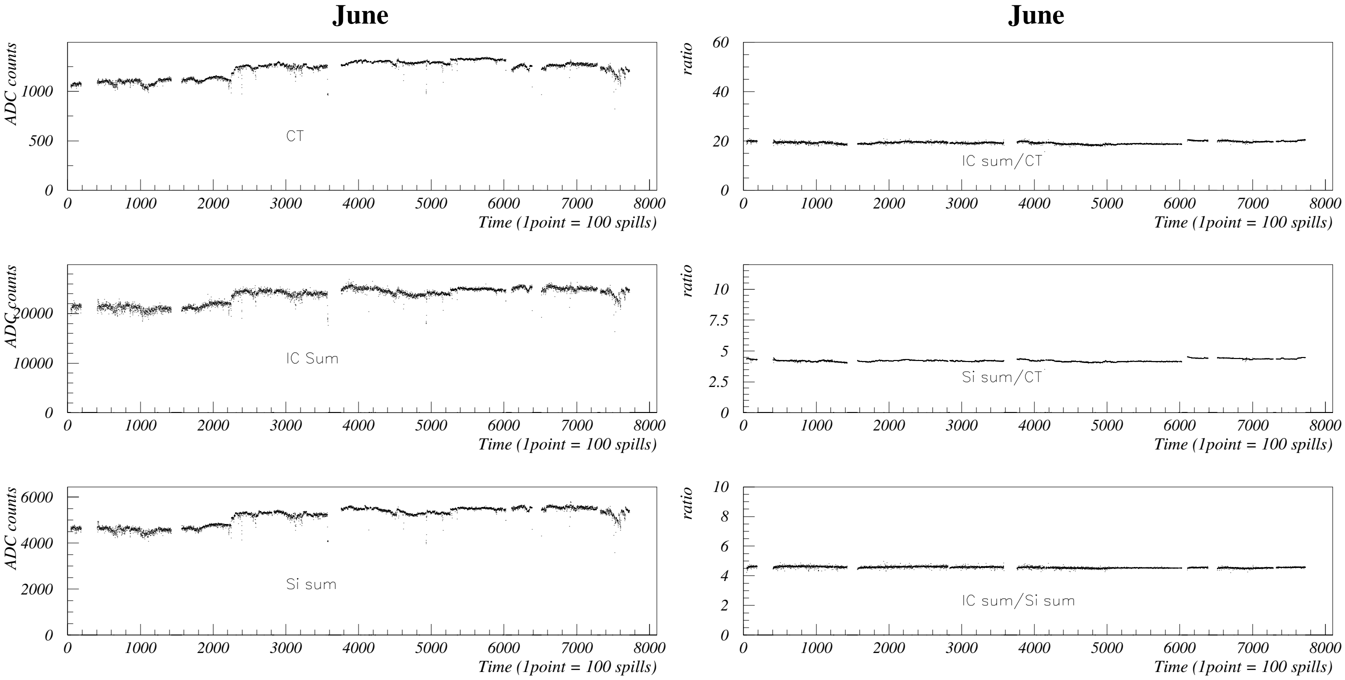

Figure 6.13: Stability of the beam intensity (during June run), Left Fig.: Time variation of the beam intensity. (From top to bottom , CT, IC total sum, Si total sum). Right Fig: (IC sum/CT),(Si sum/CT) and (IC sum/Si sum).

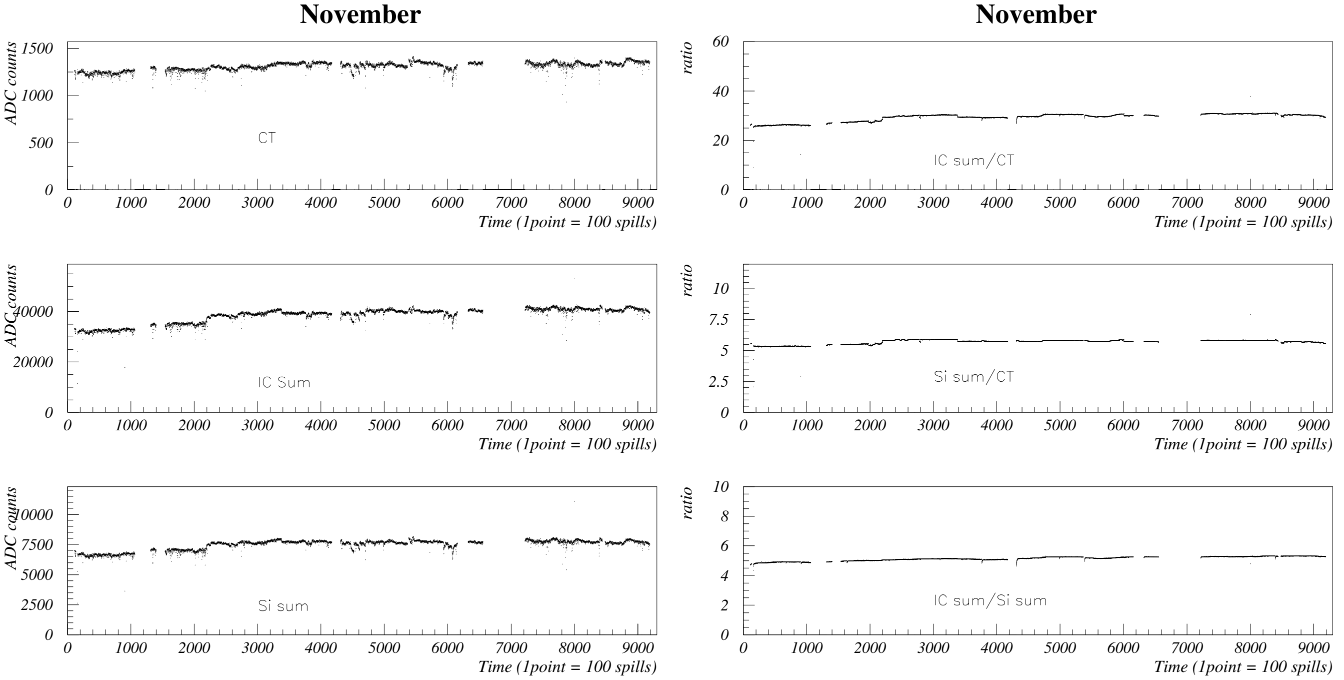

Figure 6.14: Stability of the beam intensity (during Nov. run), Left Fig.: Time variation of the beam intensity. (From top to bottom , CT, IC total sum, Si total sum). Right Fig: (IC sum/CT),(Si sum/CT) and (IC sum/Si sum). Around 6000-7000 on horizontal axis, we see low value for CT, IC and Si. This is because of the pion monitor data taking.

Chapter 7

Characteristics of K2K Neutrino Beam II (Measurement by Pion Monitor)

7.1 MC Simulation of Pion Monitor

Monte Calro simulation of the pion monitor is performed with the following procedure.

1. Using the same MC simulation as the neutrino beam MC, we record particle ID number, position and 4-momentum of each particle at the pion monitor position.
2. We generate Cherenkov photons using above information. Then photon reflection by the spherical mirror, and detection by PMTs is simulated.

Emission angle and number of Cherenkov photons are calculated using Eqs.(3.2) and (3.3), respectively. We trace photons from generation to detection. In this step, photons are assumed to have no absorption or scattering in the gas and the wall of the gas vessel.

Performance of the MC was tested in the beam test at Kyoto University[76, 77] and at T1 beamline at KEK [78]. As the results of these beam tests, we concluded this MC simulation explains Cherenkov phenomena well.

Fig. 7.1 shows the results of the pion monitor MC simulations for the K2K experiment [*] . Left figures show the 2-dimensional ring image on the focal plane at various refractive indices. Horizontal axis is x-direction on the focal plane, vertical axis is y-direction, and unit is cm. This ring image is only from the pions. Right figures show y-directional photon distribution on the focal plane sliced with a 1cm-wide strip centered at x=0.

7.2 Analysis Method

7.2.1 Basic Idea

We discuss how to extract the angle and momentum of pions from the data in this section.

At first we prepare for two dimensional kinematic plane of θ_π-p_π. This is convenient for this analysis since each point of this plane gives particular 1-dimensional Cherenkov photon distribution like Fig. 7.2, thanks to the characteristics of a spherical mirror and property of Cherenkov ring radius. Further, this point gives a particular neutrino energy at the same time.

Predicting neutrino energy from pion monitor data is possible if we reconstruct the population of pions in this map using Cherenkov information.

We must limit the region and prepare some finite bins for real analysis instead of infinite points. Actual bin number will be defined later.

---

[*] Cherenkov ring image depends on the pion production model at the target. GCALOR model is used in this figure

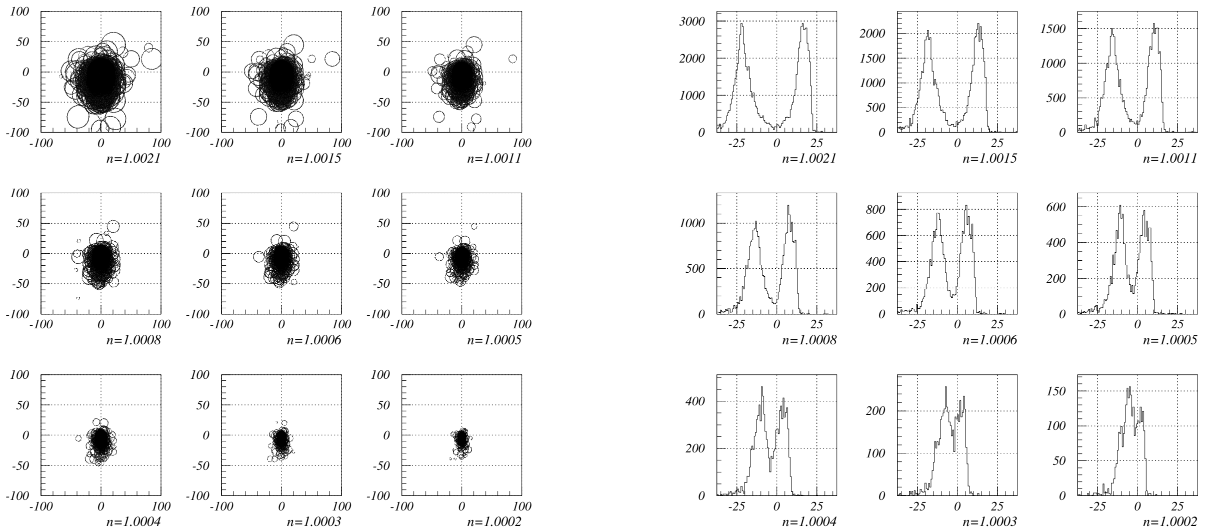

Figure 7.1: Photon distribution by the Monte Carlo simulation: Left figure shows the 2-dimensional ring image at various refractive indices, unit is cm and Cherenkov light only comes from pion. Right figure shows y-directional slice of the ring image.

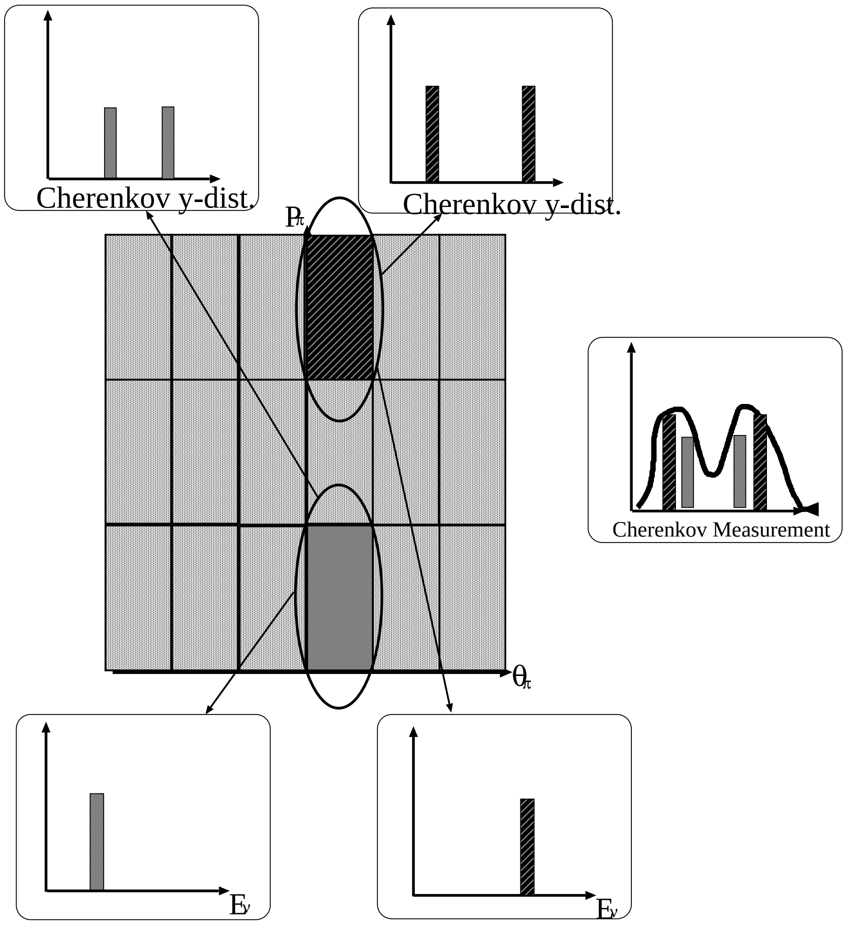

Figure 7.2: Each point of θ_π-p_π plane gives both a particular neutrino energy and a particular 1-dimensional Cherenkov photon distribution.

7.2.2 Reconstruction of Pion Population in Energy and Angle Space

To achieve our purpose, χ^2 fitting method is used.

If the regions are numbered (like region(1),region(2),region(3),..... region(m): each box in the Fig. 7.2), Cherenkov distributions are also tagged at the same time (like dist(1),dist(2),.....,dist(m)).

Then χ^2 can be calculated:

$$\chi^2 = \sum_{j=1}^{PMTmax} \frac{(dist(real)_j - \sum_{n=1}^{m} W(n) \cdot dist(n)_j)^2}{\sigma_j^2} \tag{7.1}$$

where j is the PMT number. $W(n)$ is a pion population in the n-th kinematic bin to be determined. By minimizing this χ^2, we obtain the best combination of pion populations to reconstruct the 1-dimensional Cherenkov image.

7.2.3 Combination of Measurements at Several Refractive Indices

Minimum χ^2 fit enables to reconstruct a map of the pions. However, only one refractive index measurement cannot efficiently distinguish higher momentum pions.

Therefore gas pressure is varied several times. Fig. 7.3 shows the schematic view of the advantage of measurements at various pressures. For a simple explanation, we imagine the case of only two Cherenkov rings on the PMT array at first. We cannot distinguish the three possibilities using only one pressure measurement. However, we can distinguish each possibility if we have different-pressure measurements.

To extend it to the real case, χ^2 method is a little bit changed. Fig. 7.4 shows the principle of fitting method in the real case. Low pressure data is only sensitive to high momentum pions. It helps understanding the angle distribution of the high momentum-pion. We subtract contribution of the high-momentum pion from lower pressure data using known Cherenkov phenomena. After this subtraction, we can estimate lower momentum pion distribution from higher pressure data.

The χ^2 sum of all-index-measurements is effective to determine pion momentum. Low pressure data constrains the high momentum pions population.

Total χ^2 is redefined as follows:

$$\chi^2 = \sum_{k} \left(\sum_{j=1}^{PMTmax} \frac{(dist(real)_j - \sum_{n=1}^{m} W_n \cdot dist(n)_j)^2}{\sigma_j^2} \right)_k , \tag{7.2}$$

where k is the k-th refractive index.

In actual case, we used 50 bins to be determined. These kinetic regions consist of 10 angular bins and 5 momentum bins. The angular bins are 10 mrad step covering -50 mrad$\leq \theta \leq$50 mrad. The momentum bins are 4 bins with 1 GeV/c step for 2 GeV/c$\leq$p$\leq$6 GeV/c and another bin of 6 GeV/c$\leq$p$\leq$10 GeV/c.

Fig. 7.5 shows Cherenkov images of each pion kinematic bin at n=1.0004756. These images are actually used in the fit. The image from minus angle pions are splitted into two since such pions have effectively two angles against the spherical mirror (Fig. 7.6). This is due to the definition of the divergence angle.

7.2.4 Confirmation of Analysis Method by MC Study

In order to confirm the analysis method, MC study was performed. Using the same hadron production model, we compare the neutrino flux predicted by the pion monitor and by the neutrino beam MC. The procedure is as follows (Fig. 7.7):

1. We calculate a Cherenkov photon distribution at the PMT array using the pion monitor MC simulation (Fig. 7.8: Horizontal axis is the PMT number.)

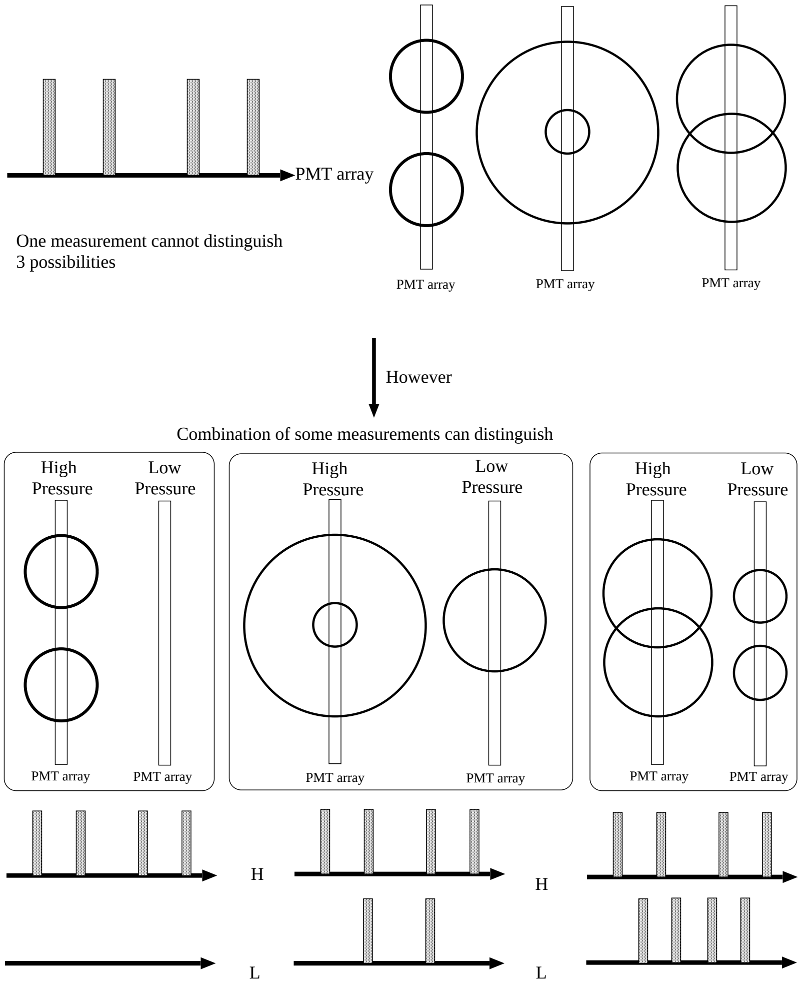

Figure 7.3: The advantage of combination measurements. One measurement cannot distinguish the possibilities of the ring combinations while several measurements distinguish it.

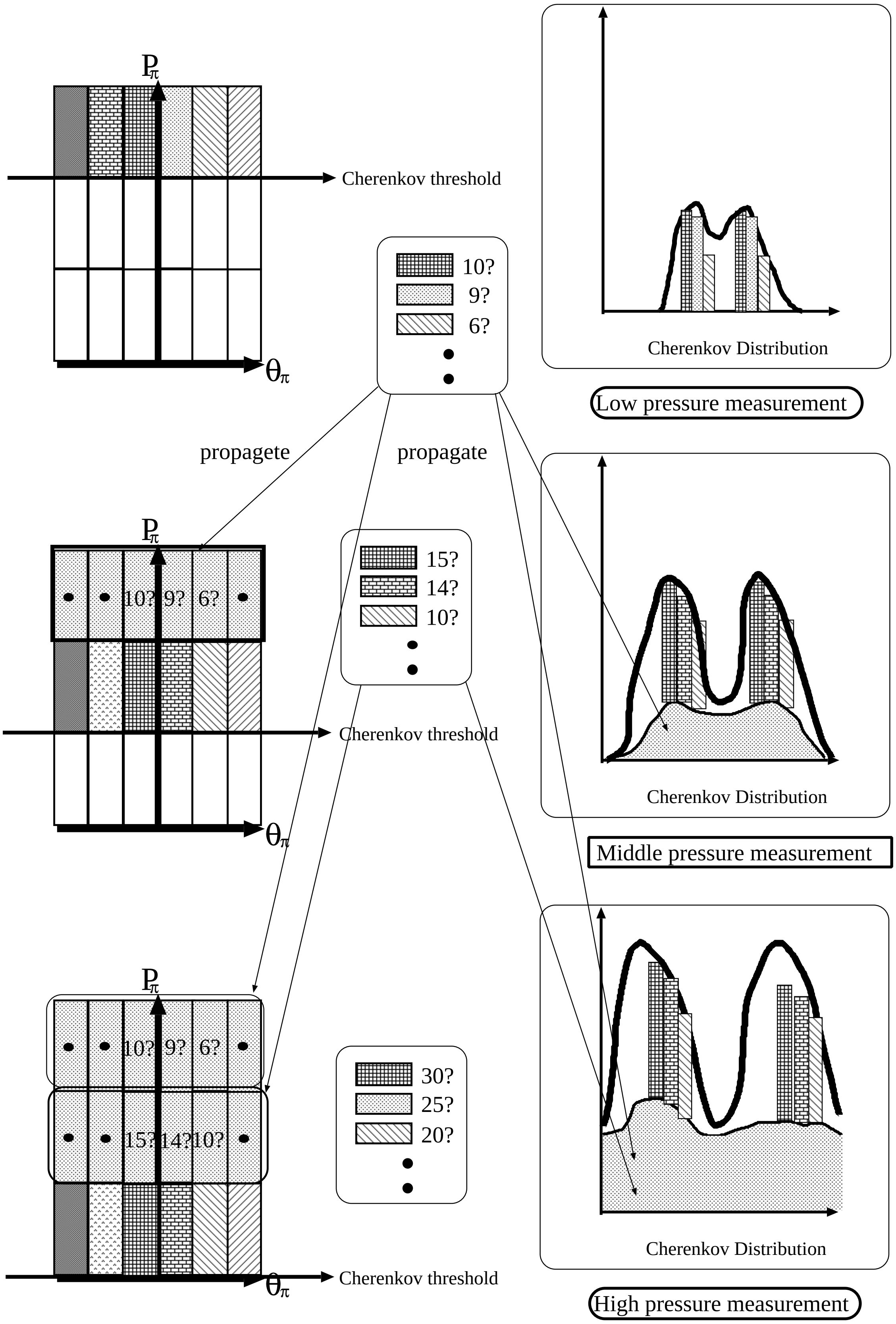

Figure 7.4: The advantage of combination measurements (real case). Low pressure measurement can determine the distribution of the high momentum pions. It can be estimated from lower pressure data.

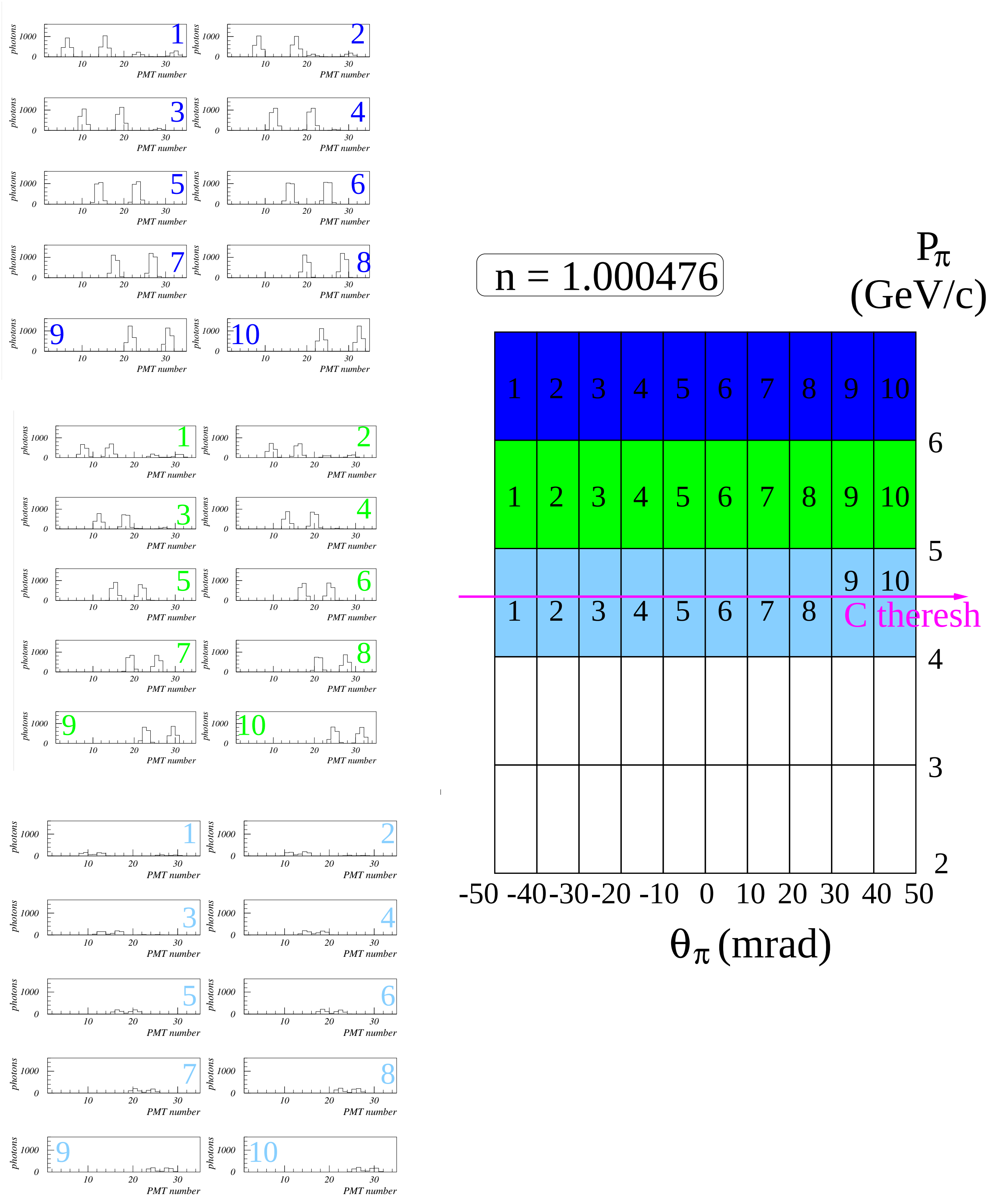

Figure 7.5: Cherenkov images of each pion kinematic bin at n=1.0004756.

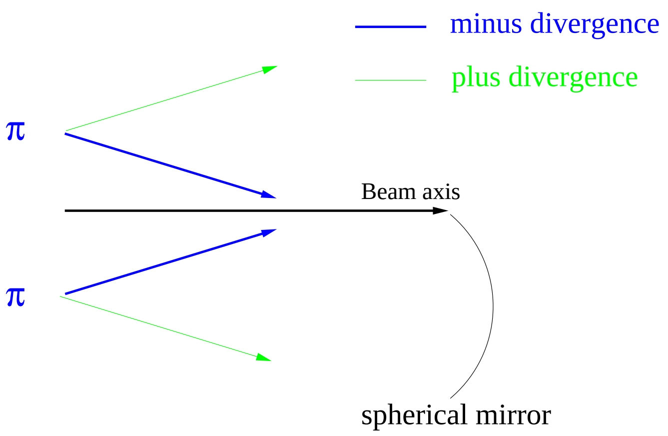

Figure 7.6: Definition of pion divergence angle

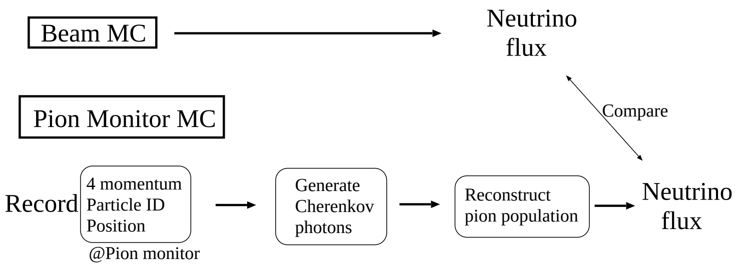

Figure 7.7: Confirmation of the analysis method by MC study. Schematic view of the procedure.

2. Reconstruct the pion kinematic bins using a least χ^2 fit. Fig. 7.9 shows the fitted result in a 2-dimensional pion kinematic distribution. Fig. 7.10 shows the projection of Fig. 7.9. We overlaid the results of the beam MC.
3. Calculate the neutrino flux from pion kinematic plane. (Fig. 7.11) We overlaid beam MC results.

Pion monitor is insensitive to the pions with lower than 2 GeV/c momentum because of available gas pressure. This means it is insensitive to the neutrinos which have energy lower than 1 GeV.

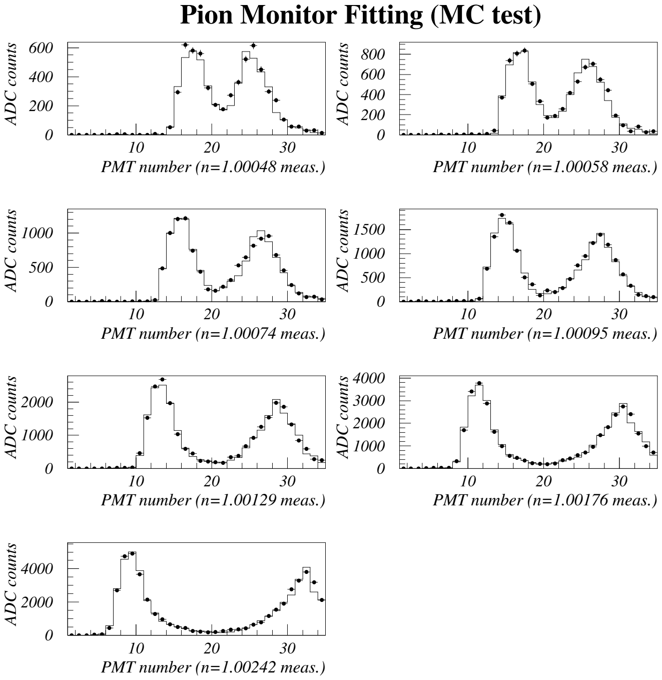

Figure 7.8: Simulated Cherenkov distribution (dots). We applied the fit method to them. Best fit results (histogram) are overlaid.

The fit answer should be same as true value of the beam MC in all figures. The difference is considered to be a systematic error.

We applied the fit method to Cherenkov photon distributions which was generated using Cho pion production model. Fig. 7.12 shows the Cherenkov distributions and the fit results on projected momentum and angle of pions.

7.3 Results from Pion Monitor Measurement

7.3.1 Beam Condition in June and November and PMT Saturation Effect

The pion monitor is not a real-time monitor. We took pion monitor data twice in 1999. One opportunity was in June and the other was in November. Each data was taken with a different horn system, as described in Chapter 6.

In order to avoid PMT saturation, we reduced the beam intensity by one or two orders during the pion monitor run. The beam intensity was about 5.0×10^{12} ppp at the target during normal experimental runs in June and November. Furthermore, we reduced number of bunches in June for the same reason. Fig. 7.13 shows the oscilloscope photographs of a typical PMT in June, which were taken in multi and single bunch mode. Use of optical filters to avoid saturation is invalid since we have lots of background coming from beam associated radiation (soft electromagnetic components)

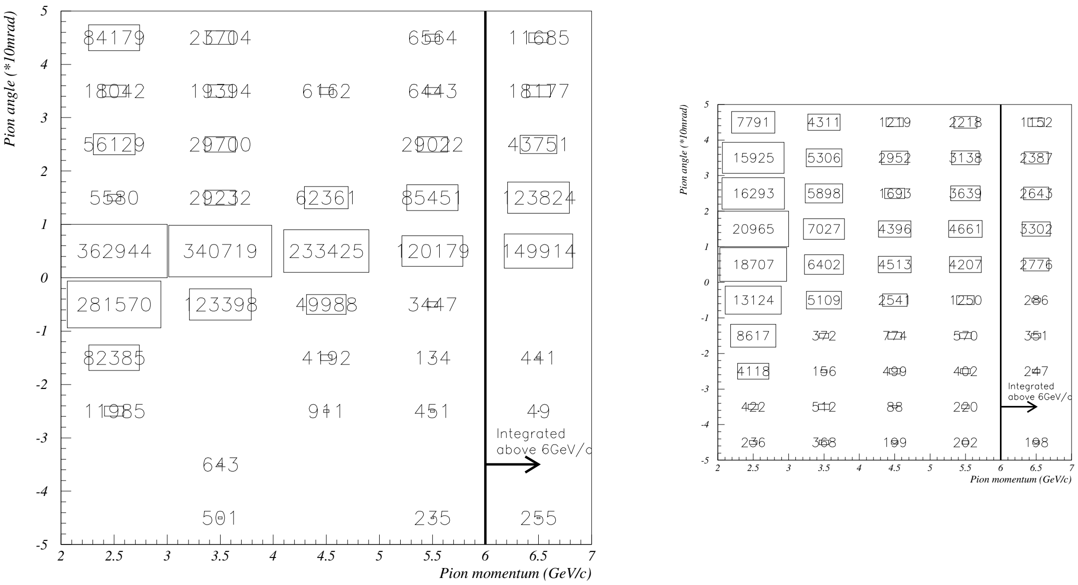

Figure 7.9: Fitted answer of pion kinematic distribution and their error(MC study). Left: fitted answer, Right: their error.

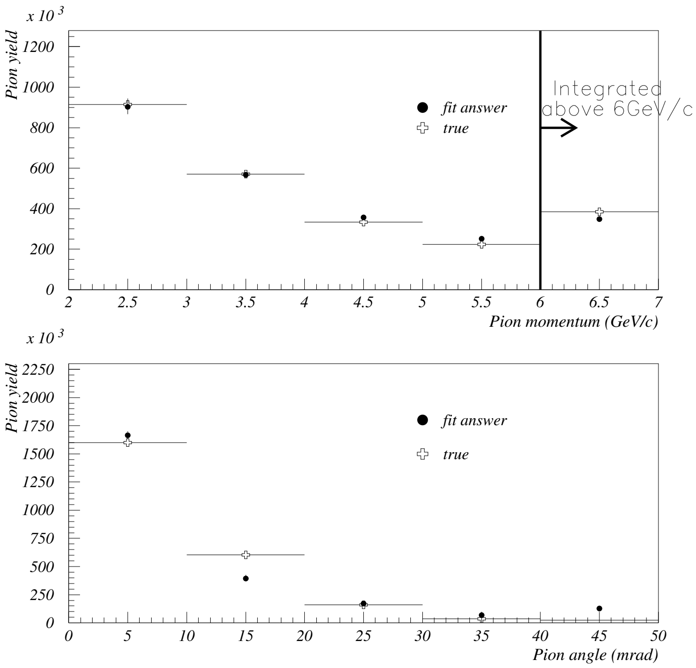

Figure 7.10: Comparison between the fit answer and the MC true on angle and momentum of pions. These are projections of Fig 7.9. Top: pion momentum, bottom: pion angle. Normalization is performed using total entry of histograms.

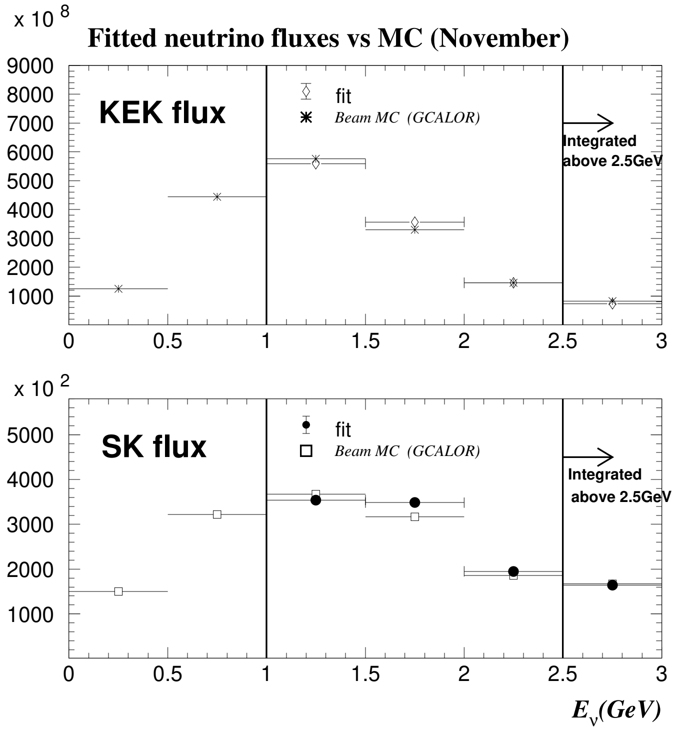

Figure 7.11: MC test of neutrino flux reconstruction using the fit method of the pion monitor. Total entry above 1 GeV at KEK is used as normalization factor.

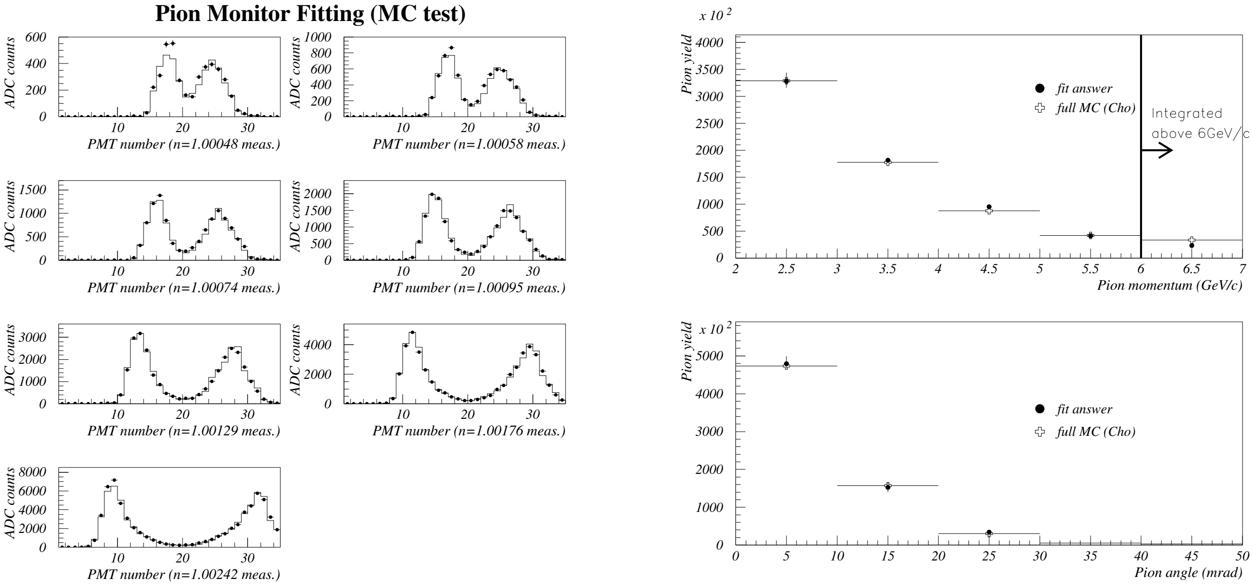

Figure 7.12: MC test for Cho pion production model. Left: Cherenkov distribution with best fit results. Right: fit answer of pion kinematics with true answer

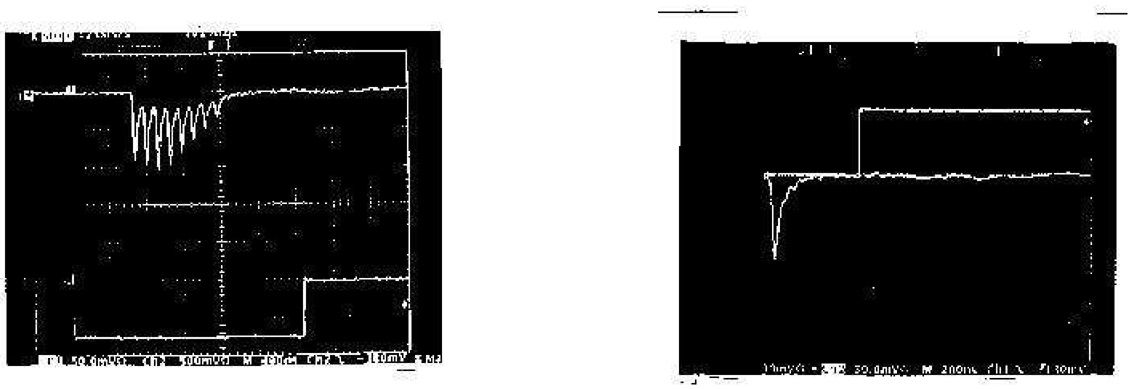

Figure 7.13: The oscilloscope photograph of a typical pion monitor PMT in June. Left: Normal operation, right: single bunch mode operation. The saturation of the PMT is clearly seen in the left figure.

hitting the photo-cathode/dynodes directly. [†] Fig. 7.14 shows the typical signal and background at refractive index of this freon gas, $n=1.00243$ and proton intensity of $\sim 1.0\times10^{11}$ in June run. We estimated this background by rotating the mirror to move off the Cherenkov ring from the PMT array (Fig. 7.15) and subtracted.

Fig. 7.16 shows PMT ADC vs. CT ADC of two typical PMTs in June, which shows the saturation effect. The correlation was fitted with the 2nd polynomial. The saturation effect was corrected by using this function.

From a result of PMT saturation study, we could use intense beam 10 times in November run. We found we could make a stable operation of PMT without saturation by supplying lower HV. PMT gain in November run was 1/6 or 1/15 of June run, which was the limit of a stable operation. We changed gain from 20 to 50 during data taking to cover a large dynamic range. Fig. 7.17 shows the same plots as Fig. 7.16 for the same PMTs in November. Only the difference is the gain of 50. The data points make 4 clusters which correspond to 3.0×10^{11}, 4.8×10^{11}, 6.4×10^{11} and 8.2×10^{11}ppp. There is no saturation at these proton intensities in November. We could get much better beam condition in November, that is much closer to that of normal runs. Table 7.1 summarizes the conditions of the pion monitor running in June and November configurations.

Parameter	June	November
Target diameter	20 mmϕ	30 mmϕ
Current supplied to horn magnets	200 kA	250 kA
Proton beam int. (in πmon. data taking)	7.0×10^{10} ppp	7.0×10^{11} ppp
Proton beam bunch#	1	9
PMT gain	300	20 or 50
PMT saturation	exist	none

Table 7.1: Comparison the beam conditions of June and November

Systematic errors due to changing beam condition from the normal run to pion monitor run are described later.

7.3.2 Correction of Proton Beam Intensity Dependence

The ADC counts of each PMT is corrected for the beam intensity dependence by using the CT

[†] We had PMT signals even if PMTs were covered by black sheet.

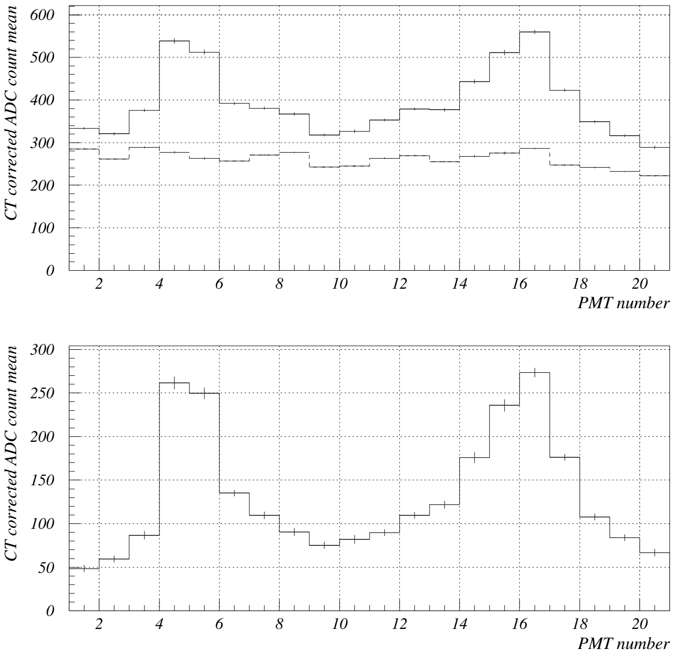

Figure 7.14: S/N ratio at n=1.00243. Top figure: Signal with the background (normal run) and only background (mirror-off run), bottom figure: the estimated signal (Cherenkov photons) after the background subtraction

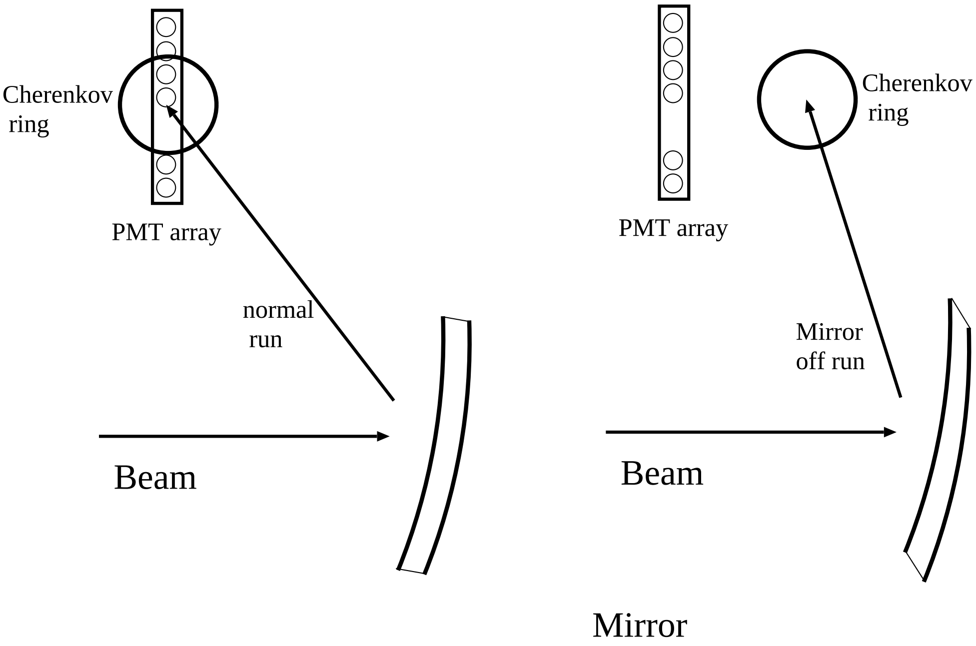

Figure 7.15: Background measurement using the rotation of the mirror. The Cherenkov ring is the off-position of the PMT array.

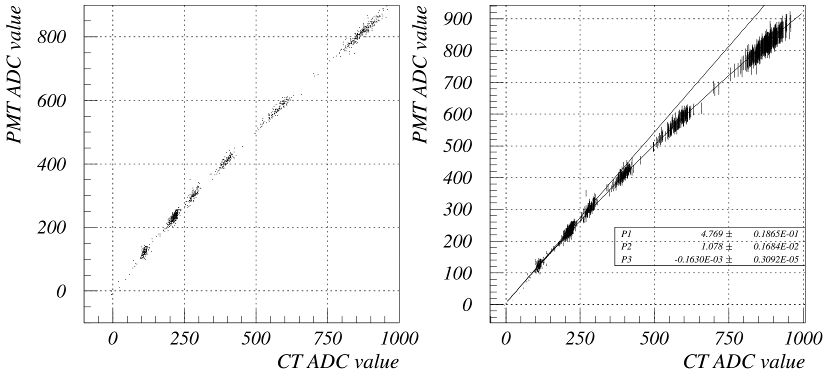

(fi_pmt(19)-rawoff(19)) VS. (fi_ct(6)-ctoff(1))

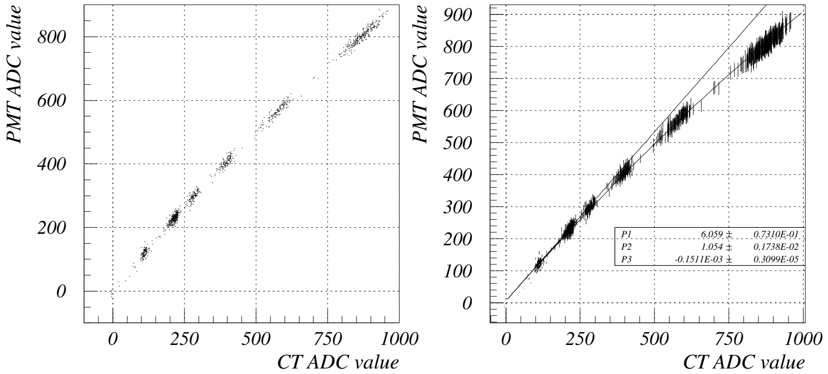

(fi_pmt(20)-rawoff(20)) VS. (fi_ct(6)-ctoff(1))

Figure 7.16: Saturation of PMT#19 and PMT#20 in June run. Top figures: PMT#19, bottom figures: PMT#20, left figures: relation between CT ADC value (represent primary proton intensity) and PMT ADC counts (scatter plot), right figures: fit with a 2nd polynomial function is overlaid on the data. A linear function is also drawn for comparison. CT ADC of 440 corresponds to the intensity of 6.8×10^{10}ppp, which was the nominal intensity of the June pion-monitor runs.

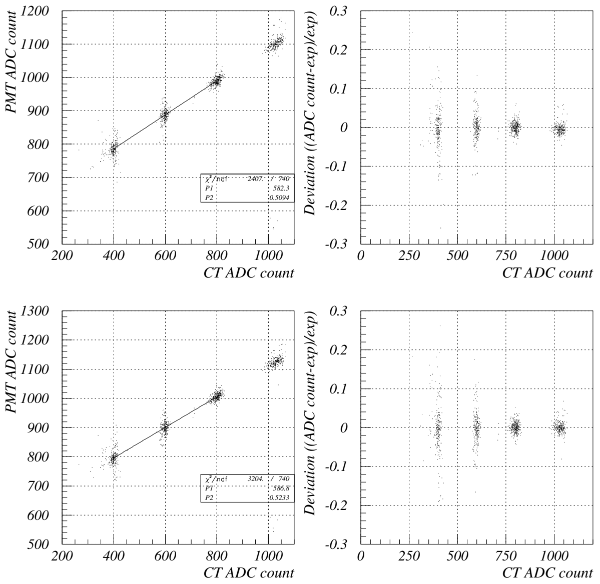

Figure 7.17: Linearity of PMT#19 and PMT#20 in November run. Top figures: PMT#19, bottom figures: PMT#20, left figures: relation between CT ADC value (represent primary proton intensity) and PMT ADC counts (scatter plot), right figures: deviations from the expectations.

ADC counts.

Fig. 7.18 shows the time variations and their projections of CT, PMT#14 and PMT#14/CT.

In this figure, the proton intensity was intentionally changed. This proves the reliability of this normalization. We use mean and RMS of each (PMT/CT) value of the corrected one for the analysis.

7.3.3 Calibration of Refractive Index

Cherenkov photon distribution from 12 GeV proton was measured to calibrate the refractive index of our freon gas. Fig. 7.19 shows the distribution. Horizontal axis shows the PMT array, and left side of the horizontal axis corresponds to the top side of the PMT array (Fig. 4.45).

Diameter of Cherenkov ring of proton beam shows that the 2.11 atm gas has refractive index of 1.00294. This is determined by comparing between data and MC simulation.

7.3.4 Cherenkov Photon Distribution at Various Refractive Indices

Figs. 7.20 and 7.21 show the real pion monitor data taken at various refractive indices in June and November, respectively. Horizontal axis shows PMT array, and vertical axis shows ADC counts of each PMT. Setting of refractive indices is a little different in June and November because setting of gas pressures is different.

ADC count of each PMT was corrected using the relative gain calibration constants taken by the Xe lamp and the saturation curve. The saturation correction is needed for only June data. We took data with two gains in November to compensate the dynamic range of PMTs: Cherenkov photon yield changes 10 times between at the lowest and the highest refractive index. The data at n=1.00176, n=1.00242 and n=1.00129 were taken with the gain=20, and other data were taken with gain=50. There is one point at n=1.00129 to check data taking with different PMT gains. Left figure in Fig. 7.21 shows the data with gain=50, while right shows gain=20. In Figs. 7.20 and 7.21, the background coming from beam associated radiation hitting the photo-cathode/dynodes directly has been subtracted using the off-mirror run data.

PMT array was moved by a half channel in each measurement to get fine data (Fig. 7.22). Hence twice finer bin can be taken.

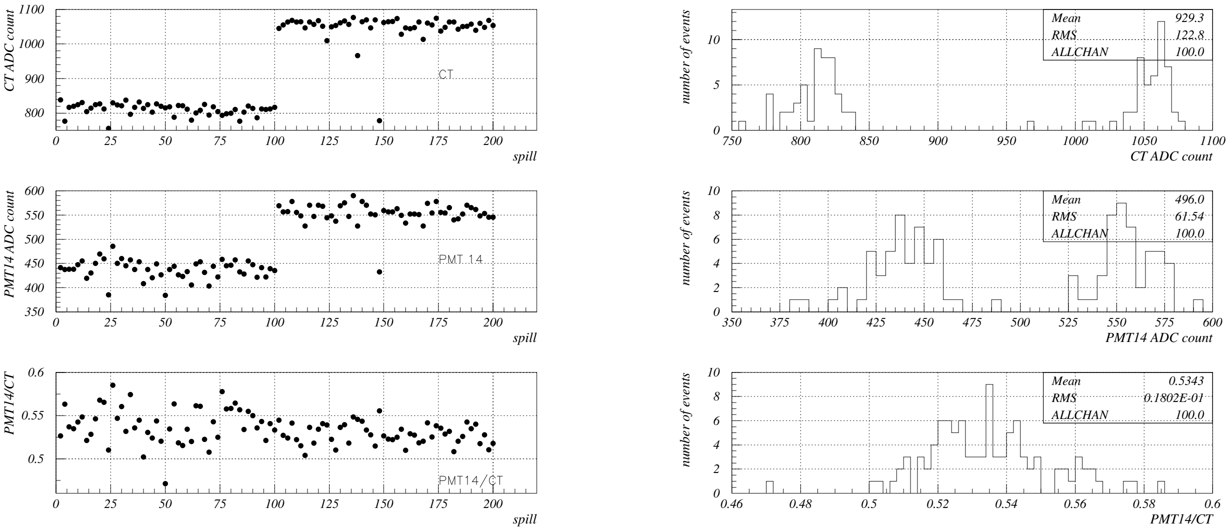

Figure 7.18: Signal ADC of PMT#14, CT and normalized value PMT14/CT

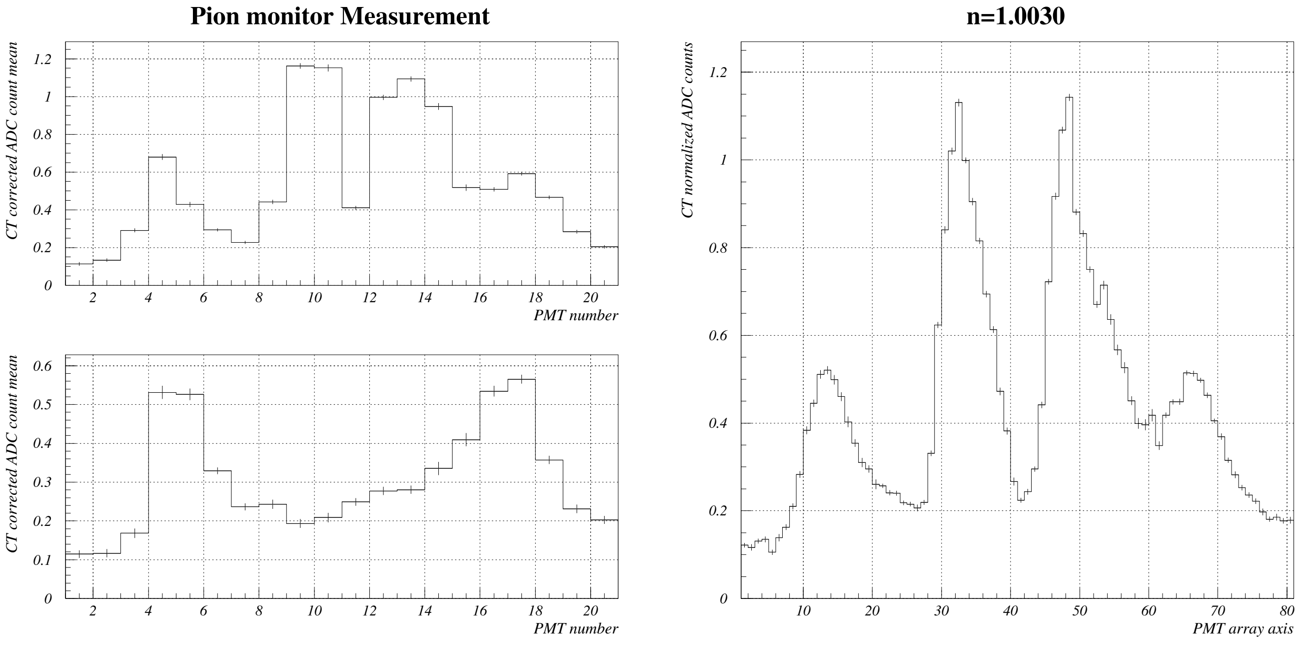

Figure 7.19: Photon distribution of 12 GeV proton mixed with pion. Two peaks around center come from the proton ring. Top-left figure shows a ring of protons with that of pions (above proton Cherenkov threshold: 2.11 atm), Bottom-left figure shows only the pion ring (below threshold 1.9 atm). Right figure shows the same configuration as the top-left figure with finer bins which was obtained by moving the PMT array.

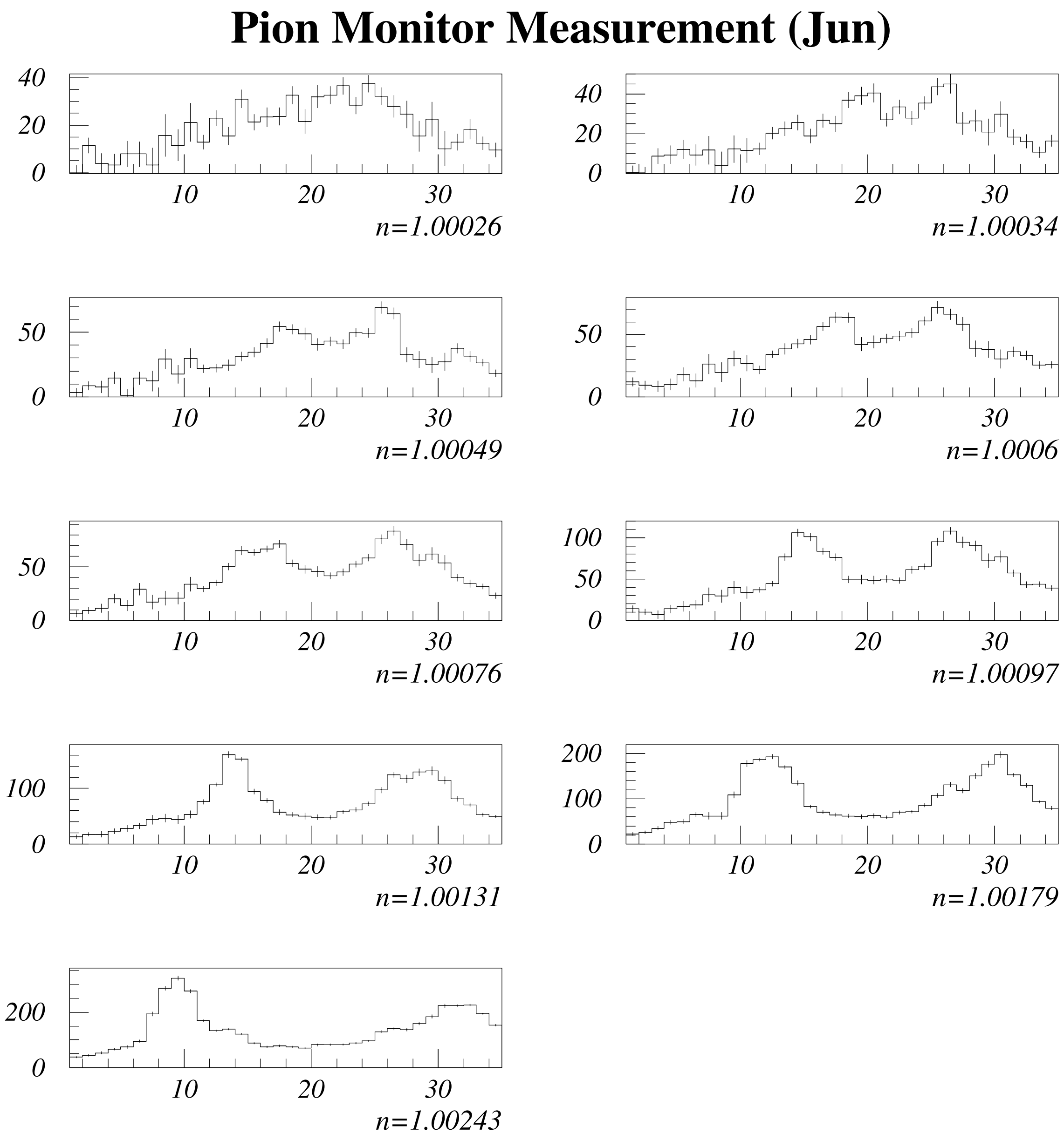

Figure 7.20: Pion ring measurements at various refractive indices (June)

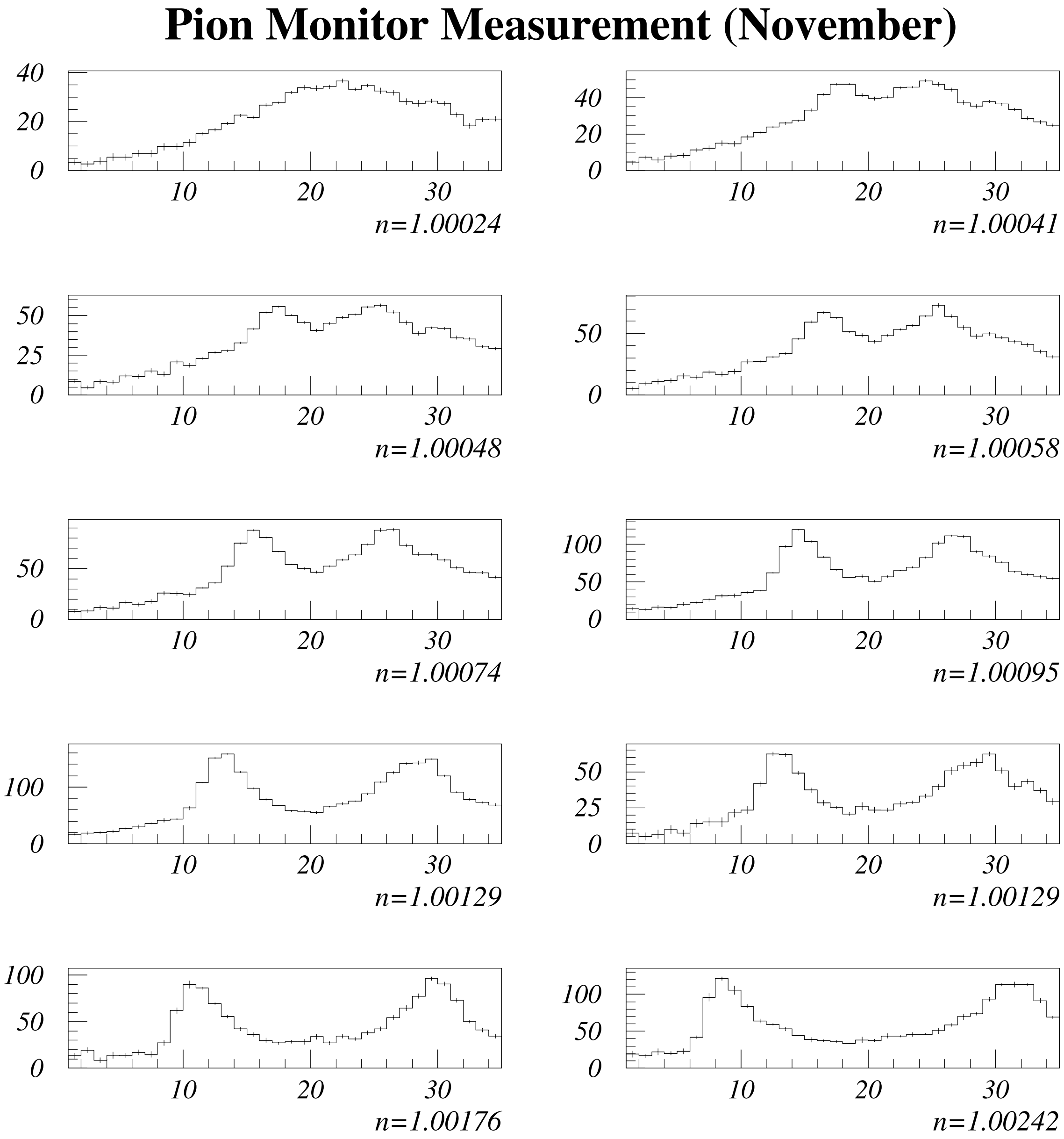

Figure 7.21: Pion ring measurements at various refractive indices (November). Data was taken with two PMT gains to compensate the dynamic range of PMTs: Cherenkov photon yield changes 10 times between at the lowest and the highest refractive index. The data at n=1.00176, n=1.00242 and n=1.00129 were taken with the gain=20, and other data are taken with gain=50. There is one point at n=1.00129 to cross check the two data sets with different PMT gains. Left figure in Fig.7.21 shows the data at gain=50, while right shows gain=20.

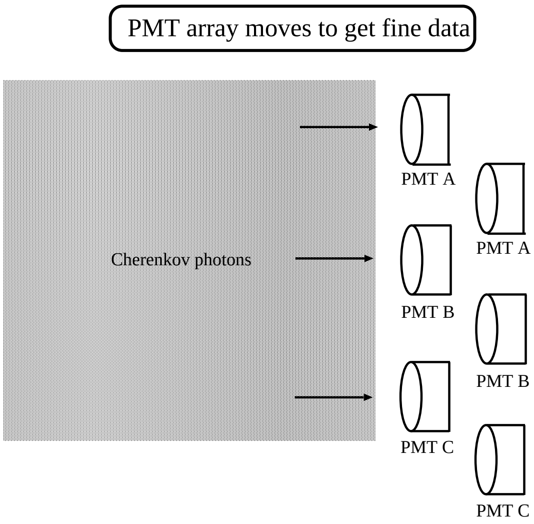

Figure 7.22: PMT array movement to get fine data

The quality of data in November is much higher than that of June since we have no saturation for PMT outputs, twice higher statistics and nearer beam condition to normal intensity run.

7.3.5 Subtraction of Cherenkov Photons from Electro-magnetic Shower

We have electro-magnetic shower components from π^0 in the main part of beam. Since electrons and positrons tend to have a large beta (v/c), they emit the Cherenkov lights easily. This becomes a possible background of Cherenkov photons for the pions in each data sample. Subtraction of this component is needed for the pion monitor analysis.

This subtraction is performed using MC. A Cherenkov photon distribution from electro-magnetic components is calculated by MC at each refractive index. The normalization factor between data and MC was determined by data at the lowest refractive index. This refractive index corresponds to Cherenkov threshold of 6.0 GeV/c pions, at which index the pion contribution is small.

Figs. 7.23 and 7.24 show the estimation of the electro-magnetic components in June and November, respectively. One normalization factor is used for the data at all refractive indices.

Since the shape of the Cherenkov photon distribution at the lowest refractive index is reproduced well by the MC simulation, reliability of the MC of the electro-magnetic components above 21 MeV is proved. 21 MeV corresponds to the Cherenkov threshold at the lowest refractive index for electron and positron. The electromagnetic components above 21MeV are the dominant background at all refractive indices. Even at the highest refractive index of 1.00243, corresponding to the Cherenkov threshold for 7 MeV electron, dominant background source is also electron with more energetic 21 MeV as shown in Fig. 7.25. It compare the Cherenkov distribution from electromagnetic components with 7 MeV $<E_e$ to that with 7 MeV$<E_e<$21 MeV at the highest refractive index. This fact shows this subtraction is good.

7.3.6 Extraction of Pion Energy and Angular Distribution

After the subtraction of the Cherenkov distribution of the electromagnetic components in the beam, a fit is applied to extract pion (θ-p) kinematic distribution. Subtracted data with best fit results are shown in Figs. 7.26 (June) and 7.27 (November). Each error bar includes the fluctuation of the ADC distribution (RMS/$\sqrt{n}$), MC statistics and an error of the calibration constant using Xe (quadratic sum). In November data set, the gain difference was corrected and error of the correction was taken into account.

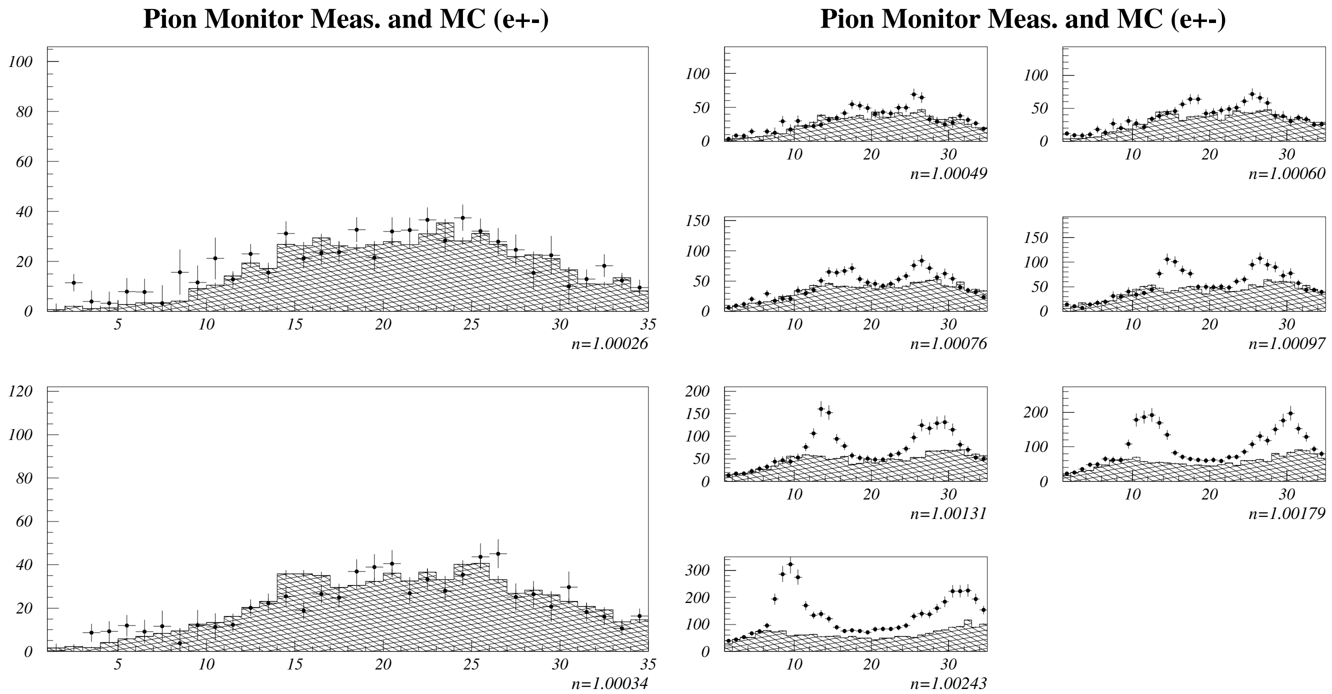

Pion Monitor Meas. and MC (e+-)

Pion Monitor Meas. and MC (e+-)

Figure 7.23: Subtraction of Cherenkov photons coming from the electro-magnetic shower component (June). Shaded area is estimated for Cherenkov photons from electro-magnetic components. Cross bar is data. Normalization is done by total ADC counts at the lowest pressure data and MC

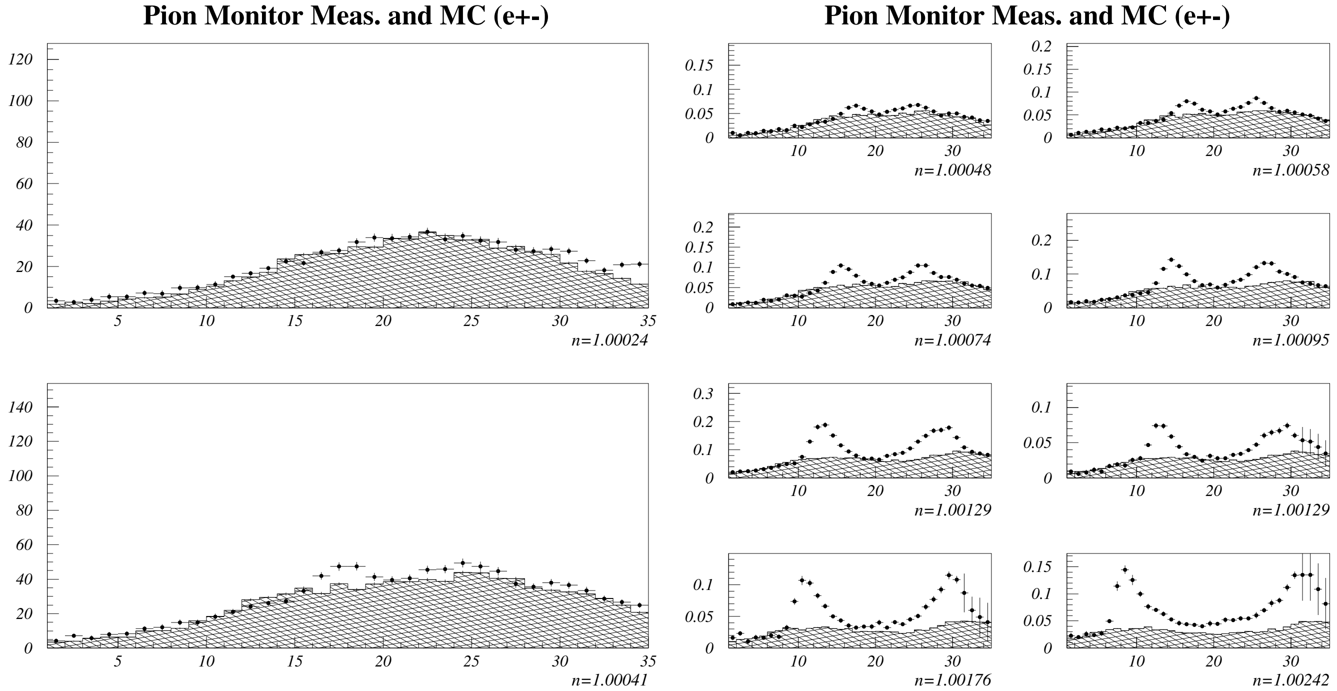

Pion Monitor Meas. and MC (e+-)

Pion Monitor Meas. and MC (e+-)

Figure 7.24: Subtraction of Cherenkov photons coming from the electro-magnetic shower component (November). Large error bars at n=1.00129, n=1,00176, n=1.00242 include the gain changing error estimated from gain cross point.

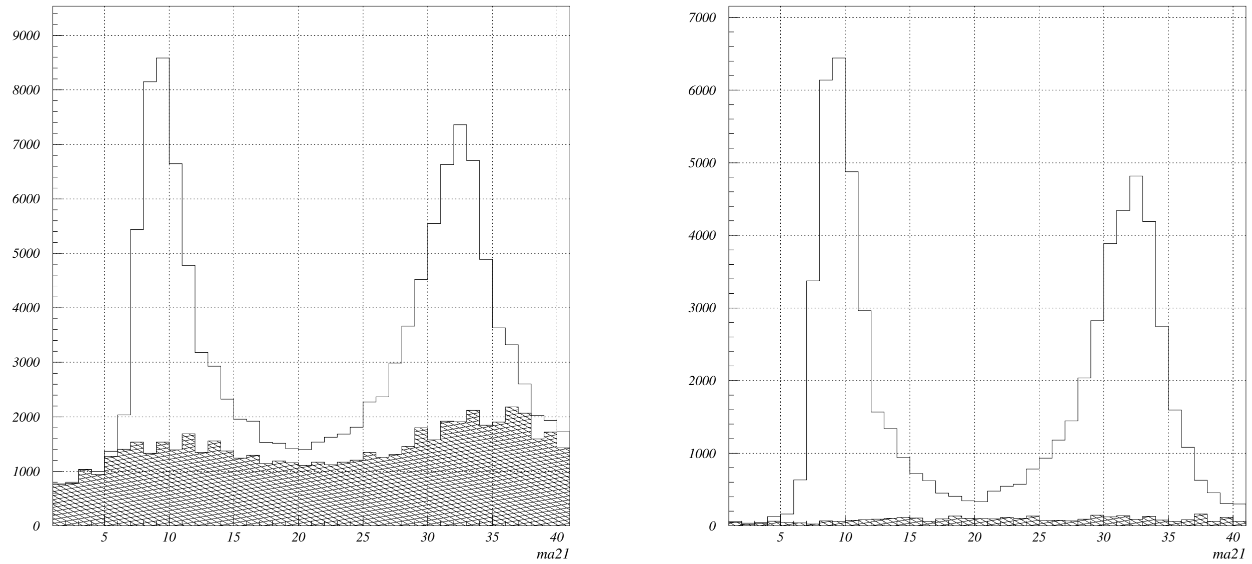

Figure 7.25: Estimated Cherenkov photons from electrons/positrons with the energy 7∼21 MeV. Open histogram shows Cherenkov photons from pions at the highest refractive index. Shaded area comes from $e^{\pm}$. Left figure: shaded area includes all $e^{\pm}$. Right figure: the energy of $e^{\pm}$ is restricted from 7 to 21 MeV. This suggests that we can estimate most of the components of $e^{\pm}$ using the lowest refractive index data.

Fitted results on pion kinematic region and their error are shown in Figs. 7.28(June) and 7.29(November). All of these numbers are relative values. Blank bin means fitted answer is 0, corresponding to negligibly small value comparing to the dominant bin.

7.3.7 Neutrino Energy Spectrum

Neutrino energy spectrum can be calculated from the pion kinematics and information on decay volume geometry. Figs. 7.30(June) and 7.31(November) show the calculated neutrino energy spectrum from the pion monitor data overlaid with the beam MC simulation. In the calculation, we corrected for the neutrino flux coming from the pion decay before the pion monitor. This uncertainty is discussed later. We use two sets of beam MC simulations using different hadron production models (GCALOR and Cho) for comparison. Normalization is done by total number above 1 GeV of the KEK flux.

SK(far)/KEK(near) ratio of the spectrum can be calculated after this calculation. (Figs. 7.32(June) and 7.33(Nov.)) All figures include systematic error. Systematic error of each bin will be described later. Pion monitor results agree with the MC using the Cho hadron model better than that using the FLUKA/GCALOR model for both spectrum and ratio.

The variation of the far/near ratio is explained as follows. The acceptance of the near detector for lower energy neutrinos is smaller since low energy pions decay near the target. Thus, far/near ratio goes down as a function of the neutrino energy below 1 GeV energy region. The near detector is more sensitive to the off axis neutrino components than the far detector due to the larger detector coverage in the transverse direction. Therefore detected neutrino energy by the near detector is softer than that by far. This causes the rise of the far/near ratio above 1 GeV neutrino energy.

To predict the number of neutrino events at SK, this neutrino flux predicted by the pion monitor is used. The center value of each bin is summarized in table 7.2. Below 1 GeV neutrino energy, we use the MC simulation based on the Cho model. Measured flux by the pion monitor and the beam MC is normalized by the total entry of the neutrino flux above 1 GeV. Neutrino flux above 2.5 GeV

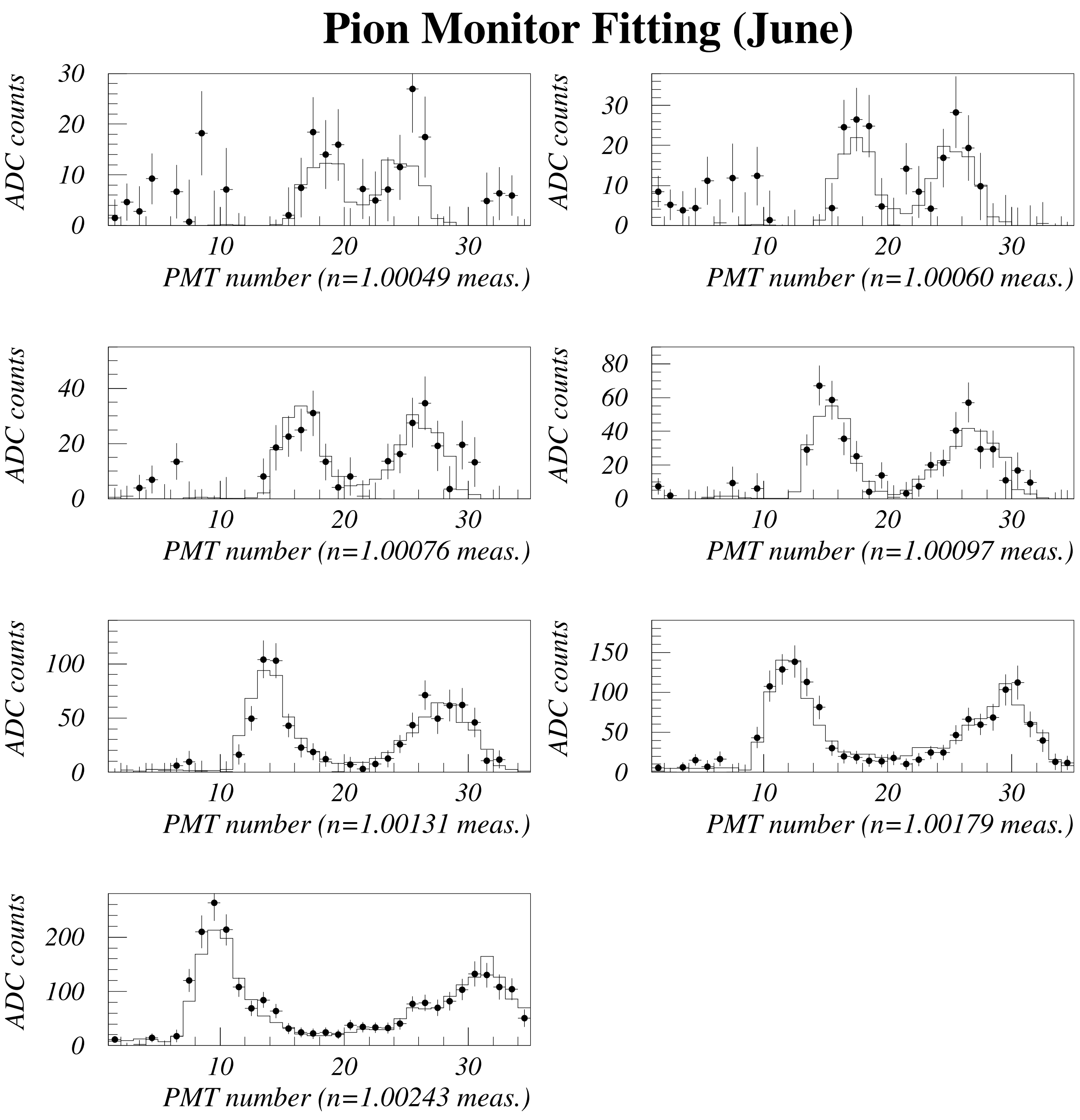

Figure 7.26: Subtracted data with best fit results. (June)

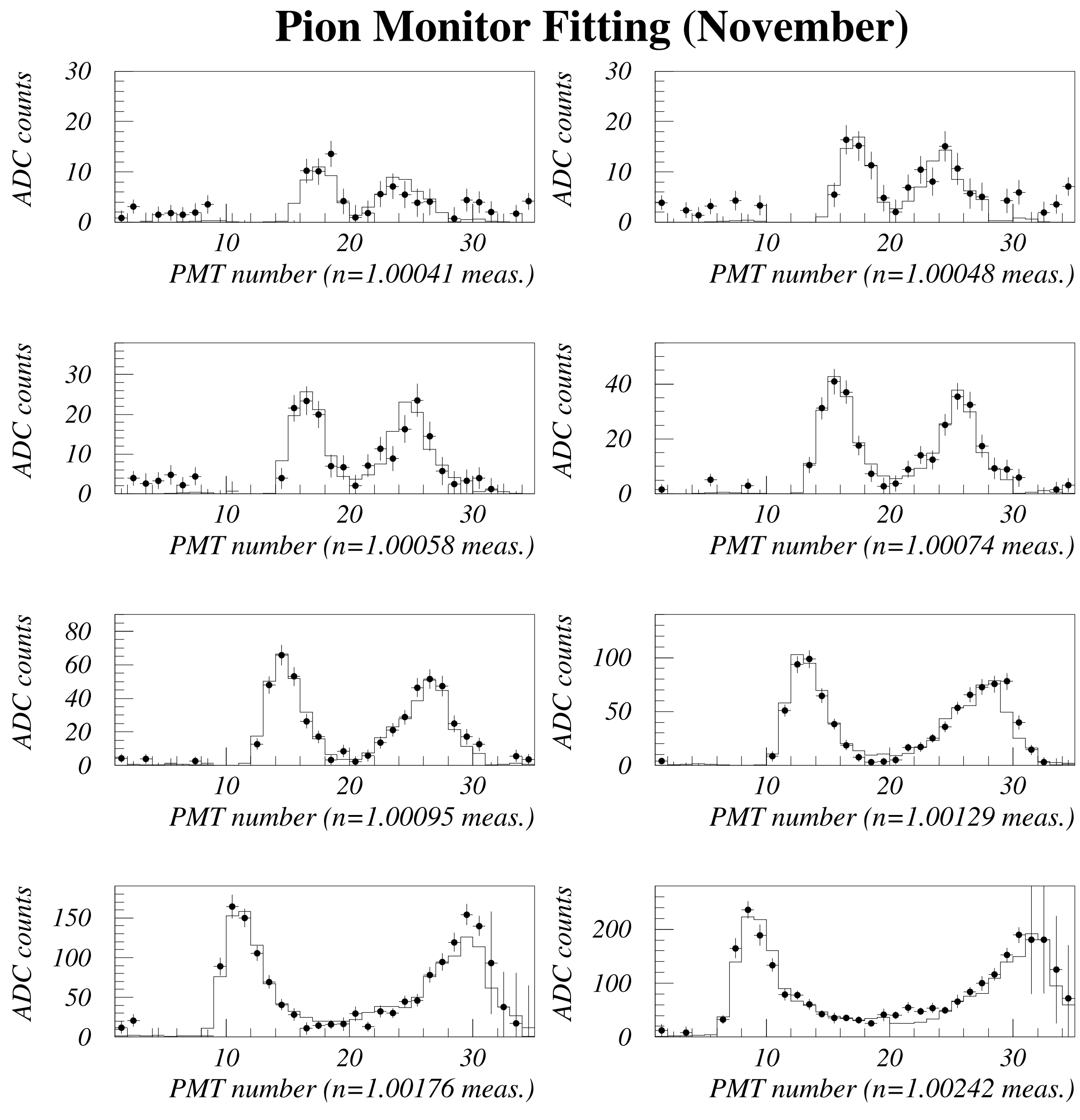

Figure 7.27: Subtracted data with best fit results (November)

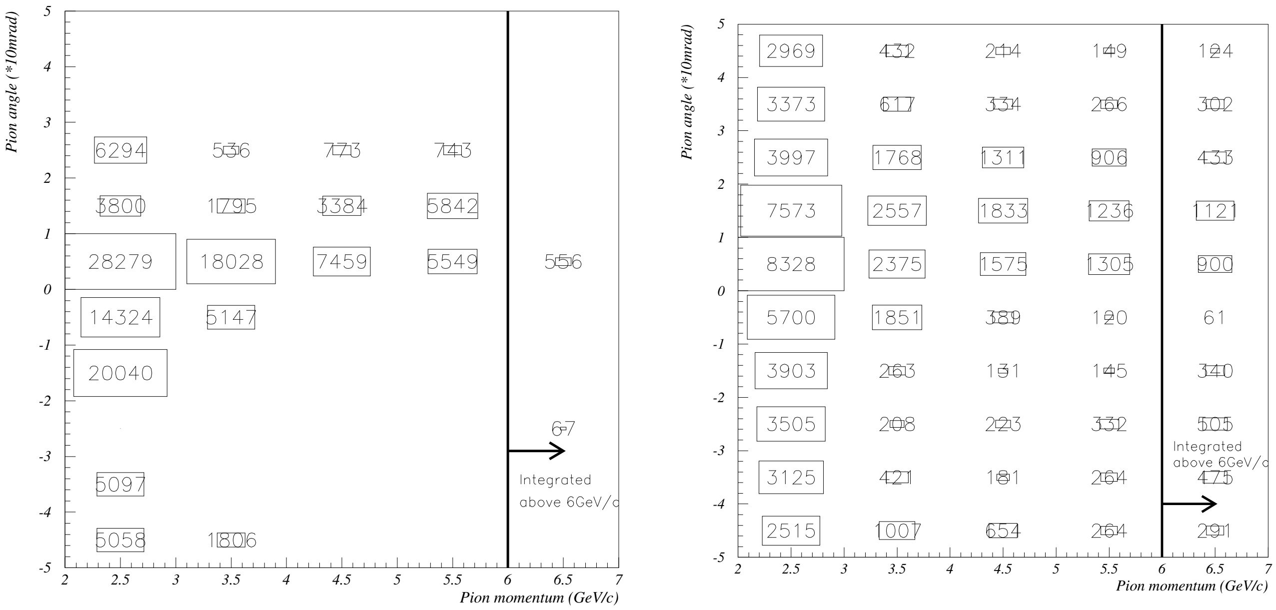

Figure 7.28: Fitted results of pion kinematic region and their error (June). Left: fitted answer, Right: their error

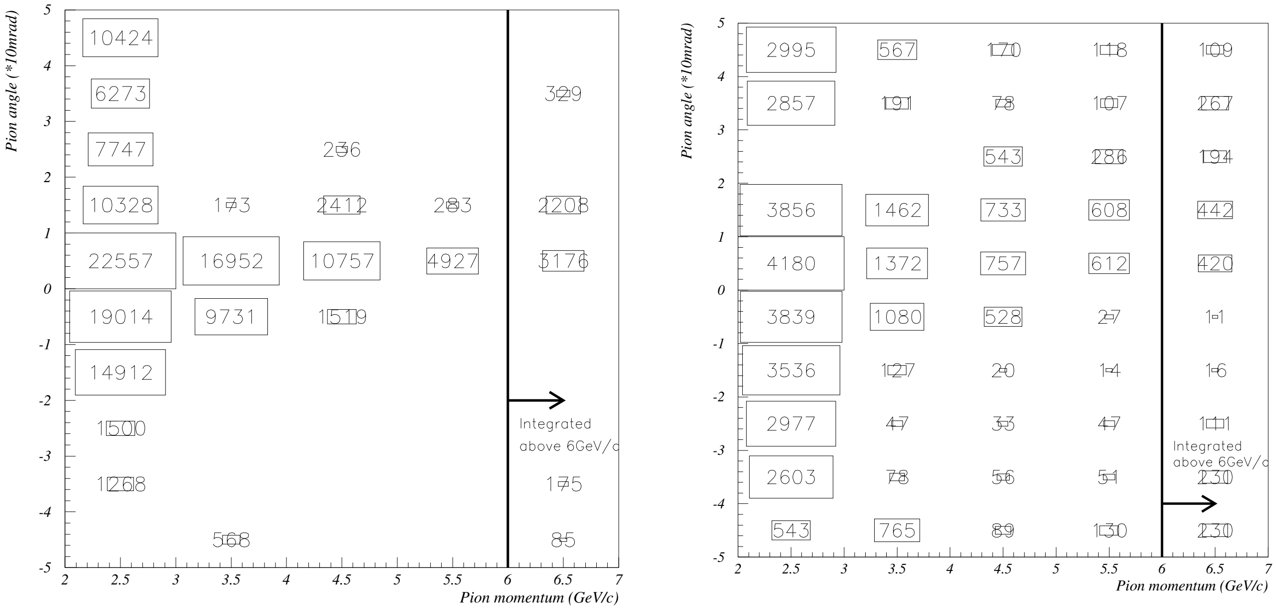

Figure 7.29: Fitted results of pion kinematic region and their error (November). Left: fitted answer, Right: their error

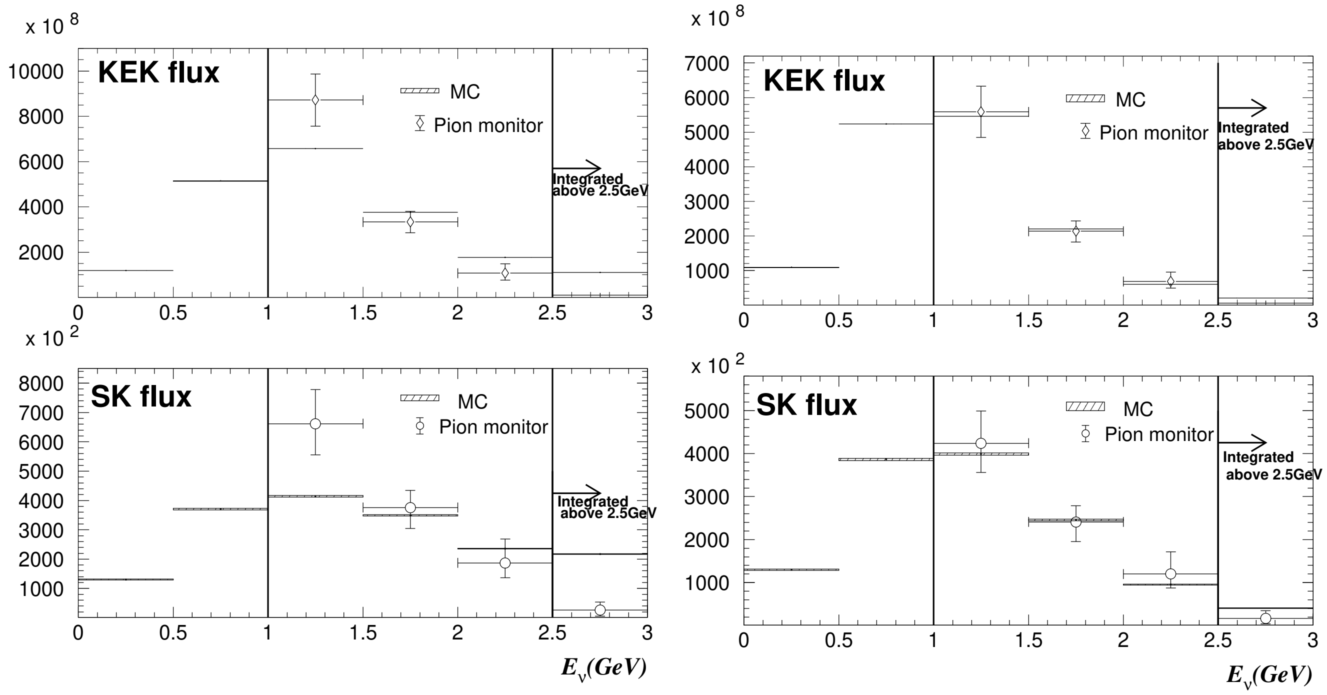

Figure 7.30: Reconstructed neutrino energy using fitted answer of pion kinematics. Full MC results are overlaid. (June) Left: Comparison with GCALOR/FLUKA model full MC, Right: Comparison with Cho model full MC

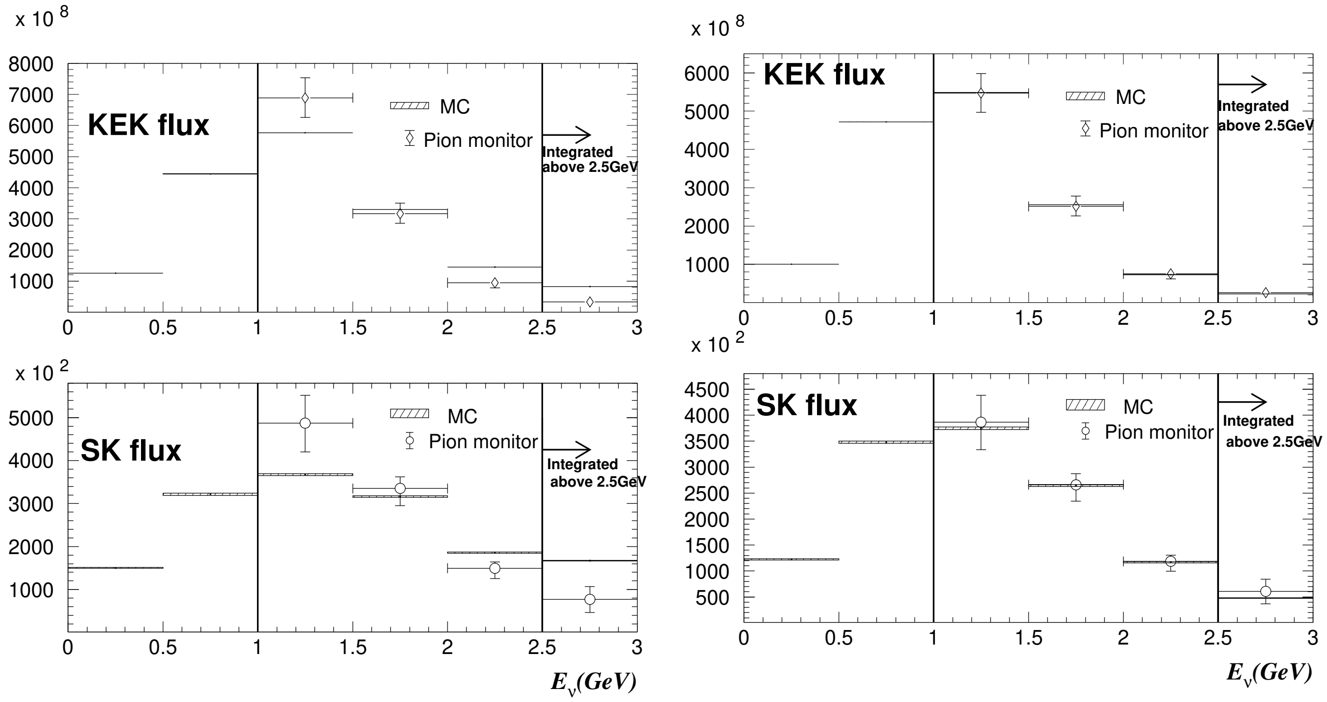

Figure 7.31: Reconstructed neutrino energy using fitted answer of pion kinematics. Full MC results are overlaid. (November) Left: Comparison with GCALOR/FLUKA model full MC, Right: Comparison with Cho model full MC

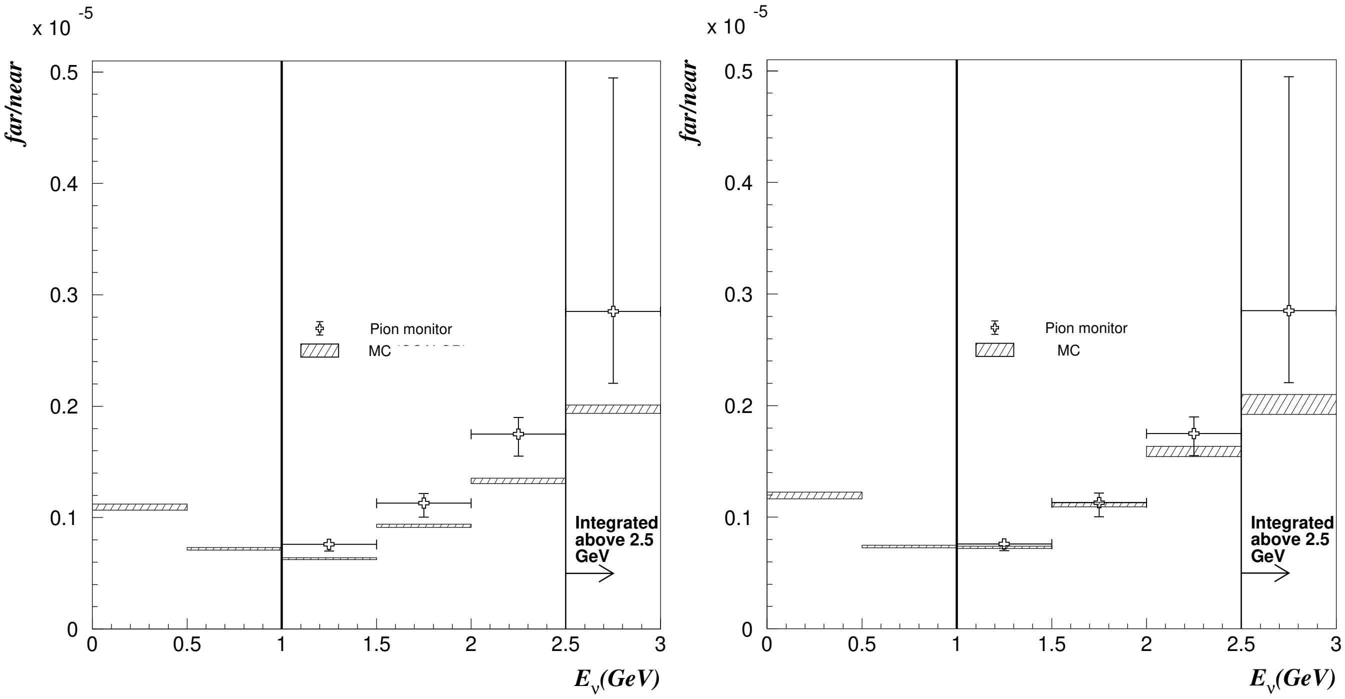

Figure 7.32: Neutrino spectrum ratio of (SK/KEK) using fitted answer of pion kinematics. MC results are overlaid. (June) Left: Comparison with GCALOR/FLUKA model beam MC, Right: Comparison with Cho model beam MC

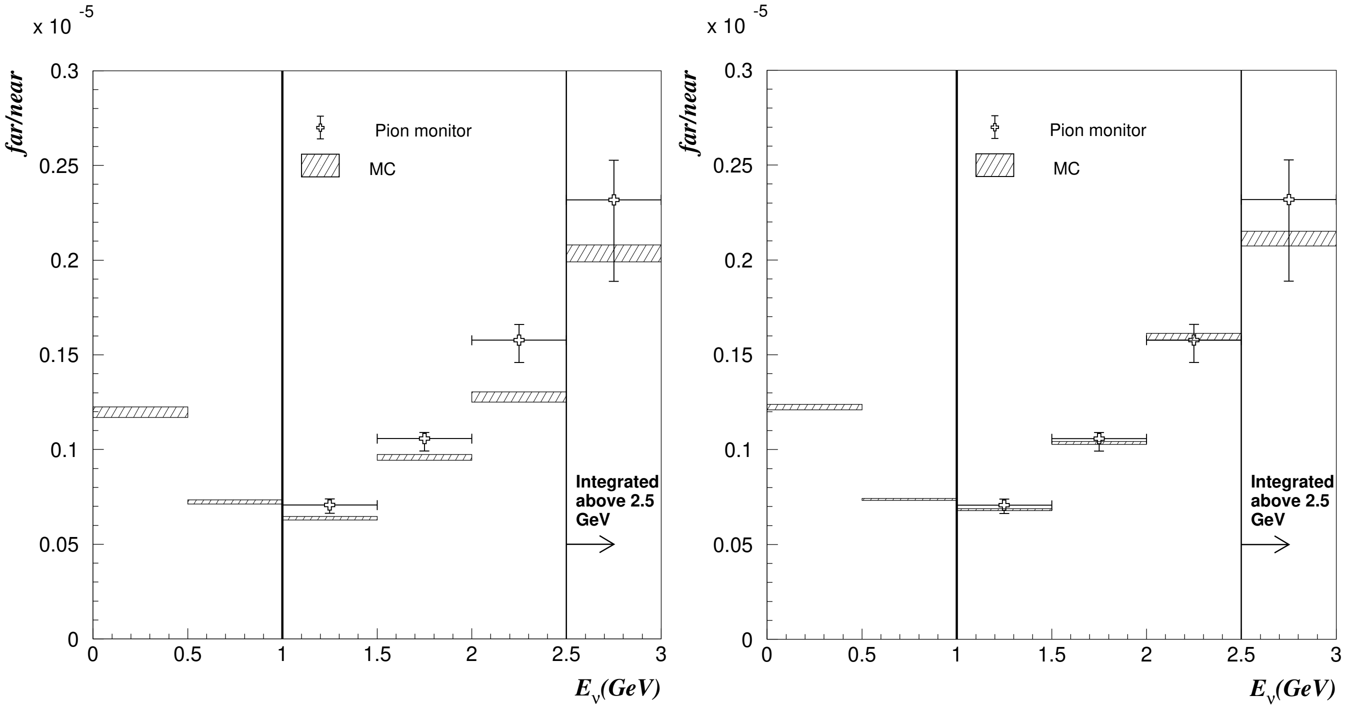

Figure 7.33: Neutrino spectrum ratio of SK(far)/KEK(near) using fitted answer of pion kinematics. MC results are overlaid. (November) Left: Comparison with GCALOR/FLUKA model beam MC, Right: Comparison with Cho model beam MC

is integrated. Unit of these values is number of neutrinos/cm^2/10^{20}POT.

		0.0-0.5GeV	0.5-1.0GeV	1.0-1.5GeV	1.5-2.0GeV	2.0-2.5GeV	>2.5GeV
June	spectrum (KEK)	1.12×10^{11}	4.81×10^{11}	5.27×10^{11}	2.05×10^{11}	6.64×10^{10}	6.68×10^{9}
	spectrum (SK)	1.39×10^{5}	3.85×10^{5}	4.22×10^{5}	2.40×10^{5}	1.19×10^{5}	1.81×10^{4}
	ratio (far/near)	1.25×10^{-6}	7.99×10^{-7}	8.00×10^{-7}	1.17×10^{-6}	1.79×10^{-6}	2.72×10^{-6}
Nov.	spectrum (KEK)	9.50×10^{10}	4.34×10^{11}	5.16×10^{11}	2.42×10^{11}	7.13×10^{10}	3.00×10^{10}
	spectrum (SK)	1.24×10^{5}	3.47×10^{5}	3.86×10^{5}	2.65×10^{5}	1.16×10^{5}	6.63×10^{4}
	ratio (far/near)	1.31×10^{-6}	8.00×10^{-7}	7.48×10^{-7}	1.10×10^{-6}	1.63×10^{-6}	2.21×10^{-6}

Table 7.2: Measured neutrino flux by the pion monitor above 1GeV and MC simulated neutrino flux below 1GeV.

7.3.8 Comparison of Cherenkov Photon Distributions between Pion Monitor Measurement and MC Simulation

We also compare the data of the pion monitor with the simulation results of photon distributions at the PMT array, directly. Figs. 7.34, 7.35(June), 7.36 and 7.37 (Nov.) show these comparisons, which used a hadron model of Cho or FLUKA/GCALOR, respectively.

Here we do not discuss quantitatively, for example χ^2 between data and MC because MC tuning is not the purpose for this thesis. However we can clearly see MC using Cho model is closer to the data.

7.4 Systematic Error on Pion Monitor Analysis

Systematic errors of the pion monitor analysis are summarized in table 7.3.

Errors	
From detector	PMT saturation correction PMT relative gain correction Mirror reflectivity Refractive index measurement Wave length dependence of refractive index
From beam	Difference between low and high beam intensity Pion monitor alignment and injection point of protons Beam stability during pion monitor measurement Azimuthal angular symmetry of magnetic field inside horn magnets
From analysis	Subtraction of light component originating from background radiation field Subtraction of Cherenkov light from Electro-magnetic shower Fitting method Pion beam profile dependence of fitting function Pion decay before pion monitor Pion beam profile dependence of pion absorption in wall Bin size of pion kinematics

Table 7.3: Systematic errors on Pion Monitor analysis

7.4.1 Detector Related Issues

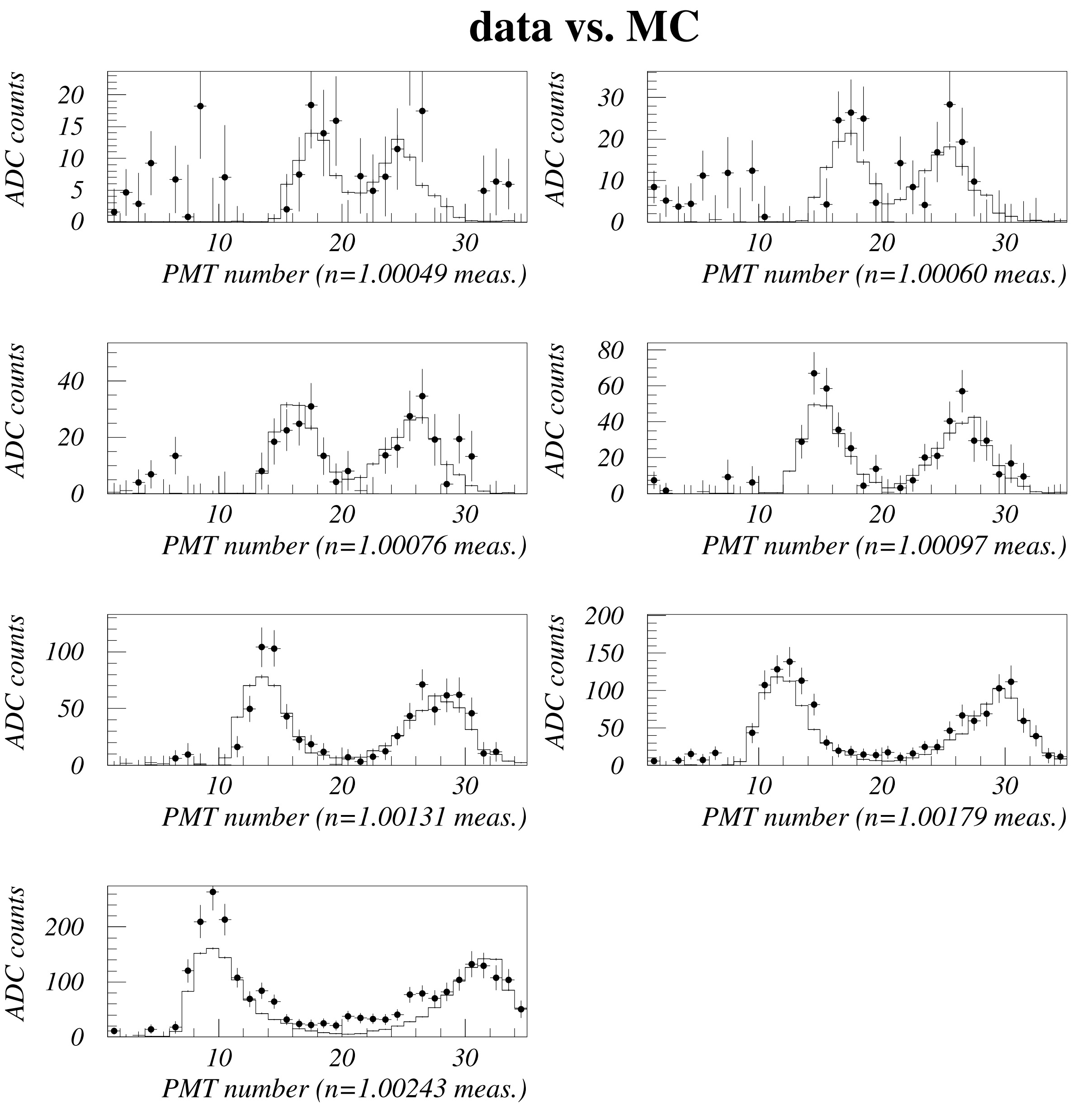

Figure 7.34: Background subtracted photon distributions data vs. MC based on the Cho model(June)

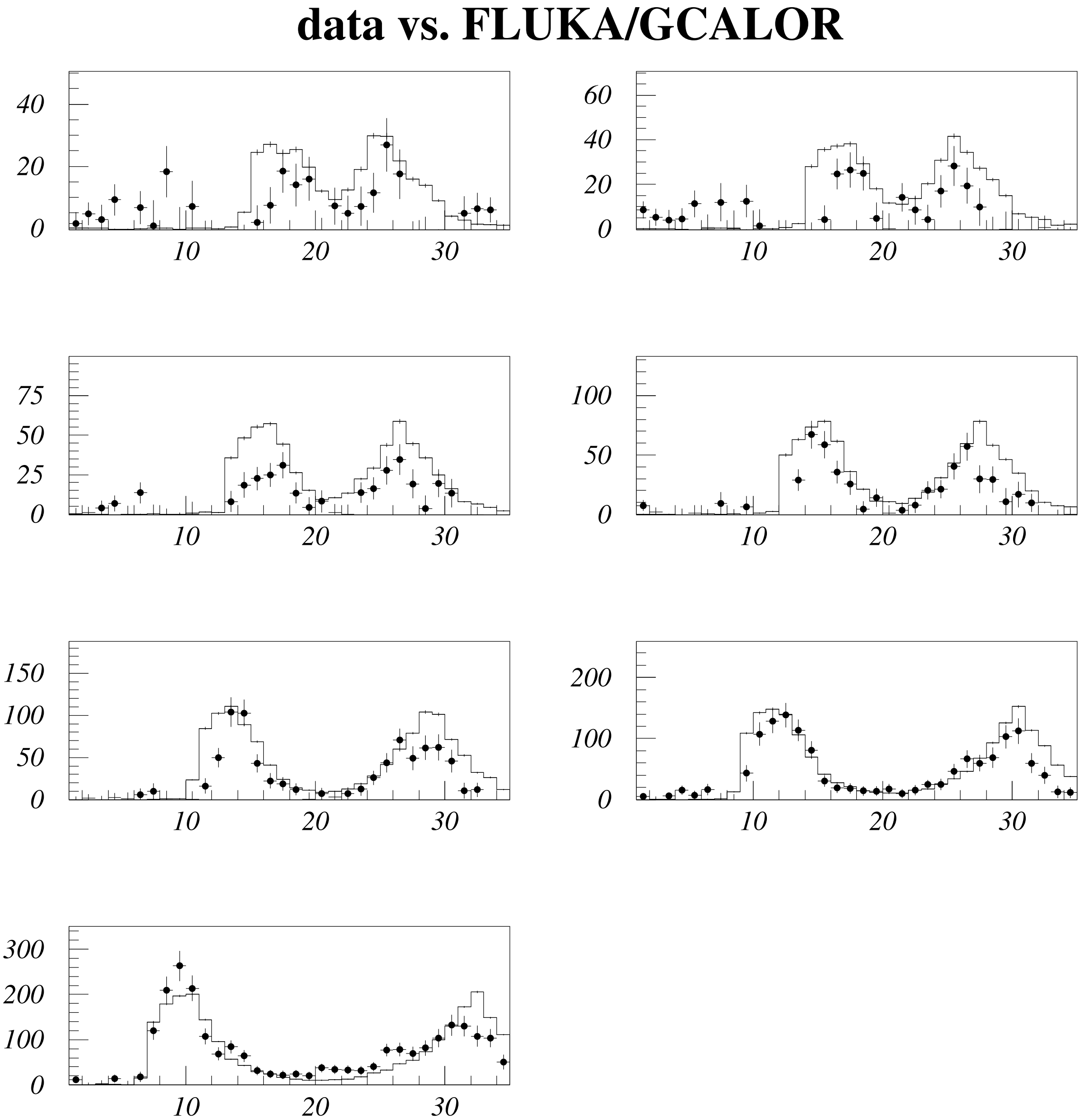

Figure 7.35: Background subtracted photon distributions data vs. MC based on the FLUKA/GCALOR model (June)

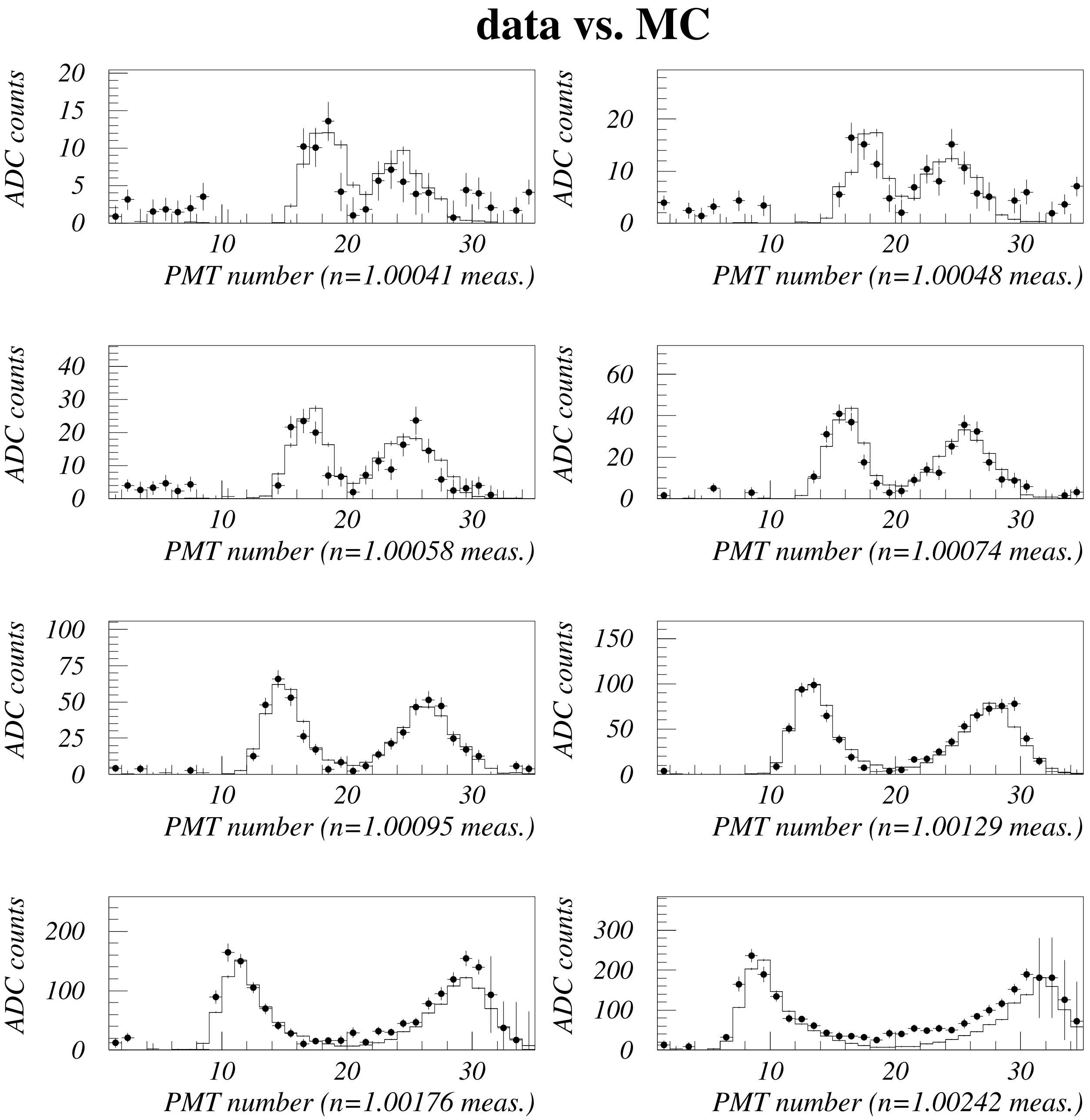

Figure 7.36: Background subtracted photon distributions data vs. MC based on the Cho model(November)

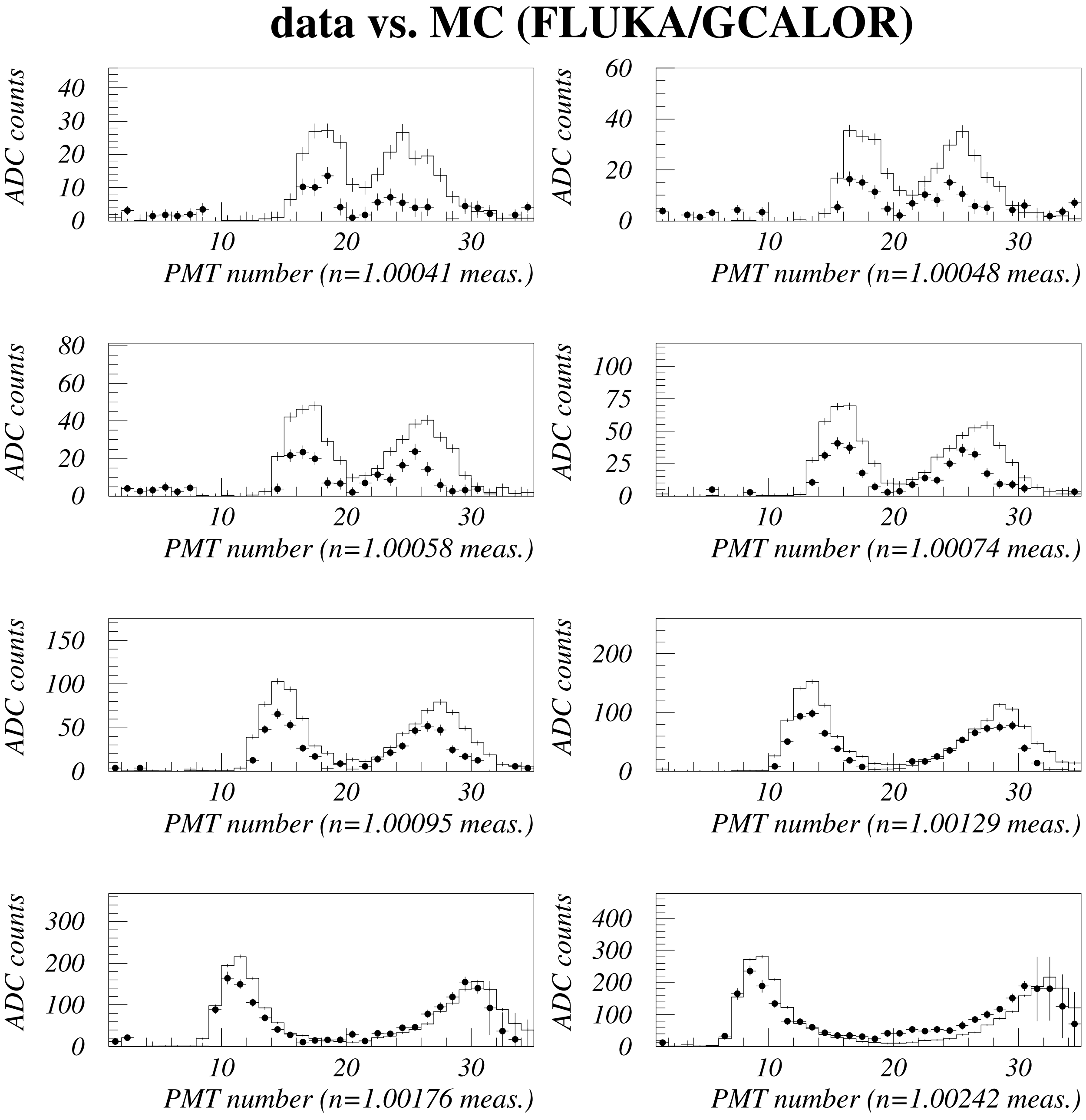

Figure 7.37: Background subtracted data vs. FLUKA/GCALOR model used MC (November)

PMT Saturation Correction

The PMT saturation correction was performed only for the June data. Some PMTs have 4% level uncertainty coming from the fitting of correction functions. The procedure to estimate the error coming from this is as follows;

1. Measured ADC counts of each PMT is fluctuated according to Gaussian distribution, which has parameters of the error of saturation correction. i.e.: if correction uncertainty is 4%, the standard deviation of the Gaussian used in the fluctuation is 4%.
2. The fit to reconstruct the pion population is applied.
3. Neutrino spectrum is reconstructed using the fitting answer.

We changed the ADC value of each PMT for 100 times. Therefore, we get 100 different neutrino spectrums and their ratios. We defined the error as RMS of that difference in each energy bin. Table. 7.4 summarized this result.

	1.0-1.5GeV	1.5-2.0GeV	2.0-2.5GeV	>2.5GeV
spectrum (KEK)	±0.5%	±1.2%	±1.4%	±30%
spectrum (SK)	±0.8%	±1.2%	±2.0%	±20%
ratio (far/near)	±0.6%	±0.5%	±1.3%	±4.2%

Table 7.4: Systematic error from the PMT saturation (June)

Relative Gain Correction of PMTs

This error is already included in the error bar when we reconstruct the pion kinematics in the standard analysis. Therefore figures in the analysis section have already taken this into account like Fig. 7.27 and so on.

We calibrated the relative gain of each PMT using the Xe lamp as described in chapter 4. In addition to this calibration, we checked the gain ratio of the neighboring PMTs by moving the PMT array. We compared these results. (Fig. 7.38)

In this figure, the horizontal axis means the gain ratio of the neighboring PMTs, ((i-1)th PMT/ ith PMT). As explained in chapter 4, we estimate the error of this constant to be 10%. In the gain ratio obtained by the Cherenkov light, the error comes from the beam intensity or the PMT signal fluctuation. These methods are reasonably consistent each other.

Mirror Reflectivity

This is not corrected in the standard analysis. The laser calibration system shows that the reflectivity of the spherical mirror is stable within ± 6% during 1999 run. Systematic uncertainty coming from this was estimated by the pion monitor MC simulation. In the MC, we change the reflectivity of the mirror using the results of the laser calibration, then we fit the Cherenkov light distribution.

Table 7.5 describes errors in June and November.

Laser data showed the reflectivity of the top part of the mirror became worse (a few percents). This local damage causes dominant part of this error since the local damage produces the profile dependence of pions.

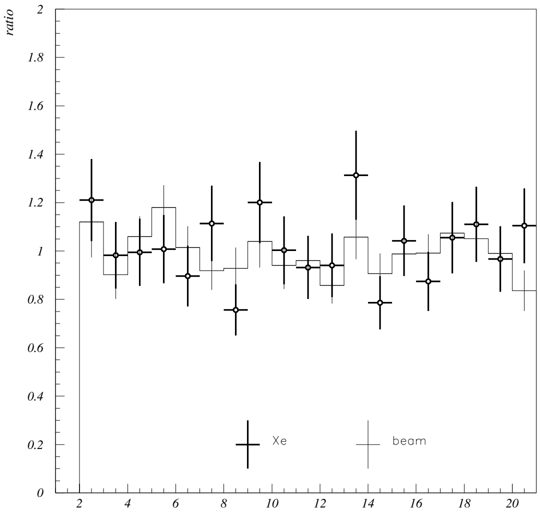

Figure 7.38: Relative gain ratio of the neighboring PMTs, ((i-1)th PMT/ ith PMT), obtained by the Xe lamp and the beam method.

		1.0-1.5GeV	1.5-2.0GeV	2.0-2.5GeV	>2.5GeV
June	spectrum (KEK)	-1.4%	+4.2%	-3.5%	-8.7%
	spectrum (SK)	-1.6%	+3.1%	—	-9.0%
	ratio (far/near)	—	+0.4%	+3.5%	—
Nov.	spectrum (KEK)	-2.0%	+2.9%	+3.4%	+0.6%
	spectrum (SK)	-3.1%	+1.8%	+4.0%	—
	ratio (far/near)	1.2%	-1.1%	+0.5%	—

Table 7.5: Systematic error from changing the reflectivity of the spherical mirror.

Refractive Index Measurement

Cherenkov photon distributions from protons was measured to calibrate the refractive index, hence we could determine it accurately, i.e. $\Delta n/(n-1) \sim 0.3\%$. Thus the systematic error comes from the error of refractive index is negligibly small. The linearity between gas pressure and refractive index was guaranteed by the interferometer system. Temperature was same within ± one degree during the pion monitor run and gives negligibly small error.

Wavelength dependence of Refractive Index

This effect is not corrected in the standard analysis. The refractive index of the gas used in the pion monitor measurement(C318) has the wavelength dependence like Fig. 7.39 ([79])

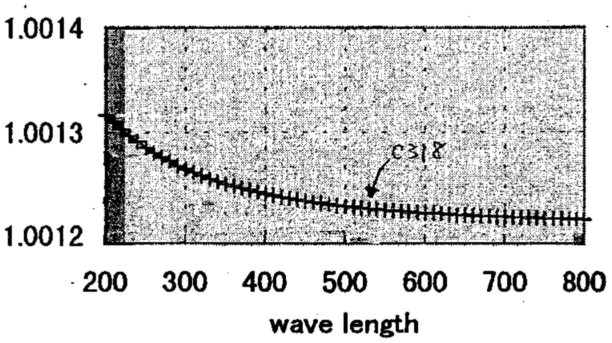

Figure 7.39: Wavelength dependence of the refractive index of the gas used in the pion monitor. The horizontal axis shows the wavelength(nm) and the vertical axis shows the refractive index.

This means that Cherenkov light with different wavelength has a different Cherenkov angle.

To estimate the systematic error from this, we made MC simulation including them. Since quartz window is transparent for shorter wavelength range photons ($\lambda > 160$ nm), the relationship shown in Fig. 7.39 was extrapolated down to 160 nm by eye. We employed the quantum efficiency of PMTs given in the specification. The pion reconstructed data with this MC are compared with the standard one. These difference are quoted as error. Table 7.6 summarizes the systematic errors coming from this.

	1.0-1.5GeV	1.5-2.0GeV	2.0-2.5GeV	>2.5GeV
spectrum (KEK)	-5.1%	+7.3%	+4.6%	+37%
spectrum (SK)	-8.6%	+5.4%	+1.1%	+33%
ratio (far/near)	-3.7%	-1.8%	+3.3%	-2.6%

Table 7.6: Systematic errors from the wavelength dependence of the gas (November).

7.4.2 Proton Beam Related Issues

Difference between Low and High Beam Intensity

This effect is not corrected in the standard analysis. A main difference between the high intensity run (normal data taking) and the low intensity run (pion monitor run) is the proton beam profiles and divergences. Typical proton profiles during the pion monitor measurement are shown in Figs. 7.40(June) and 7.41(November).

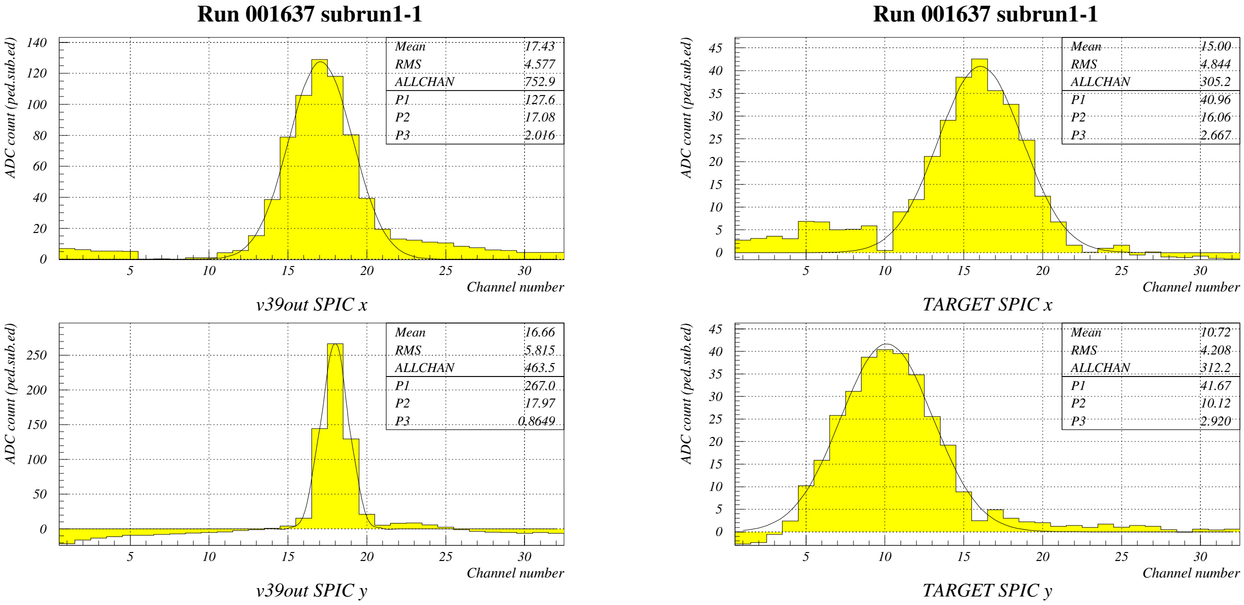

Figure 7.40: Proton beam profiles at the SPICs during the pion monitor data taking. Left: proton profile at V39out, Right: at TARGET (June)

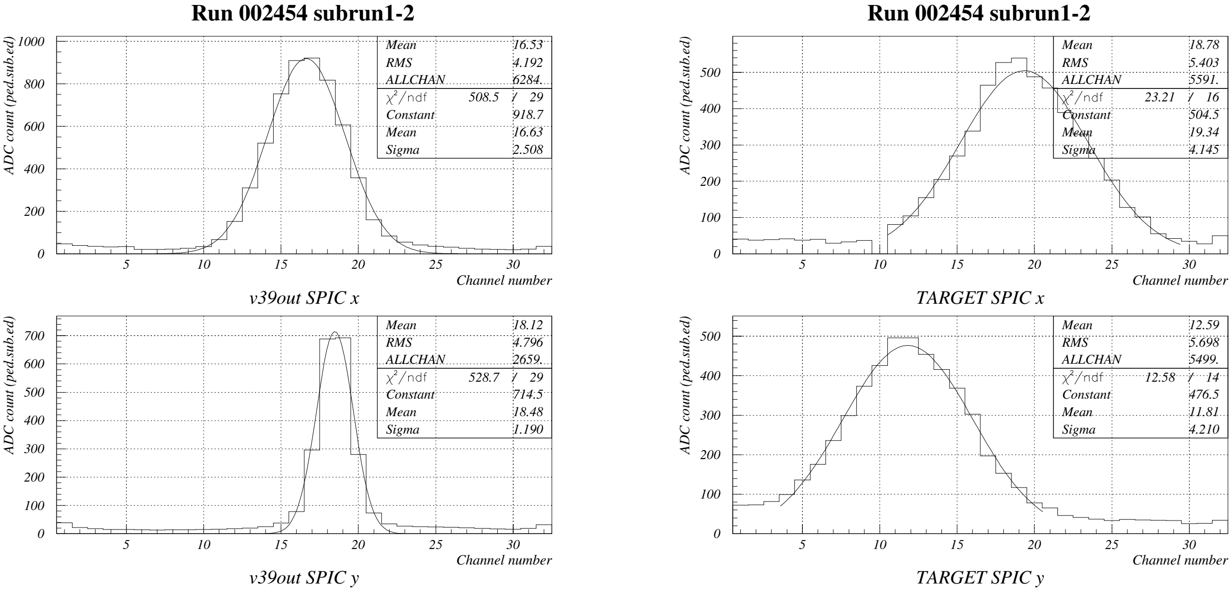

Figure 7.41: Proton beam profiles from the SPICs at the pion monitor data taking. Left: proton profile at V39out, Right: at TARGET (November)

Comparing these profiles to Figs. 5.3 and 5.6, fitted sigma by Gaussian at each SPIC in low intensity run is smaller than that of high intensity run. Particularly in June, this tendency is clearly seen.

In order to check the production rate of secondary particles at these proton profiles (targeting efficiency), we plot the CT and the muon monitor (Si detector) data in Fig. 7.42. This figure is same as Figs. 6.13 and 6.14 except the point that this includes the data points which are cut in the normal analysis. In June data, we see better targeting efficiency during the pion monitor run than the normal run by ~30%. On the other hand, the targeting efficiency is same in November data. There are some dropped points during 6600~7200 of the horizontal axis, the pion monitor run, but this is due to downs of the current supplied to the horn magnets and not used in the analysis. We are convinced this profile difference gives no effect in November.

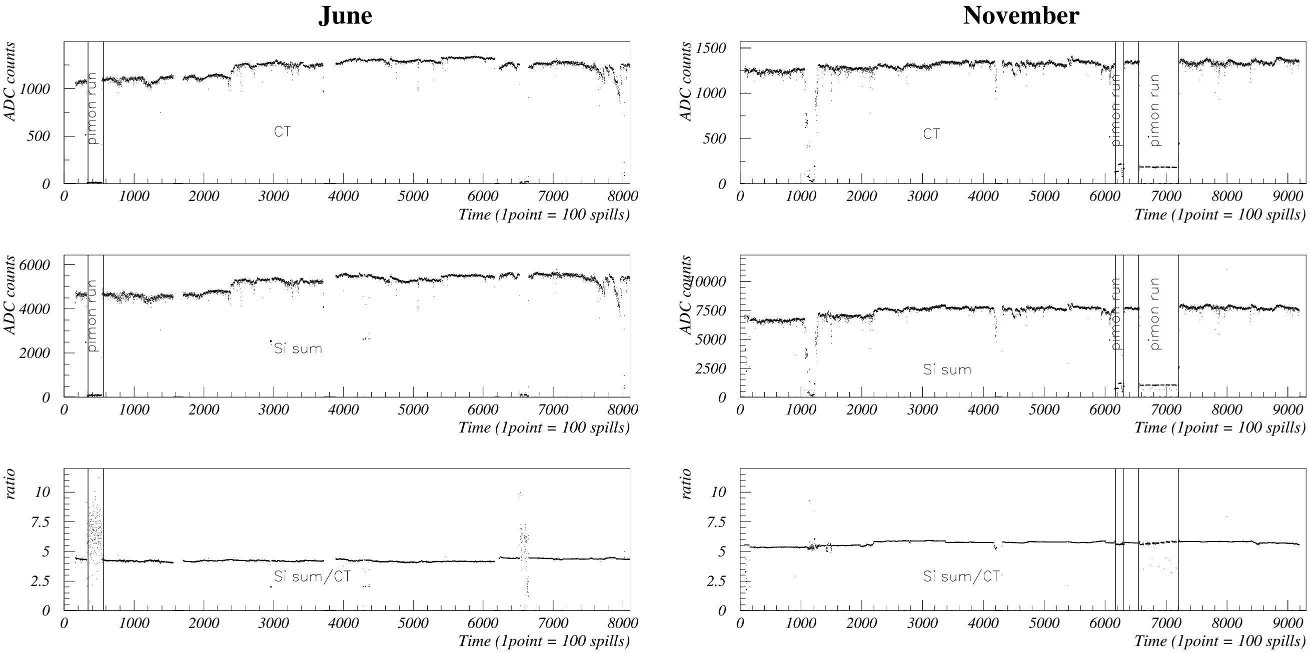

Figure 7.42: ADC counts of the CT and the muon monitor (Si detector) both in the high intensity and the low intensity

We estimate only high energy component of the secondary particles from the muon data. According to the MC simulation, proton beam profiles affect the yield of the higher energy secondary particles. The narrower proton profiles give the larger secondary particle yields. The MC simulation predicts ~30% larger muon yield in June. This reproduces the tendency of the targeting efficiency during June run well. We do not correct for this but use MC spectrum difference between the normal run and the pion monitor run as the systematic error.

Table 7.7 summarizes the systematic error.

Alignment of Pion Monitor and Injection Position of Proton Beam with respect to Target

This is not corrected in the standard analysis.

It is important to align the pion monitor along the beam line since mirror acceptance is sensitive to the beam center. The pion monitor was well aligned using laser optics system; the height of the mirror was aligned within 1mm, the horizontal position can be known using the position meter within a few hundred μm. Systematic error from this is negligibly small.

The injection point of the proton beam also causes the systematic error since this changes the pion profile center after the 2nd horn. MC study was performed to estimate this effect. In this study,

		1.0-1.5GeV	1.5-2.0GeV	2.0-2.5GeV	>2.5GeV
June	spectrum (KEK)	-5.5%	±1.0%	+10.0%	+7.0%
	spectrum (SK)	-7.0%	-6.5%	+4.5%	+6.5%
	ratio (far/near)	-6.0%	-5.3%	-6.6%	±0.5%
Nov.	spectrum (KEK)	-1.2%	+0.6%	+4.0%	+5.0%
	spectrum (SK)	-2.1%	-1.5%	+3.1%	+7.8%
	ratio (far/near)	-1.9%	-3.7%	-1.9%	+2.9%

Table 7.7: Systematic error from the beam parameter difference between the high intensity and the low intensity.

the measured injection position is used (Figs. 7.40 and 7.41). Table 7.8 summarizes the results.

		1.0-1.5GeV	1.5-2.0GeV	2.0-2.5GeV	>2.5GeV
June	spectrum (KEK)	-1.5%	+6.8%	-10.0%	+8.9%
	spectrum (SK)	-2.5%	+9.1%	-10.0%	+3.6%
	ratio (far/near)	-1.0%	+2.1%	-0.6%	-4.9%
Nov.	spectrum (KEK)	—	-2.0%	—	-4.8%
	spectrum (SK)	—	—	—	-4.9%
	ratio (far/near)	—	+1.2%	—	—

Table 7.8: Systematic errors from ambiguity of the proton beam injection point using MC study

Beam Stability during Pion Monitor Measurement

The beam stability during the pion monitor run is checked using SPICs and muon monitors. Figs. 7.43 and 7.44 show the stability of the fitted center of the primary protons measured by V39out and TARGET SPICs in June and November, respectively.

Both monitors show the primary proton beam is quite stable. The RMS of the time projections which means the stability of beam center are summarized in Table 7.9.

	V39out SPIC (x)	V39out SPIC (y)	TARGET SPIC (x)	TARGET SPIC (y)
June	3.6mm	0.25mm	0.20mm	0.60mm
November	0.17mm	0.13mm	0.077mm	0.084mm

Table 7.9: Proton beam stability during the pion monitor run.

As shown in Fig. 7.42, the targeting efficiency is quite stable during November run; the time projection of (muon yield/proton) during the pion monitor run shows that stability is 1.4%. The fitted center of muon profiles are also quite stable; stable within ±1 cm. In June, we use large Si pads to check the stability since small Si pads did not have enough charges (Fig. 7.45). Fitted center of muon monitor is stable (within 8cm), and intensity is also stable (sigma/mean = 4.6%).

Monitors on primary protons and secondary muons show that the beam stability is totally good during the pion monitor data taking.

We fluctuated the proton injection points in the MC simulation according to Table 7.9 for the systematic error estimation. Table 7.10 summarizes this error.

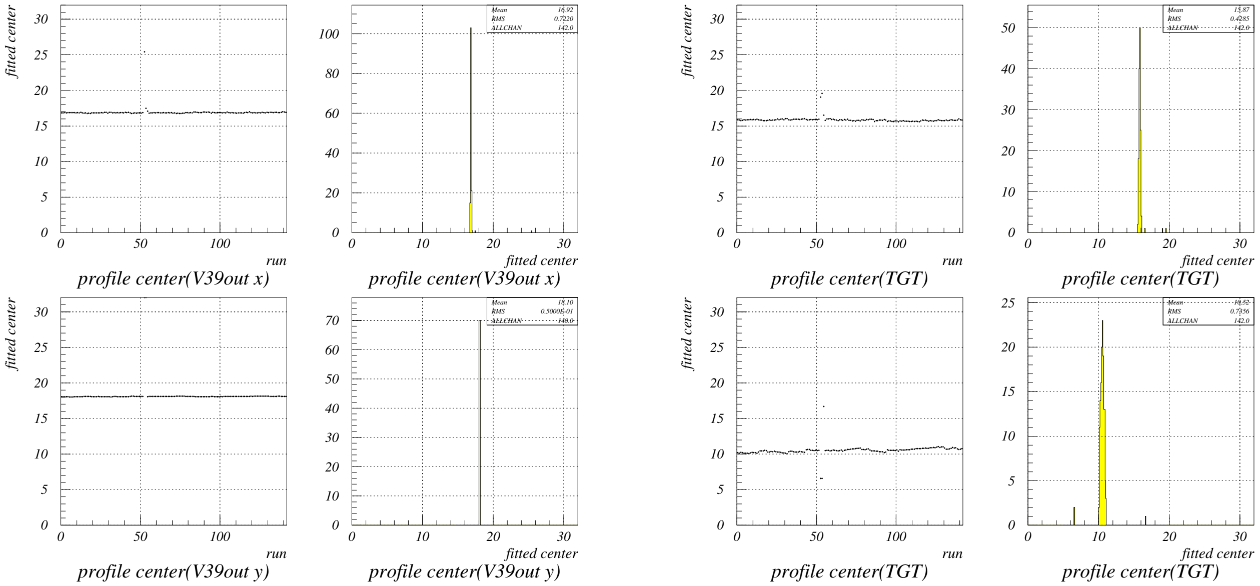

Figure 7.43: Stability of the primary proton beam center during the pion monitor run measured by SPICs (June). Left: V39out center, time variation and its projections. Right: TARGET center. It seems that some points totally break the stability, but there are no beams during those points.

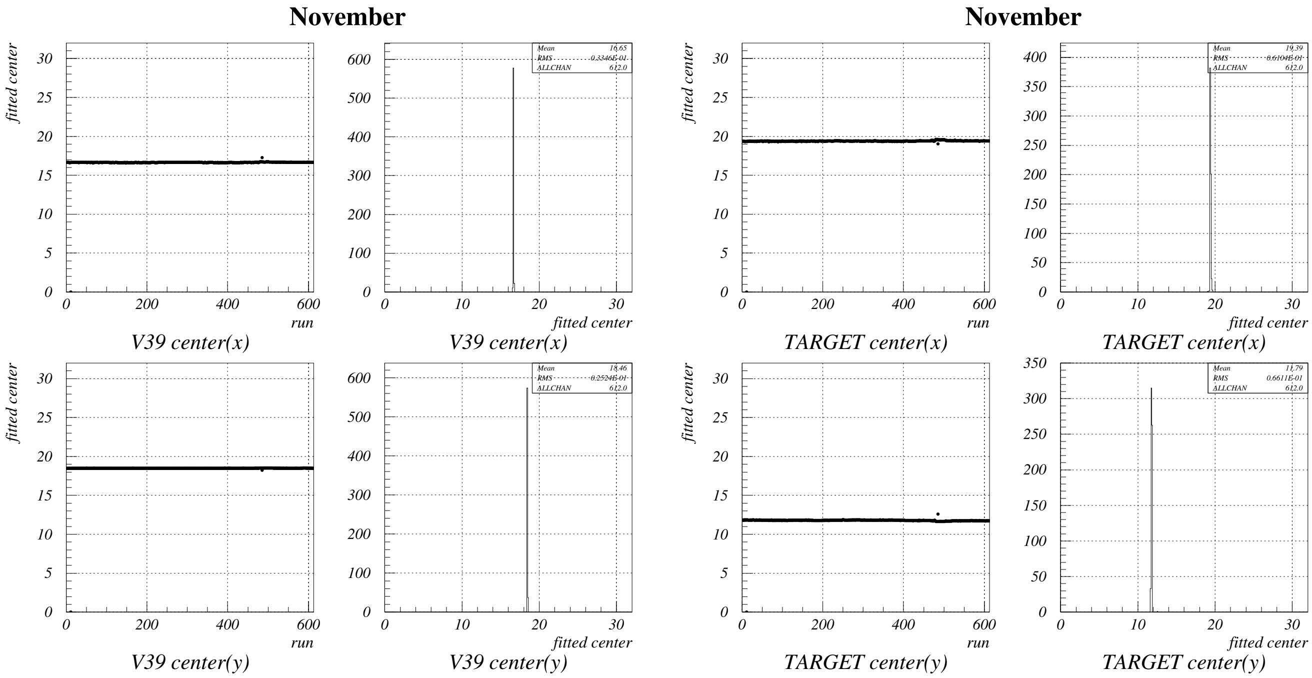

Figure 7.44: Stability of the primary proton beam center during the pion monitor run measured by SPICs (November). Left: V39out center, the time variation and its projections. Right: TARGET center.

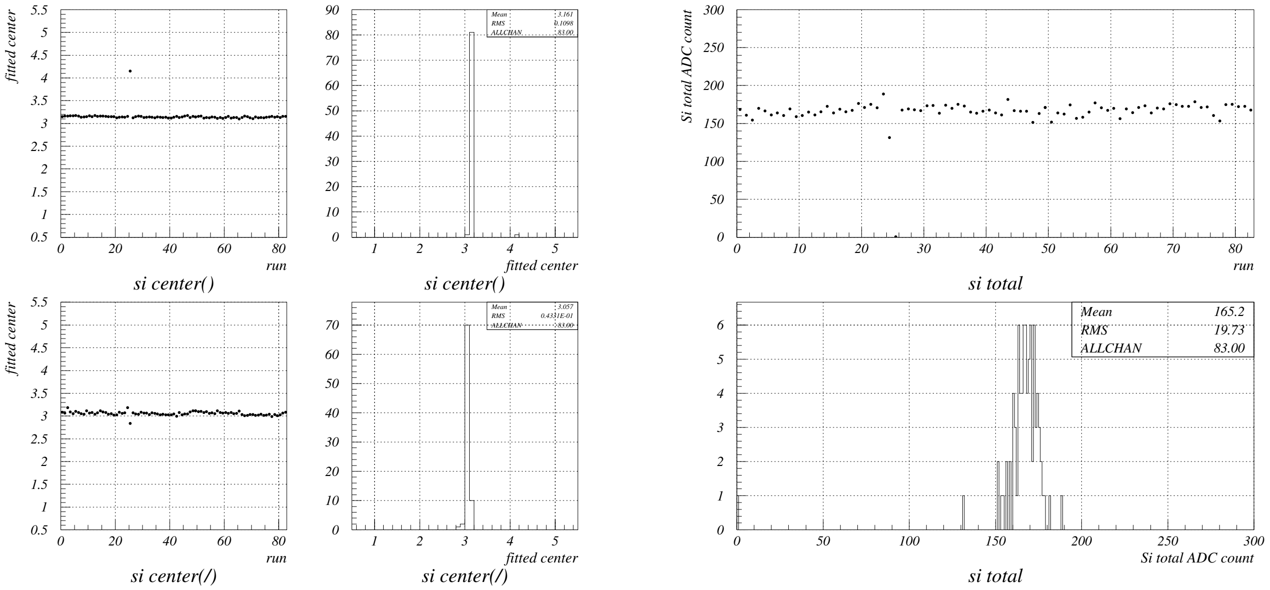

Figure 7.45: Muon monitor (large Si pad) stability during the pion monitor run (June). Left 4 figures: the time variation of the center of the large Si pads, which are installed diagonally in the muon pit. Right 2 figures: time variation of the total ADC count of the large Si pad detectors and the projection

		1.0-1.5GeV	1.5-2.0GeV	2.0-2.5GeV	>2.5GeV
June	spectrum (KEK)	±1.9%	±4.3%	±5.0%	±12.7%
	spectrum (SK)	±3.2%	±3.7%	±5.0%	±12.5%
	ratio (far/near)	±1.6%	±1.5%	±3.4%	±1.1%
Nov.	spectrum (KEK)	—	—	—	±5.5%
	spectrum (SK)	—	—	—	±4.8%
	ratio (far/near)	—	—	—	±0.5%

Table 7.10: Systematic error from the beam stability in the pion monitor data taking

Azimuthal Angular Symmetry of Magnetic Field inside Horn Magnets

This is not corrected in the standard analysis. We have some uncertainties if the horn magnetic field has an asymmetry in the azimuthal angular direction because the shape of the pion monitor mirror assume the symmetry of that direction.

As shown in Fig. 3.9, we found asymmetric magnetic field in the real case. However, we cannot exclude no asymmetric field case since this measurement has large systematic errors. We define the systematic error from this as the difference between the symmetric and asymmetric field cases. We input the magnetic field by amount of 15% shown in Fig. 3.9 for both horns in the MC. We compare fitted results of the standard and changed magnetic field cases. Table 7.11 summarizes this estimation.

		1.0-1.5GeV	1.5-2.0GeV	2.0-2.5GeV	>2.5GeV
June	spectrum (KEK)	-2.9%	-0.9%	+32.6%	-19.0%
	spectrum (SK)	-2.4%	-7.5%	+38.8%	-10.7%
	ratio (far/near)	+0.5%	+2.1%	-0.6%	+9.4%
Nov.	spectrum (KEK)	-3.6%	+5.2%	+0.7%	+10.6%
	spectrum (SK)	-5.7%	+2.5%	-0.7%	+9.8%
	ratio (far/near)	-2.6%	-2.4%	-2.4%	-1.0%

Table 7.11: Systematic error from the horn magnetic field asymmetry

7.4.3 Analysis Method Related Issues

Subtraction of Light Component Originating from Background Radiation Field

The mirror angle was changed to subtract the light component originating from background radiation field, as shown in Fig. 7.15. This angle difference might cause different background shapes if the dominant background would be created by the interaction between the mirror and the beam. In order to check the mirror angle dependence of the background shape, we check the ADC count of a PMT vs mirror angle. Fig. 7.46 shows the ADC counts of the PMT#11 as the function of the mirror angle. The horizontal axis of this figure corresponds to the mirror angle, which was changed from -0.25°to 14.5° in this figure.

This figure guarantees the background level is constant from 8.0° to 14.5° because we changed it like -0.25° → 14.5° → 8.0°. This situation is same for all PMTs. We conclude that the shape of the background is independent of the mirror angle. We estimate this error is negligibly small.

Subtraction of Cherenkov Light from Electro-magnetic Shower

We define the subtraction error to be the absolute normalization error since the shape of Cherenkov photon distribution from the electromagnetic components is well reproduced by MC simulations. The normalization factor of electromagnetic components of the MC simulation was determined as explained before. For the error estimation, we changed this factor by $\pm 1\sigma$ using χ^2 between the data at the lowest refractive index and the MC simulation. Table 7.12 shows the systematic error employing this method for June data. This error is negligibly small in November.

Fitting Method

To study this error, we performed the MC test based on two different pion production models. One is GCALOR and the other is Cho. Further, we use MC simulation with different currents supplied to the horn magnets. We had several MC sets for this study. Some parts of this test are already

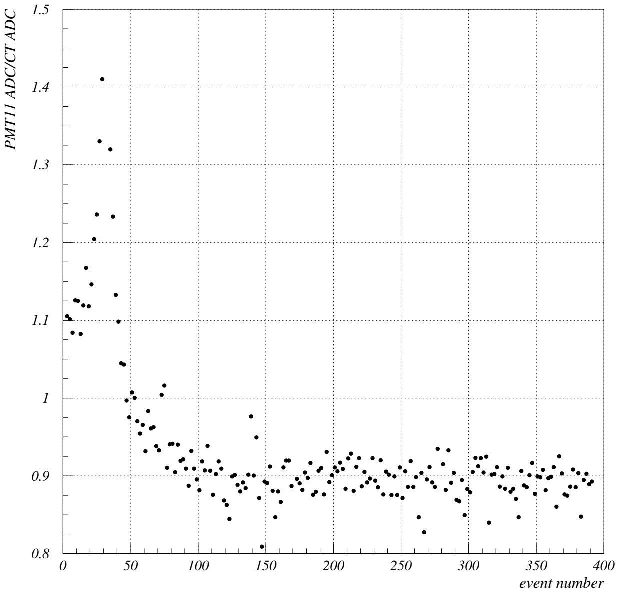

Figure 7.46: Mirror angle scan. The horizontal axis is event number, which corresponds to the mirror angle. The vertical axis is PMT#11 ADC count normalized by CT. The mirror angle was changed from -0.25 to 14.5 degree. The peak corresponds to the pion ring.

	1.0-1.5GeV	1.5-2.0GeV	2.0-2.5GeV	>2.5GeV
spectrum (KEK)	—	—	—	-74%
spectrum (SK)	—	—	—	-60%
ratio (far/near)	—	—	—	+72%

Table 7.12: Systematic error from the electro-magnetic component subtraction (June).

shown in chapter 7. According to this MC test, we regard the largest difference between the predicted neutrino flux employing the pion monitor and beam MC true as the systematic error.

The results of this study are shown in table 7.13.

	1.0-1.5GeV	1.5-2.0GeV	2.0-2.5GeV	>2.5GeV
spectrum (KEK)	+6.8%	-7.7%	-15.3%	$^{+12\%}_{-21\%}$
spectrum (SK)	+11%	-10.2%	-12.3%	$^{+1.6\%}_{-32\%}$
ratio (far/near)	+4.0%	$^{+1.4\%}_{-3.0\%}$	$^{+3.2\%}_{-4.6\%}$	-14.5%

Table 7.13: Systematic error from the fit method using MC study

Pion Beam Profile Dependence on Fitting Function

The answer of the pion population on the kinematic region can vary if pion profiles (pion radial distribution) would change the fitting functions, i.e. the Cherenkov light distribution of each kinematic bin. However, we found this error to be negligibly small from the estimation using the different hadron models. These models give almost same pion profiles after the 2nd horn in addition to the property of the spherical mirror.

Pion Decay before Pion Monitor

There are pions which decay before the pion monitor. It is sure that this also contributes to the neutrinos flux. This must be corrected using MC since the pion monitor cannot predict it. This effect is actually corrected in the standard analysis.

The difference of the correction of the two hadron production models (Cho and GCALOR) is taken as the error and is summarized in table 7.14.

		1.0-1.5GeV	1.5-2.0GeV	2.0-2.5GeV	>2.5GeV
June	spectrum (KEK)	±0.9%	±1.9%	±2.8%	±1.3%
	spectrum (SK)	±2.3%	±5.7%	±6.3%	—
	ratio (far/near)	±1.4%	±3.8%	±3.4%	±1.6%
Nov.	spectrum (KEK)	—	±0.8%	±0.5%	—
	spectrum (SK)	±0.5%	±1.5%	±1.1%	—
	ratio (far/near)	±0.7%	±0.7%	±1.7%	±0.5%

Table 7.14: Systematic error from the pion decay before the pion monitor.

Pion Beam Profile Dependence of Pion Absorption in Wall

Some pions are absorbed in the wall of the decay pipe. This probability mainly depends on the angle of the pions, but the profiles of pions also affects a little. We estimate the systematic error from this using the different profiles with the different hadron models; in the reconstruction from the pion kinematics to the neutrino energy, we use a different spatial population of pions as start point of decay. Table. 7.15 describes this difference.

Here we have larger error than the pion profile dependence of the fitting function. This is because the Cherenkov ring image reflected by the spherical mirror is independent of the pion radial distribution.

		1.0-1.5GeV	1.5-2.0GeV	2.0-2.5GeV	>2.5GeV
June	spectrum (KEK)	—	—	±2.3%	±20%
	spectrum (SK)	—	—	±1.4%	±21%
	ratio (far/near)	—	—	±1.0%	±7.2%
Nov.	spectrum (KEK)	±0.5%	±1.0%	±4.3%	±20%
	spectrum (SK)	±0.5%	±0.5%	±3.1%	±10%
	ratio (far/near)	—	±0.5%	±1.3%	±8.5%

Table 7.15: Systematic error from the pion beam profile dependence of the pion absorption in the wall.

Bin Size of Pion Kinematics

We assume the pion population inside the kinematic bin to be flat in the pion monitor analysis. There is the structure inside the bin in the actual case. Comparing the beam MC true and reconstructed neutrino flux using the flat bins, we estimated the error coming from this effect. (Table. 7.16)

		1.0-1.5GeV	1.5-2.0GeV	2.0-2.5GeV	>2.5GeV
June	spectrum (KEK)	+2.0%	-2.7%	-7.2%	-1.3%
	spectrum (SK)	+1.4%	-2.7%	-7.4%	-13%
	ratio (far/near)	-0.6%	—	—	-13%
Nov.	spectrum (KEK)	+2.7%	-2.4%	-7.0%	-10%
	spectrum (SK)	+0.5%	-2.4%	-5.4%	-15.4%
	ratio (far/near)	-2.1%	—	+1.7%	-7.1%

Table 7.16: Systematic error from the bin size of the pion kinematic region.

7.4.4 Stability of Proton Beam

We also checked the stability of the proton beam during the normal neutrino run using two SPICs and muon monitors. As already shown in Figs. 6.6, 6.13 and so on, the muon monitors show the stability of the beam used in the analysis are good. However, the injection point with respect to the target and profiles of the proton beam was a little bit changed. The systematic errors coming from this instability are summarized in table 7.17. They are estimated employing the MC simulation.

		1.0-1.5GeV	1.5-2.0GeV	2.0-2.5GeV	>2.5GeV
June	spectrum (KEK)	—	—	+0.8%	$^{+3.8\%}_{-3.2\%}$
	spectrum (SK)	+1.2%	-1.9%	$^{+1.8\%}_{-1.0\%}$	$^{+4.2\%}_{-4.3\%}$
	ratio (far/near)	+0.7%	-2.3%	$^{+0.9\%}_{-1.5\%}$	-3.4%
Nov.	spectrum (KEK)	±1.0%	$^{+1.0\%}_{-1.9\%}$	$^{+4.4\%}_{-1.1\%}$	$^{+6.3\%}_{-3.4\%}$
	spectrum (SK)	$^{+1.6\%}_{-2.1\%}$	-1.5%	$^{+4.1\%}_{-1.6\%}$	+16.0%
	ratio (far/near)	$^{+1.6\%}_{-1.8\%}$	$^{+1.5\%}_{-2.1\%}$	$^{+1.2\%}_{-1.4\%}$	+9.0%

Table 7.17: Systematic error from the beam stability during the normal data taking.

7.4.5 Uncertainty of Neutrino Flux below 1 GeV

The pion monitor cannot predict the neutrino flux below 1 GeV. We estimate the neutrino flux and their error using the beam MC. For the central value estimation, we use the formula 5.1 with the parameters of table 5.1. For the error estimation, we changed those parameters within 90% C.L. taking into account the results of various pion production experiments.

	0.0-0.5GeV	0.5-1.0GeV
ratio (far/near)	±9%	$^{+3.0\%}_{-10.0\%}$

Table 7.18: Systematic error of the neutrino flux below 1 GeV energy.

7.4.6 Summary of Systematic Errors

We summarized systematic errors which we mentioned above, in tables. 7.19, 7.20 and 7.21, and tables. 7.22, 7.23 and 7.24 for the June and November data, respectively.

Errors on spectrum at KEK (Jun)	0.0-0.5	0.5-1.0	1.0-1.5	1.5-2.0	2.0-2.5	>2.5GeV
Fitting error			±11.7%	±9.2%	±17.2%	+25.1%
PMT saturation correction			±0.5%	±1.2%	±1.4%	±30%
PMT relative gain correction			—	—	—	—
Mirror reflectivity			-1.4%	+4.2%	-3.5%	-8.7%
Refractive index measurement			—	—	—	—
Wave length dep. of the ref. index			—	—	—	—
Low and high beam intensity			-5.5%	±1.0%	+10.0%	+7.0%
Pion monitor alignment			—	—	—	—
Injection point of protons			-1.5%	+6.8%	-10.0%	+8.9%
Beam stability (pion monitor run)			±1.9%	±4.3%	±5.0%	±12.7%
Horn magnetic field uncertainty			-2.9%	-0.9%	+32.6%	-19.0%
Subtraction of BKG radiation component			—	—	—	—
Subtraction of EM shower component			—	—	—	-74%
Fitting method			+6.8%	-7.7%	-15.3%	$^{+12\%}_{-21\%}$
Pion beam profile (fitting function)			—	—	—	—
Pion decay before pion monitor			±0.9%	±1.9%	±2.8%	±1.3%
Pion Beam profile (pion absorption)			—	—	±2.3%	±20%
Bin size of pion kinematics			+2.0%	-2.7%	-7.2%	-1.3%
Beam stability (normal run)			—	—	+0.8%	$^{+3.8\%}_{-3.2\%}$
Total			$^{+13.9\%}_{-13.6\%}$	$^{+13.2\%}_{-13.3\%}$	$^{+39\%}_{-27\%}$	$^{+49\%}_{-88\%}$

Table 7.19: Systematic errors on Pion Monitor analysis (about neutrino spectrum at KEK) on June data

Errors on spectrum at SK (Jun)	0.0-0.5	0.5-1.0	1.0-1.5	1.5-2.0	2.0-2.5	>2.5GeV
Fitting error			±14.7%	±9.6%	±19.3%	+26.7%
PMT saturation correction			±0.8%	±1.2%	±2.0%	±20%
PMT relative gain correction			—	—	—	—
Mirror reflectivity			-1.6%	+3.1%	—	-9.0%
Refractive index measurement			—	—	—	—
Wave length dep. on the ref. index			—	—	—	—
Low and high beam intensity			-7.0%	-6.5%	+4.5%	+6.5%
Pion monitor alignment			—	—	—	—
Injection point of protons			-2.5%	+9.1%	-10.0%	+3.6%
Beam stability (pion monitor run)			±3.2%	±3.7%	±5.0%	±12.8%
Horn magnetic field uncertainty			-2.4%	-7.5%	+38.8%	-10.7%
Subtraction of BKG radiation component			—	—	—	—
Subtraction of EM shower component			—	—	—	-60%
Fitting method			+11.0%	-10.2%	-12.3%	$^{+1.6\%}_{-32\%}$
Pion beam profile (fitting function)			—	—	—	—
Pion decay before pion monitor			±2.3%	±5.7%	±6.3%	—
Pion Beam profile (pion absorption)			—	—	±1.4%	±21%
Bin size of pion kinematics			+1.4%	-2.7%	-7.4%	-13.0%
Beam stability (normal run)			+1.2%	-1.9%	$^{+1.8\%}_{-1.0\%}$	$^{+4.2\%}_{-4.3\%}$
Total			$^{+18.8\%}_{-17.2\%}$	$^{+15.2\%}_{-18.8\%}$	$^{+44.4\%}_{-27.1\%}$	$^{+42.3\%}_{-77.5\%}$

Table 7.20: Systematic errors on Pion Monitor analysis (about neutrino spectrum at SK), June

Errors on spectrum ratio (Jun)	0.0-0.5	0.5-1.0	1.0-1.5	1.5-2.0	2.0-2.5	>2.5GeV
Fitting error			$^{+3.2\%}_{-4.5\%}$	$^{+6.2\%}_{-4.9\%}$	$^{+2.0\%}_{-5.7\%}$	$^{+8.5\%}_{-5.8\%}$
PMT saturation correction			±0.6%	±0.5%	±1.3%	±4.2%
PMT relative gain correction			—	—	—	—
Mirror reflectivity			—	—	+3.5%	—
Refractive index measurement			—	—	—	—
Wave length dep. of the ref. index			—	—	—	—
Low and high beam intensity			-6.0%	-5.3%	-6.6%	±0.5%
Pion monitor alignment			—	—	—	—
Injection point of protons			-1.0%	+2.1%	-0.6%	-4.9%
Beam stability (pion monitor run)			±1.0%	±1.5%	±3.4%	±1.1%
Horn magnetic field uncertainty			+0.5%	-6.7%	+4.7 %	+9.4%
Subtraction of BKG radiation component			—	—	—	—
Subtraction of EM shower component			—	—	—	+72.0%
Fitting method			+4.0%	$^{+1.4\%}_{-3.0\%}$	$^{+3.2\%}_{-4.6\%}$	-14.5%
Pion beam profile (fitting function)			—	—	—	—
Pion decay before pion monitor			±1.4%	±3.8%	±3.4%	±1.6%
Pion beam profile (pion absorption)			—	—	±1.0%	±7.2%
Bin size of pion kinematics			-0.6%	—	—	-13.0%
Beam stability (normal run)			+0.7%	-2.3%	$^{+0.9\%}_{-1.5\%}$	-3.4%
Hadron model (MC)	±9%	$^{+3.0\%}_{-10.0\%}$				
Total	±9%	$^{+3.0\%}_{-10.0\%}$	$^{+5.5\%}_{-7.8\%}$	$^{+7.8\%}_{-11.3\%}$	$^{+8.7\%}_{-11.2\%}$	$^{+73.6\%}_{-22.8\%}$

Table 7.21: Systematic errors on Pion Monitor analysis (about neutrino flux ratio), June

Errors on spectrum at KEK (Nov.)	0.0-0.5	0.5-1.0	1.0-1.5	1.5-2.0	2.0-2.5	>2.5GeV
Fitting error			±6.2%	±4.8%	±7.7%	±12%
PMT saturation correction			—	—	—	—
PMT relative gain correction			—	—	—	—
Mirror reflectivity			-2.0%	+2.9%	+3.4%	+0.6%
Refractive index measurement			—	—	—	—
Wave length dep. of the ref. index			-5.1%	+7.3%	+4.6%	+37%
Low and high beam intensity			-1.2%	+0.6%	+4.0%	+5.0%
Pion monitor alignment			—	—	—	—
Injection point of protons			—	-2.0%	—	-4.8%
Beam stability (pion monitor run)			—	—	—	±5.5%
Horn magnetic field uncertainty			-3.6%	+5.2%	+0.7%	+10.6%
Subtraction of BKG radiation component			—	—	—	—
Subtraction of EM shower component			—	—	—	—
Fitting method			+6.8%	-7.7%	-15.3%	$^{+12\%}_{-21\%}$
Beam profile dependence (fitting function)			—	—	—	±2.0%
Pion decay before pion monitor			—	±0.8%	±0.5%	—
Pion Beam profile (pion absorption)			±0.5%	±1.0%	±4.3%	±20%
Bin size of pion kinematics			+2.7%	-2.4%	-7.0%	-10.0%
Beam stability (normal run)			±1.0%	$^{+1.0\%}_{-1.9\%}$	$^{+4.4\%}_{-1.1\%}$	$^{+6.3\%}_{-3.4\%}$
Total			$^{+9.2\%}_{-9.6\%}$	$^{+10.7\%}_{-9.9\%}$	$^{+12.1\%}_{-17.7\%}$	$^{+47.7\%}_{-34.0\%}$

Table 7.22: Systematic errors on Pion Monitor analysis (about neutrino spectrum at KEK), Nov

Errors on spectrum at SK (Nov)	0.0-0.5	0.5-1.0	1.0-1.5	1.5-2.0	2.0-2.5	>2.5GeV
Fitting error			±8.1%	±4.9%	±7.6%	±12%
PMT saturation correction			—	—	—	—
PMT relative gain			—	—	—	—
Mirror reflectivity			-3.1%	+1.8%	+4.0%	—
Refractive index measurement			—	—	—	—
Wave length dep. of the ref. index			-8.6%	+5.4%	+1.1%	+33%
Low and high beam intensity			-2.1%	-1.5%	+3.1%	+7.8%
Pion monitor alignment			—	—	—	—
Injection point of protons			—	—	—	-4.9%
Beam stability (pion monitor run)			—	—	—	±4.8%
Horn magnetic field uncertainty			-5.7%	+2.5%	+0.7%	+9.8%
Subtraction of BKG radiation component			—	—	—	—
Subtraction of EM shower component			—-	—	—	—
Fitting method			+11.0%	-10.2%	-12.3%	$^{+1.6\%}_{-32\%}$
Beam profile dependence (fitting function)			—	—	—	±1.8%
Pion decay before pion monitor			±0.5%	±1.5%	±1.1%	—
Pion beam profile (pion absorption)			±0.5%	±0.5%	±3.1%	±10%
Bin size of pion kinematics			+0.5%	-2.4%	-5.4%	-15.4%
Beam stability (normal run)			$^{+1.6\%}_{-2.1\%}$	−1.5%	$^{+4.1\%}_{-1.6\%}$	−0.2%
Total			±13.8%	$^{+8.1\%}_{-11.9\%}$	$^{+10.6\%}_{-15.8\%}$	$^{+42.1\%}_{-39.5\%}$

Table 7.23: Systematic errors on Pion Monitor analysis (about neutrino spectrum at SK), Nov

Errors on spectrum ratio (Nov.)	0.0-0.5	0.5-1.0	1.0-1.5	1.5-2.0	2.0-2.5	>2.5GeV
Fitting error			$^{+2.2\%}_{-2.9\%}$	$^{+2.2\%}_{-2.1\%}$	$^{+3.2\%}_{-2.9\%}$	$^{+1.0\%}_{-0.9\%}$
PMT saturation correction			—	—	—	—
PMT relative gain correction			—	—	—	—
Mirror reflectivity			-1.2%	-1.1%	+0.5%	—
Refractive index measurement			—	—	—	—
Wave length dep. of the ref. index			-3.7%	-1.8%	-3.3%	-2.6%
Low and high beam intensity			-1.9%	-3.7%	-1.9%	+2.9%
Pion monitor alignment			—	—	—	—
Injection point of protons			—	+1.2%	—	—
Beam stability (pion monitor run)			—	—	—	±0.5%
Horn magnetic field uncertainty			-2.6%	-2.4%	-2.4%	-1.0%
Subtraction of BKG radiation component			—	—	—	—
Subtraction of EM shower component			—	—	—	—
Fitting method			+4.0%	$^{+1.4\%}_{-3.0\%}$	$^{+3.2\%}_{-4.6\%}$	-14.5%
Pion beam profile (fitting function)			—	—	—	±0.3%
Pion decay before pion monitor			±0.7%	±0.7%	±1.7%	±0.5%
Pion beam profile (pion absorption)			—	±0.5%	±1.3%	±8.5%
Bin size of pion kinematics			-2.1%	—	+1.7%	-7.1%
Beam stability (normal run)			$^{+1.6\%}_{-1.8\%}$	$^{+1.5\%}_{-2.1\%}$	$^{+1.2\%}_{-1.4\%}$	+9.0%
Hadron model (MC)	±9%	$^{+3.0\%}_{-10.0\%}$				
Total	±9%	$^{+3.0\%}_{-10.0\%}$	$^{+4.9\%}_{-6.5\%}$	$^{+3.3\%}_{-6.5\%}$	$^{+5.4\%}_{-7.5\%}$	$^{+12.8\%}_{-18.5\%}$

Table 7.24: Systematic errors on Pion Monitor analysis (about neutrino flux ratio), Nov

Chapter 8

Characteristics of K2K Neutrino Beam III (Measurement by Near Detector)

8.1 Method to Identify Neutrino Interaction Event

The neutrino events are identified with the existence of muons produced by the charged current neutrino interaction with iron. The criteria to identify the neutrino interaction is as follows.

1. Select the events with the track inside the muon range detector. Track finding algorithm judges the existence using the hit information of the muon range detector like the hodoscope. It requires all hit to be put on the same straight line in each x-z and y-z plane. Further, it determines T0, which is the time of muon passing through the first cell of drift tube. T0 is determined by the TDC information of the hit tubes on the straight line. For more detail, please see Appendix A.

2. Select the good reconstructed tracks comparing in the x-z plane and y-z plane. This is the consistency requirement for T0 and vertex (end) point of the track in the different plane. Fig. 8.1 shows the T0 TDC counts in the x-z plane vs that in the y-z plane. $|T0_{xz} - T0_{yz}| \leq 10$ is required here. Fig. 8.2 shows the difference of z position between x-z plane and y-z plane. The left and the right figures show vertex (start) point and end point of the reconstructed track, respectively. We required events which have -45≤dif-z≤30 cm for the vertex point and -45≤dif-z≤80 cm for end point. Open histogram shows the total reconstructed tracks and shaded histogram shows selected tracks passed the criteria. Unselected tracks mainly come from multi-short-tracks events and chamber insensitive tracks. Multi-short-tracks make mis-fitted tracks. The gap of chamber layer (please refer to table 3.2) as well as inefficiency of the chamber also creates the mis-fitted track.

3. Reject the pion or proton track in the two or more tracks event to see only the muon information. However, we allow the 2 or more neutrino interaction events. To reject the hadron tracks, we use T0 and distance between the vertex(end) point of the longest track and the other track. Fig. 8.3 shows a correlation plot between T0 and distance of the tracks. We define the distance from the vertex(end) point of the track to other track like Fig. 8.4. Horizontal axis of Fig. 8.3 shows the distance from the vertex(left) and end(right) point to the other track (cm). Vertical axis shows the T0 difference of each track. We reject the tracks, which have T0 difference within ±10 TDC counts and the distance within 100 cm.

4. Reject cosmic ray using the timing information of the track. We select the average T0 of the x-z and y-z plane, $(T0_{xz}+T0_{yz})/2$, to be $0 \leq T0_{ave} \leq 35$. This selection corresponds to lines with two negative slopes in the Fig. 8.1.

5. Select the events with vertex and end point of the track contained inside the muon range detector.

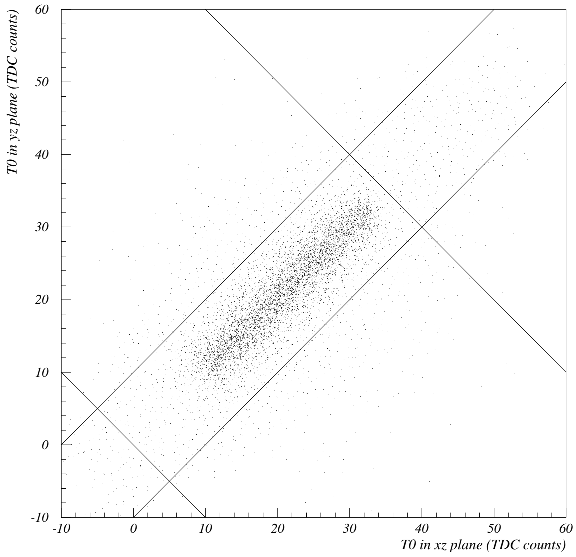

Figure 8.1: T0 TDC counts in the x-z plane vs that in the y-z plane of the muon range detector. $|T0_{xz} - T0_{yz}| \leq 10$ TDC counts is required for the consistency. Further, we require $0 \leq (\mathrm{T0}_{xz} + \mathrm{T0}_{yz})/2 \leq 35$ to reject the cosmic ray muon event. Lines correspond to these criteria.

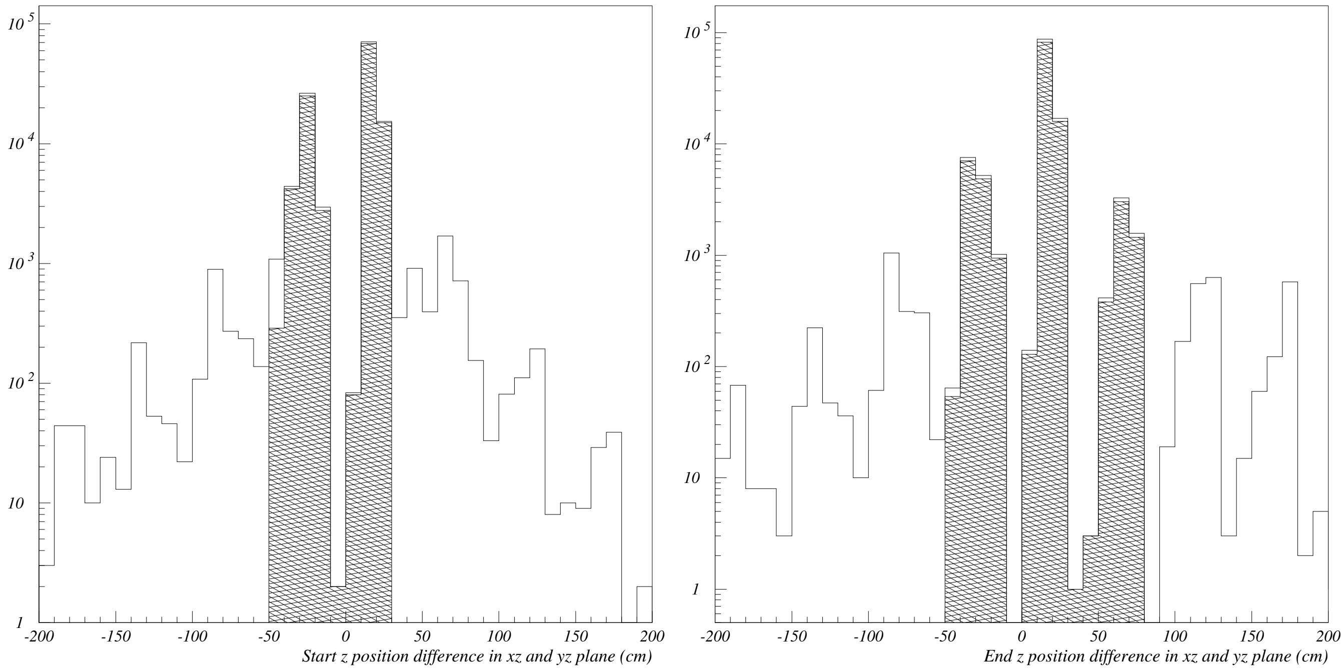

Figure 8.2: The difference of z position between x-z plane and y-z plane. The left and the right figures show vertex (start) point and end point of the reconstructed track, respectively. We required $-45 \leq$dif-z≤ 30 cm for the vertex point, and $-45 \leq$dif-z≤ 80 cm for end point. Open histogram shows the total reconstructed tracks and shaded histogram shows the tracks passed the criteria. Unselected tracks mainly come from multi-short-tracks events and chamber insensitive tracks. Multi-short-tracks make mis-fitted tracks. The gap of chamber layer (please refer to table 3.2) as well as inefficiency of the chamber also creates the mis-fitted track.

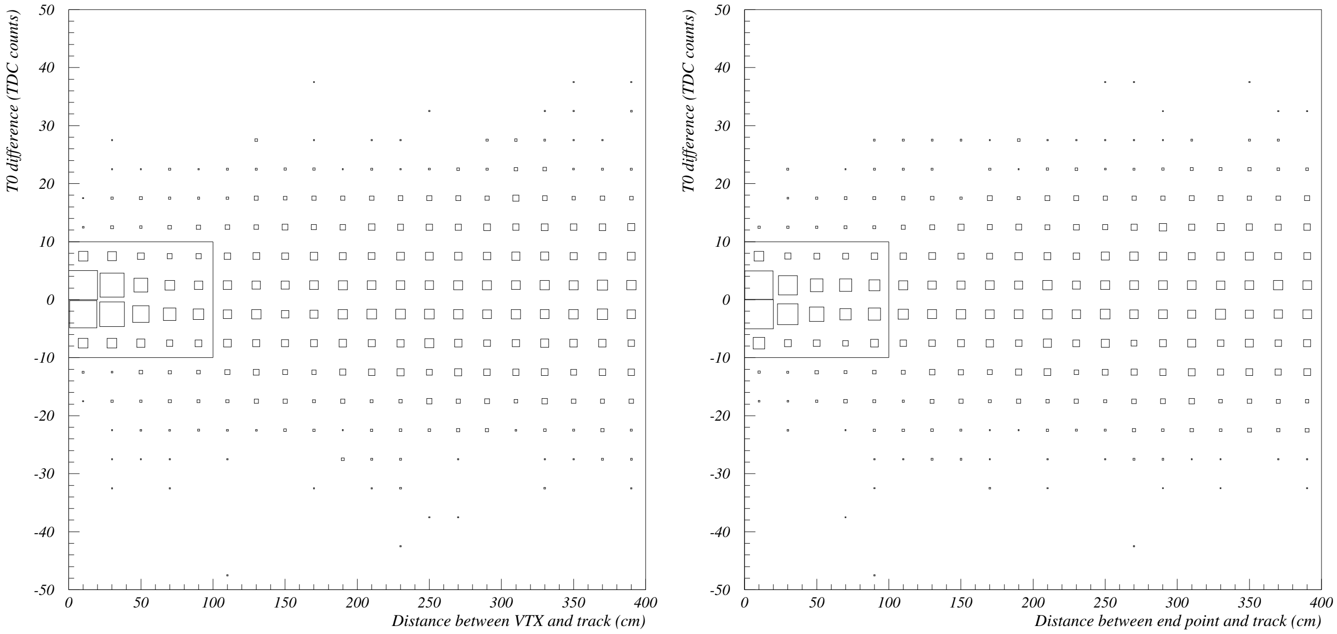

Figure 8.3: T0 and distance between the vertex point of one track and the other track. Fig. 8.4 shows the definition of the distance. Horizontal axis shows the distance from the vertex(left) and end(right) point to the other track (cm). Vertical axis shows the T0 difference of each track. We reject the tracks, which have T0 difference within ±10 TDC counts and the distance within 100 cm.

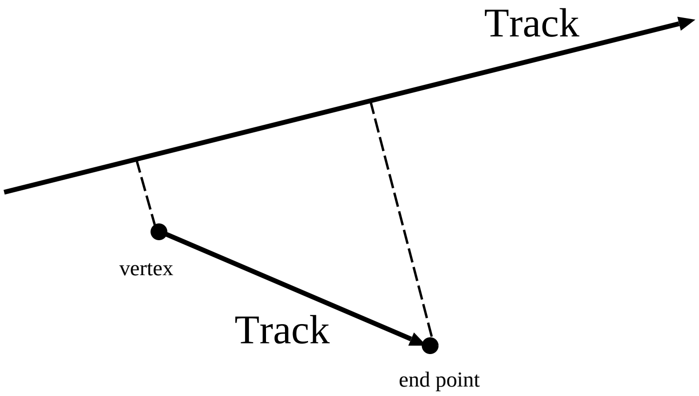

Figure 8.4: The definition of the distance from the vertex (end) point of the track to other track.

6. Select the events that z position of the vertex are in the ninth iron layer or more upstream. Fig. 8.5 shows the z position of the reconstructed tracks and shaded one shows the tracks passed the criteria.

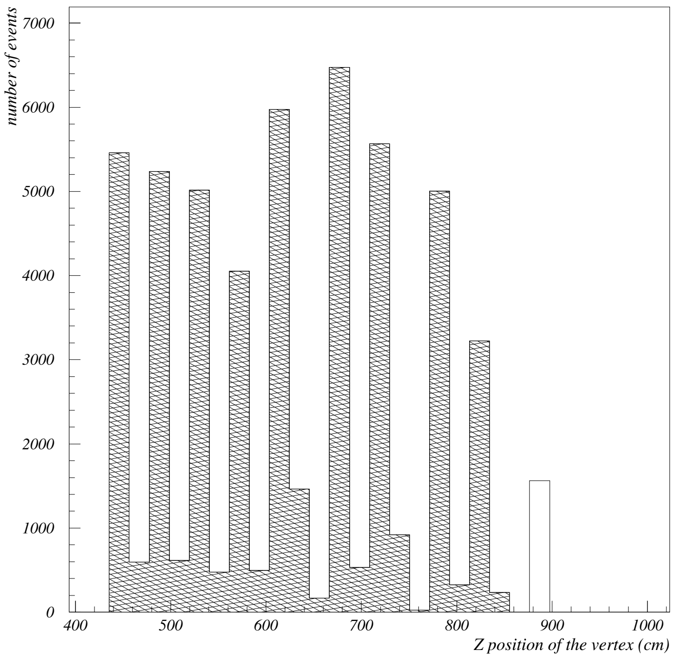

Figure 8.5: The z position of the reconstructed tracks in the muon range detector. Shaded one shows the selected tracks by the criteria.

7. Select the muon with the energy 0.5<E_μ <2.5 GeV. (for profile analysis only)
8. Select events with vertex in the fiducial volume (<3 meter radius, 312 ton).

Selection efficiency under these criteria is summarized in table 8.1.

Selection criteria	selected events/before cut
Track exist	0.2
Consistency between top-view and side-view	0.87
Reject extra track	0.93
Time window cut	0.99
Vertex and end point contained	0.50
Vertex z $\leq$ 9th layer	0.97
Profile analysis (0.5<E_μ <2.5GeV)	0.97
Fiducial volume cut	0.73

Table 8.1: Summary of the selection power of muon range detector analysis

Fig. 8.6 shows a typical selected fully contained ν-Fe event.

Number of neutrino events which are selected in the near detector is used to expect the number of neutrino events at SK. Number of events in the fiducial volume (<3 meter R; 312 ton) of the near detector is summarized in the table 8.2.

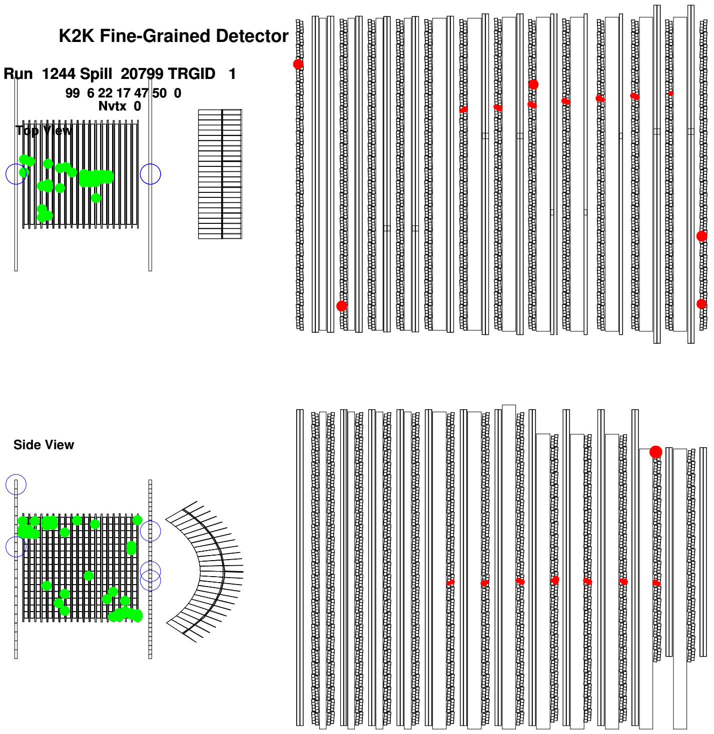

Figure 8.6: Typical fully contained ν-Fe event. Top-figure: top view of the fine grained detector. Bottom figure: side view. Both start and end points of the muon track are inside the muon range detector. (We can see noise hits inside SCIFI tracker but it is not a track.)

	June (4th $\sim$ 27th)	November (29-Oct $\sim$ 24-Nov.)
N_{sig}	27078	28241
$N_{cosmic\mu}$	23	20

Table 8.2: Number of events measured by muon range detector.

$N_{cosmic\mu}$ is estimated employing the off spill data.

8.2 Neutrino Interaction Rate as a Function of Supplied Current to Horn Magnets

Number of neutrino interactions as a function of the current supplied to the horn magnets is shown in Fig. 8.7. Neutrino flux increases as the current supplied to the horn magnets increases.

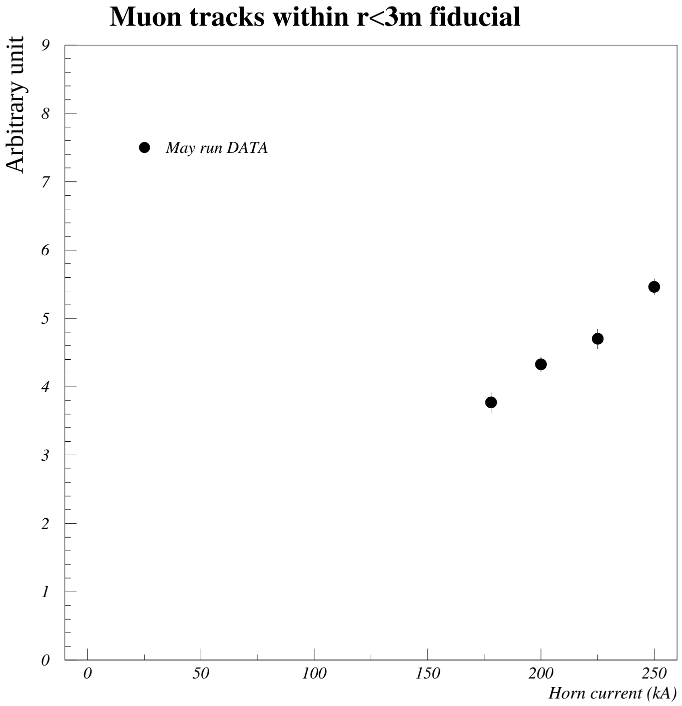

Figure 8.7: Number of neutrino interactions as a function of the current supplied to the horn magnets

8.3 Neutrino Yield with Horn/Target and with Bare Target

In order to estimate the neutrino yield produced by the pion which was created in the helium gas and/or the beam-dump, we compared the data with horn/target and with only target system. The data with only target system (Al alloy rod; 20 mmϕ and 66 cm length) was taken in the engineering run. In the case of the muon monitor measurement, we used the data without the horn/target system, but could not use it in the neutrino case because of too small statistics of the neutrino events. Further, the number of hit tubes of the muon range detector was used for larger statistics.

Table 8.3 shows the result. The comparison between the data and two sets of MC simulations is shown. One MC simulation assumes pions only come from the target, and the other assumes those come from all material. The ratio of the MC simulation also has $\sim$ 10% uncertainty, come from a neutrino flux and a neutrino interactions. These all values from MC are consistent with the data.

Neutrino yield inside fiducial volume of near detector changes with 1% if we change a MC set. Therefore, we conclude the neutrino yield inside three meter radius in the near detector come from pions created at other than the target is less than 1% in June and November configurations using MC simulation. This uncertainty is negligibly small for the K2K analysis.

	Target run	June configuration	Nov. configuration
Data	7.3±1.4%	95.1±1.7%	100%
MC (pions only from target)	7.7±0.8%	98±9.8%	100%
MC (pions from all material)	9.3±0.9%	97.1±9.7%	100%

Table 8.3: Comparison of the near detector data with target/horn system to the data with only the target. These numbers show the ratio of the number of hit tubes normalized by that of Nov. configuration.

8.4 Stability of Neutrino Beam Intensity

In order to check the stability of the neutrino beam, we check the relationship between beam-line monitors and neutrino interaction rate of the near detector in November (Fig. 8.8). We use neutrino events inside muon range detector. Horizontal axis is time adjusted by live-time of muon range detector. In the left figures, from top to bottom, 1st and 2nd figures show time variation of the proton intensity measured by two CTs. ("h37 in" and "target" in Tab. 3.1: unit of vertical axis is 1.0×10^{12} ppp.) Third and 4th figures show muon intensity measured by the Si detector and the Ion Chamber, same as Fig. 6.14 except for live-time. Fifth figure shows neutrino event rate/spill averaged by 6 hours data. Right figures show the projection of normalized neutrino event rate by each monitor.

According to the projection figures, correlation between the near detector events and beam-line monitors is within 5.8% (using CT15), 5.2% (using CT16), 4.6% (using Si detector) and 8.9% (using ionization chamber).

Same projection figures in June are shown in Fig. 8.9.

(RMS/mean) of each value are 8.0%(CT15), 7.9%(CT16), 7.7%(Si detector) and 6.2%(ionization chamber). The stability of the neutrino beam in June configuration was almost same as the November configuration.

In this thesis, neutrino yield normalized by CT16(TARGET CT) is used to estimate the uncertainty of the dead-time correction. Fluctuation of this value is almost consistent with statistical error since the event rate of muon range detector within 6 hours is $\sim$ 500.

8.5 Neutrino Beam Profile and Aiming

We measured the neutrino profile to determine the direction of the neutrino beam. Figs. 8.10 and 8.11 show the measured neutrino profiles overlaid with the MC simulation for the June and the November runs, respectively. The detector acceptance is corrected.

Fitted neutrino profiles by Gaussian are shown in Figs. 8.12 and 8.13. The center of beam is 12.9 cm(x) and -21.8 cm(y) (June); 1.6 cm(x) and -15.8 cm(y) (November), respectively.

The designed beam center at the muon range detector is $\sim$-15 cm in y-direction. Uncertainty of the profile center determination is estimated to be $\sim$20 cm including the systematic error in addition to the fitting error. We conclude the neutrino beam is directed toward Kamioka within 1 mrad from this data since 1 mrad corresponds to 30 cm in the muon range detector position.

8.6 Energy and Angular Distribution of Inclusive Muon in Neutrino Interaction

Fig. 8.14 shows the energy and polar angle of muons produced by charged current interactions in June, and Fig. 8.15 shows those in November. MC simulation are overlaid. Normalization factor of the MC is determined by total number of events. Tendency between the data and MC is agreed.

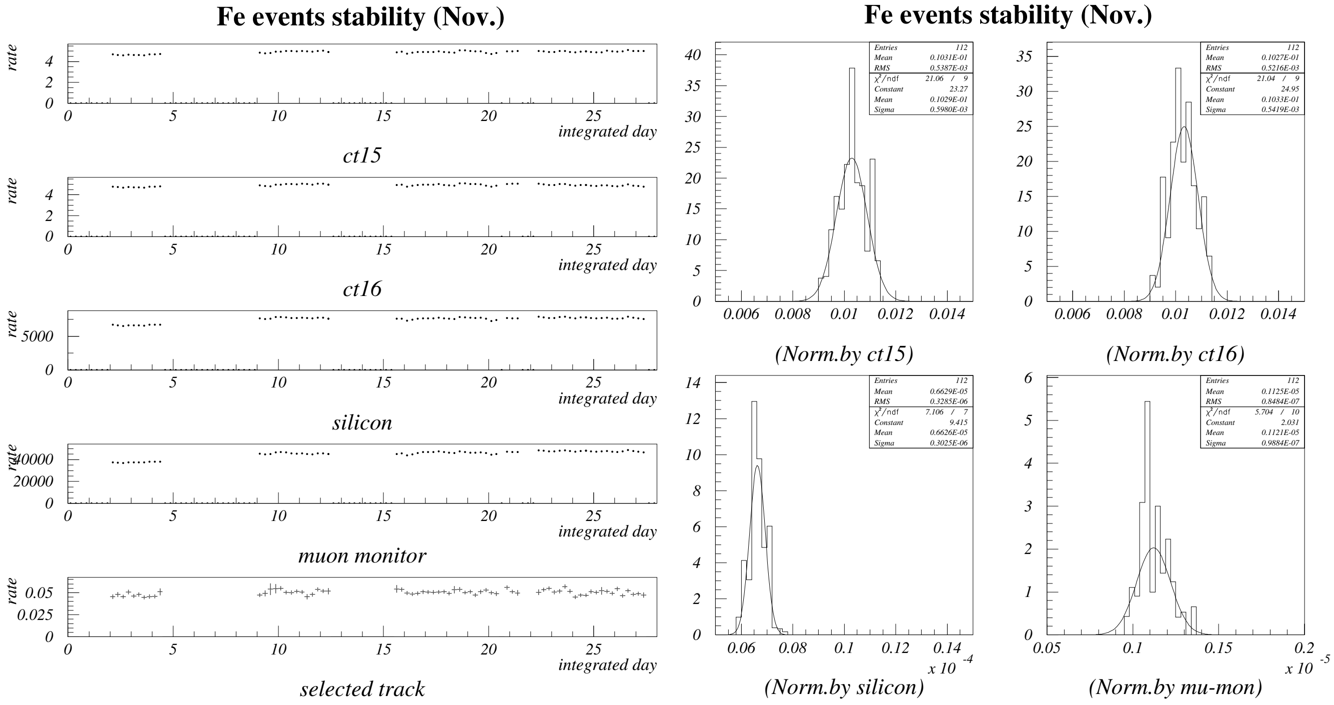

Figure 8.8: Neutrino rate (measured by muon range detector) and beam-line monitor information. In the left figures, from top to bottom, 1st and 2nd figures show time variation of the proton intensity measured by two CTs. (“h37 in” and “target” in Tab. 3.1: unit of vertical axis is 1.0×10^{12}ppp.) Third and 4th figures show muon intensity measured by the Si detector and the Ion Chamber, same as Fig. 6.14 except for live-time. All live-time of beam-line monitor is adjusted for muon range detector (neutrino rate). Fifth figure shows neutrino event rate/spill averaged by 6 hours data. at 5×10^{12}ppp. Right figures show the projection of normalized neutrino events by each monitor. (November)

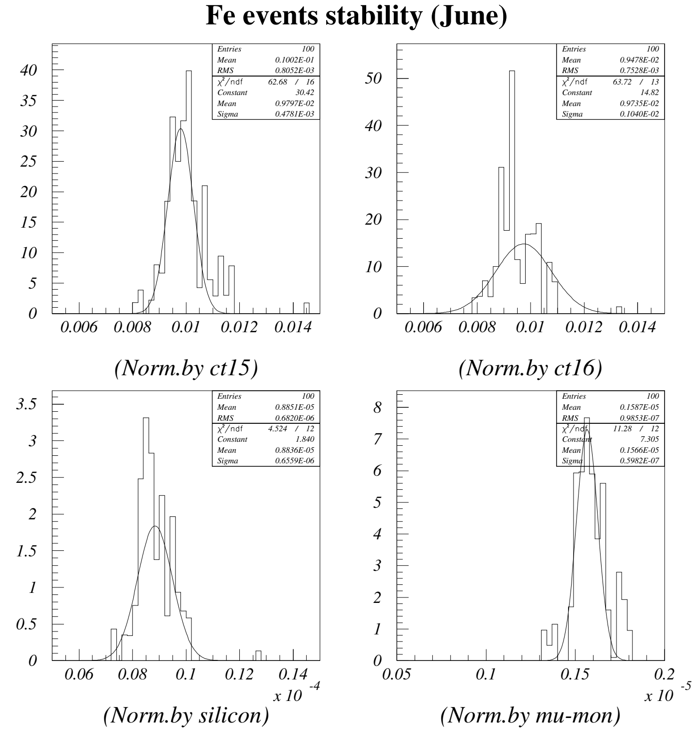

Figure 8.9: Neutrino rate (measured by muon range detector) and beam-line monitor information. Same projection plot as the Fig. 8.8(June)

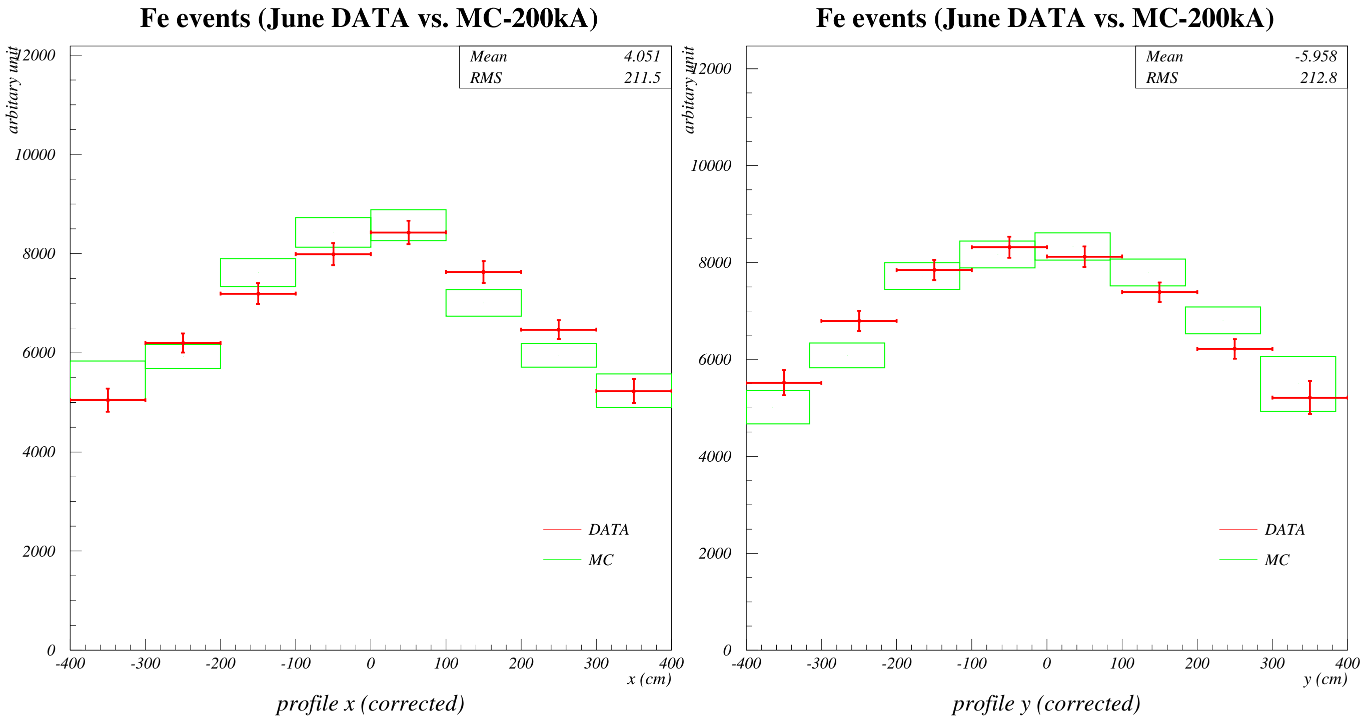

Figure 8.10: Neutrino profile measured by the muon range detector (June). Left: horizontal direction, right: vertical direction. The designed beam center is -15cm in the vertical direction. Detector acceptance is corrected.

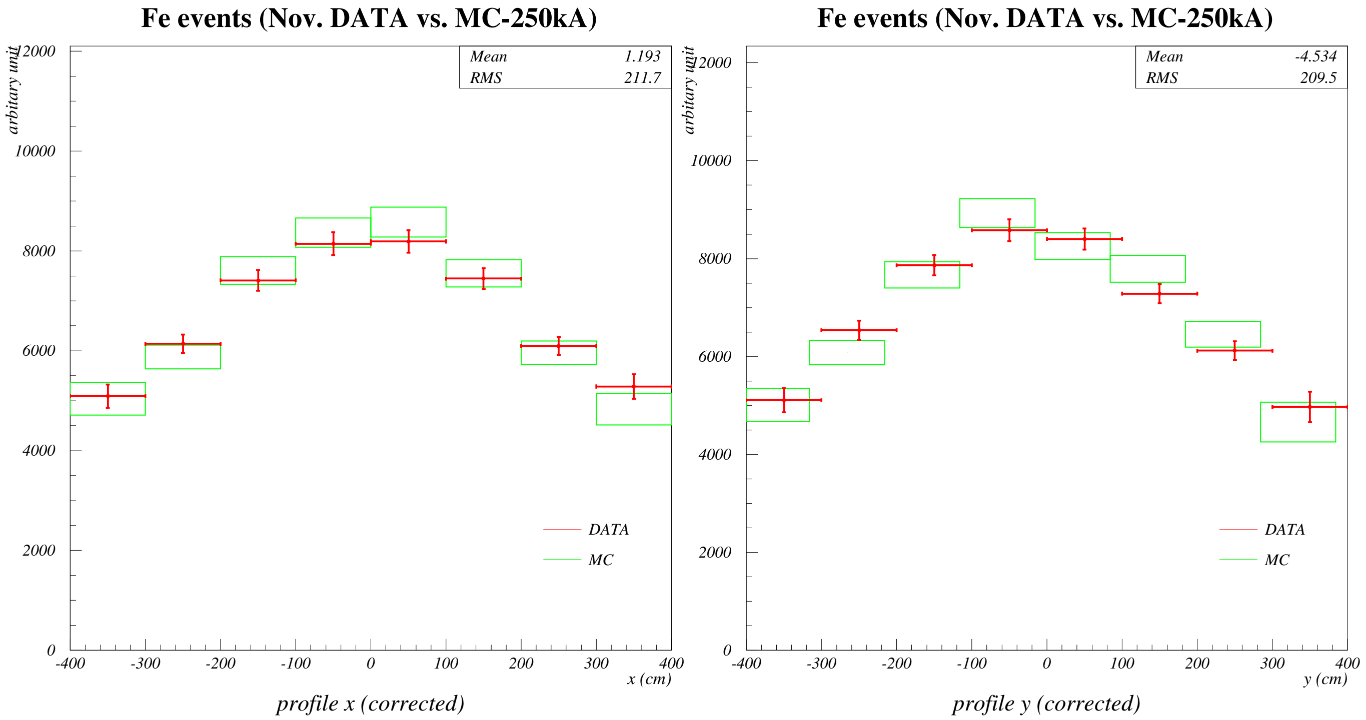

Figure 8.11: Neutrino profile measured by the muon range detector (November). Left: horizontal direction, right: vertical direction. Detector acceptance is corrected.

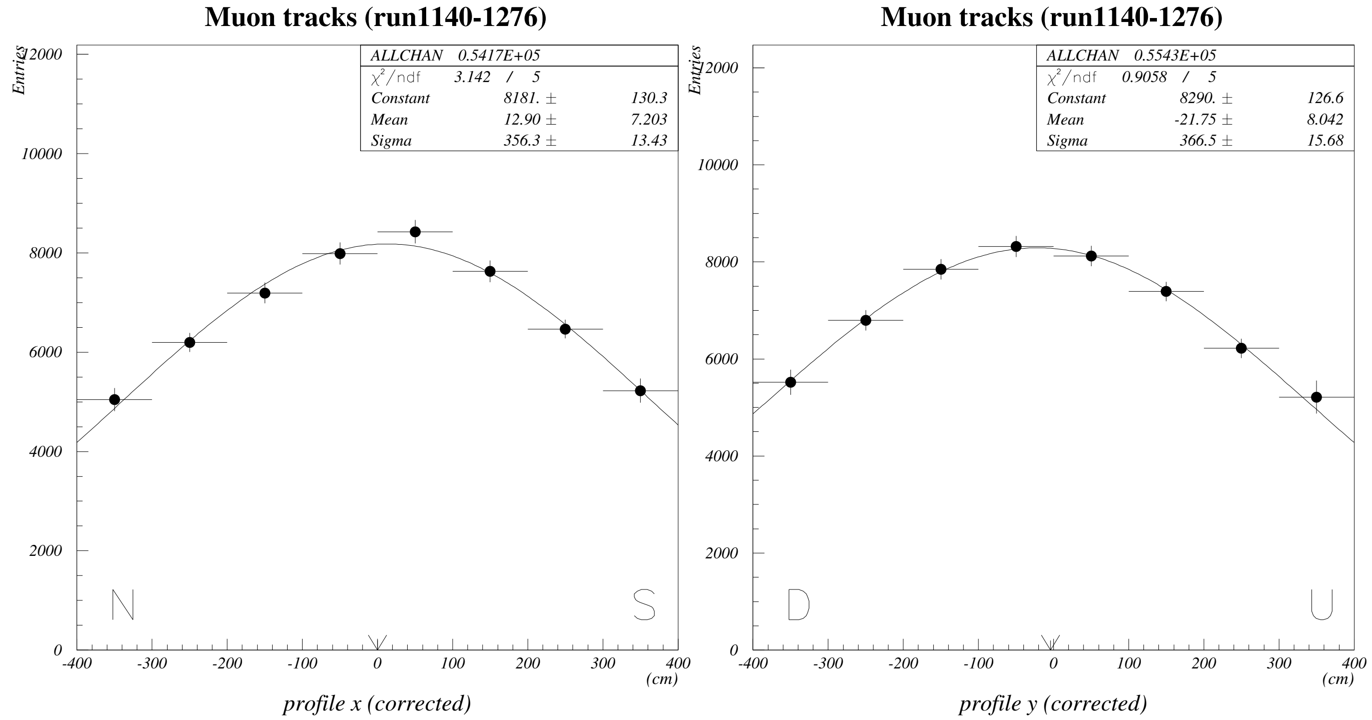

Figure 8.12: Fitted neutrino profile in the muon range detector (June). Left: horizontal direction, right: vertical direction.

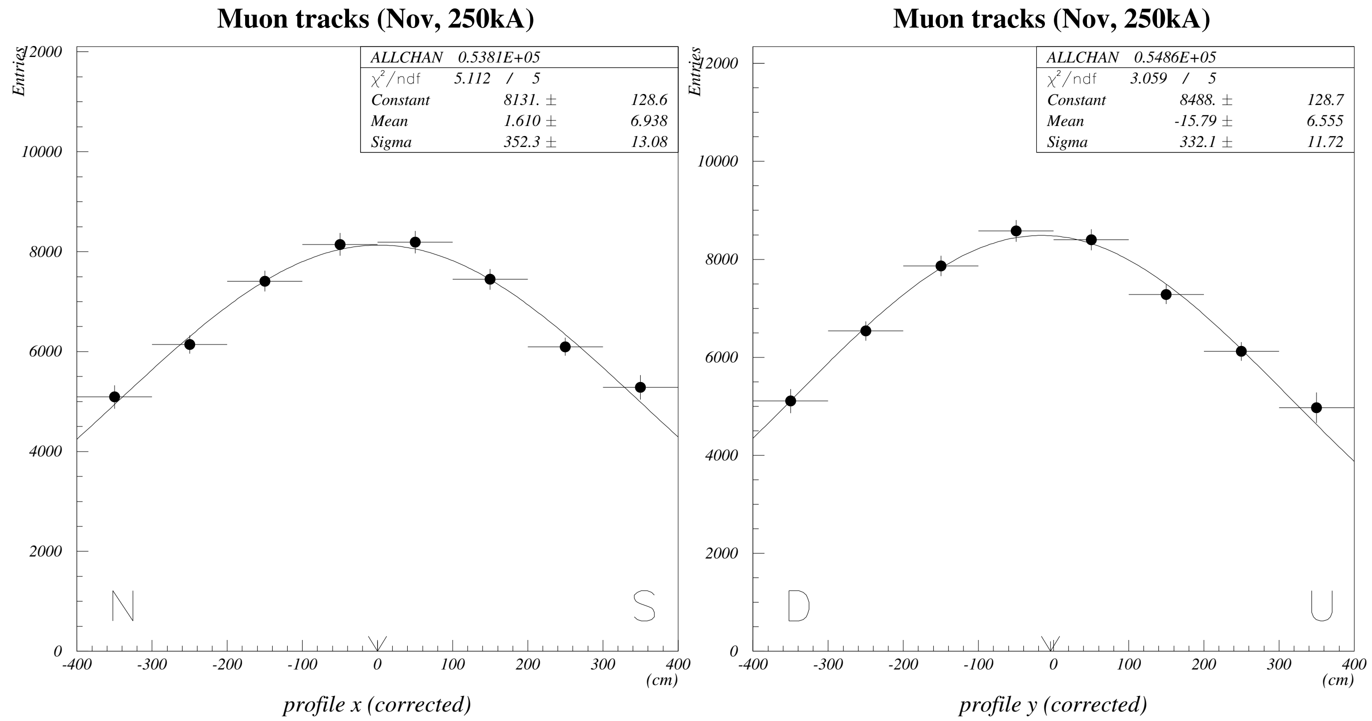

Figure 8.13: Fitted neutrino profile in the muon range detector (November). Left: horizontal direction, right: vertical direction.

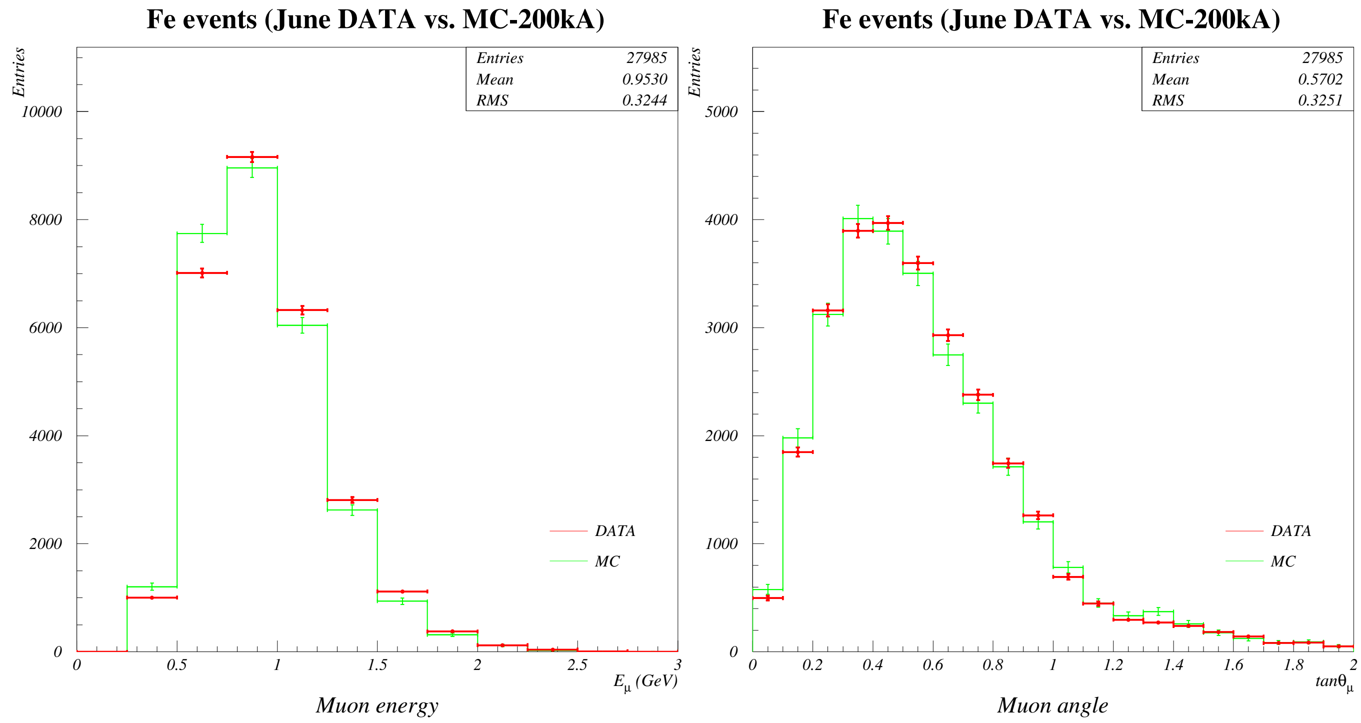

Figure 8.14: Energy and angle of muon track detected by the muon range detector (June). Left: Muon energy, right: Muon angle ($\tan\theta_\mu$). Cross is data and histogram is MC.

The uncertainty for the K2K analysis coming from this difference between MC and data is estimated later.

8.7 Detection Efficiency of Near Detector

The detection efficiency for the neutrino events in the near detector is used to expect the number of neutrino events at SK. This is defined as (detected neutrino events)/(all neutrino interactions) and estimated using the MC simulation. Fig. 8.16 shows the detection efficiency of the near detector in June. Detection efficiency in this figure is represented as the function of the neutrino energy for the analysis. These numbers are summarized in table 8.4.

	0.0-0.5GeV	0.5-1.0GeV	1.0-1.5GeV	1.5-2.0GeV	2.0-2.5GeV	>2.5GeV
June	1.7%	19%	34%	36%	38%	30%
Nov.	2.2%	19%	33%	36%	38%	31%

Table 8.4: Detection efficiency of the near detector as a function of the energy

The muon range detector is insensitive to most of NC interactions (NC is 1.6% of total reconstructed tracks according to MC), further, inefficiency for low energy muons reduce the efficiency.

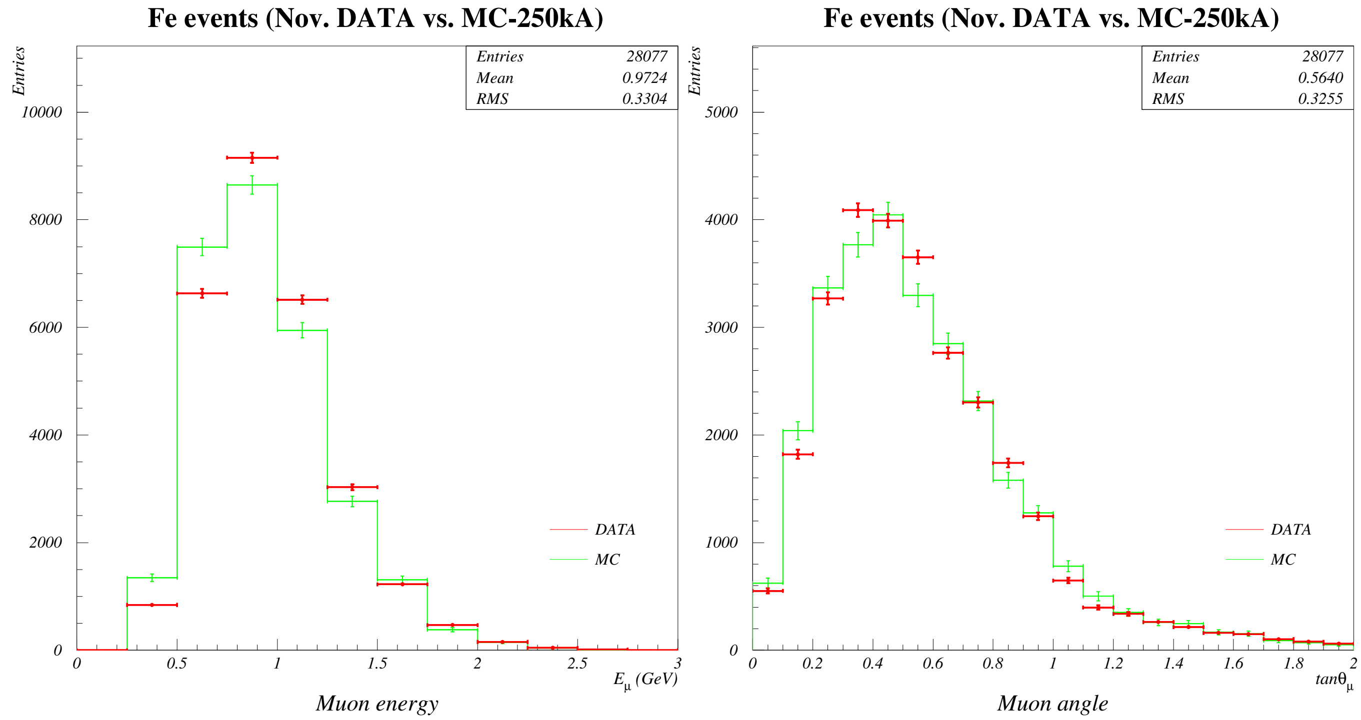

Figure 8.15: Energy and angle of muon track detected by the muon range detector (November). Left: Muon energy, right: Muon angle ($\tan\theta_\mu$).

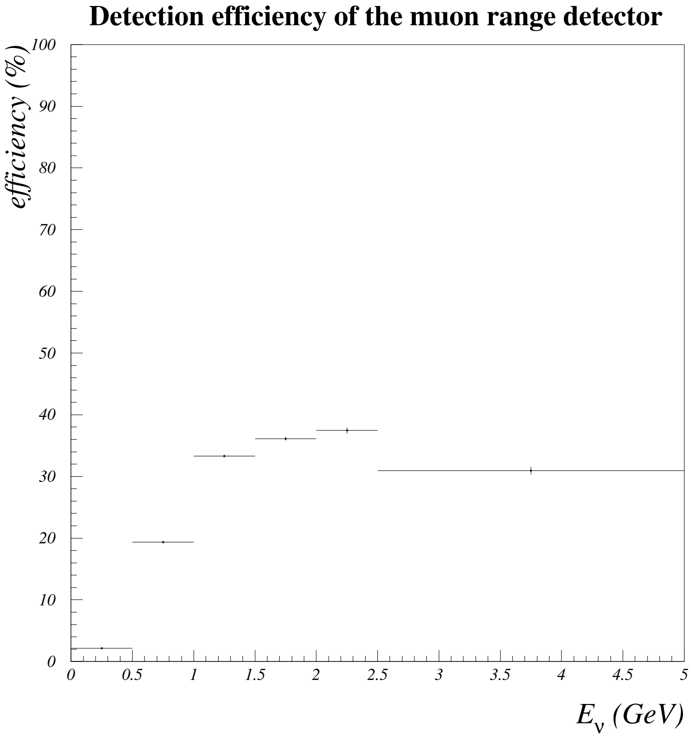

Figure 8.16: Detection efficiency of the near detector

Chapter 9

Expected Number of Neutrino Events at SK

9.1 Summary on Measurements at KEK

Fig. 9.1 shows integrated number of protons injected to the target which is estimated by TARGET CT. The day 0 is the 4th of March 1999 when engineering run started. From June, we started data taking for the K2K. Total number of protons in June and November which is utilized for the analysis in this thesis are 6.6×10^{18} protons. Used total number of spills for analysis is 1.38×10^{6}.

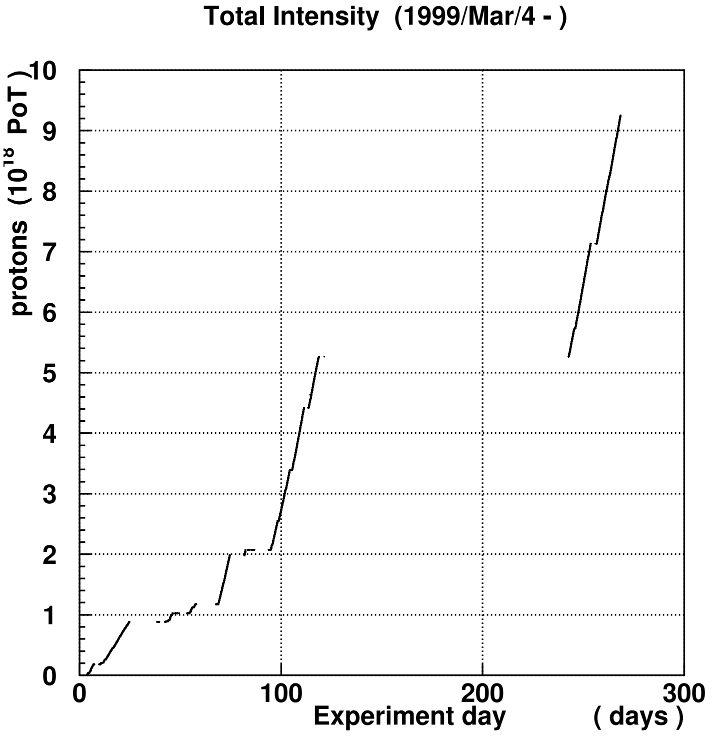

Figure 9.1: Total integrated proton number in front of the target estimated by CT. The day 0 is the 4th Mar-1999 when the engineering run started.

From the systematic study of neutrino beam using various detectors at KEK, we conclude the following facts.

1. The pion monitor successfully measured the neutrino energy spectrum at KEK and SK.

2. Our beam is directed toward SK within 1 mrad. (from the muon range detector and the muon monitor information)
3. The muon range detector measured neutrino events successfully, and their properties are consistent with the expected ones.

These facts allow us to predict the number of neutrino events at SK as planned.

9.2 Expected Number of Neutrino Events at SK

We calculate the number of neutrino events at SK using the following formula.

$$N_{SK} = \frac{N_{near}}{\epsilon_{near}} \cdot R_{SK/near} \cdot \epsilon_{SK} \cdot \left(1+\delta\right) \tag{9.1}$$

where,

$$\begin{aligned} N_{near} &= N_{sig} - N_{cosmic\mu} \\ R_{SK/near} &= \frac{\Phi_{SK} \cdot \sigma_{H_2O} \cdot Nt_{H_2O}}{\Phi_{near} \cdot \sigma_{Fe} \cdot Nt_{Fe}} \\ \delta &= \frac{POT_{SK} - POT_{near}}{POT_{near}} \end{aligned}$$

Φ_{SK}	neutrino flux at SK,
Φ_{near}	neutrino flux at the muon range detector,
σ_{H_2O}	cross section of neutrino with water,
σ_{Fe}	cross section of neutrino with iron,
Nt_{H_2O}	number of water target in the fiducial volume (SK)
Nt_{Fe}	number of iron target in the fiducial volume (Fe),
ϵ_{SK}	detection efficiency of SK,
ϵ_{near}	detection efficiency of the muon range detector,
POT_{SK}	integrated number of protons on target over analyzed spills for SK.
POT_{near}	integrated number of protons on target over analyzed spills for the muon range detector.
N_{sig}	number of selected events at the muon range detector
$N_{cosmic\mu}$	number of cosmic-ray events in the signal estimated from off-spill data.

9.2.1 Neutrino Flux at Near Detector and SK

We know Φ_{SK} and Φ_{near} from the pion monitor (Figs. 7.30 and 7.31), except for the neutrino flux below 1 GeV and the detailed structure finer than the energy bin size. In order to cover it, we use the full MC simulation using the Cho model. By taking the ratio Φ_{SK}/Φ_{near}, we can obtain better accuracy.

9.2.2 Ratio of Neutrino Event Rate at Near and SK Detectors

In order to estimate σ_{Fe}, we scale σ_{H_2O} as a function of the number of nucleons except the Fermi motion and the Pauli blocking. We do not scale the Fermi motion and the Pauli blocking but use the same ones as water. The total cross sections, σ_{H_2O} and σ_{Fe} have large uncertainties, however ratio, $\sigma_{H_2O}/\sigma_{Fe}$ cancels most of them out. The fiducial volume of the SK detector used in this thesis is 22.5 kton, and that of the muon range detector is 312 ton. Finally we get 6.929×10^{-5} (June)

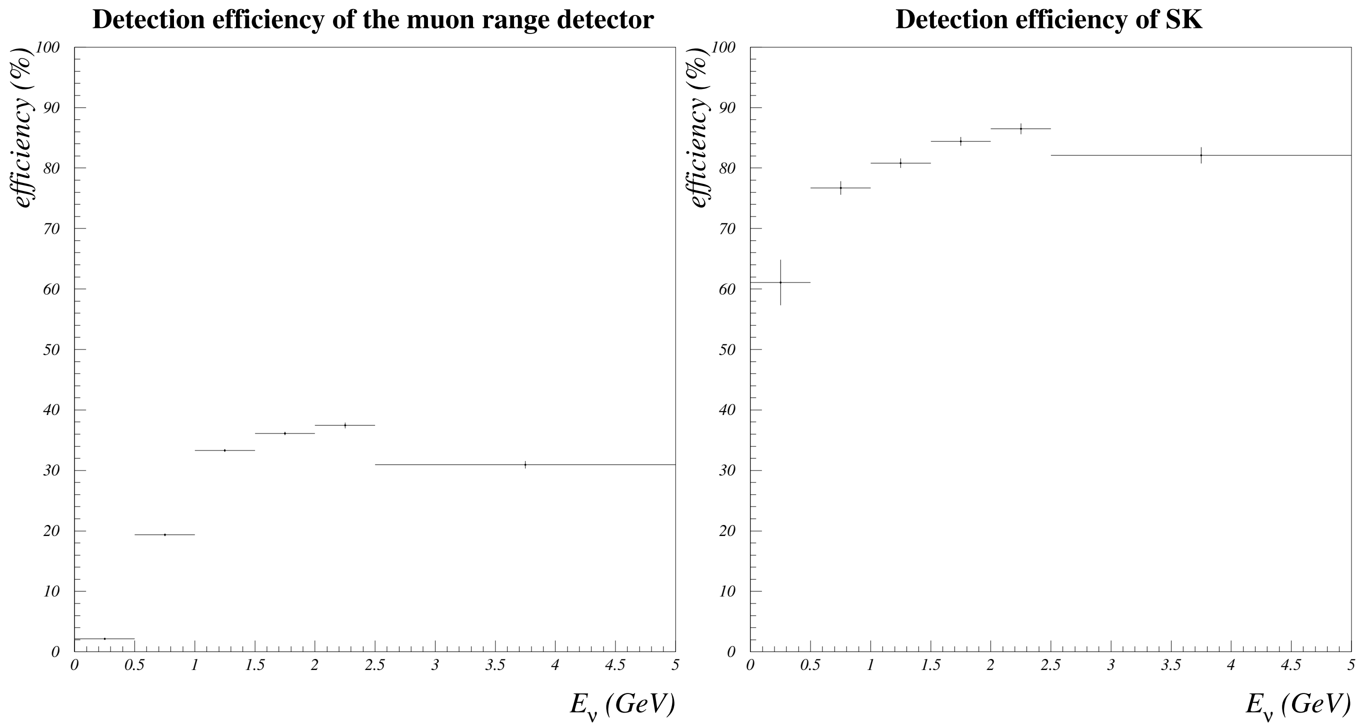
Detection efficiency of the muon range detector

Detection efficiency of SK

Figure 9.2: Detection efficiency(%) of the SK and the near detector as a function of neutrino energy (GeV)

and 6.970×10^{-5} (November) as the ratios of number of events, $R_{SK/near}$= $(\Phi_{SK} \times \sigma_{H_2O} \times Nt_{H_2O})/(\Phi_{near} \times \sigma_{Fe} \times Nt_{Fe})$.

Absolute number of the expected neutrino events at far/near detector as a function of neutrino energy is summarized in Table 9.1. These numbers are normalized to 10^{20}POT.

		0.0-0.5GeV	0.5-1.0GeV	1.0-1.5GeV	1.5-2.0GeV	2.0-2.5GeV	>2.5Ge V
June	near	5.83×10^4	7.65×10^5	1.46×10^6	8.34×10^5	3.61×10^5	5.59×10^4
	SK	4.5	41.6	84.6	60.9	43.1	10.2
Nov.	near	4.85×10^4	6.88×10^5	1.41×10^6	9.75×10^5	3.84×10^5	2.45×10^5
	SK	3.9	36.8	68.0	74.5	41.1	37.1

Table 9.1: Expected neutrino events at the near detector and SK as a function of neutrino energy.

9.2.3 Detection Efficiency of Near Detector and SK

Fig. 9.2 shows the detection efficiency of SK and the muon range detector as a function of neutrino energy. This efficiency is defined as (detected neutrino events)/(all neutrino interactions). It is estimated using MC simulations. SK is sensitive to about half of the NC events. The Fully-Contained (FC) requirement decreases the efficiency above 2.5 GeV. On the other hand, the muon range detector is insensitive to most of NC interactions (NC is 1.6% of total reconstructed tracks according to MC), further, inefficiency for low energy muons reduce the efficiency of low energy induced neutrino interactions. These efficiencies also depend on the neutrino cross section, in particular CC/NC ratio. This will be discussed later in systematic error studies.

The average detection efficiency over the neutrino energies at SK is 81.1%(June) and 81.8%(November). That of the near detector is 30.8%(June) and 31.3%(November). The small difference between two data sets is due to the neutrino spectrum difference due to the different horn/target configuration.

9.2.4 Total Number of Neutrino Events Observed at Near Detector

We correct for the dead time of the near detector using POT measured by the beam-line CT.

Table 9.2 shows the number of events in the fiducial of the muon range detector (R<3 m). We separate June data from November data.

	June (4th ~ 27th)	November (29-Oct ~ 24-Nov.)
N_{sig}	27078	28241
$N_{cosmic\mu}$	23	20
POT_{near}	3.03×10^{18}	2.86×10^{18}
POT_{SK}	3.00×10^{18}	3.59×10^{18}

Table 9.2: Number of events measured by muon range detector.

9.2.5 Expected Number of Neutrino Events at SK

Now we have numerical values necessary for evaluation of formula(9.1). The final expected number of neutrino events at SK becomes **4.89** (June) and **6.45** (November).

9.2.6 Estimated Uncertainty of Expected Number of Neutrino Events at SK

Table 9.3 summarizes uncertainties of the expected numbers.

Item	source of error	alone(June)	far/near(June)	alone(Nov.)	far/near(Nov.)
N_{near}	selection	±3.2%	±3.2%	±3.2%	±3.2%
ϵ_{near}	tracking	±3.5%	±3.5%	±3.5%	±3.5%
	NC	±9.0%	±5.0%	±9.0%	±5.0%
ϵ_{SK}	NC	±4.0%		±4.0%	
Φ_{SK}/Φ_{near}	pion monitor data and MC		$^{+9.1\%}_{-10.1\%}$		$^{+5.4\%}_{-8.7\%}$
$\sigma_{H_2O}/\sigma_{Fe}$	neutrino cross section		±10.0%		±10.0%
Nt_{Fe}	vertex (near detector)	±2.8%	±2.8%	±2.8%	±2.8%
Nt_{H_2O}	vertex (SK)	±4.0%	±4.0%	±4.0%	±4.0%
$(1+\delta)$	POT normalization	±0.3%	±0.3%	±2.0%	±2.0%
total			$^{+15.9\%}_{-16.5\%}$		$^{+14.2\%}_{-15.8\%}$

Table 9.3: Estimated errors on expected number of events at SK.

- Flux(Φ_{SK} and Φ_{Fe})
  Systematic errors of the pion monitor analysis are estimated in chapter 7. The error of the neutrino flux in each energy bin is translated into the error of $R_{SK/near}\cdot(\epsilon_{SK}/\epsilon_{near})$ using the number of neutrino event in table 9.1. Since flux far/near ratio is known with better accuracy, it is best to use this ratio to expect the neutrino event rate at SK. In order to estimate the uncertainty of $R_{SK/near}\cdot(\epsilon_{SK}/\epsilon_{near})$ coming from the uncertainty of the neutrino flux, we transform this formula as follows.

$$\begin{aligned} R_{SK/near}\cdot(\epsilon_{SK}/\epsilon_{near}) &= \frac{N^{SK}_{total}\cdot\epsilon_{SK}}{N^{near}_{total}\cdot\epsilon_{near}} \\ &= \frac{1}{N^{near}_{total}\cdot\epsilon_{near}}\cdot\sum_i N^{SK}_i\cdot\epsilon^i_{SK} \end{aligned}$$

$$
\begin{aligned}
&= \frac{1}{N_{total}^{near} \cdot \epsilon_{near}} \sum_i \Big[N_i^{near} \cdot \frac{\Phi_{SK}^i \cdot \sigma_{H_2O}^i \cdot Nt_{H_2O} \cdot \epsilon_{SK}^i}{\Phi_{near}^i \cdot \sigma_{Fe}^i \cdot Nt_{Fe} \cdot \epsilon_{near}^i} \Big] \\
&= \frac{1}{N_{total}^{near} \cdot \epsilon_{near}} \sum_i \Big[N_i^{near} \cdot \Big(\frac{\Phi_{SK}}{\Phi_{near}} \Big)_i \cdot \frac{\sigma_{H_2O}^i \cdot Nt_{H_2O} \cdot \epsilon_{SK}^i}{\sigma_{Fe}^i \cdot Nt_{Fe} \cdot \epsilon_{near}^i} \Big]
\end{aligned}
$$

where,

i	i-th energy bin,
N_{total}^{SK}	Number of neutrino events at SK,
N_{total}^{near}	Number of neutrino events at the near detector,

This formula shows the uncertainty of $(\Phi_{SK}/\Phi_{near})_i$ weighted by the other constants is the systematic error to be estimated since the error coming from the flux uncertainty is independent of the other uncertainty. The far/near ratio and the uncertainty including the detection efficiency of each detector in each energy bin was calculated according to this formula. Table 9.4 summarizes them. We summed these numbers over the energy linearly to get the final number of $R_{SK/near} \cdot (\epsilon_{SK}/\epsilon_{near})$ and the uncertainty. Those are $(1.84^{+0.17}_{-0.19}) \times 10^{-4}$(June), $(1.82^{+0.099}_{-0.16}) \times 10^{-4}$(Nov.).

		0.0-0.5GeV	0.5-1.0GeV	1.0-1.5GeV	1.5-2.0GeV	2.0-2.5GeV	>2.5Ge V
June	far/near	2.66×10^{-6}	2.93×10^{-5}	6.27×10^{-5}	4.72×10^{-5}	3.41×10^{-5}	7.34×10^{-6}
	error	$\pm2.39\times10^{-7}$	${}^{+0.92}_{-2.66} \times 10^{-6}$	${}^{+3.49}_{-4.86} \times 10^{-6}$	${}^{+3.70}_{-5.32} \times 10^{-6}$	${}^{+2.94}_{-3.85}\times10^{-6}$	${}^{+5.40}_{-1.67}\times10^{-6}$
Nov.	far/near	2.03×10^{-6}	2.39×10^{-5}	4.65×10^{-5}	5.33×10^{-5}	3.02×10^{-5}	2.58×10^{-5}
	error	$\pm1.83\times10^{-7}$	${}^{+0.68}_{-2.12}\times10^{-6}$	${}^{+2.29}_{-3.05}\times10^{-6}$	${}^{+1.78}_{-3.47}\times10^{-6}$	${}^{+1.61}_{-2.29}\times10^{-6}$	${}^{+3.31}_{-4.75}\times10^{-6}$

Table 9.4: Far/near ratio and error of each energy bin

- Cross section(σ_{H_2O} and σ_{Fe}) difference
  We changed the Fermi-momentum and nuclear potential from water to iron level to estimate this error using the MC. If we changed the nuclear potential like this, the inclusive-muon-event rate changes less than 10%. We take 10% as the error of the cross section ratio.

- NC event ratio
  The muon range detector is insensitive to most of the NC events. On the contrary, SK is sensitive to about half of them. Hence the NC/CC ratio gives an error in the detection efficiency. The NC/CC ratio in water is about 30%, and further this error is estimated to be about 30%. The uncertainty of the ratio of NC to total neutrino interactions is ~10%. Since about half of the NC interactions are detected at SK, this uncertainty is 5%.

- POT normalization
  The event rate is monitored by the near detector. The dead time of the near detector and SK is corrected by POT. In June, the live-time of near and far detectors was almost same. In November, we have a little dead time for the near detector, but as shown in Fig. 8.8, the beamline monitors show there is no serious change of targeting efficiency. The error is estimated from (RMS of (neutrino interactions/CT)) × dead time.

- Tracking efficiency
  Fig. 9.3 shows the tracking efficiency of the muon range detector as a function of muon track length. Horizontal axis shows the number of iron layers which muon passed through. Dashed lines are estimated by MC, and solid lines are real data. This difference comes from the uncertainty of the detector performance. We estimated the error by this difference weighted with the observed number of events.

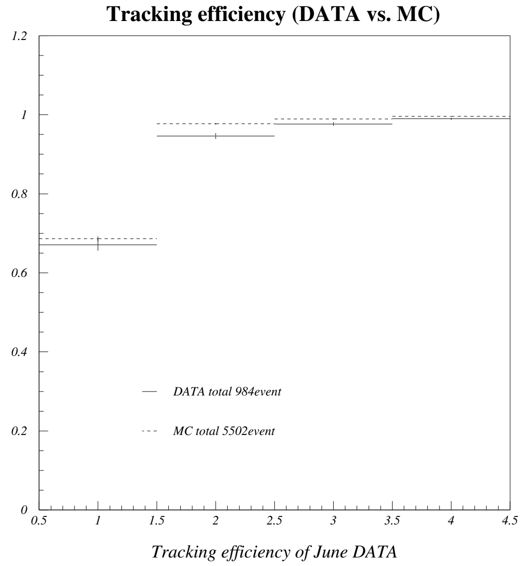

Figure 9.3: Tracking efficiency of muon range detector as a function of muon track length. The horizontal axis shows the number of iron layers which muon passed through. Dashed lines are estimated by MC, and solid lines from data.

- Selection
  We use several criteria to select FC events in the muon range detector as explained in chapter 8. We changed these criteria by a reasonable amount to study the systematic error from this.
- Vertex(ΔV/V) error of the near detector
  We compared the number of vertex points inside the various fiducial volumes, 1.5$\sim$4.0 m. We further compare the value of (data/MC) in each fiducial volume. Maximum difference of this value is 2.8%.
- Vertex(ΔV/V) error of SK
  To reconstruct the vertices of the particles, we have two different vertex fitters. These fitters reconstruct the vertices of the particles by means of different way and give the different fiducial volumes, and we regard this difference as the systematic error of the fiducial volume of SK.

Chapter 10

First Observation of Accelerator Origin Neutrino Beam after Passing through 250km of Earth

10.1 Selection Criteria for Neutrino Events at SK

We select accelerator origin neutrino beam after passing through 250 km of earth. To compare various distributions of observed events with those of the MC events, we printed the distributions of both of them at each selection step. MC event sample is generated employing the beam MC, neutrino-interaction MC and the detector simulation of SK. Interaction points of MC sample are uniformly randomized in inner detector of the SK. The selection criteria are as follows;

1. Select the events inside the time window using the GPS system. This window is ± 500 μs at this stage.
2. Select the events which have more than 30 μs time difference from previous events. This is the cut criteria to remove decay electron from muon. Dead time factor for this selection is about 1/1000 since total event rate of SK in this step is typically $\sim$35 Hz.
3. Select the events with HE trigger of SK as explained in chapter 3.
4. Select the events which have total number of photo-electrons of 200 or more within 300 ns window. This window reduces noise hits while keeping the signal hits. Fig. 10.1 shows the distribution of the number of photo-electrons with the 300 ns window. Left figure shows that of data and right one shows that of the MC. Most of unselected events of MC sample are from NC events, while that of real data are from the background events. For example, gamma rays from the rock.
5. Select the events which have total number of photo-electrons $\leq$ 50000 p.e.: This is from the consideration of the the energy of our neutrino beam. Fig. 10.2 shows the total number of photo-electron distributions of the data and MC. Unselected events mainly come from through going cosmic ray muons.
6. Select fully contained events. The number of the hit PMTs in the largest hit cluster of outer detector should be less than 10. Fig. 10.3 shows the number of hit PMTs in OD. Reduced events of the MC sample are thought to be out-going muon events from inner detector, while that of the data are from clipped muon events from cosmic ray.
7. Select the events inside the time window using the GPS system. This window is ± 5 μs at this stage. Fig. 10.4 shows the $(T_{KEK} - T_{SK})$ distribution of the SK data.

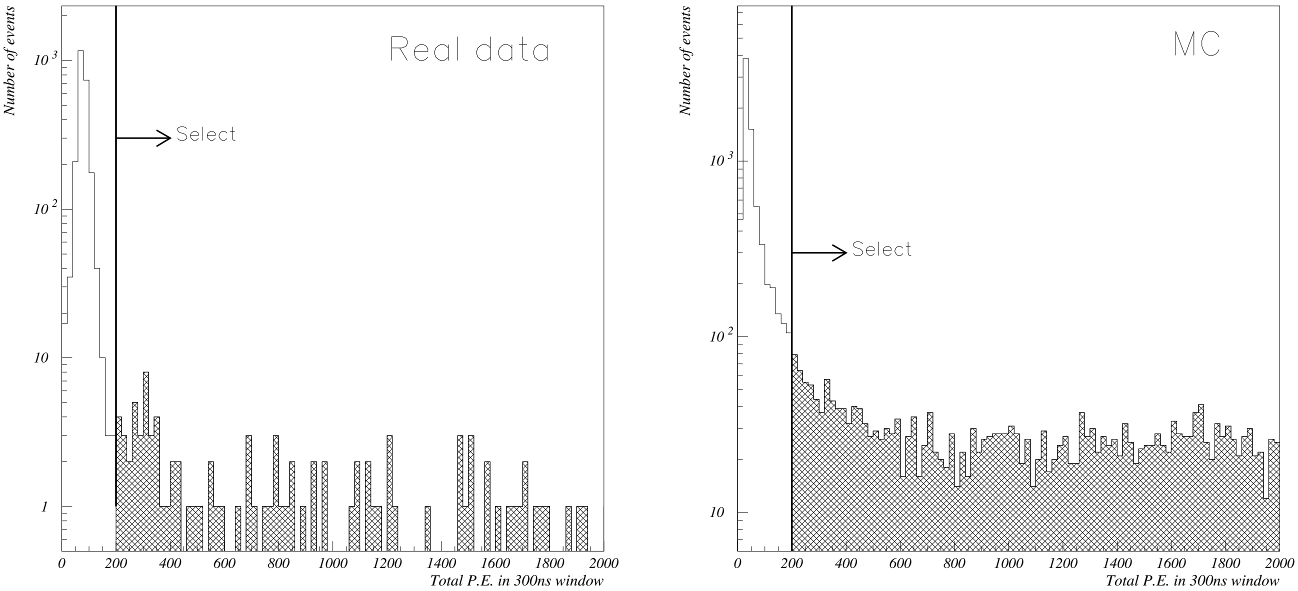

Figure 10.1: Number of photo-electrons with 300 ns window distribution of SK. Left figure shows that of data and right one shows that of MC. Most of unselected events of MC sample are from NC events, while that of data are from the background events. For example, gamma rays from the rock.

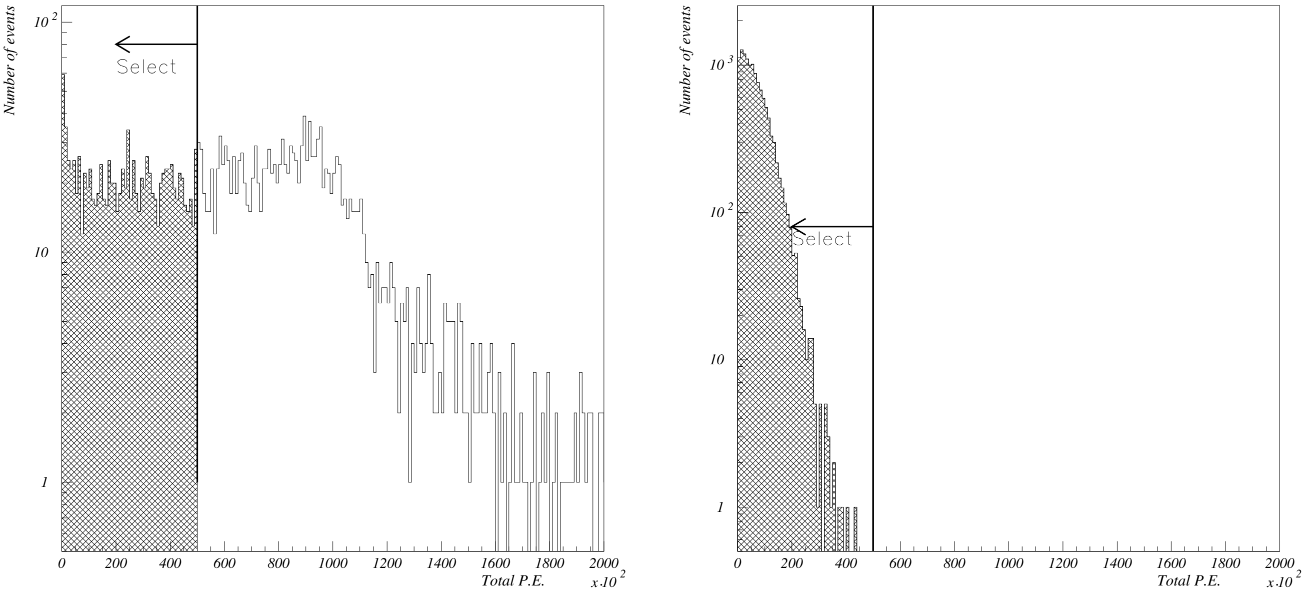

Figure 10.2: Total number of photo-electron distribution of SK events. Left figure shows that of data and right one shows that of MC. Unselected events mainly come from through going cosmic ray muons.

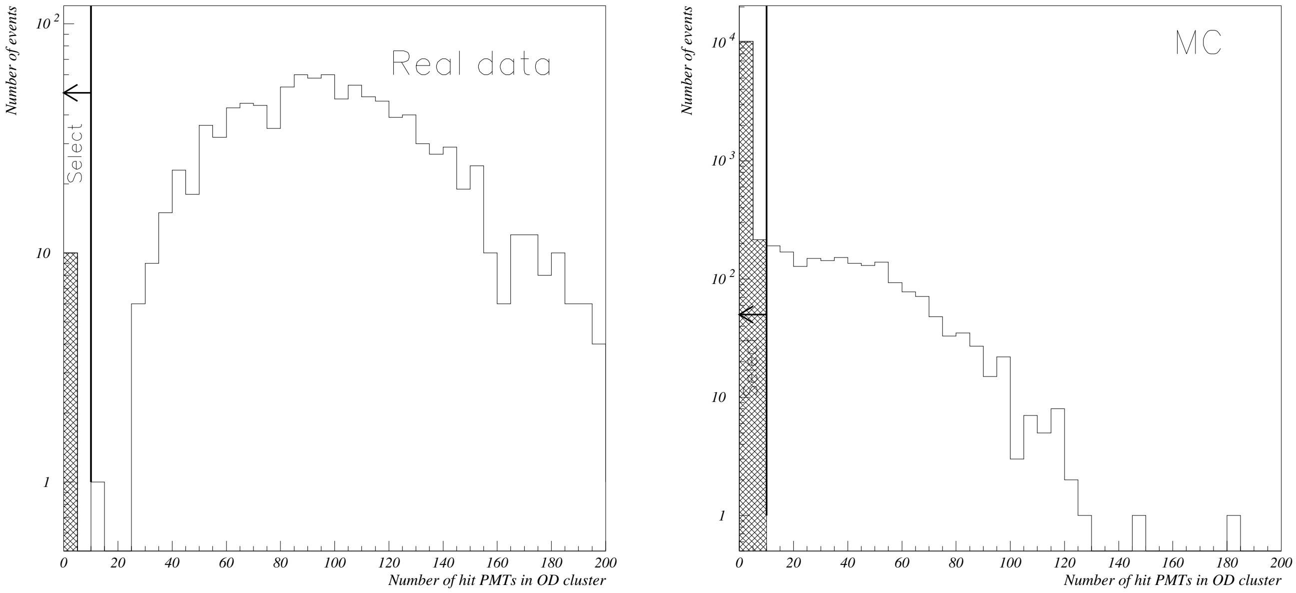

Figure 10.3: The number of OD hit PMTs in the largest hit cluster distribution of SK events. Left figure shows that of data and right one shows that of MC. Reduced events of the MC sample are thought to be out-going muon events from inner detector, while that of the data are from cripped muon events from cosmic ray.

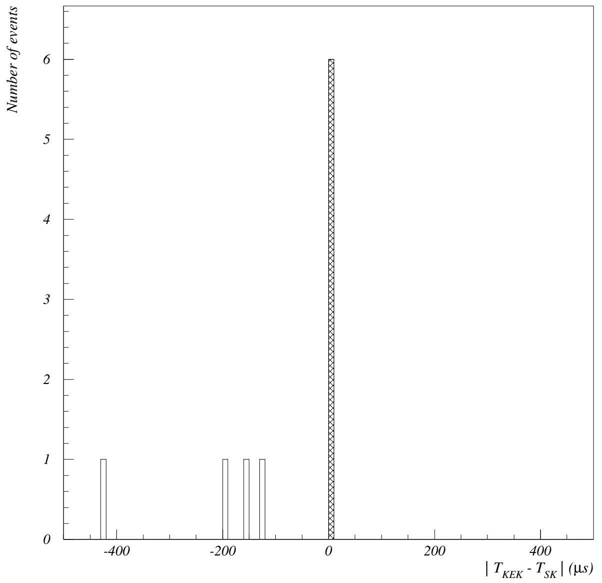

Figure 10.4: $(T_{KEK} - T_{SK})$ distribution of the SK events. We selected the events with $(T_{KEK} - T_{SK}) < \pm 5$ μs at this stage.

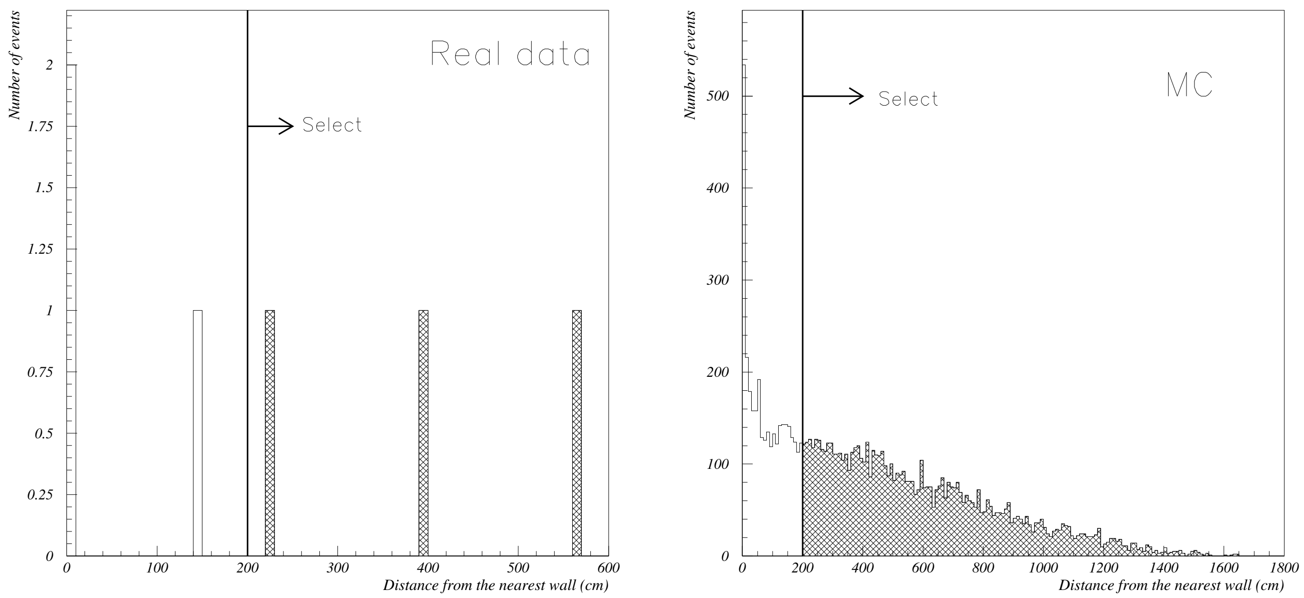

Figure 10.5: The distribution of the distance from the wall of SK events. Left figure shows that of data and right one shows that of MC.

8. Select the events which have more than 2 meter distance from the vertex to the nearest wall (Fiducial volume cut). Fig. 10.5 shows the distribution of the distance from the wall of SK events.

Number of selected events at each step is summarized in table 10.1.

Selection criteria	Data	MC
GPS ±500 μs cut	47738	19694
Decay electron cut	40279	19694
HE trigger cut	5227	19694
P.E. with 300 ns window cut	2832	12257
Total P.E. cut	1060	12257
Nhit PMTs in OD cut	10	10470
GPS ±5 μs cut	6	10470
Fiducial volume cut	3	7211

Table 10.1: Summary of the number of selected events at each step. In MC simulation, we randomized the vertex at SK inside the inner detector.

Final selected number of events is **3**. Expected number of background events from the atmospheric neutrino are 1.6×10^{-3} within ±5 μs time window* , since we used 1.38×10^{6} spills for analysis.

10.2 Charercteristics of Observed Neutrino Events at SK

After the selection, we have three candidates in 1999 Physics Runs. An event display of the first candidate is shown in Fig. 10.6. Other two samples of events are shown in Figs. 10.7 and 10.8.

The first candidate is thought to be a three-ring-event. From a timing information of the hit PMTs, one ring is guessed to come from a decay electron from a muon.

Time difference, (T_{KEK} - T_{SK}), of these events is shown in Fig. 10.9, where time of flight of neutrino and cable lengths are taken into account. This figure convinced us to have connected KEK and SK successfully with an invisible straight line of 250 km.

---

* Here the event rate of the atmospheric neutrino are assumed to be 10 event/day in fiducial volume in SK.

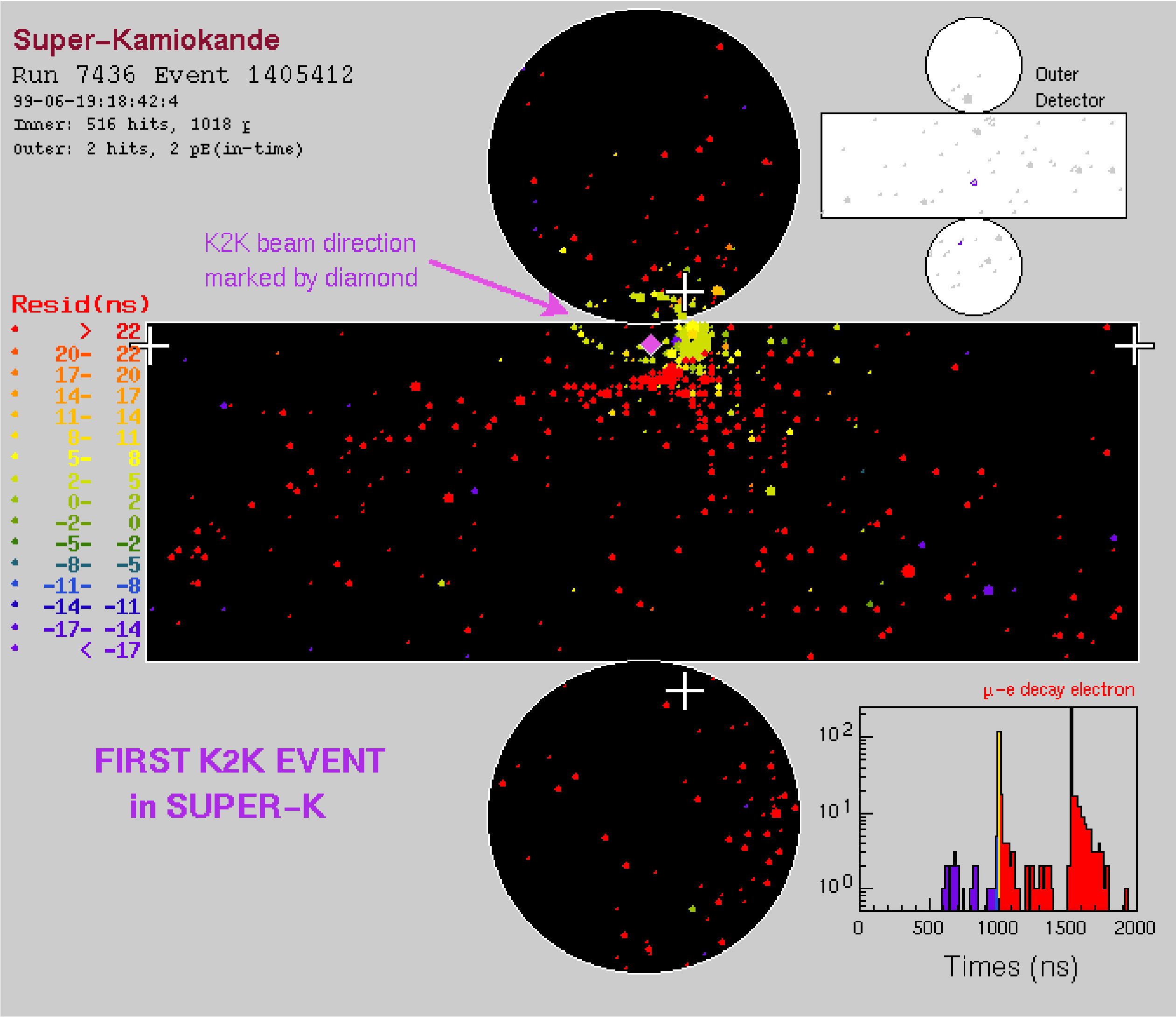

Figure 10.6: First observation of accelerator origin neutrino beam after passing through 250 km of earth.

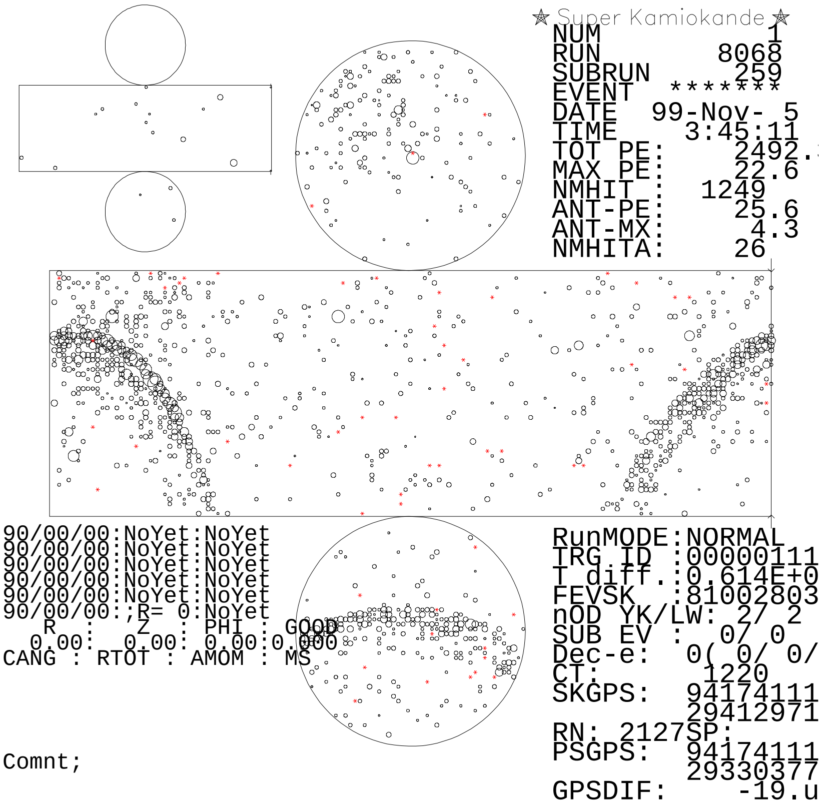

```
NUM        1
RUN     8068
SUBRUN   259
EVENT  *******
DATE   99-Nov- 5
TIME    3:45:11
TOT PE:    2492.
MAX PE:     22.6
NMHIT :   1249
ANT-PE:     25.6
ANT-MX:      4.3
NMHITA:     26

90/00/00:NoYet:NoYet
90/00/00:NoYet:NoYet
90/00/00:NoYet:NoYet
90/00/00:NoYet:NoYet
90/00/00:NoYet:NoYet
90/00/00:;R= 0:NoYet
   R  :   Z  : PHI  : GOOD
 0.00:  0.00:  0.00:0.000
CANG : RTOT : AMOM : MS

Comnt;

RunMODE:NORMAL
TRG ID :00000111
T diff.:0.614E+0
FEVSK  :81002803
nOD YK/LW: 27  2
SUB EV :   0/ 0
Dec-e:   0( 0/ 0/
CT:        1220
SKGPS:   94174111
         29412971
RN: 2127SP:
PSGPS:   94174111
         29330377
GPSDIF:     -19.u
```

Figure 10.7: Typical one ring μ-like event.

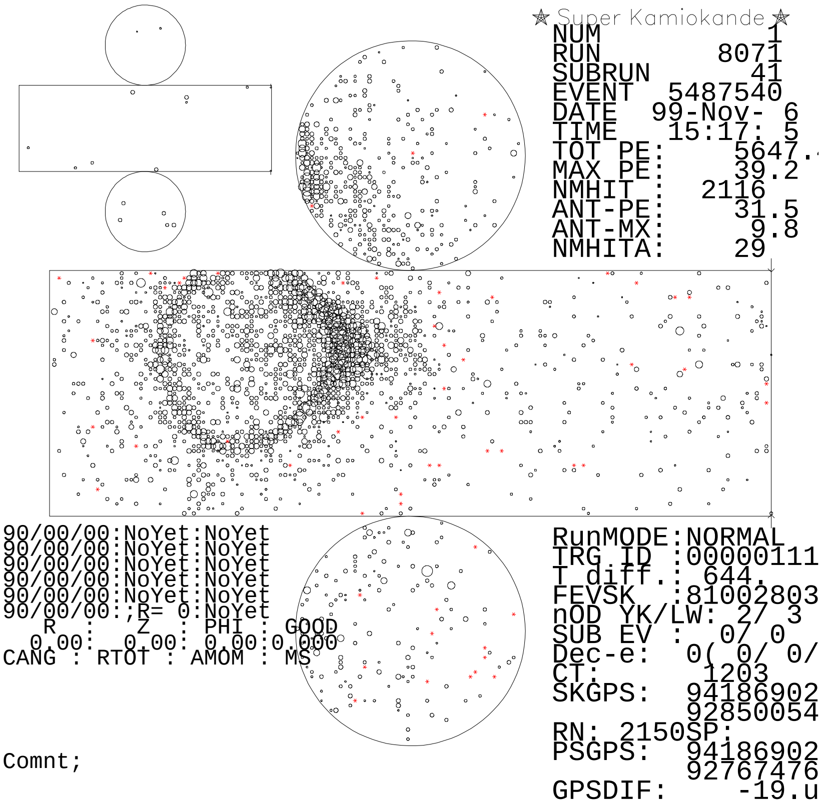

```
NUM        1
RUN     8071
SUBRUN    41
EVENT  5487540
DATE   99-Nov- 6
TIME   15:17: 5
TOT PE:    5647.
MAX PE:     39.2
NMHIT :   2116
ANT-PE:     31.5
ANT-MX:      9.8
NMHITA:     29

90/00/00:NoYet:NoYet
90/00/00:NoYet:NoYet
90/00/00:NoYet:NoYet
90/00/00:NoYet:NoYet
90/00/00:NoYet:NoYet
90/00/00:;R= 0:NoYet
   R  :   Z  : PHI  : GOOD
 0.00:  0.00:  0.00:0.000
CANG : RTOT : AMOM : MS

Comnt;

RunMODE:NORMAL
TRG ID :00000111
T diff.:  644.
FEVSK  :81002803
nOD YK/LW: 27  3
SUB EV :   0/ 0
Dec-e:   0( 0/ 0/
CT:        1203
SKGPS:   94186902
         92850054
RN: 2150SP:
PSGPS:   94186902
         92767476
GPSDIF:     -19.u
```

Figure 10.8: Third candidate of K2K

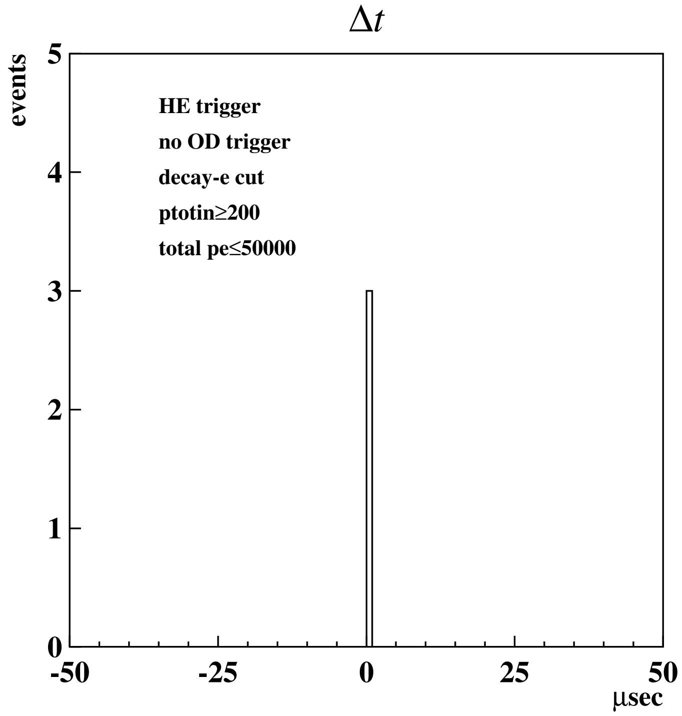

Figure 10.9: Time difference, (T_{KEK} - T_{SK}), of K2K event candidates in the fiducial volume of SK.

Chapter 11

Comparison between Expected and Observed Number of Neutrino Events at SK

We observed 3 fully contained events at SK, where $11.34^{+1.70}_{-1.83}$ is expected. In the Poisson distribution which has an average of 11.34 and is smeared by a Gaussian with the attached error, the probability which we observe 3 or less events is 0.80%. The definition of this probability is expressed as follows:

$$P(x \leq n, \mu_0 \pm \Delta\mu) = \frac{\int_0^\infty \sum_{x=0}^{n} \frac{e^{-\mu}\mu^x}{x!} \cdot e^{\frac{-(\mu-\mu_0)^2}{2\Delta\mu}} d\mu}{\sqrt{2\pi\Delta\mu}} \tag{11.1}$$

,where n, μ_0 and $\Delta\mu$ are the number of observed events, the average of the Poisson distribution and the error of μ_0, respectively. In the real case, we have an asymmetric error. It was taken into account.

By this probability test, we definitely confirmed that the muon neutrino flux of the GeV energy region decreased after traveling 250 km. The standard model neutrino hypothesis is excluded with 98.4%C.L. (Fig. 11.1).

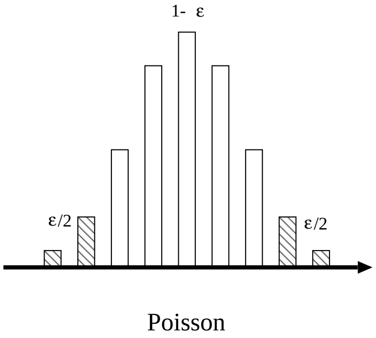

Figure 11.1: The probability test using a Poisson distribution.

We can discuss neutrino oscillation parameters, ($\sin^2 2\theta$, Δm^2), if we assume this deficit of events comes from the neutrino oscillation. However, the best fit parameter ($\sin^2 2\theta$, Δm^2) lies in the unphysical region. This may be due to the small statistics. In the near future, the high statistics data would show a reasonable and the physical solution if this deficit is caused by the neutrino oscillation. If we restricted in the physical region, our data show the most probable point to be (1.0, 7.0×10^{-3}). At this point, the expected number of events at SK is 4.18. The probability that this case occurs is 18.2%.

Chapter 12

Conclusion

We are performing the KEK-Kamioka long base-line neutrino experiment to search for the neutrino oscillation suggested by the Kamiokande results. In order to carry out this experiment successfully, we prepared a pion monitor and a muon monitor as secondary beam monitors. The pion monitor was used to determine kinematics of produced pions just after a production target to estimate neutrino beam properties. The muon monitor behind a beam-dump after a decay volume was used to measure a muon profile to steer the neutrino beam.

The pion monitor successfully measured angle and momentum of pions. From this data, we can predict the energy spectrum of the neutrino beam at the near detector and SK. Regarding the ratio of neutrino event rate at the near detector and SK, we achieved the accuracy within $^{+9.1\%}_{-10.1\%}$ for the June run and $^{+5.4\%}_{-8.7\%}$ for the November run, in 1999.

The neutrino beam-line was successfully directed toward SK employing the GPS. We steered the neutrino beam direction to SK within 1 mrad with the muon monitor. The muon range detector as near detector measured the neutrino events. The neutrino beam direction to SK was confirmed by the muon range detector to be within 1 mrad. Measured properties of the neutrino beam: the profile of the neutrino beam and the energy spectrum and the angle of generated muons by charged current neutrino interactions, are consistent with the MC expectation.

GPS system successfully synchronized the timing between KEK and SK. With utilizing this timing synchronization, $\sim 5.0\times 10^{-6}$ reduction of background events is achieved, resulting 1.6×10^{-3} background events from atmospheric neutrinos.

In June and November, 1999, we injected a total of 7.5×10^{18} protons on the target of which 6.6×10^{18} is used for the analysis. Three fully contained neutrino events were observed in the fiducial volume of SK. Expected number of neutrino events at SK is calculated by use of the pion monitor and the near detector data to be $11.34^{+1.70}_{-1.83}$. The probability that we observed 3 events or less against this expectation is 0.80%. We definitely confirmed that the muon neutrino flux of the GeV energy region decreased after traveling 250 km. The standard model neutrino hypothesis is excluded with 98.4%C.L..

If we assume this deficit of the number of neutrino events is caused by the $\nu_\mu \rightarrow \nu_\tau$neutrino oscillation, the most probable combination of ($\sin^2 2\theta$, Δm^2) in physical region is (1.0, 7.0×10^{-3}). At this point, the expected number of neutrino events at SK is 4.18, and probability of the case that we have 3 events is 18.2%.

Appendix A

K2K Result as of September 2000

We observed 27 fully contained events at SK, where $40.3^{+4.7}_{-4.6}$ is expected. Fig. A.1 shows the timing of the neutrino events observed at SK with respect to the beam timing, $(T_{SK} - T_{KEK})$. Summary of the observed number of events and the expected number of events for various event category is given in Table A.1. For this data set, the probability which we observe 27 or less events is 4.4%.

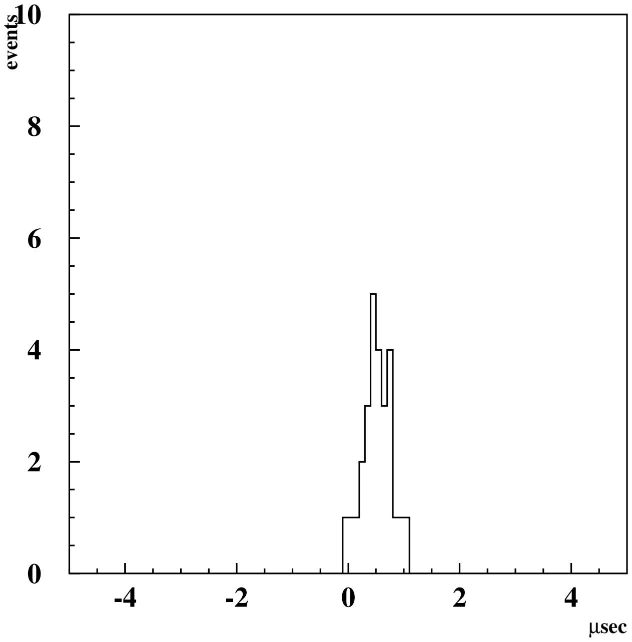

Figure A.1: The timing of the neutrino events observed at SK with respect to the beam timing, (T_{KEK} - T_{SK}). (from June 1999 to June 2000)

By this probability test, we observed that the muon neutrino flux of the GeV energy region decreased after traveling 250 km. The standard model neutrino hypothesis is excluded with 91.2%C.L..

We can discuss neutrino oscillation parameters, ($\sin^2 2\theta$, $\Delta \mathrm{m}^2$), if we assume this deficit of events comes from the neutrino oscillation. When one discusses a neutrino oscillation hypothesis based on the total number of events, the best fit parameter lies on the line in ($\sin^2 2\theta$, Δm^2) space. The most probable Δm^2 value is 3.0×10^{-3} eV^2 in case of maximal mixing.

Fig. A.2 shows the visible energy (electron equivalent energy) of 27 neutrino events at SK. The visible energy is calculated as follows:

1. The total photo-electron of each event is corrected according to the vertex position and the direction of the particle.

Event category	Observed	Expected
Single ring μ-like events	14	21.9
Single ring e-like events	1	2.4
Multi ring	12	16.0
Total	27	$40.3^{+4.7}_{-4.6}$

Table A.1: Summary of the observed number of events and the expected number of events for various event category.

2. Employing the MC simulation, the table for the relationship between the corrected photo-electron and electron energy is made.
3. We translate the corrected photo-electron to the electron equivalent energy using this table.

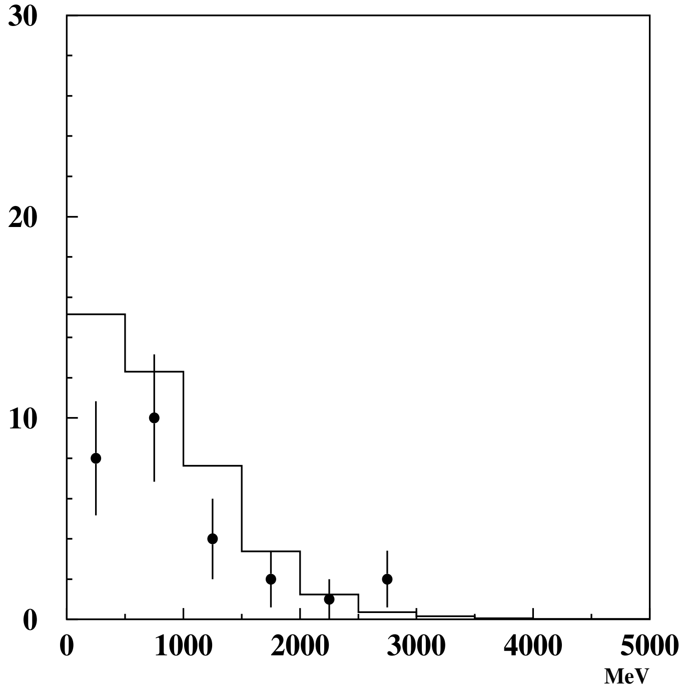

Figure A.2: Visible energy (electron equivalent energy) of the neutrino events observed at SK. Black circle with error bar shows the data and the histogram shows MC expectation without neutrino oscillation. The MC expectation still has uncertainties of the neutrino cross section, the neutrino flux, and so on, which are under study.

The MC expectation still has uncertainties of the neutrino cross section, the neutrino flux, and so on, which are under study.

Fig. A.3 shows the reconstructed muon momentum and muon angle with respect to KEK of 14 single ring muon like events. Fig. A.4 shows the reconstructed neutrino energy of the 14 single ring muon like events. We assume these muons to be the final state charged leptons generated in quasi-elastic ν_μ interaction.

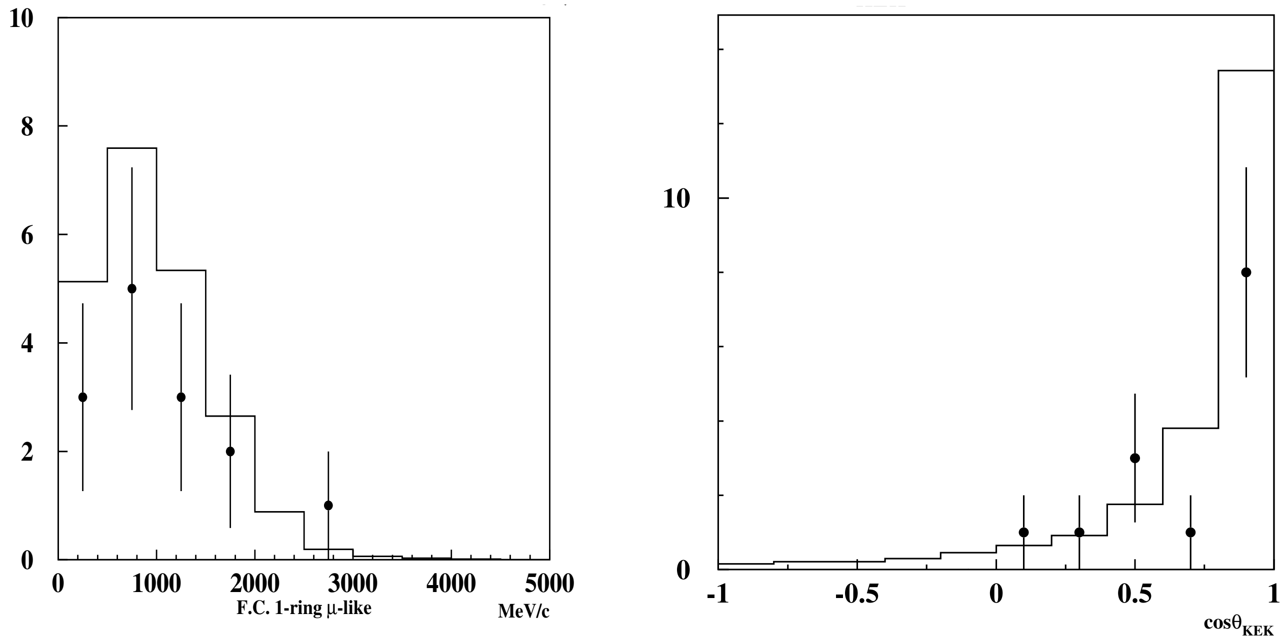

Figure A.3: The reconstructed muon momentum and muon angle with respect to KEK of 14 single ring muon like events observed at SK. Left: muon momentum, right: muon angle. Black circle with error bar shows the data and the histogram shows MC expectation without neutrino oscillation. The MC expectation still has uncertainties of the neutrino cross section, the neutrino flux, and so on, which are under study.

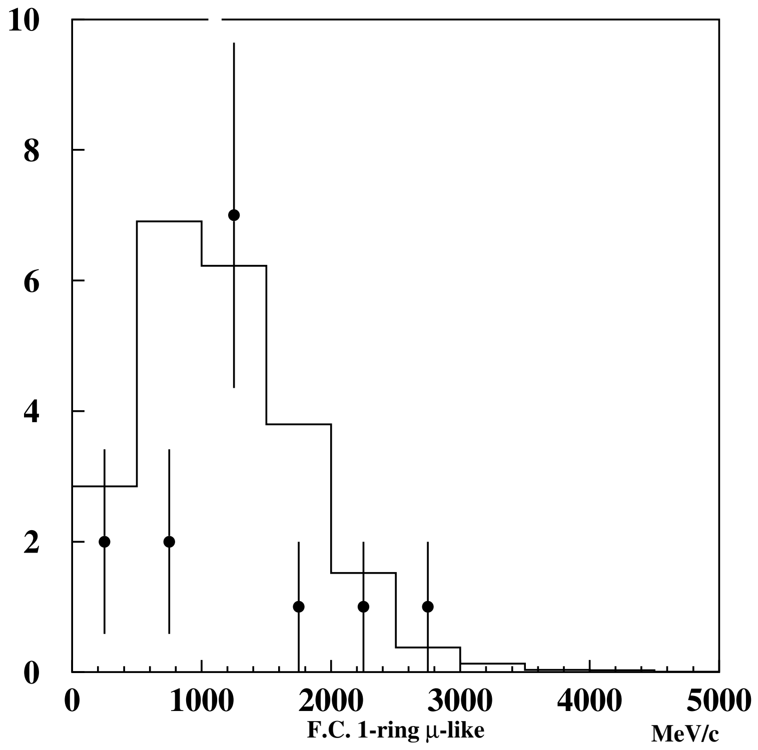

Figure A.4: Reconstructed neutrino energy of the 14 single ring muon like events observed at SK. We assume these muons to be the final state charged leptons generated in quasi-elastic ν_μ interactions. Black circle with error bar shows the data and the histogram shows MC expectation without neutrino oscillation. The MC expectation still has uncertainties of the neutrino cross section, the neutrino flux, and so on, which are under study.

Appendix B

Phenomenology of Neutrino Mass and Oscillation

B.1 Models of Neutrino Masses

We have two ways to generate the neutrino masses. One is to introduce right-handed neutrinos. The other way is to treat the neutrinos as Majorana[9] particles. One can naturally obtain small neutrino masses through the seesaw mechanism[80] utilizing the extremely heavy right-handed neutrinos.

B.1.1 Dirac Mass

The simplest way to describe the neutrino mass is to introduce right-handed neutrinos. In this case, the mass term of Lagrangian is;

$$\mathcal{L}_{Dirac} = -(\bar{\nu}_L \mathcal{M} \nu_R + \bar{\nu}_R \mathcal{M}^\dagger \nu_L), \tag{B.1}$$

where weak eigenstates,$\nu_{L,R}$, are given by

$$\nu_{L,R} = \begin{pmatrix} \nu_e \\ \nu_\mu \\ \nu_\tau \end{pmatrix}_{L,R} . \tag{B.2}$$

In general, M is the 3×3 complex matrix. Since it is not guaranteed to be positive, we need to bi-diagonalize this matrix using two Unitary matrices, U and V like,

$$U^\dagger \mathcal{M} V = m_D = \begin{pmatrix} m_1 & 0 & 0 \\ 0 & m_2 & 0 \\ 0 & 0 & m_3 \end{pmatrix}, \tag{B.3}$$

where U and V are the matrices which relate the mass eigenstates, $\nu_{L,R}^{(m)}$, to weak eigenstates, $\nu_{L,R}$, as follows;

$$\nu_L = U \nu_L^{(m)} \tag{B.4}$$

$$\nu_R = V \nu_R^{(m)}. \tag{B.5}$$

The diagonalized mass Lagrangian is expressed by following equation;

$$\mathcal{L}_{Dirac} = -\bar{\nu}_L^{(m)} m_D \nu_R^{(m)} + h.c. \quad . \tag{B.6}$$

We regard the matrix U as the leptonic Kobayashi-Maskawa[81] matrix. And we may assume the interaction between ν_R and matter is very weak since there is no evidence for existence of ν_R. Further we may expect ν_R has (V+A), (space-time vector + axial vector structure), type charged current via the $W_R^{\pm}$. This $W_R^{\pm}$ may be expected to be much heavier than observed $W^{\pm}$ exchange. However it has never been found. (Only the lower limit of the $W_R^{\pm}$ mass is given[82] experimentally.)

B.1.2 Majorana Mass

If neutrinos are the same as their anti-particles, they are called Majorana neutrinos. In this case, neutrinos are single particles and their two states are the only different helicity states with the mass. The mass of Majorana neutrinos are described using only ν_L,

$$\mathcal{L}_{Majorana} = -\frac{1}{2}\bar{\nu}_L^C \mathcal{M} \nu_L + h.c. \quad , \tag{B.7}$$

where ν_L^C is a right-handed neutrino. $\mathcal{M}$ is symmetric and can be diagonalized by one unitary matrix U. And U relates $\nu_L^{(m)}$ to ν_L,

$$\nu_L \;=\; U\nu_L^{(m)}. \tag{B.8}$$

Therefore Eq. B.7 can be rewritten using this,

$$\mathcal{L}_{Majorana} = -\frac{1}{2}\Big[\bar{\nu}_L^C m_D \nu_L + \bar{\nu}_L m_D \nu_L^C\Big]. \tag{B.9}$$

where,

$$U^{\dagger}\mathcal{M}U = m_D. \tag{B.10}$$

Moreover if we re-define the neutrino states by the formula,

$$\nu_{Maj} \equiv \nu_L + \nu_L^C, \tag{B.11}$$

this clearly shows one Majorana neutrino and the Lagrangian can be further rewritten,

$$\mathcal{L}_{Majorana} = -\frac{1}{2}\bar{\nu}_{Maj} m_D \nu_{Maj} \quad . \tag{B.12}$$

B.1.3 Dirac-Majorana Mass and Seesaw Mechanism

An interesting Dirac-Majorana Lagrangian in one generation case is expressed by a following equation.

$$\mathcal{L}_{D-M} = -\bar{\nu}_L M \nu_R - \frac{1}{2}\Big(\bar{\nu}_L^C m_L \nu_L + \bar{\nu}_R^C m_R \nu_R\Big) + h.c. \quad , \tag{B.13}$$

where M is Dirac mass and $m_L(m_R)$ are Majorana mass. If we define the left-handed neutrino status ν, as follow,

$$\nu \equiv \begin{pmatrix} \nu_L \\ \nu_R^C \end{pmatrix}, \tag{B.14}$$

Dirac-Majorana Lagrangian is similar to the Majorana case;

$$\mathcal{L} = -\frac{1}{2}\bar{\nu}^C \mathcal{M} \nu + h.c. \tag{B.15}$$

where the mass matrix $\mathcal{M}$ is

$$\mathcal{M} = \begin{pmatrix} m_L & M \\ M & m_R \end{pmatrix}. \tag{B.16}$$

Diagonalizing $\mathcal{M}$ yields;

$$m_1 = \frac{1}{2}\sqrt{4M^2 + (m_R - m_L)^2} - \frac{m_L + m_R}{2} \tag{B.17}$$

$$m_2 = \frac{1}{2}\sqrt{4M^2 + (m_R - m_L)^2} + \frac{m_L + m_R}{2} \quad . \tag{B.18}$$

Now the mass eigenstate $\nu^{(m)}$ is defined;

$$\nu^{(m)} = \begin{pmatrix} \nu_1 \\ \nu_2 \end{pmatrix} = U\nu \tag{B.19}$$

$$= \begin{pmatrix} \cos\theta\nu_L - \sin\theta\nu_R^C \\ \sin\theta\nu_L + \cos\theta\nu_R^C \end{pmatrix} \quad , \tag{B.20}$$

where mixing angle is given by $\tan 2\theta = \frac{2M}{m_R - m_L}$. We can distinguish two different cases;

1. Case with $M \gg m_L, m_R$. In this case, m_1 and m_2 are almost degenerate. (Eq. B.18 shows $m_1 \simeq m_2 \simeq M$) And ν_1 and ν_2 have opposite CP phase. This case is called as special pseudo-Dirac neutrino[83]. We have half of active ν_L and half of sterile ν_R.

2. Case with $m_R \gg M, m_L$. If we assume ν_L=0 to simplify, we can get;

   $$m_1 \simeq \frac{M^2}{m_R} \tag{B.21}$$

   $$m_2 \simeq m_R \quad . \tag{B.22}$$

   In this case, m_1 is small, while m_2 is large. Actually, ν_L and ν_R are decoupled because of $\theta \simeq 0$. This is so-called "Seesaw mechanism"[80].

We extend the above discussion to the three generation case, like

$$m_1 = \frac{M^2}{m_R} \to \bar{m}_1 = \bar{M}\frac{1}{\bar{m}_R}\bar{M}^T \tag{B.23}$$

where all bar materials are the 3×3 matrices, further $|(\bar{m}_R)_{ij}| \gg |\bar{M}_{ij}|$ is assumed. This time, the matrix corresponding to Eq. B.16 becomes a 6×6 matrix, as following $\bar{\mathcal{M}}$;

$$\bar{\mathcal{M}} = \begin{pmatrix} 0 & \bar{M} \\ \bar{M} & \bar{m}_R \end{pmatrix}. \tag{B.24}$$

B.2 Neutrino Oscillation in Vacuum

Neutrino oscillation is an example of common quantum phenomena. In general, the mass eigenstate need not be the same as the weak eigenstate if neutrinos have a mass. Suppose the state vectors of neutrinos taking part in the weak interaction are superpositions of the state vectors of neutrinos with different masses. In this case, neutrinos with the α^{th} generation, ν_α, is expressed;

$$|\nu_\alpha\rangle \;=\; \sum_i U_{\alpha i}|\nu_i\rangle \tag{B.25}$$

where ν_i is the Dirac neutrino with a mass m_i, U is the unitary matrix, with which the weak eigenstate (ν_α) is related to the mass eigenstate (ν_i). If we consider the anti-neutrinos, U is changed to U^*.

The time evolution of the state is controlled by its energy eigenvalue. If all neutrinos in the beam have common fixed momentum p, a mass eigenstate has a following energy eigenvalue,

$$E_i^2 = p^2 + m_i^2. \tag{B.26}$$

And $|\nu_i\rangle$ satisfies the following energy eigen-equation;

$$\mathcal{H}_0|\nu_i\rangle = E_i|\nu_i\rangle \quad . \tag{B.27}$$

where $\mathcal{H}_0$ is a free Hamiltonian. The time evolution of neutrino states is expressed by the following Schrödinger equation;

$$\begin{aligned} i\frac{d}{dt}|\nu_\alpha(t)\rangle &= \mathcal{H}_0|\nu_\alpha(t)\rangle \\ &= \sum_i U_{\alpha i}E_i\;|\nu_i(t)\rangle \\ &= \sum_{i,\beta} U_{\alpha i}E_iU^*_{\beta i}\;|\nu_\beta(t)\rangle. \end{aligned} \tag{B.28}$$

We can get $|\nu_\alpha(t)\rangle$ by solving the following equation analytically;

$$\begin{aligned} |\nu_\alpha(t)\rangle &= \sum_{i,\beta} U_{\alpha i}\;exp(-iE_it)\;U^*_{\beta i}\;|\nu_\beta(0)\rangle \\ &= \sum_{i,\beta} U_{\alpha i}\;exp(-i\frac{m_i^2}{2p}t)\;U^*_{\beta i}\;|\nu_\beta(0)\rangle \\ &= \sum_\beta A_{\alpha\beta}\;|\nu_\beta(0)\rangle \end{aligned} \tag{B.29}$$

where $A_{\alpha\beta}$ shows the transition amplitude from ν_β to ν_α. We can get the transition probability by taking square of $A_{\alpha\beta}$. We use the relativistic approximation, $E_i \simeq p + m_i^2/2p$. (from Eq. B.26)

$$\begin{aligned} P(\nu_\beta \to \nu_\alpha) &= |A_{\alpha\beta}|^2 \\ &= Re\sum_{j,k} U_{\alpha j}U^*_{\beta j}U^*_{\alpha k}U_{\beta k}\;exp\Big(-i\frac{\Delta m_{jk}^2 L}{2p}\Big) \\ &= \delta_{\alpha\beta} - Re\sum_{j,k} U_{\alpha j}U^*_{\beta j}U^*_{\alpha k}U_{\beta k}\Big[1 - exp\Big(-i\frac{\Delta m_{jk}^2 L}{2p}\Big)\Big] \qquad \text{(B.30)} \\ &= \delta_{\alpha\beta} - 4\sum_{j<k} U_{\alpha j}U^*_{\beta j}U^*_{\alpha k}U_{\beta k}\sin^2\Big(\frac{\Delta m_{jk}^2 L}{4p}\Big) \qquad \text{(B.31)} \end{aligned}$$

The Unitary condition,

$$\sum_j U_{\alpha j} U^*_{\beta j} = \delta_{\alpha\beta}, \tag{B.32}$$

is used in Eq. B.30. $\Delta m^2_{jk} \equiv m^2_j - m^2_k$ is the difference of the mass squared. The time t is equal to the propagation distance L in the natural unit.

Oscillations between Two Types of Neutrinos

The oscillation probability in two generation is calculated. The mixing matrix U is the real 2×2 unitary matrix if neutrinos are the Dirac particles with finite masses, ν_1 and ν_2. It has the general form;

$$U = \begin{pmatrix} \cos\theta & \sin\theta \\ -\sin\theta & \cos\theta \end{pmatrix} \quad , \tag{B.33}$$

where θ is the mixing angle (leptonic Cabbibo angle). If we enter this relation to the Eq. B.31, then the oscillation probability is simplified;

$$P(\nu_\beta \rightarrow \nu_\alpha) \;=\; \sin^2 2\theta \sin^2\Big(\frac{\Delta m^2 L}{4p}\Big) \qquad (\alpha \neq \beta) \tag{B.34}$$

$$P(\nu_\alpha \rightarrow \nu_\alpha) \;=\; 1 - \sin^2 2\theta \sin^2\Big(\frac{\Delta m^2 L}{4p}\Big) \quad . \tag{B.35}$$

The top equation shows the transition probability and bottom equation shows the survival probability. By changing the units, we can get Eq. 1.1 which we often use;

$$P(\nu_\beta \rightarrow \nu_\alpha) \;=\; \sin^2 2\theta \; \sin^2\Big(1.27\Delta m^2 \frac{L}{E}\Big) \quad .$$

where E shows the neutrino energy(GeV) and Δm^2(eV^2) shows the difference of the mass eigenvalues squared; $\Delta m^2 = m^2_2 - m^2_1$.

Oscillations Involving Three Types of Neutrinos

U is a 3×3 unitary matrix in the 3 generation case. The oscillation phenomenon is described using 3 mass eigenvalues, (m_1,m_2 and m_3), and 4 independent parameters are included in U, (3 mixing angles, θ_{12},θ_{23} and θ_{31}, and a phase δ) This is an analogy of Kobayashi-Maskawa matrix in the quark sector[81], and it is expressed as follows;

$$U = \begin{pmatrix} c_{12}c_{13} & s_{12}c_{13} & s_{13}\, e^{-i\delta} \\ -s_{12}c_{23} - c_{12}s_{23}s_{13}\, e^{i\delta} & c_{12}c_{23} - s_{12}s_{23}s_{13}\, e^{i\delta} & s_{23}c_{13} \\ s_{12}s_{23} - c_{12}c_{23}s_{13}\, e^{i\delta} & -c_{12}s_{23} - s_{12}c_{23}s_{13}\, e^{i\delta} & c_{23}c_{13} \end{pmatrix} \tag{B.36}$$

where $c_{ij} = \cos\theta_{ij}$, $s_{ij} = \sin\theta_{ij}$, θ_{ij} is the mixing angle of two mass eigenstate, ν_i and ν_j and δ is the CP violation phase.

Appendix C

Track Finding Algorithm of Muon Range Detector

We define the z-axis of our coordinate as the neutrino beam direction. From upstream of the beam, x-axis is defined from right(north) to left(south) and y-axis is from bottom to top. The x-z plane corresponds to the top view of the detector and the y-z plane to the side view.

The track finding code (tracker) searches for tracks in 2-dimensional view: x-z and y-z views. The muon chamber module has the structure like Fig. 3.18. It consists of two 4-tube planes staggered by half cell. The tracker regards one layer as two independent drift-tube planes. A schematic 2-dimensional view of a muon track with associated hits is shown in Fig. C.1.

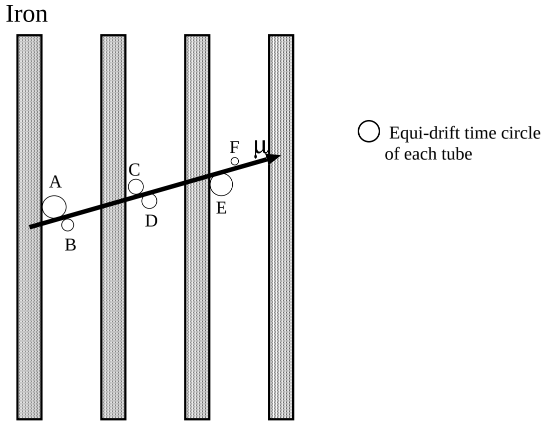

Figure C.1: A schematic 2-dimensional view of a muon track and associated hits in the muon range detector.

The muon track is found using the following procedures.

1. A straight line between two arbitrary hit tubes is considered. The hit tubes are taken in order from the longest distance. If those two hits do not satisfy the criteria, which are described below, those of the 2nd longest distance is taken. In Fig. C.1, the process to find the track starts with the tubes A and F. The shortest track passes only one iron layer. Therefore, the energy threshold of the muon track with this definition is ~250MeV, which corresponds to energy loss of a muon in one iron layer with 20cm thickness.

   The track criteria are followings. The line connecting two hits is regarded as a track if the number of hits within 1 μs along the line exceeds certain numbers. These thresholds depend on the length and the angle of the track and are summarized in table C.1. The criteria for the large angle track is tighter than small angle for the rejection of bad track made from the noise hit. We allow the distance between the hit tube and straight line to be within 7cm, considering the multiple scattering of the muon.

2. In the next step, we use timing information to get detail information of straight line and T0, which is the time of muon passing through the first drift tube (tube A in the Fig. C.1). Timing information from each tube equal to T0 Σ

Bibliography

[1] S.L. Glashow, Nucl. Phys. **22**, 579 (1961).

[2] S. Weinberg, Phys. Rev. Lett. **19**, 1264 (1967).

[3] A. Salam, "Elementary particle physics", Nobel Symp. No.8

[4] W.Pauli, *Open Letter to Radioactive Ladies and Gentlemen*, (1930) (translation into English) Physics Today **31**, 27 (1978)

[5] A.I. Belesev *et al.*, Phys. Lett. **B350**, 263 (1995)

[6] Particle Data Group, European phys. J. **C3** 1 (1998)

[7] K. Assamagan *et al.*, Phys. Rev. **D53**, 6065 (1996)

[8] R.Barate *et al.*, European Phys. J. **C2**, 395 (1998)

[9] E. Majorana, Nuo. Cim. **14**, 171 (1937).

[10] L.Baudis *et al.*, Phys. Rev. Lett. **83**, 41 (1999)

[11] Z.Maki, M.Nakagawa and S.Sakata, Prog. Theor. Phys. **28**, 870 (1962)

[12] B.Pontecorvo, Sov. Phys. **JETP6**, 429 (1957)

[13] Y. Fukuda *et al.*, Phys. Lett. **B335**, 237 (1994).

[14] R.Becker-Szendy *et al.*, Phys. Rev. **D 46**, 3720 (1992).

[15] W. W. M. Allison *et al.*, Phys. Lett. **B449**, 137 (1999).

[16] Y. Fukuda *et al.*, Phys. Lett. **B436**, 33 (1998).
Y. Fukuda *et al.*, Phys. Rev. Lett. **81**, 1562 (1998).

[17] K. Nishikawa: "A Possible Long Baseline Neutrino Oscillation Experiment Using KEK PS and Super Kamiokande", INS Report-924 Apr-1992.

[18] Development of Coordinate Transformation Program TKY2WGS, GSI technical Report, **B**·1-No.23(1994)8.

[19] H. Noumi *et al.*, Nucl. Instrum. Meth. **A398**, 399 (1997).

[20] Rika Nenpyo (Chronological Scientific Table), ed. National Astronomical Observatory, Maruzen Co., Ltd., 1997, p629, (in Japanese)

[21] OHO-'96 (written in Japanese, KEK accelerator school(1996) text).

[22] M. Ieiri *et al.*, Given at 1st Asian Particle Accelerator Conference (APAC 98), Tsukuba, Japan, 23-27 Mar 1998.

[23] KEK-PS USERS GUIDE BOOK (1992), KEK Publication.

[24] K.L. Brown *et al.*, TRANSPORT, CERN 80-04

[25] K.L. Brown and Ch Iselin, DECAY TURTLE, CERN 74-02

[26] Y. Suzuki *et al.*, Proc. of Int. Conf. on Accelerator and Large Experimental Physics Control system, (1997) 266.

[27] M.Kohama, Master thesis "The study of magnetic horns for long base-line neutrino oscillation experiment." (in japanese, unpublished)

[28] Y. Yamanoi *et al.*, KEK PREPRINT 97-225 (1997).
Y. Yamanoi *et al.*, KEK PREPRINT 99-178 (1999).

[29] F. Sauli, CERN Report 77-09 (1977).

[30] K.H. Tanaka *et al.*, KEK preprint 91-27

[31] S.Nakayama, "The data aquisition system of front water Cherenkov detector in long-baseline neutrino oscillation experiment." (Master Thesis of Tokyo U., unpublished, in japanese)

[32] A. Suzuki *et al.*, Nucl. Instrum. Meth. **A453**, 165 (2000).

[33] S. Kawabata *et al.*, Nucl. Instrum. Meth. **A270**, 11 (1988).

[34] Y. Ikegami *et al.*, IEEE Trans. Nucl. Sci. **36**, 665 (1989).

[35] KEK Data Aquisition Development Working Group, "TKO Specification",KEK Report 85-10 (1985).

[36] Y.Koshio, "Study of Solar Neutrinos at Super Kamiokande" (PhD Thesis of Tokyo U., unpublished)

[37] M.Shiozawa, "Search for Proton Decay $p \to e^+\pi^0$ in a Large Water Cherenkov Detector" (PhD Thesis of Tokyo U., unpublished)

[38] H. Kume *et al.*, Nucl. Instr. and Meth., **205**, 443 (1983).

[39] A. Suzuki *et al.*, Nucl. Instr. and Meth., **A329**, 299 (1993).

[40] C.McGrew, PhD Thesis of U.C.Irvine, unpublished

[41] T.Tanimori *et al.*, IEEE Trans. Nucl. Sci. **NS-36**, 497 (1989).

[42] "PHOTOMULTIPLIER TUBE –principle to application–" HAMAMATSU PHOTONICS K.K.

[43] GEANT–Detector Description and Simulation Tool, Application Software Group, Computing and Networks Division (1993).

[44] A.Fassó *et al.*, Proc. IV Int. Conf. on Calorimetry in High Energry Physics (1993) 493.

[45] T.A. Gabriel, J.D. Amburgey and B.L. Bishop, "'Calor': A Monte Carlo Program Package For The Design And Analysis Of Calorimeter Systems," ORNL/TM-5619.

[46] J. R. Sanford and C. L. Wang, Brookhaven National Laboratory, AGS internal report, No.BNL11299, No.BNL11479 (1967) (unpublished);
C. L. Wang, Phys. Rev. Letters **25** 1068 (1970)

[47] R.A. Lundy *et al.*, Phys. Rev. Lett. **14** 504 (1965)

[48] D. Dekkers *et al.*, Phys. Rev. **137** B962 (1965)

[49] W.F. Baker *et al.*, Phys. Rev. Lett.**7** 101 (1961)

[50] A. Yamamoto, "Study On Low-Energy Intense Kaon Beam," KEK Reports 81-13.

[51] Y. Cho *et al.*, Phys. Rev. **D 4** 1967 (1971)

[52] J. G. Asbury *et al.*, Phys. Rev. **178** 2086 (1969)

[53] G. J. Marmer *et al.*, Phys. Rev. **179** 1294 (1969)

[54] G. J. Marmer *et al.*, Phys. Rev. **D 3** 1089 (1971)

[55] J. V. Allaby *et al.*, CERN Report No. CERN-TH-70-12 (unpablished)

[56] J. D. Jackson "Classical Electrodynamics" John Wiley & Sons, Inc

[57] C. Y. Chien *et al.*, Phys. Lett. **B35** , 261 (1971).

[58] E. D. Commins & P. H. Bucksbaum, "Weak interaction of leptons and quarks" Cambridge University Press.

[59] M. Nakahata *et al.* [for KAMIOKANDE Collaboration], J. Phys. Soc. Jap. **55**, 3786 (1986).

[60] C.H.Llewellyn Smith, Phys. Rep. **3C** 261 (1972).

[61] S.J.Barish *et al.*, Phys. Rev. **D16** 3103 (1977).

[62] S.Bonetti *et al.*, Nuovo. Cimento. **A38** 260 (1977).

[63] S.V.Belikov *et al.*, Z. Phys. **A320** 625 (1985).

[64] K.Abe *et al.*, Phys. Rev. Lett. **56** 1107 (1986).

[65] C.H.Albright *et al.*, Phys. Rev. **D14** 1780 (1976).

[66] D.Rein and L.M.Sehgal, Ann. of Phy. **133** 1780 (1981).
D.Rein Z.Phys. **C35** 43 (1987).

[67] M.Glück *et al.*, Z. Phy. **C67** 433 (1995)

[68] S.J.Barish *et al.*, Phys. Rev. **D17** 1 (1978).

[69] H.Sarriko, *Neutrino 1979* 507 (1979).

[70] S.J.Barish *et al.*, Phys. Rev. **D19** 2521 (1979).

[71] P.Musset and J.P.Vialle, Phy. Rep. **C39** 1 (1978)

[72] J.E.Kim *et al.*, Rev. Mod. Phy. **53** 211 (1981)

[73] T.Sjostrand *et al.*, CERN-TH.7112/93 W5053/W5054

[74] D.Rein and L.M.Sehgal, Nucl. Phy. **B223** 29 (1983).

[75] S.Adler *et al.*, Phy. Rev. **B135** 963 (1964)

[76] T.Inagaki, Master thesis of Tokyo U. (1998: in Japanese, unpublished)

[77] J. E. Hill *et al.*, Beam Sci. Tech. **3** 18 (1998) .

[78] T.Maruyama *et al.*, K2K note 98-003 .

[79] Private comminucation with Mastumoto (AIDA experiment group)

[80] T. Yanagida, Proc. of Workshop Unified theory and Baryonn Number in the Universe (KEK, Tsukuba, Japan), 1970; Prog. Theor. Phys., **B135** (1978) 66

[81] M.Kobayashi and T.Maskawa, Prog. Theor. Phys. **49**, 652 (1979)

[82] A. Jodido *et al.*, Phys. Rev. **D 34**, 1967 (1986).
G. Barenboim *et al.*, Phys. Rev. **D 55**, 4213 (1997).
G. Beall *et al.*, Phys. Rev. Lett. **48**, 848 (1982).
W.S. Hon and A. Soni, Phys. Rev. **D32**, 163 (1985).
J. Baseq *et al.*, Phys. Rev. **D32**, 175 (1985).
P. Colaugelo and G. Nardulli , Phys. Lett. **B253**, 154 (1991).

[83] L. Wolfenstein, Nucl. Phys. **B186**, 147 (1981)